Mission-Oriented Seismic Research Program

Annual Report

2009

M-OSRP

University of Houston

Sponsors and Advisory Board representatives

Corporate Sponsors

Amerada Hess ..... Scott Morton, Jacques Leveille
Anadarko ..... Roger Reagan
BP ..... Uwe Albertin
BHP ..... Michael Richardson
ChevronTexaco ..... Debbie Bones
ConocoPhillips ..... Douglas Foster, Robert Stolt
Devon Energy ..... Kenneth Beeney
Encana ..... William Goodway, David Mackidd
ENI-Agip ..... Michele Buia
ExxonMobil ..... Peter Traynin
GX Technology ..... Nick Bernitsas, Robert Bloor
IBM ..... Tom McClure
Landmark ..... Dave Diller
Petrochina Company Limited ..... Jixiang Xu
Petrobras ..... Neiva Zago
PGS ..... Martin Widmaier, Steve Kelly
Repsol ..... Francisco Ortigosa Fernandez
Saudi Aramco ..... Yi Luo
Shell ..... Jonathan Sheiman
Statoil ..... Lasse Amundsen
WesternGeco ..... William Dragoset

Federal Support

DOE Basic Sciences award DE-FG02-05ER15697 ..... Nick Woodward
NSF-CMG award DMS-0327778 ..... Henry A. Warchall

M-OSRP Personnel

Faculty

Lasse Amundsen (Statoil) ..... Adjunct Professor (Physics)
Douglas J. Foster[1] (ConocoPhillips) ..... Adjunct Professor (Physics)
Kristopher A. Innanen (Associate Professor, University of Calgary) .. Adjunct Professor (Physics)
Robert G. Keys (ConocoPhillips) ..... Adjunct Professor (Physics)
Jacques Leveille (Amerada Hess) ..... Adjunct Professor (Physics)
Fang Liu ..... Research Assistant Professor (Physics)
Ken H. Matson (Shell) ..... Adjunct Associate Professor (Physics)
Bogdan Nita (Assistant Professor, Montclair State U.) ..... Adjunct Assistant Professor (Physics)
Partha Routh ..... Adjunct Professor (Physics)
Jon Sheiman (Shell) ..... Adjunct Professor (Physics)
Robert H. Stolt (ConocoPhillips) ..... Adjunct Professor (Physics)
T. Hing Tan (Shell) ..... Adjunct Professor (Physics)
Paolo Terenghi ..... PostDoc Fellow (Physics)
Arthur B. Weglein ..... Cullen Professor (Physics)
Daniel Whitmore (PGS) ..... Adjunct Professor (Physics)

Ph.D. Students

Xu Li ..... Physics
Zhiqiang Wang ..... Physics
Jim Mayhan ..... Physics
Shih-Ying Hsu ..... Physics
Tao Jiang ..... Geosciences
Hong Liang ..... Physics
Di Chang ..... Physics
Jinlong Yang ..... Physics

Recent Alumni

Adriana Citlali Ramirez ..... Physics
Haiyan Zhang ..... Physics
Jingfeng Zhang ..... Physics
Fang Liu ..... Physics
Zhiqiang Guo ..... Geosciences
Francisco Miranda ..... Physics
Simon A. Shaw ..... Geosciences
Jose Eduardo Lira ..... Geosciences[2]
Min Wang ..... Physics
Shansong Jiang ..... Physics

Administrative Support

Jennifer Chin-Davis ..... Business Administrator
Nguyen Tran ..... Program Accountant
Angela Cowan ..... Program Coordinator
Andrew Fortney, Marco Moncada ..... Computer/IT Support
Jesse Weglein ..... Webmaster/TLC^2
Adam Blount ..... TLC^2

[1]Chair, M-OSRP Advisory Board
[2]Petrobras, Brazil

Table of Contents

1. M-OSRP09: Introduction and Summary 1
A. B. Weglein

2. Preprocessing 3D seismic data 10
J. D Mayhan and A. B. Weglein

3. Free-Surface Multiple Prediction: numerical testing and coding update 40
P. Terenghi and A. B. Weglein

4. Efficacy determination and efficiency advances for the inverse scattering series internal multiple removal: an update, land data testing and evaluation 52
S. -Y. Hsu and A. B. Weglein

5. 3D Internal Multiple Prediction coding project: preliminary notes 61
P. Terenghi,and A. B. Weglein

6. Addressing the bandlimited nature of seismic source and rapid lateral variations of the Earth: source regularization and cascaded imaging operator 72
F. Liu and A. B. Weglein

7. Note: A derivation of the HOIS closed form 118
Z. Wang, A. B. Weglein and F. Liu

8. Note: Evaluations of the HOIS closed form and its two variations 126
Z. Wang, A. B. Weglein and F. Liu

9. New capture of direct velocity independent depth imaging in a one-dimension two-parameter acoustic Earth 137
Z. Wang, A. B. Weglein and X. Li

10. Analysis of forward and inverse series for target identification 144
X. Li and A. B. Weglein

11. An unanticipated and immediate AVO by-product (responding to pressing type I and type II AVO challenges) delivered within the ISS imaging program 154
X. Li, A. B. Weglein and H. Liang

12. Initial tests for the impact of matching and mismatching between the earth model and the processing model for the ISS imaging and parameter estimation 165
H. Liang, A. B. Weglein, and X. Li

13. Reverse-time migration and Green's theorem: A new and consistent theory that progresses and corrects current RTM concepts and methods 181
A. B. Weglein R. H. Stolt and J. D Mayhan

2009 M-OSRP Annual Report Introduction and Summary

This year was another positive year for M-OSRP with significant contributions and progress to report. Among contributions/advances are : (1) delivery of proprietary M-OSRP software for multiple removal, and advances in the soon to be delivered 3D wave theoretic preprocessing for deghosting, data reconstruction and wavelet estimation; (2) progress pushing the theory and practical fronts towards developing greater inverse scattering series (ISS) robust capability and testing of the inverse scattering series (ISS) imaging and direct non-linear AVO projects; the former development and tests indicating the next step as a first field data ISS imaging test, and the latter the early positive tests of a new direct imaging ISS exploration AVO tool; (3) first and historic on-shore tests and evaluation of ISS internal multiple effectiveness, both in absolute terms, and in comparison with other methods, and (4) a method for increased internal multiple efficiency was developed and tested and (5) a new and comprehensive Green's theory method for reverse-time migration (RTM) that addresses shortcomings in the theory and application of current Green's Theorem RTM concepts and methods where the latter can lead to imaging errors and artifacts.

The papers in this 2009 M-OSRP Annual Report represent M-OSRP contributions, while papers submitted and/or published in cooperation/collaboration with sponsors, and/or external collaborators, are in a separate file, associated with, but distinct from, the Report. Both the 2010 M-OSRP Annual Report (2010 AR)and the Associated File (AF) are on one CD/DVD. In this Introduction please find: (1) a summary of this past year's M-OSRP highlights, deliverables, and progress within our different projects, (2) a link to a set of 4 papers published in Geophysics, and their significance and impact, reference to the 3 2010 SEG Expanded Abstracts, and all are in the Associated File, and (3) our plans for the coming year. Below we provide highlights for this past year (Please see the first link below for details behind each of these highlights).

Multiples

(1) Delivery of the inverse scattering series 3D Free Surface Multiple Elimination code (ISS 3D FSME). The method was developed by P.M. Carvalho, coded for M-OSRP by S. Kaplan, and tested by a ConocoPhillips team led by Simon Shaw and Haiyan Zhang with M-OSRP support from Kris Innanen and an important debugging contribution by Zhiqiang Wang. The data tested was supplied by WesternGeco, Statoil and Livermore National Lab. This code represents the high-water mark of capability for predicting the amplitude and phase of free surface multiples, of all orders. Given its prerequisites of: (1) adequate data collection and/or data reconstruction, (2) source and receiver de-ghosting, and (3) source signature removal, the algorithm then represents both prediction and subtraction, with equal effectiveness at all offsets, and without the need for residual Radon as is common for codes delivered from other consortia or vendors. There is a removal or reduced dependence on a separate "subtraction" step, typically in practice with an adaptive subtraction algorithm. The adaptive subtraction is called upon for dealing with all of reality omitted in your

"prediction" and is especially useful for dealing with clear and isolated multiples. However, the energy minimization criteria behind adaptive "subtraction" can fail precisely when the prediction it is meant to serve, the inverse scattering series FSME code, has its greatest strength. Given its three prerequisites (listed above), the ISS FSME predicts and subtracts free surface multiples independent of whether they overlap/interfere with other events, or whether there are primaries and different orders of free-surface multiples and internal multiples in the neighborhood. The 3D ISS FSME from M-OSRP is more effective and costly than other 3D FSME algorithms. However, as an industry we didn't go from 2D to 3D to save cost in processing. We took that 2D to 3D step to gain effectiveness, and to reduce the cost of drilling dry wells, and we suggest that the 3D ISS FSME code, within your toolbox, be considered when the target and overburden are complex and difficult for other de-multiple methods, including less costly and less effective 3D FSME algorithms. This high end predictive emphasis and delivery and differential added-value is a general M-OSRP multiple removal strategic ear-mark and driver and is particularly significant for complex off-shore plays (e.g., subsalt, sub-basalt) with complicated and proximal events and for on-shore application. A list of all de-multiple and prerequisite satisfaction codes delivered to sponsors can be found in the link below. The codes themselves are in the sponsor-only portion of our web site.

Dr. Paolo Terenghi joined M-OSRP in October 2009 and continued developing the free-surface multiple prediction code in order to facilitate and extend its ability to accommodate field data and realistic synthetics. With the latest changes, the code can operate in the case of all different spatial sampling rates along spatial axes. New numerical examples have been produced using the data supplied by WesternGeco, Statoil and Livermore National Lab at an in-line aperture wider than was previously tested. Further detail can be found in this report ("3D Free-Surface Multiple Prediction: numerical testing and coding update", AR page 40) . The revised code will be available to the sponsors shortly after the June 1-4 , 2010 Annual Meeting.

(2) 3D Prerequisite satisfaction

Jim Mayhan has coded and tested 3D Green's theorem based methods for: (1) data reconstruction, (2) source wavelet estimation, and (3) deghosting, and those codes will be delivered to M-OSRP sponsors after the 2010 Annual Meeting ("Preprocessing 3D seismic data", AR page 10). Those important methods and contributions were pioneered and developed within the dissertations of M-OSRP Alumni Dr. Jingfeng Zhang (BP) and Dr. Adriana C. Ramírez (WesternGeco). These Green's theorem based prerequisite satisfaction methods are entirely consistent with the multi-dimensional wave theory inverse scattering methods for removing multiples and depth imaging primaries, that they are meant to serve, and in particular they make no assumptions about subsurface information. The water-speed imaging in the ISS imaging project is consistent with wave-theoretic imaging from Green's Theorem. Jim also completed a successful internship at ExxonMobil.

Advances in acquisition

There are important advantages to having both the pressure and its normal derivative measured along a towed streamer(s) marine experiment. PGS has provided such a dual measurement data set for M-OSRP testing. Those tests will happen in 2010 and the results will be shared with all

sponsors. Jim Mayhan is doing an excellent job progressing the prerequisite development project and managing the PGS opportunity.

On-Shore Project

(3) Shih-Ying Hsu has completed two successful back to back internships at WesternGeco and Saudi Aramco. Shih-Ying will report on her encouraging results for realistic synthetic data using ISS internal multiple algorithms at the 2010 M-OSRP Annual Meeting. Her contributions were part of collaborative research during her internships at Saudi-Aramco and WesternGeco, where evaluations and comparisons of ISS internal multiple efficacy for land data application, and advances in ISS internal multiple efficiency were developed and tested, respectively. Those SEG Expanded Abstracts are distributed associated with this Report and located in the AF.

The first Abstract "The inverse scattering series approach towards the elimination of land internal multiples" by Fu et al. (located in the AF), represents the testing and analysis of realistic synthetic and on-shore field data. Tests within the ARAMCO EXPEC ARC Geophysical Technology Team, managed by Panos Kelamis, and the multiple removal group led by Yi Luo. Shih-Ying Hsu, a graduate student from M-OSRP, interned under the mentorship of Yi Luo and participated in those tests and comparisons. On-shore internal multiples can often over-lap with primaries, making the multiple removal without damaging primaries very difficult, so difficult in fact that marine pre-salt internal multiple removal can pale in comparison. Under the most complex and daunting circumstances, the inverse scattering series internal multiple produced encouraging and positive results, and no other internal multiple method was able to match that effectiveness. This is an important advance and contribution and we congratulate Yi Luo, Panos G. Kelamis, Qiang Fu, ShouDong Huo, Ghada Sindi, Shih-Ying Hsu, and the entire Saudi Aramco team!

The second Abstract is "Quasi-Monte Carlo integration for the inverse scattering internal multiple attenuation algorithm" by Shih-Ying Hsu, M-OSRP/UH, Einar Otnes and Adriana C. Ramírez of WesternGeco (located within the AF). This research was led by Einar Otnes within Alan Teague's research group at WesternGeco, while Shih-Ying Hsu was an intern being mentored by Einar Otnes and Adriana C. Ramírez, with support from the WG team. The inverse scattering series (ISS) algorithms have a high degree of predictive effectiveness, and are automatic, and demonstrate their mettle under the most complex circumstances as demonstrated by earlier published marine examples (e.g., Carvalho et al., (1992) and Matson et al., 1998)) and now, this past year, the first published land application, Fu et al. (2010) (please see the AF). The M-OSRP High Performance Computing Committee chaired by Nicola Bienati of ENI gave a green light for us to produce a 3D internal multiple code, although the computational challenge is formidable (please see M.Perrone et al. ,IBM, 2007 M-OSRP Annual Meeting). This Abstract represents an innovative and significant response from the algorithmic side towards addressing that computational challenge, with a four fold speed-up in 2D and anticipated greater speed-up in 3D. This contribution will support applying this capability in the 3D marine arena and will spur further innovative code progress and new hardware to be developed, as well. We congratulate Shih-Ying Hsu, Einar Otnes and Adriana C. Ramírez and the entire WG team. A report "Efficacy determination and efficiency advances for the inverse scattering series internal multiple removal: an update, land data testing and evaluation" by Shih-Ying Hsu at al. (located in the AR on page 52) provides a perspective overview of all her contributions this year.

Work is progressing on a wavelet estimator for on-shore application, based on the Green's theory methods developed in Weglein and Secrest (1990). The idea is to increase the predictive capability, and simultaneously reduce the burden on the adaptive step for increased internal multiple removal effectiveness. The goal is moving towards surgical removal of multiples, which is so often essential for land application. Early synthetic tests of a wavelet estimator aimed at land application will be shown at the June 1-4, 2010 Annual Meeting.

3D ISS Internal Multiple Code development

(4) Dr. Paolo Terenghi will be coordinating these M-OSRP de-multiple efforts, and will code, test and deliver a 3D ISS Internal Multiple Attenuation code in 2010. A preliminary study ("3D Internal Multiple Prediction coding project: preliminary notes", AR page 61) outlines a plan for the new coding project and analyzes and reviews the optimizations and programming strategies adopted for the previous 2D implementations.

Imaging Project

(5) The imaging project's earlier progress is described in some detail in last year's 2008 M-OSRP Introduction to the Annual Report as well as in presentation slides in the link below. A submitted 2010 SEG Expanded Abstract "The inverse scattering series depth imaging algorithms: development, tests and progress towards field data application" is found on AF and provides a glimpse at this year's progress on the imaging project.

The ISS contains the capability to perform all processing goals directly in terms of the data and a reference medium Green's function. That's quite an undertaking, with the ISS having many issues to deal with, given the data and a "no-thank you, no-help whatsoever directly or indirectly needed attitude", the latter " no help needed" in terms of no need for actual or approximate subsurface properties. The imaging terms within the ISS respond to every type of challenge one can imagine in a direct depth imaging without subsurface information. The types of challenges depend on a set of factors, and among issues are: (1) the earth's dimension and degree of lateral variability, (2) difference between actual and reference earth properties, and the (3) spatial extent of those property differences, (4) the number of parameters in the assumed earth model, and (5) the angles of the waves reflecting from reflectors, and being used in your processing.

There are two very different types of issues in developing practical and robust imaging algorithms from the ISS

One issue has to do with the inclusion of a sufficient and adequate collection of ISS imaging terms and types of terms that address specific imaging challenges, and the second issue is how to accommodate the band-limited nature of seismic data. Significant advances on both fronts occurred this year. The imaging capability, in the pipeline, that will be delivered in the near future is described in the SEG Expanded Abstract "The inverse scattering series depth imaging algorithms: development, tests and progress towards field data application" (located in the AF) which reports the progress on several algorithmic and practical fronts within the ISS imaging project. The progress that is described in

the attached Abstract, now warrants soliciting field data from our sponsors, for our first marine field data tests. I congratulate Professor Fang Liu, and Zhiqiang Wang, Xu Li, and Hong Liang for their significant pioneering efforts and contributions that will allow the ISS imaging capability to provide for information extraction from signal, that is, depth imaging and inversion of primaries in complex media, with the same type of high-end effectiveness and added-value that ISS has brought to the removal of coherent noise (free surface and internal multiples).

One very significant and newsworthy advance by Professor Fang Liu (that occurred subsequent to the Annual Meeting in May and we described at our meeting at the SEG in Houston) was a way to robustly address the band-limited source issues for the new direct depth imaging methods and codes, that assume that both velocity and density are both variable, and both velocity and density are and remain unknown. That critically important practical step by Fang Liu means that the ISS imaging methods will work on field data. Mike Richardson of BHP Billiton alerted us to the importance of density changes in many reflections. Our imaging theory can now accommodate that reality.

A second advance labeled "cascade migration" was arrived at by accident, when a double repeated action of water speed migration was performed, where one water speed migration was called for, *i.e.*, migrating the migration rather than simply migrating. That accident led to an inadvertent but effective and valuable inclusion within the linear water speed term of certain ISS capability uniquely designed and located within higher terms of the ISS for imaging challenges that only arise with a laterally variable earth. That "use with exclusively lateral varying media ISS imaging contributors/terms " providing significant improvement in lateral positioning of e.g., the fault shadow zone when that cascaded linear term is substituted into LOIS or HOIS ("Addressing the bandlimited nature of seismic source and rapid lateral variations of the earth: source regularization and cascaded imaging operator", AR page 72). There is no complete theory to understand that revised double water speed migration, at this moment, but there is no increase in cost, and a clear added imaging value. We have no doubt that the theory and our understanding will catch-up with the algorithm. The daunting example that was previously examined of a homogeneous sphere above a single horizontal reflector, can now image the upper and lower sphere, without knowing or determining the sphere velocity. That's a significant advance and contribution and we congratulate Professor Fang Liu.

AVO, type 1 and type 2 direct exploration tool, without a velocity model

Following a suggestion by Doug Foster of ConocoPhillips, a by-product of the newer imaging theory produced an AVO reflectivity like output that preserved zero crossings at depth for the challenging and important type 1 and type 2 AVO identification application. That happens without a velocity model or common image gather (CIG) flattening and CIG ironing problems. Early tests by Xu Li and Shansong Jiang were encouraging ("Depth imaging without the velocity cares about the phase and amplitude information of events: Focusing on the use of the angle dependent amplitude information of events", M-OSRP Report 2008; "Progressing multiparameter imaging using the inverse scattering series: An initial analytic test of the leading order imaging subseries (LOIS) closed form and its extended higher order imaging subseries (HOIS) closed form for a laterally invariant two-parameter acoustic medium", M-OSRP Report 2008). An elastic test is presented in this report ("An unanticipated and immediate AVO by-product: responding to pressing type I and

type II AVO challenges delivered within the ISS imaging program", AR page 154) that significantly extends those previous studies, thereby connecting the method closer to real world application. Zhiqiang Wang ("New capture of direct velocity independent depth imaging in a one-dimension two-parameter acoustic Earth", AR page 137) developed and tested a further capture of imaging capability that can accommodate greater contrasts in velocity and duration of difference between the reference and actual subsurface properties. The imaging team consists of Fang Liu, Zhiqiang Wang, Xu Li, and Hong Liang.

Model matching and model mismatching between the earth and your algorithm

This is a relevant issue for all processing issues. The study here is confined to M-OSRP's ISS imaging and inversion algorithms. We suspect that the lessons gleaned here, concerning mismatch issues, might be relevant for algorithms outside of the methods our program pursues.

How to determine an adequate earth model type for seismic processing?

The issue of how to determine an adequate model for processing objectives must first be raised and addressed. In seismic exploration, we want a minimally complicated model adequate to achieve our predictive purposes. But how to determine model adequacy? From our point of view, a model is too simple if its output recommends drilling decisions that a more complicated and complete model would improve upon, and conversely, is too complicated if a simpler model would not change the efficacy of drilling prediction, e.g., changing and improving a drilling to no-drill or no-drill to drill decision. Our strategy for field data application of our algorithms recognizes that issue, using the minimally acceptable earth model for amplitude analysis, the isotropic elastic model.

Given that understanding of earth model adequacy, Hong Liang then studied the consequences of using an inadequate model (e.g., acoustic model for an elastic earth data) separately for ISS imaging and inversion purposes ("Initial tests for the impact of matching and mismatching between the earth model and the processing model for the ISS imaging and parameter estimation", AR page 165). The separate numerical tests of the elastic data using the ISS imaging conjecture and inversion for both acoustic and elastic media, illustrate how it's important to match the processing algorithm's model type to the model that generate the data, and the negative consequences for imaging and inversion that can result when that match is ignored.

First field data imaging test: Kristin data from North Sea

Imaging project summary: A set of different ISS imaging codes will be developed and field data tested and distributed to M-OSRP sponsors. The first field data imaging test is going to take place with the Kristin data from the North Sea, with dual streamer over- under cables, and owned by Statoil and acquired and processed by Western-Geco/Schlumberger. We express our appreciation to Statoil and Western-Geco/Schlumberger for this cooperation and opportunity. The first field tests will be carried out this year. We are grateful to Einar Otnes, Lasse Amundsen, Joachim Mispel, Ed Kragh, and Mark Thompson for arranging this data opportunity for our first field data imaging test.

M-OSRP Awards in 2009

(6) The SEG awarded two J. Clarence Karcher Awards in 2009. Both awards went for research within M-OSRP (Dr. Haiyan Zhang, now at ConocoPhillips and Dr. Bogdan Nita, at Montclair State University, Montclair, New Jersey). We congratulate Haiyan and Bogdan for their important achievements, their high impact and significant contributions.

(7) Prof. Kris Innanen and Dr. Jose Eduardo Lira, are pioneering the theory and application of inverse scattering series methods to absorptive media. Lira and Innanen together produced: (1) concepts and algorithms for Q compensation without knowing or estimating or requiring Q, and (2) using the difference between the actual and a predicted internal multiple to estimate the overburden effect on amplitude for traditional migration-inversion purposes. Professor Innanen mentored Jose Lira in his PhD thesis, and we congratulate Dr. Lira for earning his PhD, and Kris for his excellent leadership and guidance.

Below please find a link to the 4 M-OSRP papers in the Issue 74 of Geophysics:

1. "Clarifying the underlying and fundamental meaning of the approximate linear inversion of seismic data"
2. "Direct nonlinear inversion of 1D acoustic media using inverse scattering subseries",
3. "Direct nonlinear inversion of multiparameter 1D elastic media using the inverse scattering series", and
4. "Green's theorem as a comprehensive framework for data reconstruction, regularization, wavefield separation, seismic interferometry, and wavelet estimation: A tutorial".

In our view, these papers are particularly worthwhile. These papers not only describe the progress within different M-OSRP projects, but also place them within the broader context of seismic application and overall industry interest and other research programs and initiatives.

What does inversion mean? What does direct inversion communicate? The "meaning of linear paper" begins with the critical and often neglected distinction between direct inversion and "indirect" or model-matching approaches.

The only time these two are equivalent is when the direct inverse is a linear problem. For example, depth imaging for a structural map is a linear problem given an accurate velocity model. Therefore, conventional imaging with an accurate velocity model is related to modeling run backwards. For all other problems, it is misguided and incorrect to think of model matching as somehow equivalent to direct inversion. For example, the direct inversion from the inverse scattering series for the removal of free surface multiples provides an algorithm that doesn't require any subsurface information, whatsoever, and the algorithm is unchanged independent of whether the earth is acoustic, elastic, anisotropic, or absorptive. Not one line of code changes. Try to imagine that multiple removal from a model matching cost function perspective. AVO is another example. The ISS states unambiguously that all PP, PS, SS components, that is, all data components are required for explicit and direct linear and non-linear estimates of changes in mechanical properties across a reflector. With explicit formulas for the linear and non-linear direct estimates that require all components. Yet essentially

all AVO today treats the inverse problem as starting with a forward PP data modeling result, and seek to solve that forward problem in an inverse sense. That's not solving the inverse problem. Solving a direct forward problem in an inverse sense is not directly solving the inverse problem. The two papers by Dr. Haiyan Zhang delineate these lessons and requirements in full math physics detail, with synthetic and field data examples.

In the traditional seismic world, a P wave acoustic velocity and the phase of the recorded primary wave are adequate to find a depth image. If after locating the depth image the interest is in determining what property changes at the reflector produced that reflection- then it becomes an AVO issue, and an elastic isotropic reflection coefficient as a function of angle was the typical choice (except in cases of fractures when anisotropic elastic was indicated) to perform amplitude analysis. Nothing less than elastic isotropic model would be used for amplitude analysis and parameter estimation. Now the industry is rushing after an amplitude analysis model matching method, often using a single parameter acoustic model, and calling itself, "full wave-field inversion". From the amplitude analysis seismic history, experience and perspective that's a great argument against evolution.

The Inverse Scattering Series stands alone in saying that velocity and depth are not inextricably connected

Finally, the inverse scattering series promises that all processing goals can be achieved directly (including depth imaging) without a velocity model and subsurface information. We sometimes hear that there are other approaches with a similar claim, e.g. , common image gather, CIG, CFP, CRS, weighted stacks over offset trajectories, "path integrals". All of these other methods are indirect search methods that seek to satisfy a necessary (but not sufficient) property of a correct depth image. And all of these indirect imaging methods believe that a direct depth imaging method would require an accurate velocity. They believe that and they cannot find the velocity so they go the indirect route, staying entirely within a framework that believes that velocity and depth are inextricably connected. The inverse scattering series stands alone in saying that velocity and depth are not inextricably linked and in producing a direct depth imaging algorithm without the velocity. The ISS depth imaging methods are as direct as the free surface multiple elimination code, and has the same three prerequisites, described above.

A new and comprehensive method for RTM from Green's theorem

The inverse scattering depth imaging without the velocity is as direct, as , e.g., RTM is with an accurate velocity. Speaking of RTM, we have a new and consistent Green's theorem theory for RTM, that improves both the propagation model and imaging condition in current RTM practice We anticipate that location errors, artifacts and amplitude errors reported with current RTM application will be mitigated or removed. A report entitled "Reverse-Time migration and Green's theorem" (in the AR beginning on page 181), by Weglein, Stolt and Mayhan is in this Annual Report.

In the latter paper, we place Green's theorem based reverse-time migration (RTM), for the first time on a firm footing and technically consistent math-physics foundation. The required new Green function for RTM application is developed and provided, and is neither causal, anticausal, nor a

linear combination of these prototype Green functions, nor these functions with imposed boundary conditions. We describe resulting fundamentally new RTM theory and algorithms, and provide a step-by-step prescription for application in 1D, 2D and 3D, the latter for an arbitrary laterally and vertically varying velocity field. The original RTM methods of running the wave equation backwards with surface reflection data as a boundary condition is not a wave theory method for wavefield prediction, neither in depth nor in reversed time. In fact that idea corresponds to the Huygens' principle idea which was changed and evolved into a wave theory predictor by George Green in 1826. The original RTM methods, where (1) 'running the wave equation backward in time', and then (2) employing a zero lag cross-correlation imaging condition, are in both of these ingredients less accurate and effective than the Green's theorem RTM method of this paper. Furthermore, all currently available Green's theorem methods for RTM make fundamental conceptual and algorithmic errors in their Green's theorem formulations. Consequently, even with an accurate velocity model, current Green's theorem RTM formulations can lead to image location errors and other reported artifacts. Addressing the latter problems is a principle goal of the new Green's theorem RTM method of this paper. Several simple analytic 1D examples illustrate the new RTM method. We also compare the general RTM methodology and philosophy, as the high water mark of current imaging concepts and application, with the next generation and emerging Inverse Scattering Series imaging concepts and methods.

In the paper with Dr. Adriana C. Ramírez on interferometry and Green's theorem, Adriana shows that all of "interferometry" is basically Green's theorem, known and published by George Green is 1826. All of the brand new " virtual sources", "spurious multiples" , "mysterious artifacts" are nether new nor spurious but simple direct consequences of Green's second identity, or violations of that classic theorem with predicable injurious consequences. Dr. Ramírez then uses that Green's theorem foundation to build a set of ever more effective methods for data reconstruction and, exemplifies her new approaches and their added value on synthetic and field data.

Please find below the links to the M-OSRP web site regarding the following topics:

1. 2009 M-OSRP Geophysics/SEG published technical papers and tutorial (http://www.mosrp.uh.edu/2009_SEG_Papers.html)
2. 2009 Annual Meeting Photos (http://www.mosrp.uh.edu/Annual_Meeting_Dinner_Photos_2009.html)
3. 2009 Executive summary, update, deliverables, personnel and key-note addresses (http://www.mosrp.uh.edu/2009_summary.html)

In summary, it has been a very good and productive year. I want to thank you for your encouragement and support.

Best regards,
Art

Arthur B. Weglein

Preprocessing 3D seismic data

J. D. Mayhan, Jr. and A. B. Weglein, M-OSRP, Physics Department, University of Houston

Abstract

This report presents the results of designing, coding, and testing three programs for preprocessing 3D seismic data using Green's Theorem: data reconstruction, source signature estimation, and deghosting. The code will be released to the sponsors after the Annual Meeting. The report also discusses the process of transforming seismic data into the format required by M-OSRP multiple removal code.

1 Introduction

The inverse scattering series (ISS) can perform certain tasks (*e.g.*, free surface multiple elimination, internal multiple attenuation, and imaging) without estimates of the spatial distribution of subsurface information. These ISS methods assume seismic data to be used for imaging consists of primaries only, *i.e.*, ghosts, free surface multiples (FSM's), and internal multiples (IM's) have been removed and the source signature deconvolved. Free surface multiple elimination and internal multiple attenuation (based on the ISS) also assume a good estimate of the source signature. In this report, I discuss how Green's Theorem is used to deghost data and estimate the source signature.

Green's Theorem and the ISS form an integrated preprocessing and imaging chain because both are multi-dimensional wave theoretic methods which do not require subsurface information. Hence, the complete chain (data, estimating source signature, deghosting, removing FSM's, attenuating IM's, and imaging) is consistent in both number of spatial dimensions (one, two, or three) and Earth Model Type (acoustic, elastic, or anelastic). Every step in the processing chain is treated equally.

Source signature estimation and deghosting (using Green's Theorem) are based on Weglein and Secrest (1990) and Zhang (2007), respectively. Both methods use the same analytic form of Green's Theorem, *i.e.*, the source signature or deghosted data is the integral over the measurement surface of $(P\nabla G - G\nabla P)\cdot\hat{n}$ where P and $\nabla P\cdot\hat{n}$ are the measurements of the pressure wavefield and its vertical derivative and G is the analytic Green Function for the assumed reference medium. The methods differ in that Weglein and Secrest (1990) use a reference medium with a free surface (half space of air over half space of water) and a Green Function that vanishes on the free surface whereas Zhang (2007) uses a reference medium with no free surface (whole space of water) and a whole space Green Function.

M-OSRP has generated code to accomplish preprocessing goals based on Green's Theorem (data reconstruction, source signature estimation, and deghosting) and the inverse scattering series (free-surface multiple elimination, internal multiple elimination, direct nonlinear imaging, and Q compensation of primaries). The Green's Theorem methods are critically important to the success of the inverse series methods since they may be used to bring seismic data in line with the assumptions of inverse scattering methodology.

Each algorithm or subseries operates on data; the output of that algorithm or subseries is the input to the next algorithm or subseries. (1) Measured data is input to data reconstruction, whose output is the input to (2) source signature estimation and (3) deghosting, whose output is the input to (4) free surface multiple removal, whose output is the input to (5) internal multiple removal, whose output is the input to (6) imaging, (7) inversion, and (8) Q compensation. The success of any inverse scattering series task-separated algorithm hinges on the success of all the steps done before it.

Figure 1 relates how M-OSRP approaches these issues.

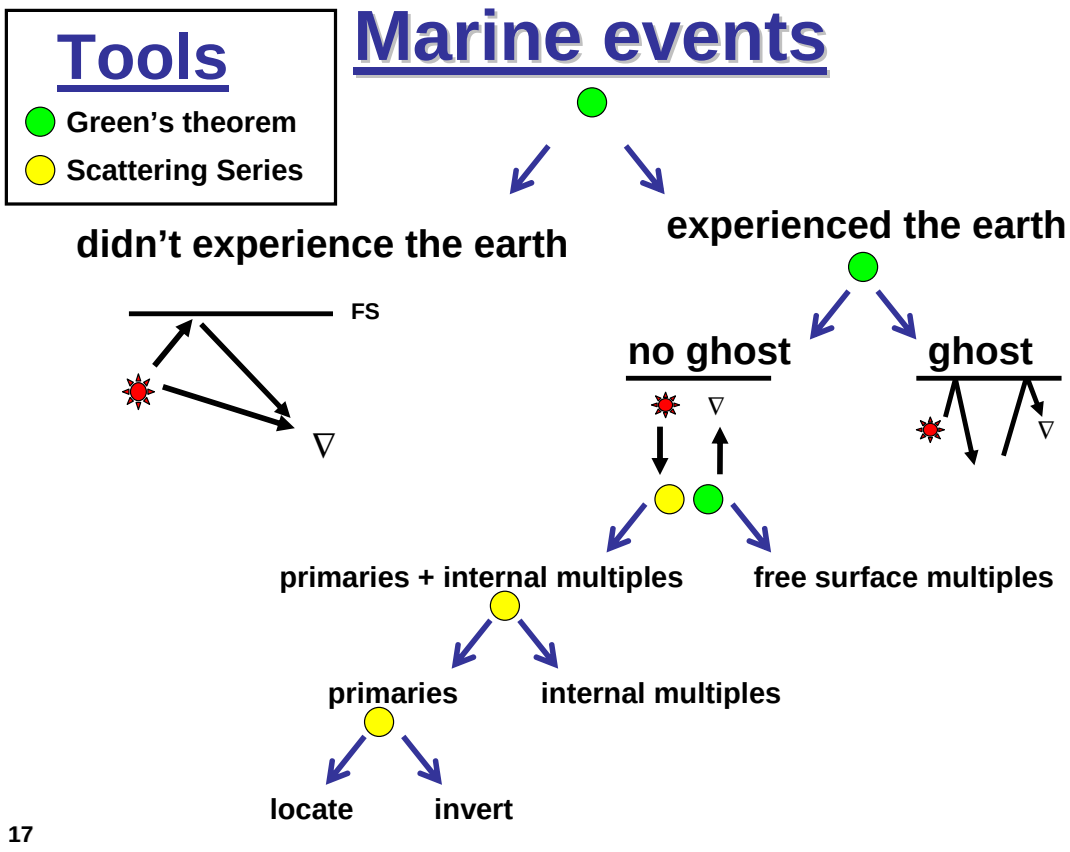

Figure 1: *Classification of marine events and how they are processed.*

The total wavefield P consists of the reference wavefield P_0 which does not experience the Earth and the scattered wavefield P_s which does. The reference wavefield consists of waves which propagate directly from the source to the receiver G_0^d and waves which have one reflection from the free surface (air water interface) G_0^{FS}. The scattered wavefield consists of ghosts, free surface multiples,

internal multiples, and primaries. Ghosts begin their propagation moving upward from the source (source ghosts), end their propagation moving downward to the receiver (receiver ghosts), or both (source/receiver ghosts). Free surface multiples have at least one upward reflection from the Earth and at least one downward reflection from the free surface. Internal multiples have more than one upward reflection from the Earth, at least one downward reflection from the Earth, and no downward reflections from the free surface. For example, an n^{th} order internal multiple has n downward reflections from the Earth. Primaries have only one upward reflection from the Earth.

The classification illustrated in Figure 1 is important because "methods for extracting subsurface information from seismic data typically assume that the data consist exclusively of primaries", so measured data is deghosted and free surface multiples and internal multiples are removed before further processing (Weglein et al., 2003, p. R28). ConocoPhillips tested M-OSRP code for removing free surface multiples from 3D seismic data (three space dimensions). The research project outlined in this report consists of developing code (in Fortran and C) to perform data reconstruction of 3D data, estimate the source signature from measured 3D data, and deghost 3D data. The output of this code is the input to the 3D free surface multiple removal code. PGS is in the process of collecting 2D and 3D seismic data using their proprietary GeoStreamer®. The preprocessing code is being tested using this new data.

This report outlines the basic theory and results of producing 3D Green's Theorem based preprocessing code and is organized as follows: the theory underpinning the code is discussed, followed by a discussion of the code itself.

2 Green's Theorem preprocessing theory - tutorial

2.1 Data reconstruction

This subsection outlines the theory used in M-OSRP's 3D data reconstruction code. The code is based on Weglein and Secrest (1990) who use Scattering Theory (a subset of Perturbation Theory) and Green's Theorem. Scattering Theory expresses (i) the actual medium as the sum of a reference medium (chosen for its mathematical convenience) and a perturbation and (ii) the actual wavefield P as the sum of a reference wavefield G (also chosen for its mathematical convenience) and a perturbation. Green's Theorem tells us a wavefield P inside a volume V can be computed from measurements of P and its (outward pointing) normal derivative $\partial P/\partial n$ on the surface S of V.

In a marine experiment, the reference medium is chosen to be a half space of air over a half space of water, and V is chosen to be a right circular cylinder bounded from below by the towed cable and from above by the free surface (the air water interface) (Figure 2.7). Green's Theorem gives the following expression for the wavefield:

$$\begin{aligned} & -P_s(\vec{r},\vec{r}_s,\omega) \\ = & \oint dS'\,\hat{n}\cdot[P(\vec{r}',\vec{r}_s,\omega)\nabla' G_0(\vec{r},\vec{r}',\omega) - G_0(\vec{r},\vec{r}',\omega)\nabla' P(\vec{r}',\vec{r}_s,\omega)]. \end{aligned} \tag{1}$$

where $\vec{r}$ is the observation/prediction point, $\vec{r}_s$ is the location of the air gun array, and the integral is taken over the surface S of the cylinder. The integral over the surface of the cylinder is reduced to one over the towed cable using the following steps:

1. The contribution to the surface integral in Equation (1) over the vertical sides of the cylinder can be made to approach zero by letting the radius of the cylinder go to infinity because the physical wavefield goes to zero at infinity (Sommerfeld radiation condition).
2. The contribution to the surface integral over the free surface is zero because (i) $P = 0$ at the free surface and (ii) the Green Function used in the surface integral is constructed to vanish on the free surface.

Hence, Equation (1) can be rewritten in the form:

$$\begin{aligned} & -P_s(\vec{r}, \vec{r}_s, \omega) \\ = & \int_{m.s.} dS' \left[P(\vec{r}', \vec{r}_s, \omega) \frac{dG_0^+}{dz'}(\vec{r}, \vec{r}', \omega) - G_0^+(\vec{r}, \vec{r}', \omega) \frac{dP}{dz'}(\vec{r}', \vec{r}_s, \omega) \right]. \end{aligned} \tag{2}$$

where P_s is the scattered wavefield produced by the Earth, $m.s.$ is the measurement surface, and the Green Function is chosen to be the causal solution of the wave equation for the reference medium so that its contribution to the surface integral goes to zero as the distance from its source goes to infinity.

The Green Function in Equations (1) and (2), constructed to vanish on the free surface, is given by (Morse and Feshbach, 1953, pp. 812-813):

- In 3D:

$$G_0^+(\vec{r}, \vec{r}', \omega) = -\frac{1}{4\pi} \left(\frac{\exp(ikR_+)}{R_+} - \frac{\exp(ikR_-)}{R_-} \right)$$

  where $k = \omega/c_0$, c_0 is the speed of sound in the reference medium, $R_\pm = \sqrt{(x - x')^2 + (y - y')^2 + (z \mp z')^2}$, (x, y, z) are the coordinates of the observation/prediction point, and (x', y', z') are the coordinates of the receivers on the towed cable.

- In 2D:

$$G_0^+(\vec{r}, \vec{r}', \omega) = -\frac{i}{4}(H_0^{(1)}(kR_+) - H_0^{(1)}(kR_-))$$

  where $H_0^{(1)}$ is the zeroth order Hankel function of the first kind (defined by $J_0 + iY_0$ where J and Y are Bessel functions of the first and second kind, respectively).

If the towed cable measures P only, one option for estimating dP/dz' is the high frequency approximation $dP/dz' = \nabla' P(\vec{r}', \vec{r}_s, \omega) \cdot \hat{n} \approx ikP(\vec{r}', \vec{r}_s, \omega)$ where $k = \omega/c_0$ (Ramírez, 2007, pp. 69-70).

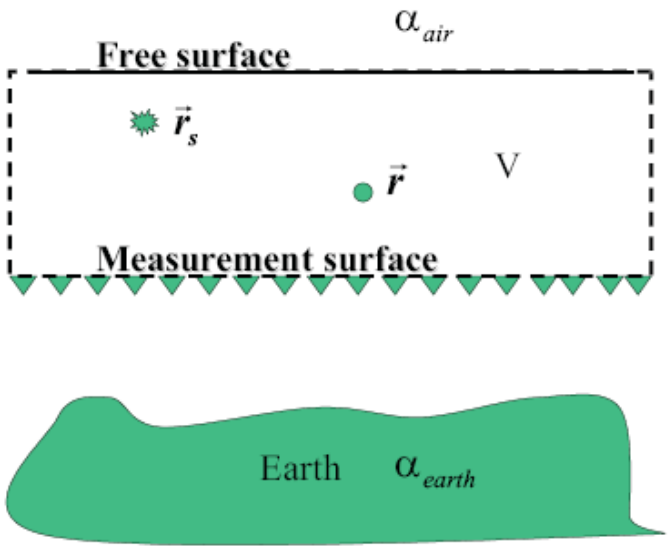

Fig. 2.7: Configuration for derivation of the field prediction algorithm.

Knowledge of the vertical derivative provides the direction of wavefield propagation (*i.e.*, whether up- or downgoing waves), and the high frequency approximation is a one-way wave approximation. In a marine experiment, ghost reflections invalidate the assumption of one way wave propagation. If the towed air gun array is above the towed cable ($s_z < g_z$), even the direct wave invalidates this assumption. Hence, the high frequency and one way wave approximation is not valid (Ramírez, 2007, p. 70) (Ramírez and Weglein, 2009, p. 22).

If the towed cable measures both P and $\partial P/\partial n$ (*e.g.*, PGS GeoStreamer®), the scattered wavefield P_s can be reconstructed above the towed cable (Ramírez, 2007).

Inside/outside the integration volume is an important concept in Green's Theorem. The measurement surface (m.s.) divides all space into inside/outside the integration volume. The normal ($\hat{n}$) to the m.s. points toward the "outside" of the integration volume. $\int_{m.s.}$ gives the wavefield inside/outside the integration volume due to sources outside/inside the integration volume (extinction theorem). Above the cable, the portion of the total wavefield P due to sources below the cable is the scattered wavefield P_s produced by the Earth, and below the cable the portion of the total wavefield P due to sources above the cable is the direct wavefield P_0 produced by the air guns. Selecting the integration volume between the free surface and the m.s. gives the scattered wavefield P_s if the observation point is inside the integration volume/above the cable or the direct wavefield P_0 if the observation point is outside the integration volume/below the cable.

Consider an electromagnetic analogy (Figure 1.2). Sources inside/outside the integration volume induce sources on the m.s. that create the field outside/inside the integration volume (Orfanidis, 2008, pp. 679-681) (Jackson, 1999, pp. 36-37).

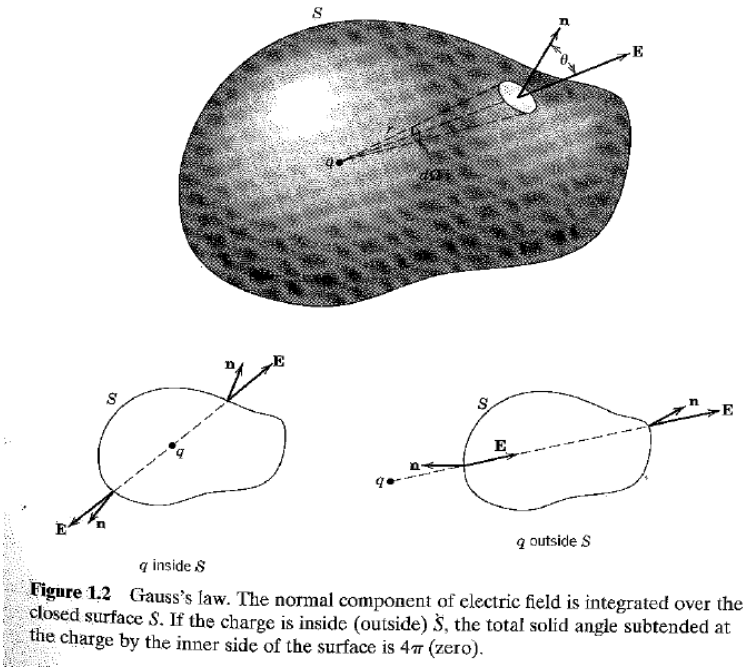

Figure 1.2 Gauss's law. The normal component of electric field is integrated over the closed surface S. If the charge is inside (outside) S, the total solid angle subtended at the charge by the inner side of the surface is 4π (zero).

2.2 Numeric insights

The form of Equation (2):

$$\begin{aligned} & -P_s(\vec{r},\vec{r}_s,\omega) \\ = & \int_{m.s.} dS' \left[P(\vec{r}',\vec{r}_s,\omega)\frac{dG_0^+}{dz'}(\vec{r},\vec{r}',\omega) - G_0^+(\vec{r},\vec{r}',\omega)\frac{dP}{dz'}(\vec{r}',\vec{r}_s,\omega)\right] \end{aligned}$$

says its images are not simple. The integrand is the difference of two spectral products, each of which indicates a convolution in the t domain for each value of $\vec{r}'$. Each term in each product is symmetric about a different point: P about the physical source at $\vec{r}_s$ and G_0^+ about the observation point at $\vec{r}$. For example, Figure (2) shows P and dP/dz for a reflectivity data set with $x_s = 0\,m$. Choosing $x = 625\,m$ offset and letting x' vary over the length of the towed cable gives Figure (3) (showing $P\,dG_0/dz$) and $G_0\,dP/dz$). Choosing $x = 3750\,m$ offset gives Figure (4), and choosing $x = 3750\,m$ offset gives Figure (5). Note that the time depth of the horizontal line in Figures (3)-(5) corresponds to the time required for the wavefield to traverse the horizontal distance between $\vec{r}_s$ and $\vec{r}$. For example, in Figure (4) the time depth is $\approx 2.5\,s$ which is $3750\,m/1500\,m/s$.

More on M-OSRP's theory of Green's Theorem based data reconstruction can be found in Ramírez (2007, chap. 4).

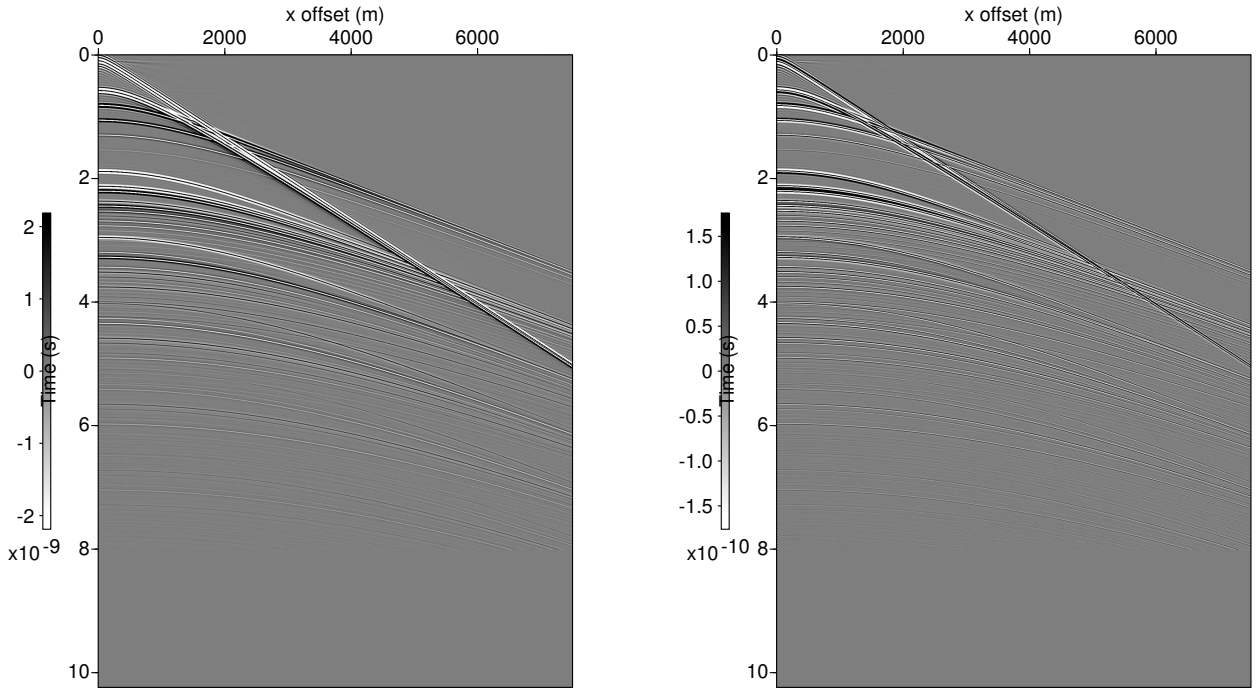

Figure 2: P (left), dP/dz (right)

2.3 Source signature estimation

This subsection outlines the theory used in the 3D source signature estimation code. M-OSRP's source signature estimation code is also based on Weglein and Secrest (1990) who derive two equations containing the source signature: the Lippmann-Schwinger Equation and a second equation derived from Green's Theorem. Comparing the two equations gives an equation for the source signature as a function of measured 3D data and a reference medium Green Function. The same geometry is used as in data reconstruction except the observation point $\vec{r}$ is below the towed cable, *i.e.*, outside the integration volume (Figure 2.2).

The Lippmann-Schwinger part begins with the constant density acoustic wave equation for the pressure field P created by a source $A(t)$ at position $\vec{r}_s$, restates wave speed $c(\vec{r})$ as a function of reference medium speed c_0 and a perturbation $\alpha(\vec{r})$, and converts the partial differential equation into an integral equation (the Lippmann-Schwinger Equation) involving a causal Green Function (to ensure a causal solution for P). The result is

$$\tilde{P}(\vec{r},\vec{r}_s,\omega) = \tilde{A}(\omega)G_0^+(\vec{r},\vec{r}_s,\omega) + \int_\infty d\vec{r}\,' \, G_0^+(\vec{r},\vec{r}\,',\omega)\frac{\omega^2}{c_0^2}\alpha(\vec{r}\,')\tilde{P}(\vec{r}\,',\vec{r}_s,\omega). \tag{3}$$

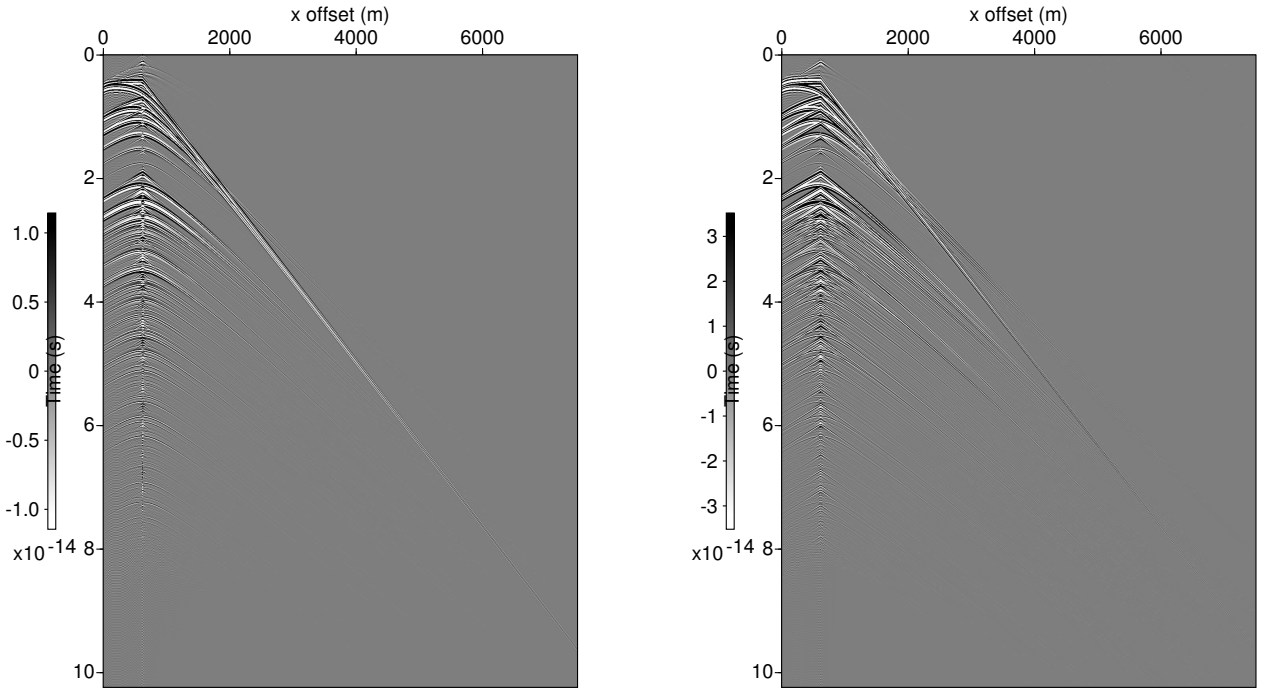

Figure 3: $P\,dG_0/dz$ (left), $G_0\,dP/dz$ (right) for $625m$ offset

The Green's Theorem part begins with: (1) a reference medium consisting of a half space of air overlaying a half space of water, (2) a perturbation $\alpha(\vec{r})$ which parameterizes the difference between the lower part of the half space of water and Earth, (3) an integration volume V consisting of a hemisphere bounded from above by the measurement surface, (4) a free surface (air-water interface) above the measurement surface (*i.e.*, outside V), and (5) a source $\vec{r}_s$ on or above the measurement surface (*i.e.*, outside V). Substituting the above, the partial differential equation for the pressure field P, and the corresponding reference medium Green Function differential equation into Green's Theorem, and for consistency with Equation (3) choosing a causal Green Function gives

$$\begin{aligned}\tilde{P}(\vec{r},\vec{r}_s,\omega) &= \int_\infty d\vec{r}\,' G_0^+(\vec{r}\,',\vec{r},\omega)\frac{\omega^2}{c_0^2}\alpha(\vec{r}\,')\tilde{P}(\vec{r}\,',\vec{r}_s,\omega) \\ &\quad + \oint_S dS'\,\hat{n}\cdot[\tilde{P}(\vec{r}\,',\vec{r}_s,\omega)\nabla' G_0^+(\vec{r}\,',\vec{r},\omega) - G_0^+(\vec{r}\,',\vec{r},\omega)\nabla'\tilde{P}(\vec{r}\,',\vec{r}_s,\omega)]. \qquad (4)\end{aligned}$$

Equation (3) is valid for all space, whereas Equation (4) is valid only for the volume V. Comparing Equations (3) and (4) in V gives an equation for the source signature:

$$\tilde{A}(\omega) = \frac{1}{G_0^+(\vec{r},\vec{r}_s,\omega)}\oint_S dS'\,\hat{n}\cdot[\tilde{P}(\vec{r}\,',\vec{r}_s,\omega)\nabla' G_0^+(\vec{r}\,',\vec{r},\omega)$$

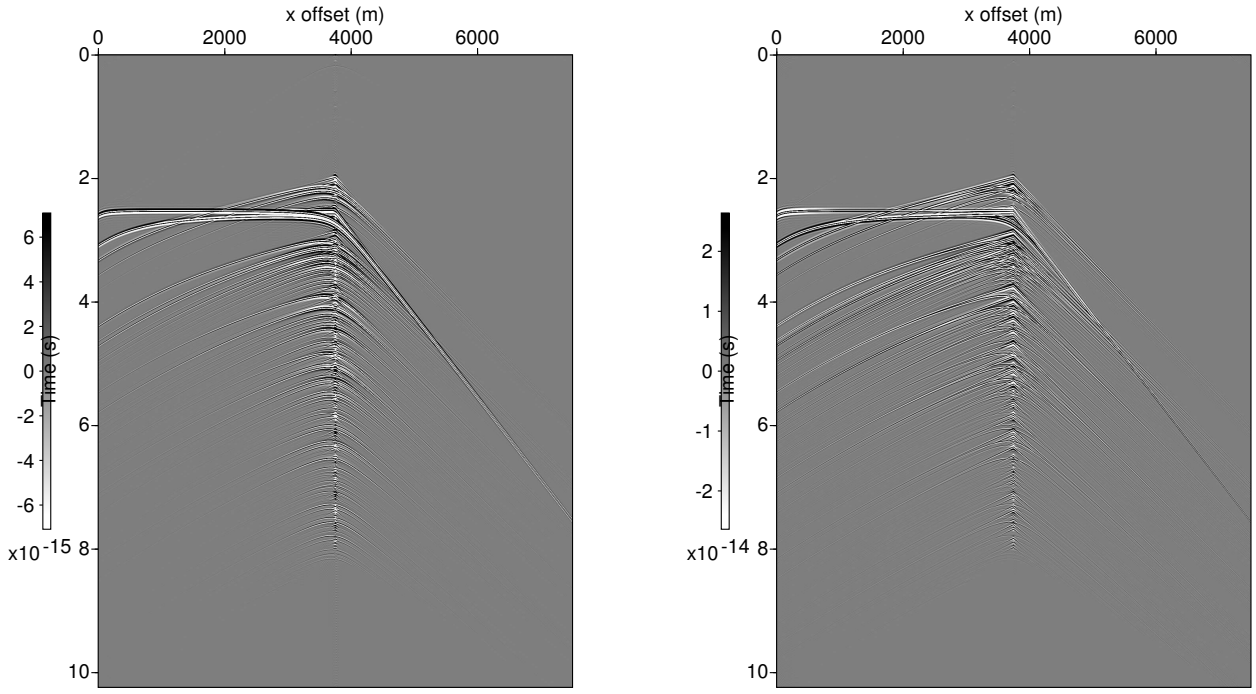

Figure 4: $P\,dG_0/dz$ (left), $G_0\,dP/dz$ (right) for $3750m$ offset

$$-G_0^+(\vec{r}',\vec{r},\omega)\nabla'\tilde{P}(\vec{r}',\vec{r}_s,\omega)]. \tag{5}$$

Note that Equation (5) is computing more than a traditional source signature, *i.e.*, instrument response is included. The integral provides an estimate of the source signature for an air gun array including anisotropic radiation pattern. How to incorporate this nonanalytic source signature into the existing M-OSRP formalism is an active research topic for another graduate student in M-OSRP (Jinlong Yang).

The details of the above derivation can be found in Appendix A.

2.4 Deghosting

This section outlines the theory used in the 3D deghosting code. The theory of deghosting based on Green's Theorem is covered in Zhang (2007, chap. 2). The geometry differs from that used in data reconstruction and source signature estimation. The reference medium is a whole space of water with three sources (air guns, Earth, and free surface) (Figure 2.10).

The procedure begins with (1) a reference medium consisting of a whole space of water, (2) a perturbation $\alpha_{air}(\vec{r}')$ which parameterizes the difference between the reference medium and air, (3)

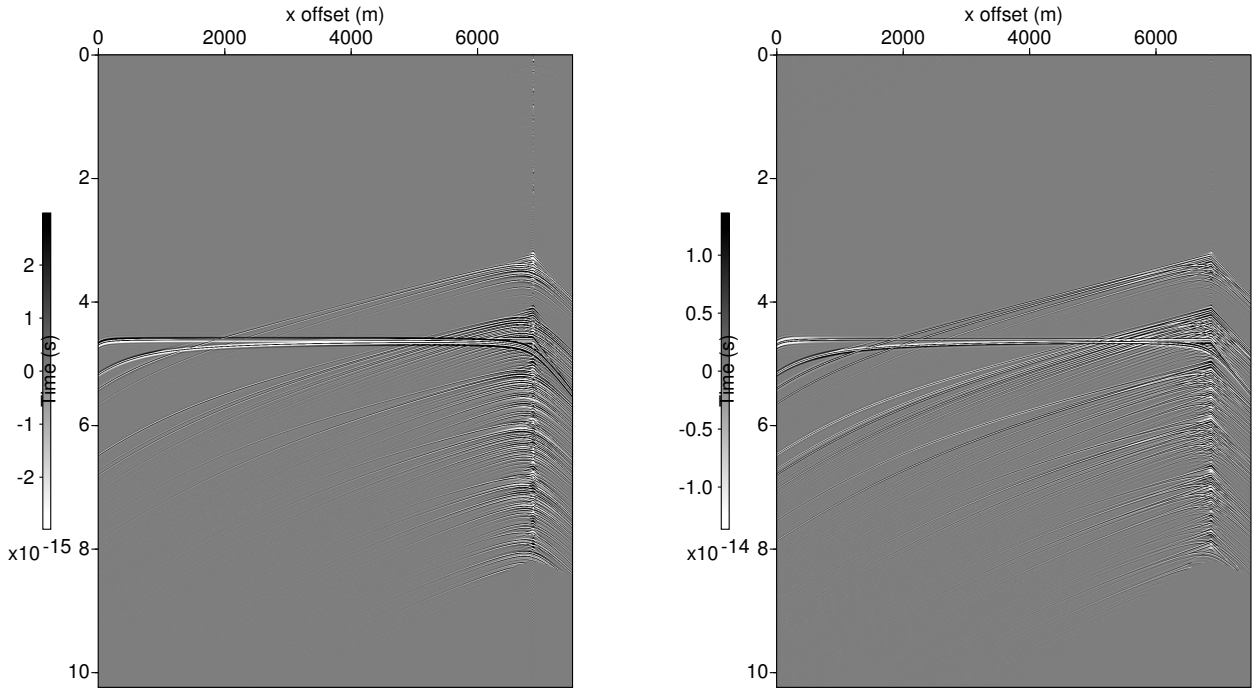

Figure 5: $P\,dG_0/dz$ (left), $G_0\,dP/dz$ (right) for $6875m$ offset

a perturbation $\alpha_{Earth}(\vec{r}\,')$ which parameterizes the difference between the reference medium and Earth, (4) an integration volume V consisting of a hemisphere bounded below by the measurement surface, (5) a free surface (air-water interface) above the measurement surface (*i.e.*, inside V), and (6) a source $\vec{r}_s$ on or above the measurement surface (*i.e.*, inside V). Substituting the above into Green's Theorem and invoking the Sommerfeld radiation condition give the receiver side deghosting equation:

$$\begin{aligned} &\tilde{P}^{deghosted}_{receiver}(\vec{r},\vec{r}_s,\omega) \\ &= \int_{m.s.} dS'\,[\tilde{P}(\vec{r}\,',\vec{r}_s,\omega)\frac{dG_0^+}{dz'}(\vec{r}\,',\vec{r},\omega) - G_0^+(\vec{r}\,',\vec{r},\omega)\frac{d\tilde{P}}{dz'}(\vec{r}\,',\vec{r}_s,\omega)]. \end{aligned} \tag{6}$$

where $\tilde{P}^{deghosted}_{receiver}(\vec{r},\vec{r}_s,\omega)$ is the deghosted (receiver side) wavefield, and $\tilde{P}(\vec{r}\,';\vec{r}_s;\omega)$ and $d\tilde{P}/dz'(\vec{r}\,';\vec{r}_s;\omega)$ are the hydrophone measurements and their spatial derivatives (in the frequency domain). Using reciprocity, a similar integration on the source side will remove source ghosts, *i.e.*,

$$\begin{aligned} &\tilde{P}^{deghosted}(\vec{r},\vec{r}_s,\omega) \\ &= \int_{m.s.} dS'\,[\tilde{P}(\vec{r}\,',\vec{r}_s,\omega)\frac{dG_0^+}{dz'}(\vec{r}\,',\vec{r}_s,\omega) - G_0^+(\vec{r}\,',\vec{r}_s,\omega)\frac{d\tilde{P}}{dz'}(\vec{r}\,',\vec{r}_s,\omega)]. \end{aligned} \tag{7}$$

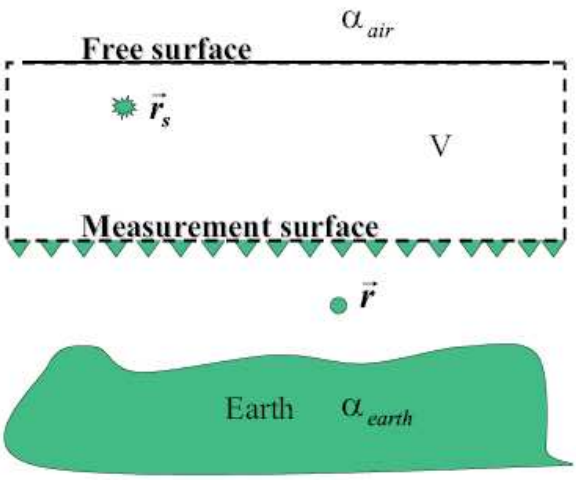

Fig. 2.2: Second configuration for derivation of the wavelet estimation algorithm.

In Equation (7) $\tilde{P}(\vec{r}', \vec{r}_s, \omega)$ is the output of Equation (6) and the m.s. is at the source depth.

In 2D Equation (6) can be written in the form

$$\begin{aligned} & \oint_S dS' \, \hat{n} \cdot [\tilde{P}(\vec{r}', \vec{r}_s, \omega) \nabla' G_0^+(\vec{r}', \vec{r}, \omega) - G_0^+(\vec{r}', \vec{r}, \omega) \nabla' \tilde{P}(\vec{r}', \vec{r}_s, \omega)] \\ = \; & \tilde{P}(\vec{r}, \vec{r}_s, \omega) - \int_V d\vec{r}' G_0^+(\vec{r}', \vec{r}, \omega) k_0^2 \alpha_{air}(\vec{r}') \tilde{P}(\vec{r}', \vec{r}_s, \omega) \\ & - \tilde{A}(\omega) G_0^+(\vec{r}, \vec{r}_s, \omega). \end{aligned} \tag{8}$$

The physical meaning of Equation (8) is that the total wavefield at $\vec{r}$ can be separated into three parts: (1) the direct wave which travels from the source at $\vec{r}_s$ to $\vec{r}$ (third term on the right-hand side), (2) the pressure field whose last motion is downward from the free surface (second term on the right-hand side), and (3) the pressure field whose last motion is upward from the Earth (the entire right-hand side).

The details of the above derivation can be found in Appendix B.

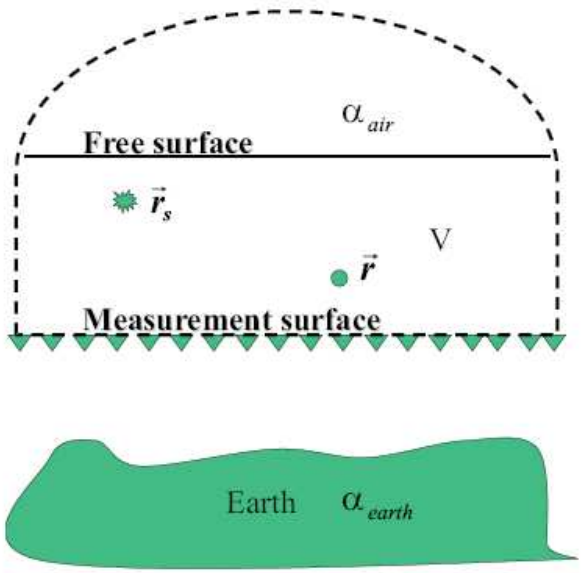

Fig. 2.10: First configuration for derivation of the deghosting algorithm.

3 Results

3.1 Testing Green's Theorem code

The code was tested using the following data sets (listed chronologically):

Data set	Type	No. cables	No. receivers	No. shots	$\nabla P \cdot \hat{n}$
Reflectivity (BP)	Synthetic	1	121	1	(a)
WesternGeco/Statoil/ Lawrence Livermore	Synthetic	41	801	281	(a)
ExxonMobil	Synthetic	1	1201	1	(b)
PGS	Field	1	648	(c)	Given
Reflectivity (OASES)	Synthetic	1	501	1	(a)
"Simple"	Synthetic	1	601	1	Given

(a) Data contains P only so the code was tested using the high frequency and one way wave approximation $\nabla P \cdot \hat{n} \approx ikP$.
(b) Data contains P and V_z (vertical component of particle velocity) so the code was tested using

$P_z = -i\rho\omega V_z$ where ρ is the mass density of the reference medium.
(c) Varies with line.

Here are some sample numeric results using WesternGeco synthetic data. Figure 6 is shot 140 (left) and the Ricker wavelet used to generate the WesternGeco data (right). Figure 7 is the estimated source signatures using shot 140/cable 21/receivers 301-501 (left) and shot 1/cable 21/receivers 1-801 (right). The WesternGeco synthetic data (P only) does not satisfy the assumptions of the Green's Theorem code so the high frequency and one way wave approximation $\nabla P \cdot \hat{n} \approx ikP$ was used, yet the code managed to extract reasonable source signatures.

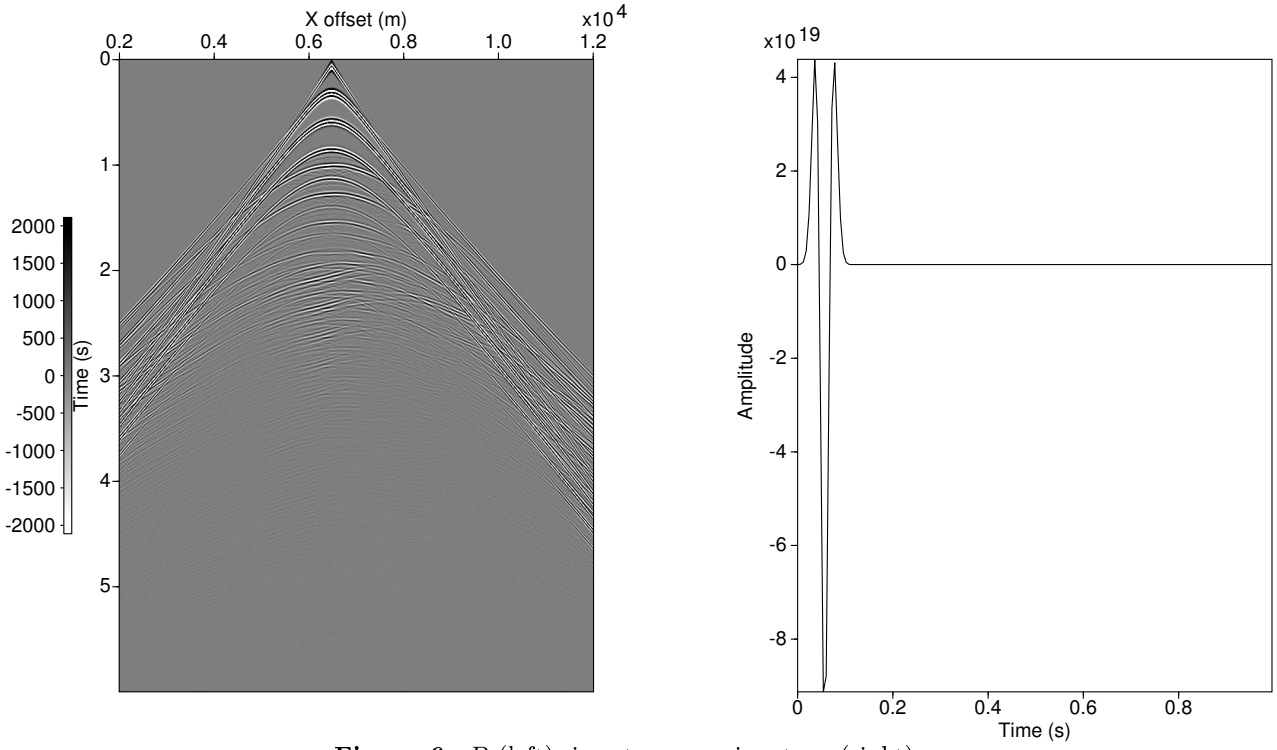

Figure 6: P (left), input source signature (right)

Here are some sample results using reflectivity synthetic data. Figure 8 is P (left) and dP/dz (right) for cable depth $140\,m$ where the latter was estimated by taking P for cable depth $150\,m$ minus P for cable depth $140\,m$ and dividing by $10\,m$. Figure 9 shows the estimated wavefield using the high frequency and one way wave approximation (left) and dP/dz (right). Comparing the two panels shows that using dP/dz gives a weaker direct wave and stronger primaries and multiples, *i.e.*, a more reasonable predicted wavefield. In like manner, Figure 10 shows the estimated source signature using ikP (left) and dP/dz (right). Using the latter extracts a more reasonable source signature.

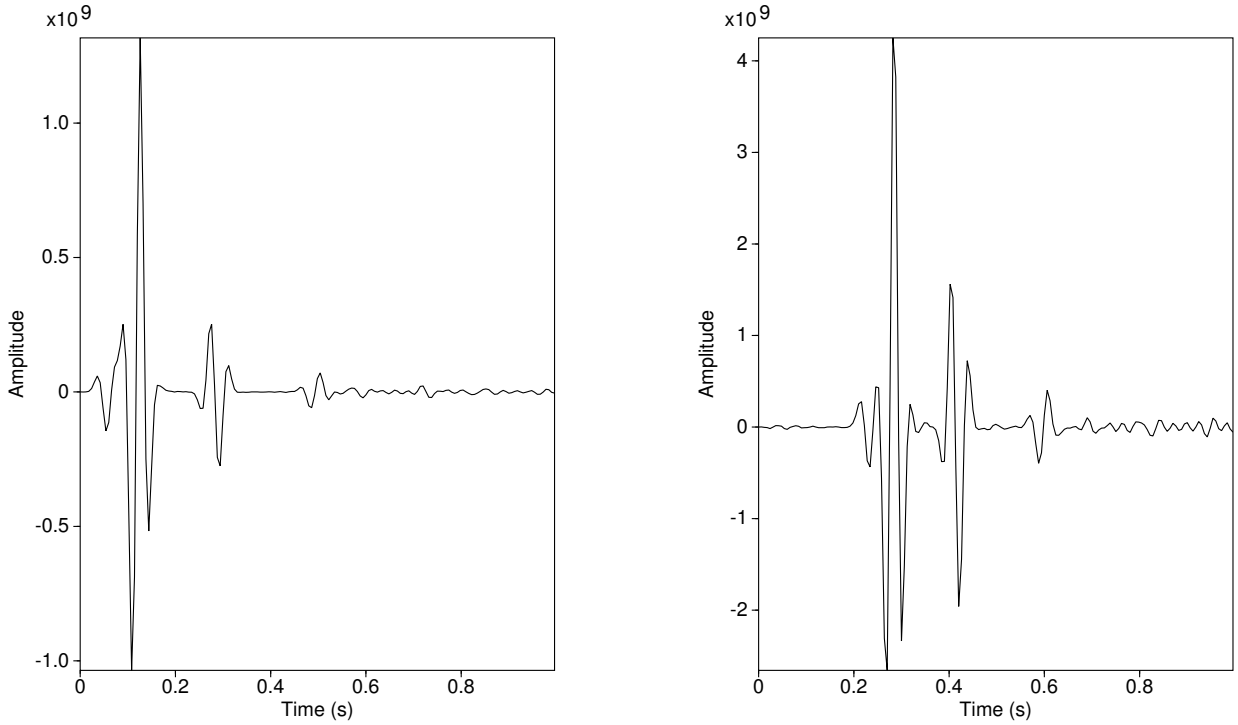

Figure 7: *Est. source signatures*

3.2 "Unfolding" data for input to 3D free surface multiple elimination code

The input to the 3D free surface multiple elimination (FSME) code must have colocated sources and receivers. Hence, the data output by the Green's Theorem code must be "unfolded" from a physical pattern to a pattern of colocated sources and receivers. The WesternGeco synthetic data consists of 22-physical files, 20 with data, one with the source Ricker wavelet, and one with the direct arrival. Each data file contains 14-shots (with 15-shots in file number 20), so our first output was a $14 \times 14 \times 14 \times 14$ hypercube, *i.e.*, with 14-points along each of the four mutually orthogonal axes: sx, sy, gx, and gy. A Unix shell was used which: (1) reads one line of 14-shots and 14-lines each of 14-receivers, (2) "mirrors" 13-lines each of 14-receivers through the line of shots (which is coincident with the first line of receivers) to form a 14×27 grid, and (3) replicates and trims the 14×27 grid to create a $14 \times 14 \times 14 \times 14$ hypercube. The data created by this process increased from 100M (input) to 163M (output), a 63% increase.

Our second Unix shell was designed to replicate the data used by ConocoPhillips in the Spring of 2009 to test the 3D FSME code. The WesternGeco synthetic data has 41-lines of 801-receivers so they created a $41 \times 41 \times 41 \times 41$ hypercube with 41-points along each of the four mutually orthogonal axes. The data created by our Unix shell increased from 292M (input) to 12.0G (output), a 4100%

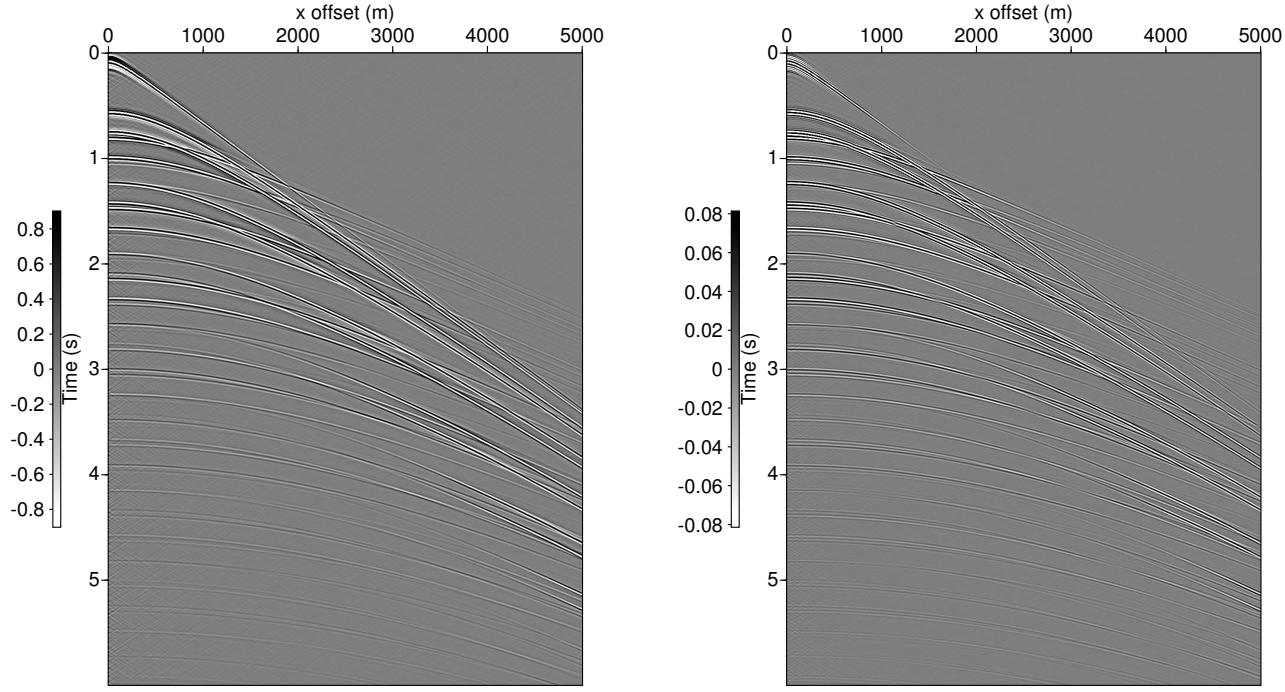

Figure 8: P (left) and dP/dz (right)

increase.

Please note the Unix shells work only because they take advantage of the symmetry properties of the WesternGeco synthetic data in the cross line direction and the fact that the receivers are not moving. Field data is not as symmetric. Creating the data necessary for colocated sources and receivers will require (i) using "nearby" shots to approximate a given shot or (ii) reconstructing near offset data. During the first author's internship it was learned that Green's Theorem code can not do near offset data reconstruction. The hypothesis that the weighted limited aperture migration/inversion method (stationary phase approximation) is better for data extrapolation may be tested (Ramírez, 2007, chap. 3).

3.3 3D free surface multiple elimination code with and without preprocessing by Green's Theorem code

The reader is referred to Terenghi (2010).

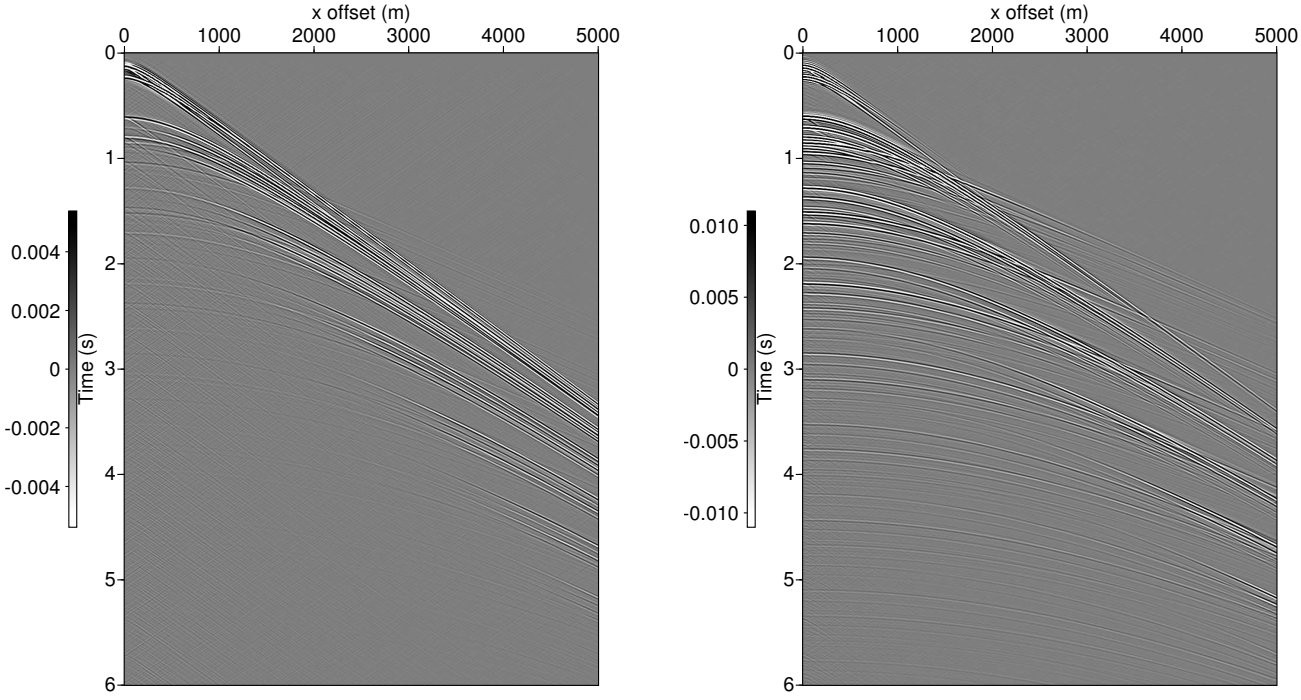

Figure 9: Using ikP (left) and dP/dz (right)

4 Summary

3D Green's Theorem code has been developed and tested on synthetic data. The problem of transforming synthetic data into colocated sources and receivers (required by multiple removal code) has been addressed. Future work will involve testing 3D Green's Theorem code on field data and addressing the problem of transforming field data.

5 Acknowledgements

The first author is grateful to all M-OSRP sponsors for their support of this research and to Dr. Mamadou Diallo (ExxonMobil), Dr. Fang Liu (M-OSRP), Einar Otnes (WesternGeco), and Dr. Paolo Terenghi (M-OSRP) for their instruction in Unix, C, Fortran, and Seismic Unix. Furthermore, my special appreciation to Dr. Arthur Weglein for his teaching, guidance, and patience.

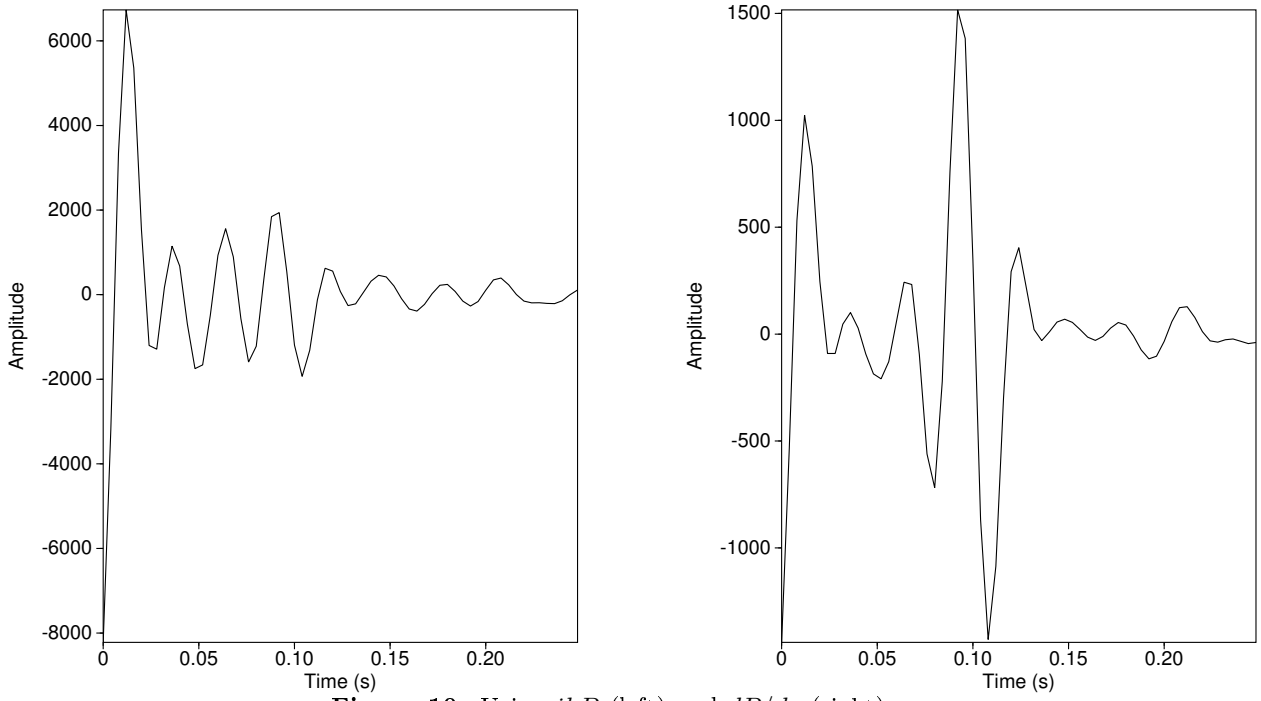

Figure 10: Using ikP (left) and dP/dz (right)

6 Appendices

A Theory of source signature estimation

M-OSRP's theory of source signature estimation is covered in Weglein and Secrest (1990) who derive two equations containing the source signature: the Lippmann-Schwinger equation and a second equation derived from Green's Theorem. Comparing the two equations gives an equation for the source signature as a function of measured 3D data and a reference medium Green Function.

A.1 Lippmann-Schwinger Approach

The constant density acoustic wave equation for the pressure field P created by a source $A(t)$ at position $\vec{r}_s$ is

$$\left(\nabla^2 - \frac{1}{c^2(\vec{r})}\frac{\partial^2}{\partial t^2}\right) P(\vec{r}, \vec{r}_s, t) = A(t)\delta(\vec{r} - \vec{r}_s). \tag{9}$$

Fourier transforming from the time domain to the frequency domain gives:

$$\left(\nabla^2 + \frac{\omega^2}{c^2(\vec{r})}\right)\tilde{P}(\vec{r},\vec{r}_s,\omega) = \tilde{A}(\omega)\delta(\vec{r}-\vec{r}_s). \tag{10}$$

Restating wave speed $c(\vec{r})$ as a function of reference medium speed c_0 and an actual medium perturbation $\alpha(\vec{r})$ gives:

$$\frac{1}{c^2(\vec{r})} = \frac{1}{c_0^2}(1-\alpha(\vec{r})). \tag{11}$$

Substituting Equation (11) into Equation (10) gives:

$$\left(\nabla^2 + \frac{\omega^2}{c_0^2}\right)\tilde{P}(\vec{r},\vec{r}_s,\omega) = \tilde{A}(\omega)\delta(\vec{r}-\vec{r}_s) + \frac{\omega^2}{c_0^2}\alpha(\vec{r})\tilde{P}(\vec{r},\vec{r}_s,\omega). \tag{12}$$

Converting Equation (12) from a partial differential equation into an integral equation (the Lippmann-Schwinger equation) gives

$$\tilde{P}(\vec{r},\vec{r}_s,\omega) = \tilde{A}(\omega)\tilde{G}_0(\vec{r},\vec{r}_s,\omega) + \int_\infty d\vec{r}\,'\tilde{G}_0(\vec{r},\vec{r}\,',\omega)\frac{\omega^2}{c_0^2}\alpha(\vec{r}\,')\tilde{P}(\vec{r}\,',\vec{r}_s,\omega). \tag{13}$$

Because the Lippmann-Schwinger equation covers all space, there is no boundary condition to impose a causal solution; therefore, choose a causal Green Function $\tilde{G}_0^+$ to get a causal solution $\tilde{P}(\vec{r},\vec{r}_s,\omega)$:

$$\tilde{P}(\vec{r},\vec{r}_s,\omega) = \tilde{A}(\omega)\tilde{G}_0^+(\vec{r},\vec{r}_s,\omega) + \int_\infty d\vec{r}\,'\tilde{G}_0^+(\vec{r},\vec{r}\,',\omega)\frac{\omega^2}{c_0^2}\alpha(\vec{r}\,')\tilde{P}(\vec{r}\,',\vec{r}_s,\omega). \tag{14}$$

A.2 Green's Theorem Approach

Weglein and Secrest (1990) define the following to isolate the source signature:
(1) a reference medium consisting of a half space of air above a half space of water,
(2) a perturbation $\alpha(\vec{r})$ which converts the lower part of the half space of water into Earth,
(3) an integration volume V consisting of a hemisphere bounded from above by the measurement surface (the plane $z=0$),
(4) a free surface (air-water interface) above the measurement surface (*i.e.*, outside V), and
(5) a source $\vec{r}_s$ on or above the measurement surface (again outside V).

Substituting $\tilde{P}$ and $\tilde{G}_0$ into Green's Theorem gives

$$\begin{aligned}&\int_V d\vec{r}\,'[\tilde{P}(\vec{r}\,',\vec{r}_s,\omega)\nabla'^2\tilde{G}_0(\vec{r}\,',\vec{r},\omega) - \tilde{G}_0(\vec{r}\,',\vec{r},\omega)\nabla'^2\tilde{P}(\vec{r}\,',\vec{r}_s,\omega)] = \\ &\oint_S dS'\,\hat{n}\cdot[\tilde{P}(\vec{r}\,',\vec{r}_s,\omega)\nabla'\tilde{G}_0(\vec{r}\,',\vec{r},\omega) - \tilde{G}_0(\vec{r}\,',\vec{r},\omega)\nabla'\tilde{P}(\vec{r}\,',\vec{r}_s,\omega)],\end{aligned} \tag{15}$$

where V is the hemispheric volume defined above, and S is the hemisphere's surface. Substituting Equation (12) and its corresponding reference medium Green Function differential equation into Equation (15) gives:

$$\begin{aligned}
&\oint_S dS'\,\hat{n}\cdot[\tilde{P}(\vec{r}',\vec{r}_s,\omega)\nabla'\tilde{G}_0(\vec{r}',\vec{r},\omega)-\tilde{G}_0(\vec{r}',\vec{r},\omega)\nabla'\tilde{P}(\vec{r}',\vec{r}_s,\omega)]\\
=&\int_V d\vec{r}'[\tilde{P}(\vec{r}',\vec{r}_s,\omega)\underbrace{\nabla'^2\tilde{G}_0(\vec{r}',\vec{r},\omega)}_{(-\omega^2/c_0^2)\tilde{G}_0(\vec{r}',\vec{r},\omega)+\delta(\vec{r}'-\vec{r})}\\
&-\tilde{G}_0(\vec{r}',\vec{r},\omega)\underbrace{\nabla'^2\tilde{P}(\vec{r}',\vec{r}_s,\omega)}_{(-\omega^2/c_0^2)\tilde{P}(\vec{r}',\vec{r}_s,\omega)+\frac{\omega^2}{c_0^2}\alpha(\vec{r}')\tilde{P}(\vec{r}',\vec{r}_s,\omega)+\tilde{A}(\omega)\delta(\vec{r}'-\vec{r}_s)}]\\
=&\int_V d\vec{r}'[\underbrace{-\frac{\omega^2}{c_0^2}\widetilde{G}_0(\vec{r}',\vec{r},\omega)\widetilde{P}(\vec{r}',\vec{r}_s,\omega)}_{cancels}+\delta(\vec{r}'-\vec{r})\widetilde{P}(\vec{r}',\vec{r}_s,\omega)\\
&+\underbrace{\frac{\omega^2}{c_0^2}\widetilde{P}(\vec{r}',\vec{r}_s,\omega)\widetilde{G}_0(\vec{r}',\vec{r},\omega)}_{cancels}-\frac{\omega^2}{c_0^2}\alpha(\vec{r}')\widetilde{P}(\vec{r}',\vec{r}_s,\omega)\widetilde{G}_0(\vec{r}',\vec{r},\omega)\\
&-\widetilde{A}(\omega)\delta(\vec{r}'-\vec{r}_s)\widetilde{G}_0(\vec{r}',\vec{r},\omega)]\\
=&\int_V d\vec{r}'[\widetilde{P}(\vec{r}',\vec{r}_s,\omega)\delta(\vec{r}'-\vec{r})-\frac{\omega^2}{c_0^2}\alpha(\vec{r}')\widetilde{P}(\vec{r}',\vec{r}_s,\omega)\widetilde{G}_0(\vec{r}',\vec{r},\omega)\\
&-\widetilde{A}(\omega)\delta(\vec{r}'-\vec{r}_s)\widetilde{G}_0(\vec{r}',\vec{r},\omega)].
\end{aligned}\tag{16}$$

Choosing $\vec{r}\in V$ gives:

$$\begin{aligned}
&\oint_S dS'\,\hat{n}\cdot[\widetilde{P}(\vec{r}',\vec{r}_s,\omega)\nabla'\widetilde{G}_0(\vec{r}',\vec{r},\omega)-\widetilde{G}_0(\vec{r}',\vec{r},\omega)\nabla'\widetilde{P}(\vec{r}',\vec{r}_s,\omega)]\\
=&\int_V d\vec{r}'[\underbrace{\widetilde{P}(\vec{r}',\vec{r}_s,\omega)\delta(\vec{r}'-\vec{r})}_{\widetilde{P}(\vec{r},\vec{r}_s,\omega)}-\frac{\omega^2}{c_0^2}\alpha(\vec{r}')\widetilde{P}(\vec{r}',\vec{r}_s,\omega)\widetilde{G}_0(\vec{r}',\vec{r},\omega)\\
&-\widetilde{A}(\omega)\underbrace{\delta(\vec{r}'-\vec{r}_s)}_{0}\widetilde{G}_0(\vec{r}',\vec{r},\omega)]\\
=&\widetilde{P}(\vec{r},\vec{r}_s,\omega)-\int_V d\vec{r}'\frac{\omega^2}{c_0^2}\alpha(\vec{r}')\widetilde{P}(\vec{r}',\vec{r}_s,\omega)\widetilde{G}_0(\vec{r}',\vec{r},\omega).
\end{aligned}\tag{17}$$

If the support for $\alpha\in V$, rearranging Equation (17) gives:

$$\begin{aligned}
&\widetilde{P}(\vec{r},\vec{r}_s,\omega)\\
=&\int_V d\vec{r}'\widetilde{G}_0(\vec{r}',\vec{r},\omega)\frac{\omega^2}{c_0^2}\alpha(\vec{r}')\widetilde{P}(\vec{r}',\vec{r}_s,\omega)
\end{aligned}$$

$$
\begin{aligned}
&+ \oint_S dS', \hat{n} \cdot [\widetilde{P}(\vec{r}', \vec{r}_s, \omega) \nabla' \widetilde{G}_0(\vec{r}', \vec{r}, \omega) - \widetilde{G}_0(\vec{r}', \vec{r}, \omega) \nabla' \widetilde{P}(\vec{r}', \vec{r}_s, \omega)] \\
= &\int_\infty d\vec{r}' \widetilde{G}_0(\vec{r}', \vec{r}, \omega) \frac{\omega^2}{c_0^2} \alpha(\vec{r}') \widetilde{P}(\vec{r}', \vec{r}_s, \omega) \\
&+ \oint_S dS' \, \hat{n} \cdot [\widetilde{P}(\vec{r}', \vec{r}_s, \omega) \nabla' \widetilde{G}_0(\vec{r}', \vec{r}, \omega) - \widetilde{G}_0(\vec{r}', \vec{r}, \omega) \nabla' \widetilde{P}(\vec{r}', \vec{r}_s, \omega)]. \qquad (18)
\end{aligned}
$$

In Equation (18) the surface integral involves actual pressure measurements and their vertical derivatives. Hence, the surface integral will choose a causal solution. For consistency with Equation (14) choose a causal Green Function which gives:

$$
\begin{aligned}
\widetilde{P}(\vec{r}, \vec{r}_s, \omega) &= \int_\infty d\vec{r}' \widetilde{G}_0^+(\vec{r}', \vec{r}, \omega) \frac{\omega^2}{c_0^2} \alpha(\vec{r}') \widetilde{P}(\vec{r}', \vec{r}_s, \omega) \\
&+ \oint_S dS' \, \hat{n} \cdot [\widetilde{P}(\vec{r}', \vec{r}_s, \omega) \nabla' \widetilde{G}_0^+(\vec{r}', \vec{r}, \omega) - \widetilde{G}_0^+(\vec{r}', \vec{r}, \omega) \nabla' \widetilde{P}(\vec{r}', \vec{r}_s, \omega)] \qquad (19)
\end{aligned}
$$

A.3 Comparing approaches

Comparing Equations (14) and (19) gives an equation for the source signature:

$$
\begin{aligned}
\widetilde{A}(\omega) &= \frac{1}{\widetilde{G}_0^+(\vec{r}, \vec{r}_s, \omega)} \oint_S dS' \, \hat{n} \cdot [\widetilde{P}(\vec{r}', \vec{r}_s, \omega) \nabla' \widetilde{G}_0^+(\vec{r}', \vec{r}, \omega) \\
&\quad - \widetilde{G}_0^+(\vec{r}', \vec{r}, \omega) \nabla' \widetilde{P}(\vec{r}', \vec{r}_s, \omega)]. \qquad (20)
\end{aligned}
$$

A few comments about Equation (20):
(1) Equation (20) is one form of the "triangle relation" relating the pressure wavefield $\widetilde{P}(\vec{r}', \vec{r}_s, \omega)$ and its vertical derivative $\nabla' \widetilde{P}(\vec{r}', \vec{r}_s, \omega)$ along with the source signature $\widetilde{A}(\omega)$. In this instance, the first two variables are used to calculate the third.
(2) The numerator and denominator in Equation (20) can be evaluated at any $\vec{r} \in V$.
(3) The source signature estimation code uses the 3D form $\widetilde{G}_0^+(\vec{r}, \vec{r}_s, \omega) = \exp(ikR)/R$ where $k = \omega/c_0$ and $R = |\vec{r} - \vec{r}_s|$ (Morse and Feshbach, 1953, p. 810).
(4) If the air gun array is replaced by a single isotropic source at $\vec{r}_s$ then $P_0(\vec{r}, \vec{r}_s, \omega) = A(\omega) G_0^+(\vec{r}, \vec{r}_s, \omega)$ and:

$$
\begin{aligned}
A(\omega) &= \frac{1}{N} \sum_{i=1}^{N} \frac{P_0(\vec{r}_i, \vec{r}_s, \omega)}{G_0^+(\vec{r}_i, \vec{r}_s, \omega)} \\
&= \frac{1}{N} \sum_{i=1}^{N} \frac{A_i(\omega) G_0^+(\vec{r}_i, \vec{r}_s, \omega)}{G_0^+(\vec{r}_i, \vec{r}_s, \omega)} = \frac{1}{N} \sum_{i=1}^{N} A_i(\omega) \qquad (21)
\end{aligned}
$$

Equation (21) can be unstable near $\vec{r}_s$ because $1/G_0^+$ can "blow up", so the code uses $1/(G_0^+ + \epsilon)$. Thanks to Dr. Warren Ross (ExxonMobil) for suggesting the form Equation (21).

B Theory of deghosting

M-OSRP's theory of Green's Theorem deghosting is covered in Zhang (2007, pp. 19-23). The procedure defines the following to separate upward moving and downward moving waves:
(1) a reference medium consisting of a whole space of water,
(2) a perturbation $\alpha_{air}(\vec{r}')$ which converts the upper part of the whole space into air,
(3) a perturbation $\alpha_{Earth}(\vec{r}')$ which converts the lower part of the whole space into Earth,
(4) an integration volume V consisting of a hemisphere bounded from below by the measurement surface (the plane $z = 0$),
(5) a free surface (air-water interface) above the measurement surface (*i.e.*, inside V), and
(6) a source $\vec{r}_s$ on or above the measurement surface (again inside V).

The procedure also defines the following:
(7) a causal Green Function $G_0^+(\vec{r}', \vec{r}, \omega)$ in the whole space reference medium,
(8) $k_0 = \omega/c_0$,
(9) $\vec{r} \in V$ and on or below the free surface, and
(10) S as the hemisphere's surface.

Substituting the above into Green's Theorem (Equation (15)) gives:

$$
\begin{aligned}
& \oint_S dS'\, \hat{n} \cdot [\widetilde{P}(\vec{r}', \vec{r}_s, \omega) \nabla' G_0^+(\vec{r}', \vec{r}, \omega) - G_0^+(\vec{r}', \vec{r}, \omega) \nabla' \widetilde{P}(\vec{r}', \vec{r}_s, \omega)] \\
= & \int_V d\vec{r}' [\underbrace{\widetilde{P}(\vec{r}', \vec{r}_s, \omega) \delta(\vec{r}' - \vec{r})}_{\widetilde{P}(\vec{r}, \vec{r}_s, \omega)} \\
& - k_0^2 (\alpha_{air}(\vec{r}') + \underbrace{\alpha_{Earth}(\vec{r}')}_{0}) \widetilde{P}(\vec{r}', \vec{r}_s, \omega) G_0^+(\vec{r}', \vec{r}, \omega) \\
& - \underbrace{\widetilde{A}(\omega) \delta(\vec{r}' - \vec{r}_s) G_0^+(\vec{r}', \vec{r}, \omega)}_{\widetilde{A}(\omega) G_0^+(\vec{r}_s, \vec{r}, \omega)}] \\
= & \widetilde{P}(\vec{r}, \vec{r}_s, \omega) - \int_V d\vec{r}' k_0^2 \alpha_{air}(\vec{r}') \widetilde{P}(\vec{r}', \vec{r}_s, \omega) G_0^+(\vec{r}', \vec{r}, \omega) \\
& - \widetilde{A}(\omega) \underbrace{G_0^+(\vec{r}_s, \vec{r}, \omega)}_{G_0^+(\vec{r}, \vec{r}_s, \omega)} \\
= & \widetilde{P}(\vec{r}, \vec{r}_s, \omega) - \int_V d\vec{r}' G_0^+(\vec{r}', \vec{r}, \omega) k_0^2 \alpha_{air}(\vec{r}') \widetilde{P}(\vec{r}', \vec{r}_s, \omega) \\
& - \widetilde{A}(\omega) G_0^+(\vec{r}, \vec{r}_s, \omega). \qquad (22)
\end{aligned}
$$

The physical meaning of Equation (22) is that the total wavefield at $\vec{r}$ can be separated into three parts:
(1) the direct wave which travels from the source at $\vec{r}_s$ to $\vec{r}$ (third term on the right hand side),
(2) the pressure field whose last motion is downward from the free surface (second term on the

right-hand side), and
(3) the pressure field whose last motion is upward from the Earth (the entire right-hand side).
Hence, Equation (22) is the receiver side deghosting algorithm.

Letting the radius of the hemisphere go to ∞, the Sommerfeld radiation condition gives:

$$\begin{aligned}\widetilde{P}^{deghosted}(\vec{r},\vec{r}_s,\omega) &= \int_{m.s.} dS'\,\hat{n}\cdot[\widetilde{P}(\vec{r}',\vec{r}_s,\omega)\nabla' G_0^+(\vec{r}',\vec{r},\omega) \\ &\quad -G_0^+(\vec{r}',\vec{r},\omega)\nabla'\widetilde{P}(\vec{r}',\vec{r}_s,\omega)], \end{aligned} \tag{23}$$

where $\widetilde{P}(\vec{r}';\vec{r}_s;\omega)$ and $\nabla'\widetilde{P}(\vec{r}';\vec{r}_s;\omega)$ are respectively the hydrophone measurements and their spatial derivatives (in the frequency domain). Using reciprocity, a similar integration on the source side will remove source ghosts.

If the derivative of the pressure is not measured, M-OSRP's procedure predicts the pressure and its vertical derivative on a "pseudo-measurement surface" located between the free surface and the measurement surface using pressure measurements on the cable plus the source signature. The procedure includes a "double Dirichlet" Green Function $G_0^{DD}(\vec{r}',\vec{r},\omega)$ which vanishes on the measurement surface as well as the free surface. $G_0^{DD}(\vec{r}',\vec{r},\omega)$ is a solution of:

$$\nabla'^{\,2} G_0^{DD}(\vec{r}',\vec{r},\omega) + k_0^2 G_0^{DD}(\vec{r}',\vec{r},\omega) = \delta(\vec{r}'-\vec{r}) + \sum_{n=1}^{\infty} a_i \delta(\vec{r}'-\vec{r}_i), \tag{24}$$

where $a_i = \pm 1$, and $\vec{r}_i$ is the position of the ith mirror image of $\vec{r}$ as the wavefield reflects from the Earth and free surface. Substituting Equation (24) into Green's Theorem (Equation (15)) gives:

$$\begin{aligned}
&\oint_S dS'\,\hat{n}\cdot[\widetilde{P}(\vec{r}',\vec{r}_s,\omega)\nabla' G_0^{DD}(\vec{r}',\vec{r},\omega) - G_0^{DD}(\vec{r}',\vec{r},\omega)\nabla'\widetilde{P}(\vec{r}',\vec{r}_s,\omega)] \\
= &\int_V d\vec{r}'[\widetilde{P}(\vec{r}',\vec{r}_s,\omega)\nabla'^{\,2} G_0^{DD}(\vec{r}',\vec{r},\omega) - G_0^{DD}(\vec{r}',\vec{r},\omega)\nabla'^{\,2}\widetilde{P}(\vec{r}',\vec{r}_s,\omega)] \\
= &\int_V d\vec{r}'[\widetilde{P}(\vec{r}',\vec{r}_s,\omega)\left(\underbrace{-k_0^2 G_0^{DD}(\vec{r}',\vec{r},\omega)}_{cancel} + \delta(\vec{r}'-\vec{r}) + \sum_{n=1}^{\infty} a_i\delta(\vec{r}'-\vec{r}_i)\right) \\
&-G_0^{DD}(\vec{r}',\vec{r},\omega)\left(\underbrace{-k_0^2\widetilde{P}(\vec{r}',\vec{r}_s,\omega)}_{cancel} + A(\omega)\delta(\vec{r}'-\vec{r}_s) + k_0^2(\alpha_{air}(\vec{r}')+\alpha_{Earth}(\vec{r}'))\widetilde{P}(\vec{r}',\vec{r}_s,\omega)\right)] \\
= &\int_V d\vec{r}'\widetilde{P}(\vec{r}',\vec{r}_s,\omega)\delta(\vec{r}'-\vec{r}) + \int_V d\vec{r}'\widetilde{P}(\vec{r}',\vec{r}_s,\omega)\sum_{n=1}^{\infty} a_i\delta(\vec{r}'-\vec{r}_i) \\
&-\int_V d\vec{r}' G_0^{DD}(\vec{r}',\vec{r},\omega)A(\omega)\delta(\vec{r}'-\vec{r}_s) \\
&-\int_V d\vec{r}' G_0^{DD}(\vec{r}',\vec{r},\omega)k_0^2\alpha_{air}(\vec{r}')\widetilde{P}(\vec{r}',\vec{r}_s,\omega) \\
&-\int_V d\vec{r}' G_0^{DD}(\vec{r}',\vec{r},\omega)k_0^2\alpha_{Earth}(\vec{r}')\widetilde{P}(\vec{r}',\vec{r}_s,\omega).
\end{aligned} \tag{25}$$

Choosing V to be the space sandwiched between the free surface and measurement surface and $\vec{r} \in V$ gives:

$$\begin{aligned}
&\int_{m.s.} dS'\, \hat{n} \cdot [\widetilde{P}(\vec{r}', \vec{r}_s, \omega) \nabla' G_0^{DD}(\vec{r}', \vec{r}, \omega) - \underbrace{G_0^{DD}(\vec{r}', \vec{r}, \omega)}_{=0} \nabla' \widetilde{P}(\vec{r}', \vec{r}_s, \omega)] \\
= \; & \underbrace{\int_V d\vec{r}' \widetilde{P}(\vec{r}', \vec{r}_s, \omega) \delta(\vec{r}' - \vec{r})}_{=\widetilde{P}(\vec{r}, \vec{r}_s, \omega)} + \underbrace{\int_V d\vec{r}' \widetilde{P}(\vec{r}', \vec{r}_s, \omega) \sum_{n=1}^{\infty} a_i \delta(\vec{r}' - \vec{r}_i)}_{=0} \\
& - \underbrace{\int_V d\vec{r}' G_0^{DD}(\vec{r}', \vec{r}, \omega) A(\omega) \delta(\vec{r}' - \vec{r}_s)}_{=G_0^{DD}(\vec{r}_s, \vec{r}, \omega) A(\omega)} \\
& - \int_V d\vec{r}' G_0^{DD}(\vec{r}', \vec{r}, \omega) k_0^2 \underbrace{\alpha_{air}(\vec{r}')}_{=0} \widetilde{P}(\vec{r}', \vec{r}_s, \omega) - \int_V d\vec{r}' G_0^{DD}(\vec{r}', \vec{r}, \omega) k_0^2 \underbrace{\alpha_{Earth}(\vec{r}')}_{=0} \widetilde{P}(\vec{r}', \vec{r}_s, \omega) \\
= \; & \widetilde{P}(\vec{r}, \vec{r}_s, \omega) - G_0^{DD}(\vec{r}_s, \vec{r}, \omega) A(\omega).
\end{aligned}$$

Hence:

$$\widetilde{P}(\vec{r}, \vec{r}_s, \omega) = A(\omega) G_0^{DD}(\vec{r}_s, \vec{r}, \omega) + \int_{m.s.} dS', \hat{n} \cdot \widetilde{P}(\vec{r}', \vec{r}_s, \omega) \nabla' G_0^{DD}(\vec{r}', \vec{r}, \omega). \tag{26}$$

Taking the derivative of Equation (26) gives:

$$\frac{\partial}{\partial z} \widetilde{P}(\vec{r}, \vec{r}_s, \omega) = A(\omega) \frac{\partial}{\partial z} G_0^{DD}(\vec{r}_s, \vec{r}, \omega) + \int_{m.s.} dS'\, \hat{n} \cdot \widetilde{P}(\vec{r}', \vec{r}_s, \omega) \nabla' \frac{\partial}{\partial z} G_0^{DD}(\vec{r}', \vec{r}, \omega). \tag{27}$$

The procedure predicts the pressure and its vertical derivative on the pseudo measurement surface using Equations (26) and (27), respectively, and performs receiver side deghosting on the pseudo-measurement surface using Equation (23) (Zhang and Weglein, 2005, p. 2).

After receiver side deghosting, using reciprocity, the procedure predicts the pressure and its vertical derivative on the source side using:

$$\widetilde{P}(\vec{r}, \vec{r}_s, \omega) = \int_{m.s.} dS'\, \hat{n} \cdot \widetilde{P}(\vec{r}', \vec{r}_s, \omega) \nabla' G_0^{DD}(\vec{r}', \vec{r}, \omega), \tag{28}$$

$$\frac{\partial}{\partial z} \widetilde{P}(\vec{r}, \vec{r}_s, \omega) = \int_{m.s.} dS'\, \hat{n} \cdot \widetilde{P}(\vec{r}', \vec{r}_s, \omega) \nabla' \frac{\partial}{\partial z} G_0^{DD}(\vec{r}', \vec{r}, \omega). \tag{29}$$

which are the same as Equations (26) and (27) with their first right-hand side terms omitted. When the receivers are below the source, all field components (the direct wave, the downward moving pressure field reflected from the free surface, and the deghosted pressure field) are $\in V$. However, when the receiver is above the sources, only two components (the downward moving pressure field reflected from the free surface and the deghosted pressure field) are $\in V$; the direct wave is $\notin V$.

After predicting the pressure and its vertical derivative using Equations (28) and (29), the procedure performs source side deghosting on the pseudo-measurement surface using Equation (23).

When coding the above, it was assumed that $\partial P/\partial n$ is measured and the following forms were used in the code (Morse and Feshbach, 1953, p. 810):
In 3D $G_0^+(\vec{r},\vec{r}_s,\omega) = \exp(ikR)/R$ where $k = \omega/c_0$ and $R = |\vec{r}-\vec{r}_s|$, and
$G_0^{DD}(\vec{r},\vec{r}_s,\omega) = \exp(ikR_+)/R_+ - \exp(ikR_-)/R_-$ where $k = \omega/c_0$, and
$R_\pm = \sqrt{(x-x_s)^2+(y-y_s)^2+(z\mp z_s)^2}$.
In 2D $G_0^+(\vec{r},\vec{r}_s,\omega) = -\frac{i}{4}H_0^{(1)}(kR_+)$ and
$G_0^{DD}(\vec{r},\vec{r}_s,\omega) = -\frac{i}{4}(H_0^{(1)}(kR_+) - H_0^{(1)}(kR_-))$.

C Running the code

The Green's Theorem code will be released to the sponsors after the Annual Meeting. It will be posted on the M-OSRP website (mosrp.uh.edu) along with test data and user documentation.

D Theory of free surface multiple elimination

M-OSRP's theory of Free Surface Multiple Elimination (FSME) is derived in Carvalho (1992). This derivation has been included here because the first author is running the 3D FSME code with and without the 3D Green's Theorem code (using synthetic and field data) to test the hypothesis that deghosting and source signature estimation by the 3D Green's Theorem code will enable more competent prediction of free surface multiples by the 3D FSME code.

If a given term in the forward scattering series creates a certain type of data, that term in the inverse scattering series removes that type of data, *e.g.*, if there is no free surface, there are no ghosts and free surface multiples in the data. Hence, G_0 must be of the form $G_0^d + G_0^{FS}$ where G_0^{FS} acts to create and remove ghosts and free surface multiples.

Deghosting is accomplished by multiplying each inverse scattering series equation from the left and right by G_0^{-1} then G_0^d; now the outer G_0's have been replaced by G_0^d (but the inner G_0's are still $G_0^d + G_0^{FS}$).

$$G_0^d V_1 G_0^d = D \tag{30}$$
$$G_0^d V_2 G_0^d = -G_0^d V_1 G_0 V_1 G_0^d \tag{31}$$
$$G_0^d V_3 G_0^d = -G_0^d V_1 G_0 V_2 G_0^d - G_0^d V_2 G_0 V_1 G_0^d - G_0^d V_1 G_0 V_1 G_0 V_1 G_0^d \tag{32}$$
$$\vdots$$

Reasoning by analogy, the subseries for free surface multiple elimination is developed by replacing the inner instances of G_0 in the above equations with G_0^{FS}.

$$G_0^d V_1 G_0^d = D_1' \tag{33}$$

$$
\begin{aligned}
G_0^d V_2 G_0^d &= -G_0^d V_1 G_0^{FS} V_1 G_0^d && (34)\\
G_0^d V_3 G_0^d &= -G_0^d V_1 G_0^{FS} V_2 G_0^d - G_0^d V_2 G_0^{FS} V_1 G_0^d \\
&\quad -G_0^d V_1 G_0^{FS} V_1 G_0^{FS} V_1 G_0^d && (35)\\
&\vdots
\end{aligned}
$$

where D_1' is deghosted data.

Rewrite Equation (35) in the suggestive form:

$$
\begin{aligned}
G_0^d V_3 G_0^d &= -G_0^d V_1 G_0^{FS} V_2 G_0^d - G_0^d V_2 G_0^{FS} V_1 G_0^d \\
&\quad -G_0^d \underbrace{V_1 G_0^{FS} V_1}_{-V_2} G_0^{FS} V_1 G_0^d \\
&= -G_0^d V_1 G_0^{FS} V_2 G_0^d \underbrace{-G_0^d V_2 G_0^{FS} V_1 G_0^d}_{cancels} \underbrace{+G_0^d V_2 G_0^{FS} V_1 G_0^d}_{cancels} \\
&= -G_0^d V_1 G_0^{FS} V_2 G_0^d && (36)\\
G_0^d V_n G_0^d &= -G_0^d V_1 G_0^{FS} V_{n-1} G_0^d && (37)\\
D' &= \sum_{n=1}^{\infty} D_n' = \sum_{n=1}^{\infty} G_0^d V_n G_0^d. && (38)
\end{aligned}
$$

Fourier transform Equation (38) into the (k_g, k_s, ω) domain:

$$
\begin{aligned}
D'(k_g, k_s, \omega) &= \sum_{n=1}^{\infty} D_n'(k_g, k_s, \omega), && (39)\\
\text{where } D_n'(k_g, k_s, \omega) &= \frac{1}{i\pi\rho_0 B(\omega)} \int_{-\infty}^{\infty} dk\, q \exp\left(iq(\epsilon_g + \epsilon_s)\right) \\
&\quad \times D_1'(k_g, k, \omega) D_{n-1}'(k, k_s, \omega) && (40)
\end{aligned}
$$

for $n = 2, 3, 4, \ldots$ Equations (40) and (39) are used in M-OSRP's 2D free surface multiple elimination code.

The procedure Carvalho (1992, pp. 12–14, 29–30) derives Equation (40) from Equation (30) and a causal Green Function (Equation (43) derived below). The procedure defines the following in 2D:
$B(\omega)$ is the source signature,
$c_0 = \sqrt{\kappa_0/\rho_0}$ is the speed of sound in the reference medium (water),
$k = \sqrt{k_x^2 + k_z^2}$,
k_g, k_s, and k_x are the Fourier conjugates of x_g, x_s, and x, respectively,
$k_z = -(q_g + q_s)$,
κ_0 is the bulk modulus of water,
$q = sgn(\omega)\sqrt{(\omega/c_0)^2 - k_x^2}$,
$q_g = sgn(\omega)\sqrt{(\omega/c_0)^2 - k_g^2}$,
$q_s = sgn(\omega)\sqrt{(\omega/c_0)^2 - k_s^2}$,

ρ_0 is the density of water,
(x, z) is a point in 2D space,
(x_g, ϵ_g) is the line receiver location, and
$(x', z') = (x_s, \epsilon_s)$ is the line source location.

D.1 Derivation of the Green Function

The procedure chooses a reference medium consisting of a half space of water with a free surface at $z = 0$. $L_0 G_0 = \delta$ takes the form

$$\left(\nabla^2 + \frac{\omega^2}{c_0^2}\right) G_0(x, z, x', z'; \omega) = -\rho_0 \delta(x - x')[\delta(z - z') - \delta(z + z')]. \tag{41}$$

$\delta(z - z')$ models an impulsive source at depth z', and $\delta(z + z')$ models an impulsive source that "looks like" it originates at height $-z'$ above the free surface because its pressure wave has reflected off the free surface (method of images). Fourier transforming Equation (41) with respect to x gives:

$$\begin{aligned}
& \left((-ik_x)^2 + \frac{d^2}{dz^2} + \frac{\omega^2}{c_0^2}\right) G_0(k_x, z, x', z'; \omega) \\
= & \left(\frac{d^2}{dz^2} + \underbrace{\frac{\omega^2}{c_0^2} - k_x^2}_{q^2}\right) G_0(k_x, z, x', z'; \omega) \\
= & -\frac{\rho_0}{\sqrt{2\pi}} \exp(-ik_x x')[\delta(z - z') - \delta(z + z')].
\end{aligned} \tag{42}$$

The causal solution of Equation (42) is:

$$G_0^+(k_x, z, x', z'; \omega) = \frac{\rho_0}{\sqrt{2\pi}} \frac{\exp(-ik_x x')}{-2iq} (\exp(iq|z - z'|) - \exp(iq|z + z'|)) \tag{43}$$

$$= \underbrace{-\frac{\rho_0}{\sqrt{2\pi}} \frac{\exp(-ik_x x')}{2iq} \exp(iq|z - z'|)}_{G_0^d} + \underbrace{\frac{\rho_0}{\sqrt{2\pi}} \frac{\exp(-ik_x x')}{2iq} \exp(iq|z + z'|)}_{G_0^{FS}} \tag{44}$$

(De Santo, 1992, Chapter 2) (Carvalho, 1992, (2.3) p. 12).

D.2 Derivation of Equation (40)

Letting $D_0(k_g, k_s, \omega) = D(k_g, k_s, \omega)/B(\omega)$ gives:

$$D_0(k_g, k_s, \omega) = G_0^d V_1 G_0^d$$

$$
\begin{aligned}
&= \int_{-\infty}^{\infty}\int_{-\infty}^{\infty} dx\,dz\,\frac{\rho_0}{\sqrt{2\pi}}\frac{\exp(-ik_g x)}{-2iq_g} \\
&\quad \times(\exp(iq_g|z-\epsilon_g|)-\exp(iq_g|z+\epsilon_g|))V_1(x,z,\omega) \\
&\quad \times\frac{\rho_0}{\sqrt{2\pi}}\frac{\exp(ik_s x)}{-2iq_s}(\exp(iq_s|z-\epsilon_s|)-\exp(iq_s|z+\epsilon_s|)) \\
&= \frac{\rho_0^2}{2\pi}\,\frac{1}{(2i)^2 q_g q_s}\int_{-\infty}^{\infty}\int_{-\infty}^{\infty} dx\,dz \\
&\quad \times\exp(-ik_g x)(\exp(iq_g(z-\epsilon_g))-\exp(iq_g(z+\epsilon_g)))V_1(x,z,\omega) \\
&\quad \times\exp(ik_s x)(\exp(iq_s(z-\epsilon_s))-\exp(iq_s(z+\epsilon_s))) \\
&= \frac{\rho_0^2}{2\pi}\,\frac{1}{(2i)^2 q_g q_s}\int_{-\infty}^{\infty}\int_{-\infty}^{\infty} dx\,dz \\
&\quad \times\exp(-ik_g x)\exp(iq_g z)\underbrace{(\exp(-iq_g\epsilon_g)-\exp(iq_g\epsilon_g))}_{-2i\sin(q_g\epsilon_g)}V_1(x,z,\omega) \\
&\quad \times\exp(ik_s x)\exp(iq_s z)\underbrace{(\exp(-iq_s\epsilon_s)-\exp(iq_s\epsilon_s))}_{-2i\sin(q_s\epsilon_s)} \\
&= \frac{\rho_0^2}{2\pi}\,\frac{\sin(q_g\epsilon_g)\sin(q_s\epsilon_s)}{q_g q_s}\int_{-\infty}^{\infty}\int_{-\infty}^{\infty} dx\,dz \\
&\quad \times\exp(-ik_g x)\exp(iq_g z)V_1(x,z,\omega)\exp(ik_s x)\exp(iq_s z) \qquad (45)
\end{aligned}
$$

(Carvalho, 1992, (2.5) p. 12 and (2.6) p. 13).

Now V_1 is needed.

$$
\begin{aligned}
V &= L_0 - L = \nabla\cdot\frac{1}{\rho_0}\nabla+\frac{\omega^2}{\kappa_0}-\left(\nabla\cdot\frac{1}{\rho(\vec{r})}\nabla+\frac{\omega^2}{\kappa(\vec{r})}\right) \\
&= \nabla\cdot\left(\frac{1}{\rho_0}-\frac{1}{\rho(\vec{r})}\right)\nabla+\omega^2\left(\frac{1}{\kappa_0}-\frac{1}{\kappa(\vec{r})}\right) \\
&= \nabla\cdot\frac{1}{\rho_0}\left(\underbrace{1-\frac{\rho_0}{\rho(\vec{r})}}_{\beta(\vec{r})}\right)\nabla+\omega^2\,\frac{1}{\kappa_0}\left(\underbrace{1-\frac{\kappa_0}{\kappa(\vec{r})}}_{\alpha(\vec{r})}\right) \\
&= \nabla\cdot\frac{\beta(\vec{r})}{\rho_0}\nabla+\omega^2\frac{\alpha(\vec{r})}{\kappa_0} \qquad (46)
\end{aligned}
$$

(Carvalho, 1992, (1.6) p. 6).

Combining Equations (45) and (46) gives:

$$
\begin{aligned}
D_0(k_g,k_s,\omega) &= \frac{\rho_0^2}{2\pi}\,\frac{\sin(q_g\epsilon_g)\sin(q_s\epsilon_s)}{q_g q_s}\int_{-\infty}^{\infty}\int_{-\infty}^{\infty} dx\,dz \\
&\quad \times\exp(-ik_g x)\exp(iq_g z)\left(\nabla\cdot\frac{\beta_1(\vec{r})}{\rho_0}\nabla+\omega^2\frac{\alpha_1(\vec{r})}{\kappa_0}\right)
\end{aligned}
$$

$$
\begin{aligned}
& \times \exp(ik_s x)\exp(iq_s z) \\
= \; & \frac{\rho_0^2}{2\pi}\frac{\sin(q_g\epsilon_g)\sin(q_s\epsilon_s)}{q_g q_s}(I_1+I_2) \\
\text{where } I_1 \; \equiv \; & \int_{-\infty}^{\infty}\int_{-\infty}^{\infty} dx\,dz\, \exp(-ik_g x)\exp(iq_g z)\omega^2\frac{\alpha_1(\vec{r})}{\kappa_0} \\
& \times \exp(ik_s x)\exp(iq_s z) \qquad (47) \\
\text{and } I_2 \; \equiv \; & \int_{-\infty}^{\infty}\int_{-\infty}^{\infty} dx\,dz\, \exp(-ik_g x)\exp(iq_g z)\nabla\cdot\frac{\beta_1(\vec{r})}{\rho_0}\nabla \\
& \times \exp(ik_s x)\exp(iq_s z). \qquad (48)
\end{aligned}
$$

Rewriting Equation (48) gives:

$$
\begin{aligned}
I_2 \; = \; & \int_{-\infty}^{\infty}\int_{-\infty}^{\infty} dx\,dz\,\nabla\cdot\left[\exp(-ik_g x)\exp(iq_g z)\frac{\beta_1(\vec{r})}{\rho_0}\right. \\
& \left.\times\nabla(\exp(ik_s x)\exp(iq_s z))\right] \\
& -\int_{-\infty}^{\infty}\int_{-\infty}^{\infty} dx\,dz\,\frac{\beta_1(\vec{r})}{\rho_0}\nabla(\exp(ik_s x)\exp(iq_s z)) \\
& \cdot\nabla(\exp(-ik_g x)\exp(iq_g z)). \qquad (49)
\end{aligned}
$$

(Jackson, 1999, inside front cover, 7th Vector Formula).

The first integral in Equation (49) vanishes (use the divergence theorem, then the expression inside the square brackets vanishes at ∞ by causality). The second integral in Equation (49) gives:

$$
\begin{aligned}
I_2 \; = \; & -\int_{-\infty}^{\infty}\int_{-\infty}^{\infty} dx\,dz\,\frac{\beta_1(\vec{r})}{\rho_0}(ik_s\hat{x}+iq_s\hat{z})(\exp(ik_s x)\exp(iq_s z)) \\
& \cdot(-ik_g\hat{x}+iq_g\hat{z})(\exp(-ik_g x)\exp(iq_g z)) \\
= \; & -\int_{-\infty}^{\infty}\int_{-\infty}^{\infty} dx\,dz\,\frac{\beta_1(\vec{r})}{\rho_0}(k_s k_g - q_s q_g) \\
& \times\exp(ik_s x)\exp(iq_s z)\exp(-ik_g x)\exp(iq_g z). \qquad (50)
\end{aligned}
$$

Substituting Equations (47) and (50) into Equation (45) gives:

$$
\begin{aligned}
D_0(k_g,k_s,\omega) \; = \; & \frac{\rho_0^2}{2\pi}\frac{\sin(q_g\epsilon_g)\sin(q_s\epsilon_s)}{q_g q_s}\int_{-\infty}^{\infty}\int_{-\infty}^{\infty} dx\,dz \\
& \exp(-i(k_g-k_s)x)\exp(-i(-q_g-q_s)z) \\
& \times\left[\omega^2\frac{\alpha_1(x,z)}{\kappa_0}+(q_g q_s - k_g k_s)\frac{\beta_1(x,z)}{\rho_0}\right]. \qquad (51)
\end{aligned}
$$

Performing the Fourier transforms gives:

$$
D_0(k_g,k_s,\omega) \; = \; \frac{\rho_0^2}{2\pi}\frac{\sin(q_g\epsilon_g)\sin(q_s\epsilon_s)}{q_g q_s}\left[\omega^2\frac{\widetilde{\widetilde{\alpha}}_1(k_g-k_s,-q_g-q_s)}{\kappa_0}\right.
$$

$$+ (q_g q_s - k_g k_s) \frac{\widetilde{\widetilde{\beta}}_1(k_g - k_s, -q_g - q_s)}{\rho_0} \Bigg] . \tag{52}$$

where $[\ldots] = V_1(k_g, k_s, \omega)$. Therefore:

$$\begin{aligned}
V_1(k_g, k_s, \omega) &= \frac{2\pi}{\rho_0^2} \frac{q_g q_s}{\sin(q_g \epsilon_g) \sin(q_s \epsilon_s)} D_0(k_g, k_s, \omega) \\
&= \frac{2\pi}{\rho_0^2} \frac{(2i)^2 q_g q_s D_0(k_g, k_s, \omega)}{(\exp(iq_g\epsilon_g) - \exp(-iq_g\epsilon_g))(\exp(iq_s\epsilon_s) - \exp(-iq_s\epsilon_s))} \\
&= \frac{2\pi}{\rho_0^2} \frac{-4 q_g q_s \exp(iq_g\epsilon_g) \exp(iq_s\epsilon_s)}{(\exp(2iq_g\epsilon_g) - 1)(\exp(2iq_s\epsilon_s) - 1)} \underbrace{D_0(k_g, k_s, \omega)}_{D(k_g,k_s,\omega)/B(\omega)} \\
&= 2\pi \frac{-4}{B(\omega)} \frac{q_g q_s}{\rho_0^2} \exp(iq_g\epsilon_g) \exp(iq_s\epsilon_s) \\
&\quad \times \underbrace{\frac{D(k_g, k_s, \omega)}{(\exp(2iq_g\epsilon_g) - 1)(\exp(2iq_s\epsilon_s) - 1)}}_{D_1'(k_g,k_s,\omega)}
\end{aligned} \tag{53}$$

Using Equation (44) to transform Equation (37) into the (k_g, k_s, ω) domain gives:

$$V_n(k_g, k_s, \omega) = \frac{1}{2\pi} \int_{-\infty}^{\infty} dk \, \frac{\rho_0}{-2iq} V_1(k_g, k, \omega) V_{n-1}(k, k_s, \omega) \tag{54}$$

Substituting Equation (53) into Equation (54) (for all terms except the first) give the desired result:

$$\begin{aligned}
V_n(k_g, k_s, \omega) &= \frac{1}{2\pi} \frac{\rho_0}{-2i} \int_{-\infty}^{\infty} \frac{dk}{q} \\
&\times \underbrace{2\pi \frac{-4}{B(\omega)} \frac{q_g q}{\rho_0^2} \exp(iq_g\epsilon_g) \exp(iq\epsilon_s)}_{drop} D_1'(k_g, k, \omega) \\
&\times \underbrace{2\pi \frac{-4}{B(\omega)} \frac{q q_s}{\rho_0^2} \exp(iq\epsilon_g) \exp(iq_s\epsilon_s)}_{modify} D_{n-1}'(k, k_s, \omega) \\
&= \frac{1}{2\pi} \frac{\rho_0}{-2i} \int_{-\infty}^{\infty} \frac{dk}{q} D_1'(k_g, k, \omega) \\
&\times 2\pi \frac{-4}{B(\omega)} \frac{q^2}{\rho_0^2} \exp(iq\epsilon_g) \exp(iq\epsilon_s) D_{n-1}'(k, k_s, \omega) \\
&= 2\pi \frac{1}{i\pi\rho_0 B(\omega)} \int_{-\infty}^{\infty} dk \, q \, \exp(iq(\epsilon_g + \epsilon_s)) \\
&\times D_1'(k_g, k, \omega) D_{n-1}'(k, k_s, \omega)
\end{aligned} \tag{55}$$

which is the desired form to within a factor of 2π.

References

Carvalho, P. M. *Free-surface multiple reflection elimination method based on nonlinear inversion of seismic data.* PhD thesis, Universidade Federal da Bahia, 1992.

De Santo, J. A. *Scalar Wave Theory: Green's Functions and Applications.* Springer-Verlag, 1992.

Jackson, J. D. *Classical Electrodynamics.* Third edition. New York: John Wiley & Sons, Inc., 1999.

Morse, P. M. and H. Feshbach. *Methods of theoretical physics.* McGraw-Hill Book Co., 1953.

Orfanidis, S. J. *Electromagnetic Waves and Antennas.* http://www.ece.rutgers.edu/~orfanidi/ewa/. 2008.

Ramírez, A. C. *I. - Inverse scattering subseries for removal of internal multiples and depth imaging primaries; II. - Green's theorem as the foundation of interferometry and guiding new practical methods and applications.* PhD thesis, University of Houston, 2007.

Ramírez, A. C. and A. B. Weglein. "Green's theorem as a comprehensive framework for data reconstruction, regularization, wavefield separation, seismic interferometry and wavelet estimation: a tutorial." *Geophysics* 74 (November-December 2009): W35–W62.

Terenghi, P. "3D Free Surface Multiple Prediction: numerical testing and coding update." *M-OSRP 2009 Annual Meeting.* 2010.

Weglein, A. B., F. V. Araújo, P. M. Carvalho, R. H. Stolt, K. H. Matson, R. T. Coates, D. Corrigan, D. J. Foster, S. A. Shaw, and H. Zhang. "Inverse Scattering Series and Seismic Exploration." *Inverse Problems* (2003): R27–R83.

Weglein, Arthur B. and Bruce G. Secrest. "Wavelet estimation for a multidimensional acoustic earth model." *Geophysics* 55 (July 1990): 902–913.

Zhang, Jingfeng. *Wave theory based data preparation for inverse scattering multiple removal, depth imaging and parameter estimation: analysis and numerical tests of Green's theorem deghosting theory.* PhD thesis, University of Houston, 2007.

Zhang, Jingfeng and Arthur B. Weglein. 2005 "Documentation for the M-OSRP Extinction Theorem Deghosting code.".

3D Free-Surface Multiple Prediction: numerical testing and coding update

P. Terenghi and A.B. Weglein

Abstract

M-OSRP maintains a highly optimized three-dimensional implementation of the inverse scattering free-surface multiple elimination algorithm designed to run on largely distributed computing systems. Thanks to the contributions of many researchers, the project is currently at a stage where the code is being refined in order to facilitate testing on field data, realistic synthetics, and where possible to relax assumptions which are not required by theory. This note provides new results on synthetic data and coding updates with respect to the version released in Summer 2009.

1 Theory and requirements

The M-OSRP three-dimensional free-surface multiple prediction code implements the theory presented in Carvalho (1992), Araujo et al. (1994), Weglein et al. (1997) and in Section 5 of Weglein et al. (2003). The derivation begins with the choice of a homogeneous half-space of water as a background medium and considers wave-propagation according to the laws governing 2D media. However, the choice of propagation and model-type (whether the medium is acoustic or elastic, 2D or 3D) becomes completely transparent in the final expression. Ultimately, the algorithm may be considered multi-dimensional and model-type independent.

The inverse scattering algorithm for free-surface multiple prediction is formulated according to a series whose first term involves a de-ghosted version of the difference between the responses of the actual (G) and reference medium (G_0), according to:

$$(G - G_0)^{deghost} = G_0^d V_1 G_0^d \tag{1}$$

where V_1 represents a first order approximation to the earth properties, obtained in terms of the input data.

The response of the reference medium (a half-space of water) may be decomposed in two contributions: the direct arrival G_0^d and its ghost reflections (G_0^{fs}) traveling from the source up to the free-surface and from the free-surface down to the receivers:

$$G_0 = G_0^d + G_0^{fs}. \tag{2}$$

on the other hand, G_0^d may be regarded as the impulse response of a whole-space of water without a free-surface.

The quantity on the right-hand side of Equation (1) represents the input data: the first step for the elimination of surface multiples is the subtraction of the reference wave-field from the total wave-field. The algorithm is in fact set to operate on data without a direct arrival and its ghost reflections either on the source and the receiver side.

Additionally, both source and receiver-side ghost-reflections should be eliminated for the part of the wave-field resulting from the actual medium where its properties differ form those of the reference medium. Further, the knowledge of the source signature will largely improve the estimation of multiples and facilitate the task of subtracting them from the initial data. Clearly, an optimal best result in multiple elimination will depend on how accurately the requirements are met.

A family of data-driven pre-processing algorithms, including wave-field separation (cancels the direct wave-field and its ghost), wavelet estimation, ghost removal (removes source and receiver ghosts), data-reconstruction, suitable for the said purpose may be obtained starting from Green's second identity (Green, 1828), (Ramirez and Weglein, 2009). Those algorithms naturally compliment the inverse scattering theory in establishing wave-equation compliant end-to-end processing of seismic data from acquisition to imaging and inversion.

The expression for V_1 obtained by resolving the first-order Expression (1) may be used in the second-order expression:

$$(G_0 V_2 G_0)_m = -(G_0 V_1 G_0 V_1 G_0)_m \tag{3}$$

where the subscript m indicates evaluation at the measurement surface. The inverse scattering free-surface multiple prediction algorithm is then obtained by selecting the contribution to V_2 from the Green's Function deriving from the free-surface G_0^{fs} only. The final expression is a series for deghosted and free-surface-multiple-free data D' in terms of deghosted data $D'1$, where the initial term is:

$$D'(k_g, k_s, \omega) = \sum_{n=1}^{\infty} D'_n(k_g, k_s, \omega) \tag{4}$$

with the symbols k_g, k_s and ω representing the wave-numbers along the source and receiver axes and the angular frequency, respectively. All subsequent terms are computed using the recursive expression:

$$D'_n = \frac{1}{i\pi\rho_0 A(\omega)} \int_{-\infty}^{+\infty} dk\ q\ e^{iq(z_g+z_s)}\ D'_1(k_g, k, \omega)\ D'_{n-1}(k, k_s, \omega) \tag{5}$$

where q is an obliquity factor given by:

$$q \;=\; sign(\omega)\,\sqrt{\frac{\omega^2}{c_o^2} \;-\; k^2}, \tag{6}$$

and z_s and z_g are the depth below the free surface of the sources and receivers, respectively. The source wavelet $A(\omega)$ appears in the denominator, to represent spectral deconvolution by the source signature.

2 Coding update

The 3D free surface inverse scattering series multiple removal code was written by Sam Kaplan during his collaboration with M-OSRP between 2004 and 2006 (Kaplan et al., 2005). Before the code could be extensively tested, Sam Kaplan began his PhD studies at the University of Alberta and the code was subsequently debugged by in Simon Shaw (ConocoPhillips) and Kris Innanen (M-OSRP) (Innanen et al., 2008). Further undocumented efforts are due to Haiyan Zhang (Conoco Phillips) and Zhiqiang Wang (M-OSRP) during 2009.

The majority of the code remains to date unchanged vs. the version released during Summer 2009. It was however deemed convenient to review some coding choices regarding the organization of data samples in the Fourier domain. The old code operated on Fourier transformed data sampled on a discontinuous axis:

$$[0, \Delta k_x, ..., +\frac{1}{2\Delta x}, -\frac{1}{2\Delta x}, ..., -\Delta k_x],$$

a strategy that requires a large number of indices to keep track of positive and negative frequencies separately. In the new version, we implement spectral shifts (fftshift) and re-arrange the Fourier spectra in monotonically increasing order:

$$[-\frac{1}{2 * \Delta x}, ..., 0, ..., +\frac{1}{2 * \Delta x}].$$

The cost of performing the additional re-shuffling is largely compensated by the simplification in the indexing scheme for the most intensive internal loops. Because of the new layout convention, separate loops along the positive and negative spatial frequency axes can be merged into single loops and many related variables can be discarded.

In connection with the said modification, the code now can handle any relationships between spatial sampling rates in the four directions of space, while the older versions assumed equal or denser sampling on the receiver side than on the source side ($dx_s > dx_g$) (Kaplan et al., 2005).

It is however important to point out that the theoretical requirement remains, that the input data must represent an actual wave-field. That condition is met if the recording area (or receiver spread)

covers the same surface area as the shooting area. In practice,the code only checks that the following conditions hold:

$$nx_s \cdot \Delta x_s \ = nx_g \cdot \Delta x_g \ , \quad ny_s \cdot \Delta y_s \ = ny_g \cdot \Delta y_g$$

within limits dependent on the minimum wavelength in the data. It thus remains the user's responsibility to make sure that the absolute locations match.

3 Numerical Examples: isolated diffractor

This example demonstrates the new capability of the 3D FS multiple code to handle all different spatial sampling rates for sources and receivers in the in-line and cross-line directions. Here, the sampling parameters are as follows:

$$\begin{aligned} \Delta x_s = 12.5m \ , \ \Delta x_g = 10.0m \ , \ nx_s = 40 \ , \ nx_g = 50, \\ \Delta y_s = 10.0m \ , \ \Delta y_g = 12.0m \ , \ ns_y = 30 \ , \ ny_g = 25. \end{aligned}$$

The data feature two seismic events (a ghost-free primary and its surface multiple) generated by an ideal point-diffractor in an acoustic half-space characterized by water speed. Figure (1) displays a two-dimensional section, parallel to the receiver in-line axis, extracted from the five-dimensional input data hyper-volume.

The source signature is a zero-phase Ricker wavelet with a peak amplitude at 30Hz and maximum frequency at 60Hz. Given the sampling rates in all four dimensions of space, the dataset satisfies anti-aliasing criterion:

$$\Delta x \leq \frac{c}{2f_{max}} \tag{7}$$

where Δx is a generic spatial sampling increment, c is the speed of seismic waves and f_{max} is the highest temporal frequency in the data.

Figure (2) shows a two-dimensional section of the output prediction corresponding to the input profile portrayed above. The result appears accurate despite some diagonal coherent artifacts which can be attributed to the abrupt truncation of seismic events and insufficient spatial tapering.

4 Numerical examples: WesternGeco synthetics

The numerical exercise described here is the natural continuation of work carried out at ConocoPhillips during 2009, which led to the first release of the 3D inverse scattering free-surface prediction code. A set of acoustic synthetic seismic data generated using the finite difference method

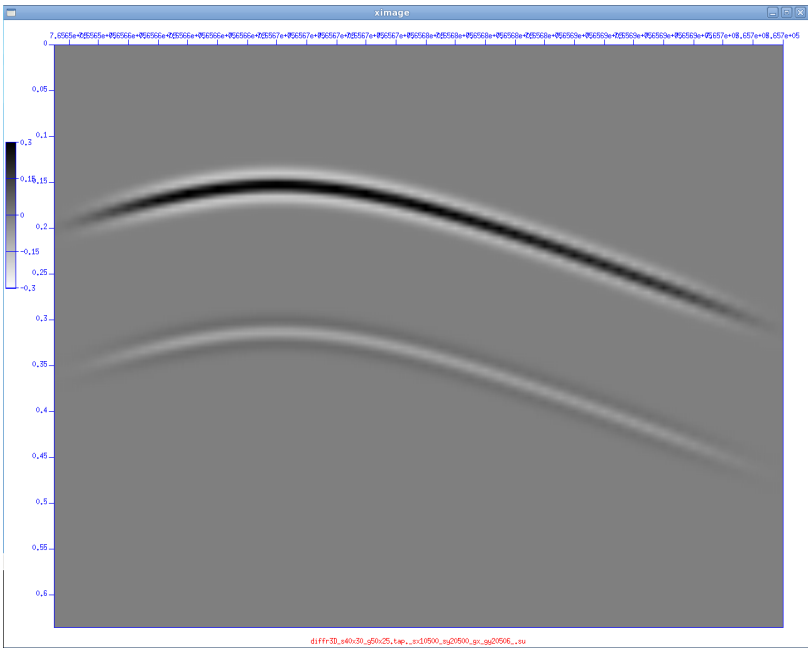

Figure 1: Isolated diffractor: in-line section of the input data.

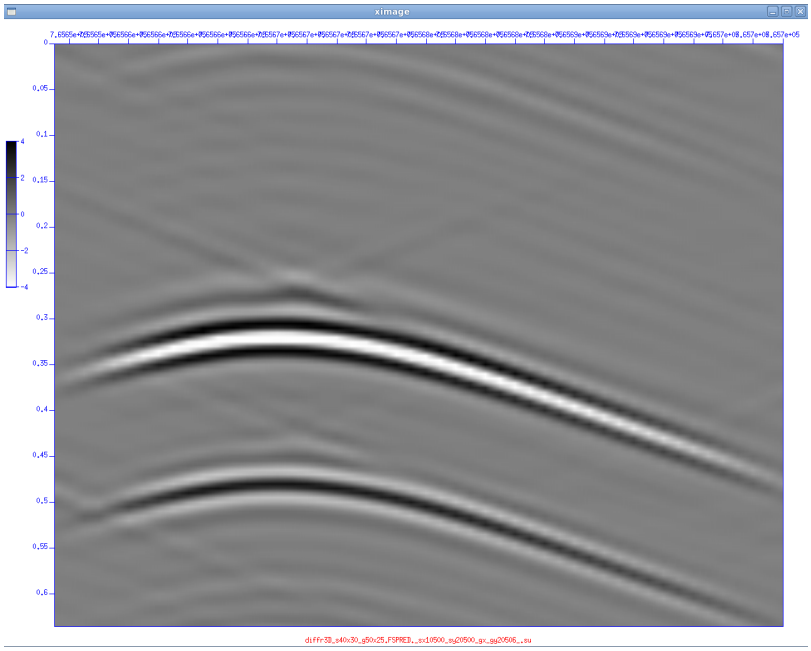

Figure 2: Isolated diffractor: multiples predicted by the 3D algorithm.

was made available by WesternGeco during 2009 for the purpose of testing and debugging the 3D inverse scattering free-surface multiple prediction code.

The data simulate a 3D marine acquisition over a set of realistic geological structures. The employed subsurface model is characterized by cylindrical symmetry, where steep dips and rapid velocity variations only occur along one horizontal direction of space (in-line), while no variations occur along the orthogonal cross-line direction.

The virtual acquisition covers an area of 7Km in the in-line direction (parallel to the sail line) and 0.5Km along the cross-lines. While previous tests favored cross-line aperture (Innanen et al., 2008) involving only a limited in-line extent, for this exercise we choose to begin from a narrow azimuth 3D geometry composed of 5 sail lines and the corresponding 5 lines of receivers used in their entire in-line length. The utilized data geometry thus covers an area of 7000m by 50m. Further, we make provisions for further testing at larger cross-line apertures of 125m, 250m and 500m.

Spectral analysis reveals how this data yield significant amplitudes up to a temporal frequency of $f_{max} = 60Hz$. For that value of f_{max}, the synthetic only satisfies the spatial anti-aliasing criterion (7) on the receiver side while some negative effect of source-side aliasing may be expected in our final results.

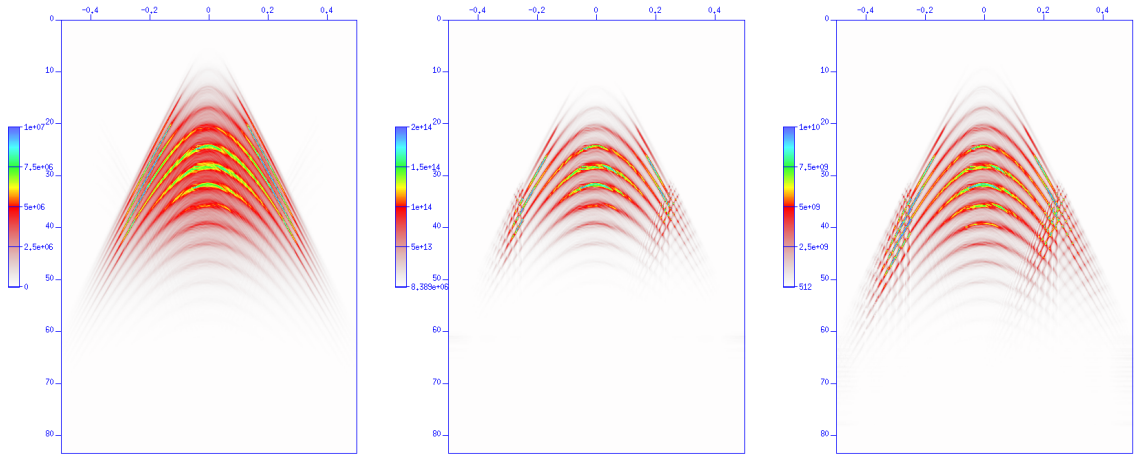

Figure 3: FK spectra of a sample shot: left frame: input; middle frame: multiples obtained without wavelet information; right frame: multiples obtained using wavelet information.

Figure (5) displays five shot gathers (receiver line at zero cross-line offset) selected at equal distance along the in-line direction. A simple visual inspection of the data reveals the increasing geologic complication in the data for increasing depth.

In our first attempt, we chose to predict free-surface multiples ignoring the wavelet requirement. The Algorithm (5) is then evaluated with $A(\omega) = 1$. Figure (6) shows the leading order ($n = 2$) predicted surface multiples at the same locations as in Figure (5). As expected, the results show that multiples are correctly predicted at any depth (recording time) regardless of the level of geologic

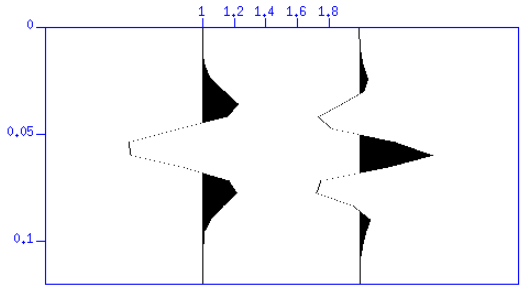

Figure 4: Wavelets used within the multiple prediction algorithm. Left: true source signature used for modeling of the data; right: effective wavelet, incorporating the averaged effect of source and receiver ghosts.

complication. The expected negative effect of spatial aliasing on the source side can be noticed in the surroundings of all predicted events in the form of a small-amplitude diagonal "checkerboard texture". In a more careful analysis, we notice how the differences in temporal resolution and a moderate time shift between the input data and the prediction would make the elimination of multiples ineffective in practice.

Such differences can be further characterized using the f-k amplitude spectra of the input data and of the result. In Figure (3), the frame on the left represents the f-k spectrum of an input shot gather while the middle frame represents the f-k spectrum of the multiples predicted at that same location. The frequency extent (along the vertical axis) of the spectrum in the left frame is clearly smaller than in that in the middle as a result of the missing compensation (deconvolution) for the input source signature.

In an ideal situation where the wavelet information is available, the Algorithm (5) offers the chance to compute predictions closer to the actual multiples recorded in the input data. However, the optimal choice of wavelet depends on whether or not the ghost reflections have been previously removed in the input data. For the case of previously deghosted data, the optimal choice is certainly the theoretical signature of the source which, for synthetics, corresponds to the waveform fed into the finite difference modeling tool. For the case of non-deghosted data, the best result in multiple prediction is obtained using the combined effect of the theoretical source and its ghost reflection (an example of both cases is described in Figure 4).

Since the data made available for our example do not include measurements for the wave-field's vertical derivative (which is fundamental for Green's Theorem deghosting described elsewhere in this report), our results are presented using the second approach. We therefore estimate the effective source signature by singling out the first arrival at an intermediate offset (wavelet on the right in Figure (4)).

Figure (7) displays the same leading order result as in Figure (6) when a suitable estimate of the input wavelet is used. Visual inspection reveals a better correspondence between the computed mul-

tiples and the multiples in the input data (Figure (5)). The improved correspondence is confirmed by the spectral plot in the right frame of Figure (3). In the middle and right frames, it is worth noticing how source-side spatial aliasing affects the prediction in the well-sampled receiver domain starting at 30Hz.

5 Conclusion and Future plan

The inverse scattering series provides a rigorous framework for the formulation of a free-surface multiple prediction and elimination algorithm. We provided an update on the status of the three-dimensional implementation which has been simplified and modified to release restrictions on the sampling of the input data.

The new code and its new features were tested on new and larger synthetic examples. The results confirm both the accuracy of the method and its dependence on the accuracy of all pre-processing requirements, including the removal of ghost reflections and the estimation of the source signature.

The updated version of the code will be made available to the sponsors shortly after the annual meeting.

6 Acknowledgements

We are grateful to all M-OSRP sponsors for long-term encouragement and support in this research. All members in M-OSRP are thanked for their help finishing this paper and valuable discussions in this research program.

References

Araujo, Fernanda V., Arthur B. Weglein, Paulo Marcus Carvalho, and R. H. Stolt. "Inverse scattering series for multiple attenuation: An example with surface and internal multiples." *SEG Technical Program Expanded Abstracts* 13 (1994): 1039–1041.

Carvalho, P. M. *Free-surface multiple reflection elimination method based on nonlinear inversion of seismic data.* PhD thesis, Universidade Federal da Bahia, 1992.

Green, George. An essay on the application of mathematical analysis to the theories of electricity and magnetism. Printed for the author by T. Wheelhouse, 1828.

Innanen, Kristopher A., Simon A. Shaw, and Arthur B. Weglein. "3D free-surface multiple elimination implementation project status." *Mission-Oriented Seismic Research Program (M-OSRP) Annual Report.* 2008.

Kaplan, S. T., K. A. Innanen, and A. B. Weglein. "Updates to M-OSRP internal and free surface multiple coding projects." *Mission-Oriented Seismic Research Program (M-OSRP) Annual Report*. 2005.

Ramirez, Adriana Citlali and Arthur B. Weglein. "Green's theorem as a comprehensive framework for data reconstruction, regularization, wavefield separation, seismic interferometry, and wavelet esti mation: A tutorial." *Geophysics* 74 (2009): W35–W62.

Weglein, A. B., F. V. Araújo, P. M. Carvalho, R. H. Stolt, K. H. Matson, R. T. Coates, D. Corrigan, D. J. Foster, S. A. Shaw, and H. Zhang. "Inverse Scattering Series and Seismic Exploration." *Inverse Problems* (2003): R27–R83.

Weglein, A. B., F. A. Gasparotto, P. M. Carvalho, and R. H. Stolt. "An Inverse-Scattering Series Method for Attenuating Multiples in Seismic Reflection Data." *Geophysics* 62 (November-December 1997): 1975–1989.

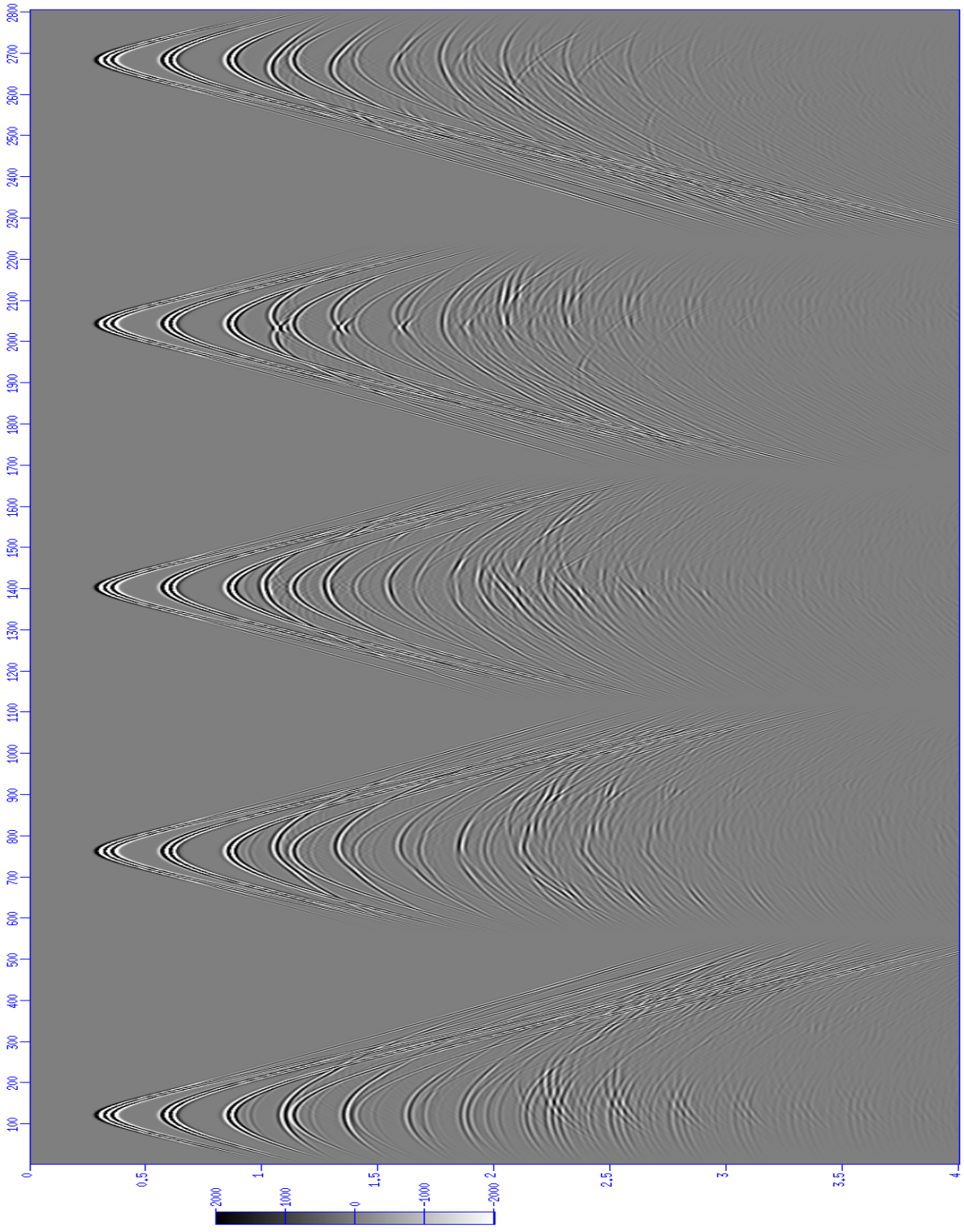

Figure 5: Input data: five shot gathers at zero crossline-offset taken along the central in-line from the WesternGeco data.

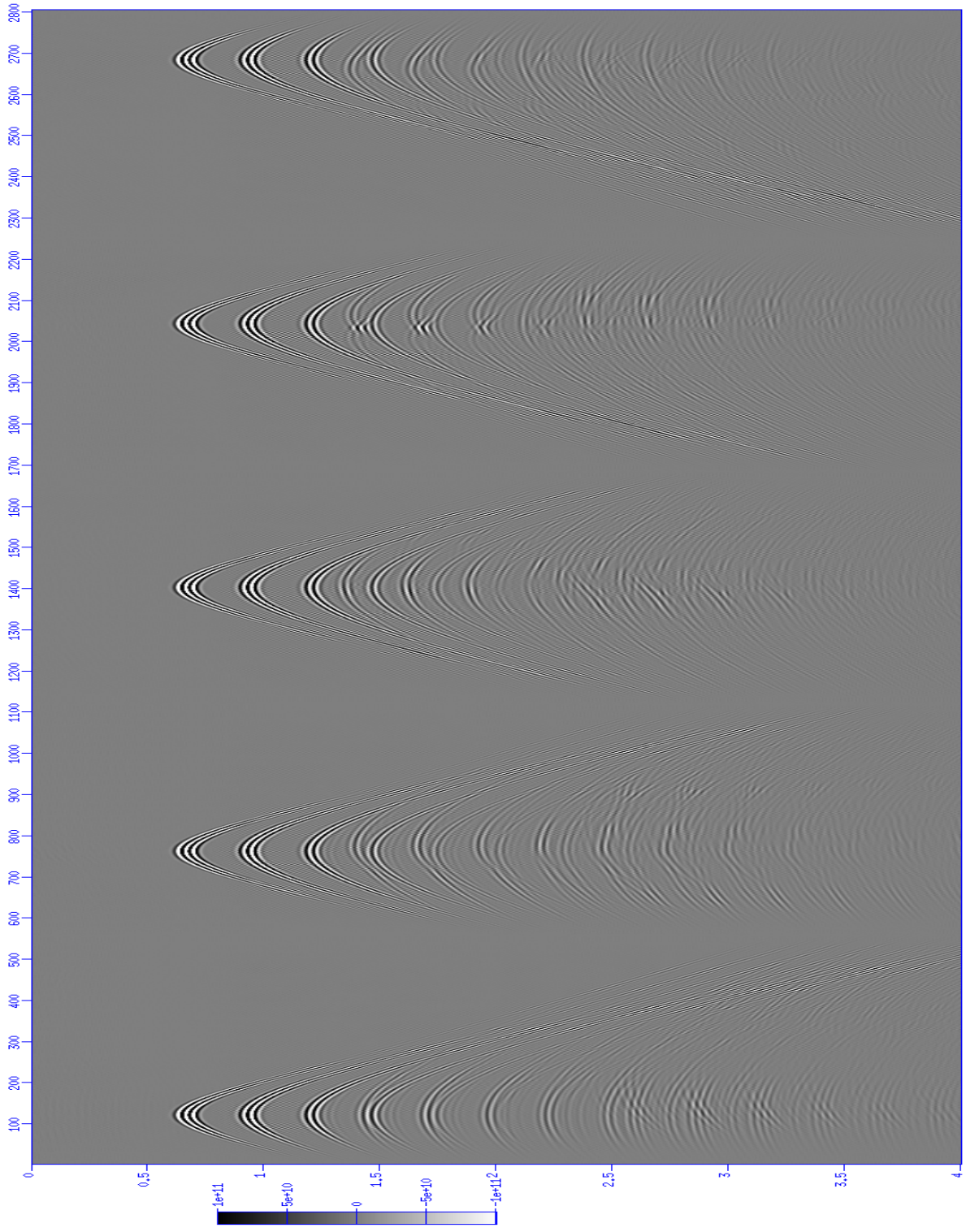

Figure 6: Input data: surface multiples predicted by the inverse scattering algorithm without using wavelet information. The data locations are the same as shown in Figure (5).

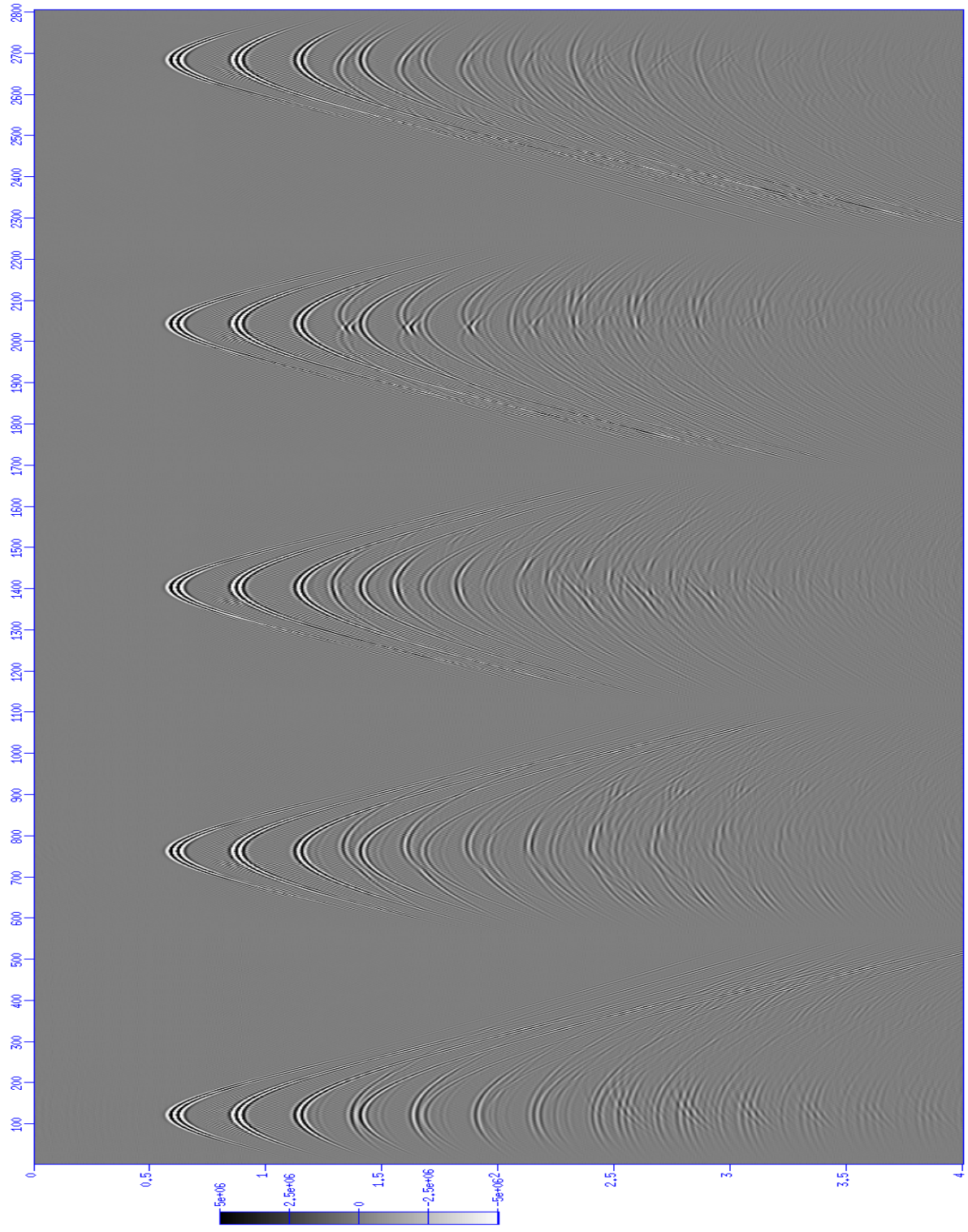

Figure 7: Input data: surface multiples predicted by the inverse scattering algorithm using wavelet information. The data locations are the same as shown in Figure (5).

Efficacy determination and efficiency advances for the inverse scattering series internal multiple removal: an update, land data testing and evaluation

Shih-Ying Hsu and Arthur B. Weglein

Abstract

In this report, we review the inverse scattering series (ISS) internal multiple attenuation algorithm and outline changes to the current implementation of the 1D algorithm. The effectiveness of the 1D algorithm and efficiency improvement of the multi-dimensional version of the algorithm are discussed as well. The first published results on land data demonstrate the efficacy of the 1D ISS internal multiple attenuation algorithm (Fu et al., 2010) . For increasing efficiency of the multi-dimensional version of the algorithm, the preliminary results show a 75% cost savings of the current 2D ISS internal multiple code using quasi-Monte Carlo integration (Hsu et al., 2010) and we anticipate greater cost savings for a $3D$ implementation of the ISS internal multiple algorithm.

1 Introduction

Multiple removal/attenuation has long been recognized as an important research subject in seismic exploration. Multiples are seismic events that propagate down from the source and are recorded as upgoing waves at a receiver with at least one downward reflection. Depending on the location of the downward reflections, multiples are divided into free-surface multiples and internal multiples. Free-surface multiples have at least one downward reflection at the free-surface. Internal multiples have all downward reflections below the measurement surface. When exploring offshore areas, the most dominant multiples are associated with the reflections at the free surface; thus, performing free surface de-multiple is often sufficient. However, when exploring complex marine areas, internal multiples become relevant. When exploring onshore areas, the internal multiples predominate and can have destructive interference with primaries or be misinterpreted as primaries if not attenuated/removed properly.

Free surface de-multiple technology has reached a mature status in seismic processing. There is a toolbox available with effective and practical algorithms (see, e.g., Verschuur et al., 1992; Carvalho, 1992). On the other hand, effective and efficient algorithms for internal multiple removal still need development work to be robust in practice. The ISS internal multiple attenuation algorithm was first proposed by Araújo et al. (1994) and Weglein et al. (1997). It is a data-driven algorithm, independent of subsurface information that predicts internal multiples for all horizons at once. This algorithm predicts the correct traveltimes and an approximated amplitude of the true internal multiples in the data. Ramírez and Weglein (2005) extended the theory from attenuation towards elimination by improving the amplitude prediction. Matson (1997) extended the theory for land

and ocean bottom applications (see also Matson and Weglein, 1996) and showed the first towed-streamer field data example using the $2D$ version of the algorithm (Matson et al., 1999). Other implementations were done by Coates and Weglein (1996), Otnes et al. (2004) and Kaplan et al. (2005).

In this note, we briefly review the ISS internal multiple attenuation algorithm in the second section and outline the status of the ISS internal multiple code in Section 3. In Section 4, we summarize the effectiveness of inverse scattering internal multiple attenuation (IMA) algorithm on land data (Fu et al., 2010). The implementation of quasi-Monte Carlo integration method to increase the computational efficiency of the IMA 2D code (Hsu et al., 2010) is addressed in Section 5, followed by conclusions.

2 Theory

We start with the forward scattering series derived from the Lippmann-Schwinger equation:

$$G = G_0 + G_0 V G, \tag{1}$$

which can be expanded in a forward series:

$$G = G_0 + G_0 V G_0 + G_0 V G_0 V G_0 + \cdots, \tag{2}$$

where G and G_0 are the actual and reference Green's functions. Define $D = G - G_0$ as the measurement of the scattered field and expand the perturbation V as a series:

$$V = V_1 + V_2 + V_3 + \cdots, \tag{3}$$

where V_n is the portion of V corresponding to the n-th order in the data.

Substituting $V_n = \sum_n V_n$ into equation (2) and set terms of equal order in the data equal gives the inverse scattering series in terms of data:

$$\begin{aligned}
D &= G_0 V_1 G_0, && (4)\\
0 &= G_0 V_2 G_0 + G_0 V_1 G_0 V_1 G_0, && (5)\\
0 &= G_0 V_3 G_0 + G_0 V_2 G_0 V_1 G_0 + G_0 V_1 G_0 V_2 G_0 + G_0 V_1 G_0 V_1 G_0 V_1 G_0, && (6)\\
&\vdots
\end{aligned}$$

Equation (6) can be written as:

$$\begin{aligned}
G_0 V_3 G_0 &= -G_0 V_1 G_0 V_2 G_0 - G_0 V_2 G_0 V_1 G_0 - G_0 V_1 G_0 V_1 G_0 V_1 G_0 \\
&= G_0 V_{31} G_0 + G_0 V_{32} G_0 + G_0 V_{33} G_0,
\end{aligned} \tag{7}$$

where

$$\begin{aligned}
V_{31} &= -V_1 G_0 V_2, \\
V_{32} &= -V_2 G_0 V_1, \\
V_{33} &= -V_1 G_0 V_1 G_0 V_1.
\end{aligned} \tag{8}$$

The first two terms in equation (7) are refraction-like events associated with primaries. They contribute to imaging and inversion and hence are not chosen for removing internal multiples. The third term in equation (7), $G_0V_{33}G_0$, is defined as a reflection-like inverse scattering if it changes propagation direction with respect to the measurement point after being altered by V_1. Note that for reflection-like scattering the geometric relationship between scatterers must be lower-higher-lower (Weglein et al., 1997).

The ISS internal multiple attenuation algorithm for a 2D earth begins with the input data, $D = G_0V_1G_0$, which is assumed to be deghosted and free-surface demultipled. For an homogeneous background, the 2D Green's function G_0 satisfies:

$$(\nabla^2 + \frac{\omega^2}{c_0^2})G_0(x, x', z, z'; \omega) = -\delta(x - x')\delta(z - z'). \tag{9}$$

The parameter ω is temporal frequency, c_0 is the constant background velocity, (x', z') denotes the source location and (x, z) is any point in 2D space. Fourier transforming equation (9) over $x - x'$ gives:

$$(\frac{\partial^2}{\partial z^2} - k_x^2 + \frac{\omega^2}{c_0^2})G_0(k_x, z, z'; \omega) = -\delta(z - z') \tag{10}$$

where k_x is the Fourier conjugate of $x - x'$. The casual solution to equation (10) is

$$G_0(k_x, z, z'; \omega) = \frac{e^{iq|z-z'|}}{-2iq}, \tag{11}$$

where the vertical wavenumber q is defined as:

$$q = sgn(\omega)\sqrt{\frac{\omega^2}{c_0^2} - k_x^2}. \tag{12}$$

In the frequency-wavenumber (f-k) domain, the input data $G_0V_1G_0$ is given by:

$$\begin{aligned} D(k_g, k_s, \omega) &= \int dx_1\ dx_2\ dz\ G_0(x_1, z_g, z; \omega)V_1(x_1, x_2, z)G_0(x_2, z, z_s; \omega) \\ &= \frac{e^{iq_g z_g}}{-2iq_g}V_1(k_g, k_s, q_g + q_s)\frac{e^{-iq_s z_s}}{-2iq_s}, \end{aligned} \tag{13}$$

where $x_1 = x_g - x$ and $x_2 = x - x_s$.

The parameters k_g and k_s are the horizontal wavenumbers for source and receiver coordinates. The vertical source and receiver wavenumbers, q_g and q_s, are given by $q_i = sgn(\omega)\sqrt{\frac{\omega^2}{c_0^2} - k_i^2}$ for $i = (g, s)$; c_0 is the constant background velocity; z_s and z_g are source and receiver depths.

Following similar steps, $V_{33} = -V_1G_0V_1G_0V_1$ becomes:

$$\begin{aligned} V_{33}(k_g, k_s, q_g + q_s) = &\frac{1}{(2\pi)^2}\int V_1(k_g, k_1, q_g + q_1)\frac{dk_1}{-2iq_1} \\ &\times \int V_1(k_1, k_2, -q_1 - q_2)\frac{dk_2}{-2iq_2}V_1(k_2, k_s, q_2 + q_s) \\ &+ \text{residues due to poles in } V_1. \end{aligned} \tag{14}$$

The effective data corresponding to a single frequency plane-wave incident field is defined as

$$b_1(k_g, k_s, q_g + q_s) = -2iq_s \; D(k_g, k_s, \omega). \tag{15}$$

Substituting (15) into equation (14), we have:

$$\begin{aligned} b_{33}(k_g, k_s, q_g + q_s) = &- \frac{1}{(2\pi)^2} \int dk_1 \; e^{-iq_1(z_g - z_s)} \; b_1(k_g, k_1, q_g + q_1) \\ &\times \int dk_2 \; e^{iq_2(z_g - z_s)} \; b_1(k_1, k_2, -q_1 - q_2) \; b_1(k_2, k_s, q_2 + q_s) + \text{residues}. \end{aligned} \tag{16}$$

Note that the effective data $b_1(k_g, k_s, q_g + q_s)$ can be written as:

$$\begin{aligned} b_1(k_g, k_s, q_g + q_s) &= \int_{-\infty}^{\infty} b_1(k_g, k_s, z) \; e^{i(q_g + q_s)z} dz \\ &= \int_{-\infty}^{z'} b_1(k_g, k_s, z) \; e^{i(q_g + q_s)z} dz + \int_{z'}^{\infty} b_1(k_g, k_s, z) \; e^{i(q_g + q_s)z} dz \end{aligned} \tag{17}$$

where the first part satisfies $z < z'$ and the second part satisfies $z > z'$.

By substituting (17) into equation (16), b_{33} can be split into four parts corresponding to the four diagrams in Figure 1. The portion associated with internal multiples is shown in Figure 1(d) which satisfies a lower-higher-lower relationship given by

$$\begin{aligned} b_3^{IM}(k_g, k_s, \omega) = \frac{1}{(2\pi)^2} &\int_{-\infty}^{\infty} \int_{-\infty}^{\infty} dk_1 \; e^{-iq_1(z_g - z_s)} dk_2 \; e^{iq_2(z_g - z_s)} \\ &\times \int_{-\infty}^{\infty} dz_1 \; b_1(k_g, k_1, z_1) \; e^{i(q_g + q_1)z_1} \\ &\times \int_{-\infty}^{z_1 - \epsilon} dz_2 \; b_1(k_1, k_2, z_2) \; e^{-i(q_1 + q_2)z_2} \\ &\times \int_{z_2 + \epsilon}^{\infty} dz_3 \; b_1(k_2, k_s, z_3) \; e^{i(q_2 + q_s)z_3} \quad \text{(Araújo, 1994; Weglein et al., 1997).} \end{aligned} \tag{18}$$

The pseudo depth z_i $(i = 1, 2, 3)$ is the depth location resulting from constant velocity migration. The quantity $b_1(k_g, k_s, z)$ corresponds to an un-collapsed migration (Weglein et al., 1997) of effective incident plane-wave data, $b_1(k_g, k_s, q_g + q_s)$. The small positive number ϵ ensures that z_1 and z_3 are always greater than z_2. For band-limited data, ϵ is related to the width of the wavelet. The output of equation (18), b_3^{IM}, is associated with the measured data through the relationship:

$$D^{IM}(k_g, k_s, \omega) = \frac{1}{-2iq_s} b_3^{IM}(k_g, k_s, q_g + q_s). \tag{19}$$

When we inverse Fourier transform $D^{IM}(k_g, k_s, \omega)$ back to the space-time domain and subtract the estimated internal multiples from the input data, all first order internal multiples are attenuated and higher order internal multiples are altered.

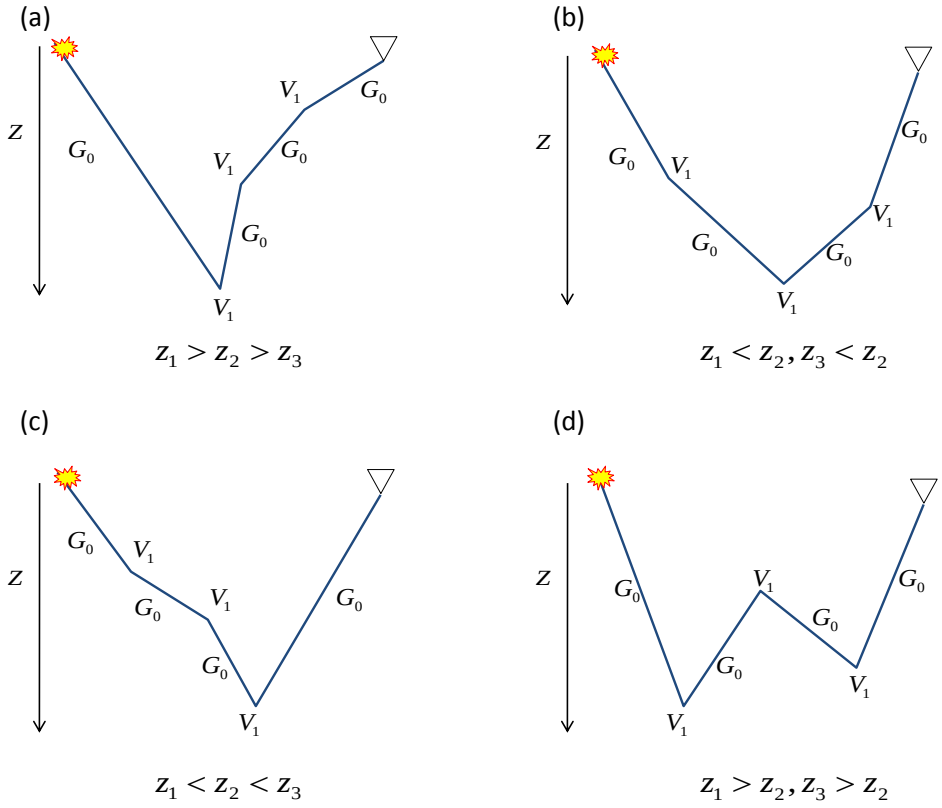

Figure 1: Diagrams corresponding to different portions of $G_0V_1G_0V_1G_0V_1G_0$. The three portions shown in (a), (b) and (c) which corresponds to primaries. The only portion contributes to the first-order internal multiples is shown in (d).

3 Updates on internal multiple attenuation code

The released IMA codes were written by Sam Kaplan (see Kaplan et al., 2004; 2005, for the detail). We fix the missing step that removes the obliquity factor $-2iq_s$ from $b_3^{IM}(k_g, k_s, q_g + q_s)$ to obtain the internal multiple attenuator in terms of measured data D^{IM} (see equation (19)).

Other changes including bug-fixes and improvements contributed by Ian Moore and Adriana C. Remírez (WesternGeco), Simon Shaw (ConocoPhillips), and Sam Kaplan (University of Alberta):

- Fixes to 'oneside' option in 1D code based on Fourier Transform property:
  if $f(x) = f(-x)$, then $F(k_x) = F^*(k_x)$.
- Fixes to scaling factors

In addition to the updates, after the collaboration and discussions with the research team in Saudi Aramco, we are revising the sampling of obliquity factor and are currently investigating and resolving

other issues including artifacts in the prediction. More data are being tested and the updates will be released after the annual meeting. The coding project for the $3D$ ISS internal multiple algorithm will be addressed in Terenghi and Weglein (2009).

4 Land data applications

In the theory section, we show that the ISS solves for the perturbation V using reference a Green's function G_0 and measured data D. One reasonable question to ask is what to choose for the reference medium. To simplify the problem, the ISS needs the reference medium to agree with the actual medium at and above the measurement surface so that the perturbation exists only below the measurement surface. Hence, the known near surface properties, including reference velocity, are required. This requirement may be difficult to obtain for onshore applications where near surface complexity often produces unavoidable errors in reference velocity measurement. However, the task of the ISS internal multiple subseries is not solving the earth properties and thus is less demanding on accurate reference properties. Hsu and Weglein (2008) have shown that the ISS internal multiple attenuation algorithm is independent of the reference velocity for an 1D earth with elastic background. The capability of predicting exact travel time of internal multiples without an accurate reference velocity is essential for land applications.

The tests on realistic synthetic and land field data from Saudi Arabia have been shown in Fu et al. (2010). The synthetic data used in this work were modeled based on a field sonic log which has a large number of layers with one-foot thickness. The result of this synthetic data shows that the strong internal multiples in the zone of interest are eliminated completely and the main primaries are preserved. This demonstrates the strength of the ISS internal multiple algorithm, i.e., it does not require any information about where the multiple generators reside or interpretive intervention and it predicts internal multiples for all horizons at once. With the confidence of the prediction obtained from the ISS method, the land field data test is performed. In this case, strong internal multiples are all generated within the complex, thin layers of the near surface. The overall suppression of the internal multiple has improved the definition of the primaries, which resulted in better interpretability of the data. Those results from Saudi Aramco are encouraging and no other internal multiple method was able to provide similar effectiveness.

It should be mentioned that those data tested in Fu et al. (2010) have significant interferences between primaries and internal multiples. Hence, the degradation of the primaries due to adaptive least-squares subtraction may occur in the results. In response to the degraded effectiveness due to the presence of close interference between primaries and internal multiples, there is a pressing need to improve the prediction and reduce the reliance on adaptive subtraction since the later may damage the primaries.

The high predictive potential requires the amplitude and phase of internal multiples to be predicted by the algorithm, which requires a known source signature as one of the prerequisites. Performing source signature deconvolution reduces interference between primaries and multiples in the data, which enables the ISS internal multiple attenuation to be extended toward elimination (Ramírez and Weglein, 2005). The reason is that the elimination algorithm uses events in the data to predict

arrival times and amplitudes of internal multiples. The presence of inference between primaries and multiples gives incorrect amplitudes of primaries; hence, using an interfered primary as a subevent in the elimination algorithm will affect the amplitude prediction and result in degraded efficacy.

5 Quasi-Monte Carlo integration method

As mentioned previously, the ISS internal multiple attenuation algorithm is a data-driven algorithm. It does not require any information about the internal multiple generators, moveout differences, or interpretive intervention. The algorithm predicts internal multiples for all horizons at once by trying all possible combinations of the three subevents that can generate an internal multiple. These are the advantages of the algorithm but there are issues as well. The major challenge of the algorithm is its efficiency. The computation cost of the multi-dimensional version of this algorithm is very high and increases with the maximum output frequency in the prediction. Hence, improving the efficiency of the algorithm is important.

The multi-dimensional version of the ISS internal multiple attenuation algorithm requires evaluation of multiple integrals over the entire dataset (five integrals in 2D and seven integrals in 3D). One possible solution in improving the efficiency in evaluating multiple integrals is to use a statistical integration approach based on random sampling. A well-known method is Monte Carlo integration. The idea is to pick a set of random points within the integration domain and then estimate the multi-dimensional integral by averaging the values of the integrand at these selected points. Using the Monte Carlo method, a d-dimensional integral is estimated by randomly selecting points in a d-dimensional hypercube and averaging the value of the integrand at these points:

$$\int_{a_1}^{b_1} \cdots \int_{a_d}^{b_d} f(x_1, x_2, \cdots, x_d) dx_1 \cdots dx_d \approx \frac{V}{N} \sum_{j=1}^{N} f(\theta_{1j}, \cdots, \theta_{dj}), \tag{20}$$

where x_i is the variable of integration for $i = 1, ..., d$, the coordinates of the randomly selected points in the d-dimensional space are denoted by $(\theta_{1j}, \cdots, \theta_{dj})$, and N is the total number of random samples. The hypercube volume is denoted by V. The error in Monte Carlo integration is independent of the dimension of the problem at hand which makes it suitable for higher-dimensional integration. However, the convergence rate of the error is $1/\sqrt{N}$, which is slow compared to classic integration methods where regularly sampled points are used.

The quasi-Monte Carlo method, an adaptive version of Monte Carlo method, uses low-discrepancy sampling instead of uncorrelated random sampling. Low-discrepancy points are generated by a deterministic formula that picks sample points in a self-avoiding way. Hence, low-discrepancy points fill the integration space more uniformly and quickly than random points. Using low-discrepancy points makes the quasi-Monte Carlo method more efficient than the Monte Carlo method. In optimal cases, the error associated with quasi-Monte Carlo decreases as fast as $1/N$. The preliminary results with numerical examples are shown in Hsu et al. (2010). With a 75% cost savings of the current 2D IMA code using quasi-Monte Carlo integration, we anticipate greater cost savings for a $3D$ implementation of the ISS internal multiple algorithm (see Hsu et al. (2010) for further details).

6 Conclusions

The 1D internal multiple algorithm has demonstrated its effectiveness on realistic synthetic and land field data. The significant interference between primaries and internal multiples makes subtraction without damaging the primaries very difficult to achieve. The field data tests indicated that the 1D algorithm is robust even with the presence of interference events. However, the degradation of the primaries due to adaptive subtraction is visible which requires improving the prediction. Performing source signature deconvolution enables more predictive results and hence reduces the need for adaptive subtraction. Tests on source signature deconvolved data are underway.

In response to the computational challenge on a multi-dimensional version of the new algorithm, a quasi-Monte Carlo integration method has been developed. The numerical tests have shown encouraging results for a 2D implementation and greater cost savings for a 3D implementation is anticipated. The progress on increasing efficiency shows the potential for the algorithm to be more realistic in the 3D marine field data. Further study on improving efficiency will be continued in collaboration with Einar Otnes and Adriana Remírez in WesternGeco.

7 Acknowledgments

The authors thank Saudi Aramco and WesternGeco for providing internship opportunities and permission to present this work. Shih-Ying Hsu wishes to thank Kevin Erickson, Qiang Fu, Shaodong Huo, Panos Kelamis and Yi Luo at Saudi Aramco and Debra Dishberger, Bill Dragoset, Einar Otnes, Adriana Remírez, Alan Teague and James Wu at WesternGeco for valuable discussion and technical support. The authors also wish to thank Jim Mayhan and Paolo Terenghi for their help with preparing and proofreading the manuscript.

References

Araújo, F. V. *Linear and non-linear methods derived from scattering theory: backscattered tomography and internal multiple attenuation.* PhD thesis, Universidade Federal da Bahia, 1994.

Araújo, F. V., A. B. Weglein, P. M. Carvalho, and R. H. Stolt. "Inverse scattering series for multiple attenuation: An example with surface and internal multiples." *64th Annual International Meeting, SEG, Expanded Abstracts* (1994): 1039–1042.

Carvalho, P. M. *Free-surface multiple reflection elimination method based on nonlinear inversion of seismic data.* PhD thesis, Universidade Federal da Bahia, 1992.

Coates, R. T. and A. B. Weglein. "Internal multiple attenuation using inverse scattering: Results from prestack 1 & 2D acoustic and elastic synthetics." *66th Annual International Meeting, SEG, Expanded Abstracts* (1996): 1522–1525.

Fu, Q., Y. Luo, P. G. Kelamis, S. Huo, G. Sindi, S.-Y. Hsu, and A. B. Weglein. "The inverse scattering series approach towards the elimination of land internal multiples." *submitted* (2010).

Hsu, S.-Y., E. Otnes, and A. C. Ramírez. "Quasi-Monte Carlo integration for the inverse scattering internal multiple attenuation algorithm." *submitted* (2010).

Hsu, S.-Y. and A. B. Weglein. "An analysis example examining the reference velocity sensitivity of the elastic internal multiple attenuation algorithm." *Mission-Oriented Seismic Research Program (M-OSRP) Annual Report.* 2008.

Kaplan, S. T., K. A. Innanen, E. Otnes, and A. B. Weglein. "Internal multiple attenuation code-development and implementation." *Mission-Oriented Seismic Research Program (M-OSRP) Annual Report.* 2004, 83–102.

Kaplan, S. T., B. Robinson, and K. A. Innanen. "Optimizing internal multiple attenuation algorithms for large distributed computing systems." *Mission-Oriented Seismic Research Program (M-OSRP), Annual Report.* 2005.

Matson, K. H. *An inverse-scattering series method for attenuating elastic multiples from multi-component land and ocean bottom seismic data.* PhD thesis, University of British Columbia, 1997.

Matson, K. H., D. C. Corrigan, A. B. Weglein, C. Y. Young, and P. M. Carvalho. "Inverse scattering internal multiple attenuation: results from complex synthetic and field data examples." *69th Annual International Meeting, SEG, Expanded Abstracts* (1999): 1060–1063.

Matson, K. H. and A. B. Weglein. "Removal of elastic interface multiples from land and ocean bottom data using inverse scattering." *66th Annual International Meeting, SEG, Expanded Abstracts.* (1996): 1526–1529.

Otnes, E., K. Hokstad, and R. Sollie. "Attenuation of internal multiples for multicomponent- and towed streamer data.." *74th Annual International Meeting, SEG, Expanded Abstracts* (2004): 1297–1300.

Ramírez, A. C. and A. B. Weglein. "An inverse scattering internal multiple elimination method: Beyond attenuation, a new algorithm and initial tests." *75th International Annual Meeting, SEG, Expanded Abstracts* (2005): 2115–2118.

Terenghi, P. and A. B. Weglein. "3D Internal multiple prediction coding project: preliminary notes." *Mission-Oriented Seismic Research Program (M-OSRP), Annual Report.* 2009.

Verschuur, D. J., A. J. Berkhout, and C. P. A. Wapenaar. "Estimation of multiple scattering by iterative inversion, Part I: considerations." *Geophysics* 62 (September-October 1992): 1975–1989.

Weglein, A. B., F. A. Gasparotto, P. M. Carvalho, and R. H. Stolt. "An Inverse-Scattering Series Method for Attenuating Multiples in Seismic Reflection Data." *Geophysics* 62 (November-December 1997): 1975–1989.

3D Internal Multiple Prediction coding project: preliminary notes

P. Terenghi and A.B. Weglein

Abstract

M-OSRP is starting a new coding project aimed at obtaining a 3D implementation of the inverse scattering series internal multiple prediction algorithm. The new implementation will build on the body of experiences and solutions built previously for the optimization and parallelization of the existing 2D code. In particular, we recognize the 2D code written for the Blue Gene supercomputer as the optimal starting point for developing the new code. In the first part of this note, we review the previously experimented algoritmic optimization devices and adapt them to the 3D case. In the second part, we estimate the size of the computational effort and the minimum amount of computer memory required by the 3D algorithm for a range of input data sizes. We find that careful management of computer memory is critical and that an adequate parallelization strategy ought to be designed around that issue.

1 Algorithmic optimizations

The inverse scattering internal multiple attenuation algorithm was first derived by Araújo (1994) and Weglein et al. (1997) as a subset of the inverse scattering series. A leading order expression for internal multiples can be obtained by manipulating the rightmost term in the third order inverse scattering formula:

$$G_0V_3G_0 \;=\; -G_0V_1G_0V_2G_0 - G_0V_2G_0V_1G_0 - G_0V_1G_0V_1G_0V_1G_0$$

and selecting the portion which complies with a "lower-upper-lower" relationship between scattering interactions.

The key expression for the leading order two-dimensional algorthm (Weglein et al., 1997) is:

$$\begin{aligned} b_3^{IM}(k_g,k_s,\omega) = \frac{1}{(2\pi)^2}\int_{-\infty}^{+\infty}\int_{-\infty}^{+\infty} dk_1\; e^{-iq_1(z_g-z_s)}\; dk_2\; e^{iq_2(z_g-z_s)} \\ \times \int_{-\infty}^{+\infty} dz_1\; b_1(k_g,k_1,z_1)e^{i(q_g+q_1)z_1} \\ \times \int_{-\infty}^{z_1-\epsilon} dz_2\; b_1(k_1,k_2,z_2)e^{-i(q_1+q_2)z_2} \\ \times \int_{z_2+\epsilon}^{\infty} dz_3\; b_1(k_2,k_s,z_3)e^{i(q_2+q_s)z_3}, \end{aligned} \tag{1}$$

where ω is temporal frequency; k_g and k_s are the horizontal wavenumbers for source and receiver coordinates, respectively; the vertical source and receiver wavenumbers, q_g and q_s, are given by the dispersion relation $q_i = sgn(\omega)\sqrt{\frac{\omega^2}{c_0^2} - k_i^2}$ for $i = (g, s)$; c_0 is the constant background velocity; z_s and z_g are source and receiver depths and z_i $(i = 1, ..., 3)$ represents pseudo-depth (depth location given by migration with background velocity).

The integrand b_1 represents effective plane-wave incident data (data scaled by an obliquity factor):

$$b_1(k_g, k_s, q_g + q_s) = -2iq_s D(k_g, k_s, \omega),, \tag{2}$$

where $D(k_g, k_s, \omega)$ is the Fourier-transformed prestack data. The effective data are introduced in Equation (1) after an uncollapsed Stolt migration (Weglein et al., 1997) maps $b_1(k_g, k_s, q_g + q_s)$ into the pseudo-depth domain $b_1(k_g, k_s, z_i)$ using the constant background velocity c_0.

Using a simple mathematical device, Kaplan et al. (2004) decoupled two of the inner integrals in Equation (1) and proposed a new expression for the 2D internal multiple attenuation algorithm ([1]):

$$\begin{aligned} b_3^{IM}(k_g, k_s, \omega) = \frac{1}{(2\pi)^2} \int_{-\infty}^{+\infty} \int_{-\infty}^{+\infty} & dk_1 \; e^{-iq_1(z_g - z_s)} \; dk_2 \; e^{iq_2(z_g - z_s)} \\ & \times \int_{-\infty}^{+\infty} dz_1 \; b_1(k_1, k_2, z_1) e^{-i(q_1+q_2)z_1} \\ & \times \int_{z_1+\epsilon}^{+\infty} dz_2 \; b_1(k_g, k_1, z_2) e^{i(q_g+q_1)z_2} \\ & \times \int_{z_1+\epsilon}^{+\infty} dz_2 \; b_1(k_2, k_s, z_2) e^{i(q_2+q_s)z_2} \end{aligned} \tag{3}$$

Expression (3) is mathematically identical to Expression (1) and yet computationally more efficient by an order of magnitude as the two integrals in dz_2 can be computed in a single loop.

Starting from Equation (3), an expression of the leading order inverse scattering internal multiple attenuator suitable for 3D data can be written as:

$$\begin{aligned} b_3^{IM}(k_{xg}, k_{yg}, k_{xs}, k_{ys}, \omega) = \frac{1}{(2\pi)^4} \int\int\int\int_{-\infty}^{+\infty} & dk_{x1} dk_{y1} \; e^{-iq_1(z_g - z_s)} \; dk_{x2} dk_{y2} \; e^{iq_2(z_g - z_s)} \\ & \times \int_{-\infty}^{+\infty} dz_1 \; b_1(k_{x1}, k_{y1}, k_{x2}, k_{y2}, z_1) e^{-i(q_1+q_2)z_1} \\ & \times \int_{z_1+\epsilon}^{+\infty} dz_2 \; b_1(k_{xg}, k_{yg}, k_{x1}, k_{y1}, z_2) e^{i(q_g+q_1)z_2} \end{aligned}$$

[1] Expression (3) is implemented in all versions of the internal multiple prediction code currently released by M-OSRP.

$$\times \int_{z_1+\epsilon}^{+\infty} dz_2 \; b_1(k_{x2}, k_{y2}, k_{xs}, k_{ys}, z_2) e^{i(q_2+q_s)z_2}, \tag{4}$$

where the newly introduced symbols $k_{x(i)}$ and $k_{y(i)}$, with $i = g, 1, 2, s$, represent the horizontal wave-numbers along the coordinate axes x (in-line) and y (cross-line). The vertical wave-number q is re-defined through the 3D dispersion relation

$$q_i = sgn(\omega)\sqrt{\frac{\omega^2}{c_0^2} - k_{x(i)}^2 - k_{y(i)}^2} \tag{5}$$

for i=(g,1,2,s) . We notice that in the 3D theory, both the input data D and the effective data b_1 are described by 5-dimensional quantities, replacing the 3-dimensional quantities of the 2D case:

$$b_1(k_{xg}, k_{yg}, k_{xs}, k_{ys}, q_g + q_s) = -2iq_s D(k_{xg}, k_{yg}, k_{xs}, k_{ys}, \omega). \tag{6}$$

Following the thread in Kaplan et al. (2004) we establish an intermediate function ρ:

$$\begin{aligned} \rho(k_{xg}, k_{yg}, k_{x1}, k_{y1}, k_{x2}, k_{y2}, k_{xs}, k_{ys}, \omega) \; &= \; \int_{-\infty}^{+\infty} dz_1 \; b_1(k_{x1}, k_{y1}, k_{x2}, k_{y2}, z_1) e^{-i(q_1+q_2)z_1} \\ &\times \int_{z_1+\epsilon}^{+\infty} dz_2 \; b_1(k_{xg}, k_{yg}, k_{x1}, k_{y1}, z_2) e^{i(q_g+q_1)z_2} \\ &\times \int_{z_1+\epsilon}^{+\infty} dz_2 \; b_1(k_{x2}, k_{y2}, k_{xs}, k_{ys}, z_2) e^{i(q_2+q_s)z_2} \end{aligned} \tag{7}$$

such that Expression (4) becomes:

$$\begin{aligned} b_3^{IM}(k_{xg}, k_{yg}, k_{xs}, k_{ys}, \omega) \; &= \; \frac{1}{(2\pi)^4} \int\int\int\int_{-\infty}^{+\infty} dk_{x1} dk_{y1} \; e^{-iq_1(z_g - z_s)} \; dk_{x2} dk_{y2} \; e^{iq_2(z_g - z_s)} \\ &\times \; \rho(k_{xg}, k_{yg}, k_{x1}, k_{y1}, k_{x2}, k_{y2}, k_{xs}, k_{ys}, \omega) \end{aligned} \tag{8}$$

Further, we define the functions G and H as:

$$\begin{aligned} G(k_{xg}, k_{yg}, k_{x1}, k_{y1}, z_1, \omega) \; &= \; \int_{z_1}^{+\infty} dz_2 \; b_1(k_{xg}, k_{yg}, k_{x1}, k_{y1}, z_2) \; e^{i(q_g+q_1)z_2} \\ H(k_{x2}, k_{y2}, k_{xs}, k_{ys}, z_1, \omega) \; &= \; \int_{z_1}^{+\infty} dz_2 \; b_1(k_{x2}, k_{y2}, k_{xs}, k_{ys}, z_2) \; e^{i(q_2+q_2)z_2} \end{aligned} \tag{9}$$

whose discrete values G_i and H_i can be conveniently computed by recursion (Kaplan et al., 2004), starting from the highest available pseudo-depth z_n (for simplicity, dependence on angular frequency and horizontal wavenumbers is omitted):

$$\begin{aligned} G_n &= b_1(k_{xg}, k_{yg}, k_{x1}, k_{x2}, z_n)\ e^{i(q_g+q_1)z_n} \\ H_n &= b_1(k_{x2}, k_{y2}, k_{xs}, k_{ys}, z_n)\ e^{i(q_2+q_2)z_n} \end{aligned} \tag{10}$$

and then up to the surface using expressions:

$$\begin{aligned} G_{i-1} &= G_i + \Delta z_2\ b_1(k_{xg}, k_{yg}, k_{x1}, k_{y1}, z_{i-1})\ e^{i(q_g+q_1)z_{i-1}} \\ H_{i-1} &= H_i + \Delta z_2\ b_1(k_{x2}, k_{y2}, k_{xs}, k_{ys}, z_{i-1})\ e^{i(q_2+q_s)z_{i-1}} \end{aligned} \tag{11}$$

where Δz indicates the discrete counterpart of dz. We now rewrite Equation (4) as:

$$\begin{aligned} &\rho(k_{xg}, k_{yg}, k_{x1}, k_{y1}, k_{x2}, k_{y2}, k_{xs}, k_{ys}, \omega) \ = \\ &\int_{-\infty}^{+\infty} dz_1\ b_1(k_{x1}, k_{y1}, k_{x2}, k_{y2}, z_1)\ e^{-i(q_1+q_2)z_1}\ G(k_{xg}, k_{yg}, k_{yg}, k_{x1}, k_{y1}, z_1, \omega)\ H(k_{x2}, k_{y2}, k_{xs}, k_{ys}, z_1, \omega) \end{aligned} \tag{12}$$

and notice how a single realization of ρ for a fixed set of horizontal wavenumbers k_{xg}, k_{yg}, k_{x1}, k_{y1}, k_{x2}, k_{y2}, k_{xs}, k_{ys} (three integrals in dz) can now be computed in a single loop over the depth axis.

A second important observation is that every realization of ρ requires the same amount of computation, regardless of the choice of k_{x1}, k_{y1}, k_{x2} and k_{y2} (Kaplan et al., 2005).

2 Parallelization

In this section we focus on parallelization as a means to expedite the outer integrations along the horizontal wave-number axes. Based on an estimate of the CPU and memory resources required for the computation of the 3D algorithm, we review here the suitability of certain parallelization solutions devised previously for the 2D case.

2.1 Load balance

It is useful to anticipate that the optimal parallelization strategy results from distributing the load equally across all computing nodes. At the end of the previous section we identified a single

realization of ρ as a convenient unit for work load, characterized by a constant computing cost per realization. That unit is the base for the parallelization strategy which constitutes the backbone of our horizontal optimizations.

Therefore, optimal load balancing depends on an accurate estimate of the number of realizations of ρ required to compute the algorithm.

The 3D Algorithm (4) shows that determining a single element in b_3^{IM} (for given values of k_{xg}, k_{yg}, k_{xs}, k_{ys} and ω) requires the integration of function ρ along four dimensions k_{x1}, k_{y1}, k_{x2} and k_{y2}. However, the dispersion relation relates the vertical wavenumbers to their horizontal counterparts and factually limits the range of integration along those four axes.

In particular, on the right-hand side of Equation (4) we have:

$$q_1 \;=\; sgn(\omega)\,\sqrt{\frac{\omega^2}{c_0^2}-k_{x1}^2-k_{y1}^2} \qquad q_2 \;=\; sgn(\omega)\,\sqrt{\frac{\omega^2}{c_0^2}-k_{x2}^2-k_{y2}^2}. \tag{13}$$

The effective integration range will be given by the domain of the non-evenescent wave-field, which is characterized by real-valued vertical wave-numbers q_1 and q_2:

$$\mathfrak{D}^{rhs} \;=\{(k_{x1}\;,\;k_{y1}\;,\;k_{x2}\;,\;k_{y2}\;,\;\omega)\;\mid\;(\sqrt{k_{x1}^2+k_{y1}^2}\;,\;\sqrt{k_{x2}^2+k_{y2}^2})\le\frac{\omega^2}{c_0^2}\}. \tag{14}$$

Clearly, the range of the integrals in k_{x1}, k_{y1}, k_{x2} and k_{y2} will increase with the value of ω. If n_k is the number of samples along each of the two-sided spatial wave-number axes k_{xi} and k_{yi} (with $i=1,2$), then, at a given angular fequency ω, the number of discrete wave-number samples in Domain (14) is proportional to the product of the areas of two circles $k_{xi}^2+k_{yi}^2=\frac{\omega^2}{c_0^2}$ with $i=1,2$:

$$N_\omega^{rhs} \;=\; \pi(\frac{n_k}{2})^2\cdot\pi(\frac{n_k}{2})^2 \;=\; \pi^2(\frac{n_k}{2})^4. \tag{15}$$

Similarly, on the left-hand side of Equation (4) we have:

$$q_g \;=\; sgn(\omega)\,\sqrt{\frac{\omega^2}{c_0^2}-k_{xg}^2-k_{yg}^2} \qquad q_s \;=\; sgn(\omega)\,\sqrt{\frac{\omega^2}{c_0^2}-k_{xs}^2-k_{ys}^2} \tag{16}$$

Since only the non-evanescent portion of the output b_3^{IM} is of interest, then only the combinations of k_{xg}, k_{yg}, k_{xs}, k_{ys} and ω which correspond to real values of q_g and q_s will be considered:

$$\mathfrak{D}^{lhs} \;=\{(k_{xg}\;,\;k_{yg}\;,\;k_{xs}\;,\;k_{ys}\;,\;\omega)\;\mid\;(\sqrt{k_{xg}^2+k_{yg}^2}\;,\;\sqrt{k_{xs}^2+k_{ys}^2})\le\frac{\omega^2}{c_0^2}\} \tag{17}$$

Again, at a given angular fequency ω, the number of discrete wave-number samples in domain (17) can be compared to the product of the areas of two circles $k_{xi}^2 + k_{yi}^2 = \frac{\omega^2}{c_0^2}$ with $i = s, g$:

$$N_\omega^{lhs} \;=\; \pi(\frac{n_k}{2})^2 \cdot \pi(\frac{n_k}{2})^2 = \;\pi^2(\frac{n_k}{2})^4. \tag{18}$$

Considering the non-evanescence conditions on both sides of Equation (4), the domain of calculations is

$$\begin{aligned} \mathfrak{D}^{3D} \;=\; \{\; (k_{xs}\;,\; k_{ys}\;,\; k_{xg}\;,\; k_{yg}\;,\; k_{x1}\;,\; k_{y1}\;,\; k_{x2}\;,\; k_{y2}\;,\; \omega) \;\;\mid \\ (\sqrt{k_{xs}^2 + k_{ys}^2}\;,\; \sqrt{k_{xg}^2 + k_{yg}^2}\;,\; \sqrt{k_{x1}^2 + k_{y1}^2}\;,\; \sqrt{k_{x2}^2 + k_{y2}^2} \leq \frac{\omega^2}{c_0^2}) \;\}. \end{aligned} \tag{19}$$

The total number of sample points in Domain (19) equals the number of realizations of ρ required to compute the algorithm for a full 3D dataset. Assuming the maximum values of angular frequency and horizontal wavenumbers ω_{Nyq} and k_{Nyq} are such that $\omega_{Nyq} \;\approx\; c_0\; k_{Nyq}$, the total number of realizations of ρ may be estimated as a combination of (18) and (15):

$$N^{3D} \;=\; \frac{1}{9}\pi^4 n_w (\frac{n_k}{2})^8 \qquad (n_\omega, n_k > 1) \tag{20}$$

with n_ω is the number of samples in the one-sided temporal frequency axis ω.

For comparison, in the 2D case the number of sample points in the computation domain (Kaplan et al., 2005):

$$\mathfrak{D}^{2D} \;=\; \{\; (k_{xs}\;,\; k_{xg}\;,\; k_{x1}\;,\; k_{x2}\;,\; \omega) \;\mid\; -\;\frac{\omega}{c_0} \leq (k_{xs}\;,\; k_{xg}\;,\; k_{x1}\;,\; k_{x2}\;) \leq \frac{\omega}{c_0}) \;\}. \tag{21}$$

may be estimated as proportional to the volume of a 5-dimensional hyper-pyramid constructed over the lengths of the frequency and wave-number axes. Such a volume, representative of the 2D algorithm, is:

$$N^{2D} \;=\; \frac{n_\omega \cdot n_k^4}{5} \qquad (n_\omega, n_k > 1). \tag{22}$$

A selection of example values for the extent of the computation domain for the 3D and 2D cases may be found in Tables (1) and (2). However, it should be noticed that values tabulated therein do not result from simply evaluating Expressions (20) and 22. On the contrary, they result from testing the non-evanescence conditions numerically for discrete values of ω and k (more detail can be found in the caption to Tables (1) and (2)). The values tabulated in Tables (1) and (2) therefore represent a more accurate estimate of the computation domain away from the condition $\omega_{Nyq} \;\approx\; c_0\; k_{Nyq}$, which was assumed for Expression (20).

Based on the total count, an equal number of realizations will be assigned to every compute process.

	$n_k = 10$	$n_k = 20$	$n_k = 50$	$n_k = 100$	$n_k = 200$	$n_k = 500$	$n_k = 1000$
$n_\omega = 100$	1.9e+11	3.6e+13	4.6e+16	1.1e+19	2.8e+21	4.1e+24	1.1e+27
$n_\omega = 200$	7.6e+11	1.4e+14	1.8e+17	4.4e+19	1.1e+22	1.6e+25	4.2e+27
$n_\omega = 500$	4.7e+12	9.0e+14	1.1e+18	2.7e+20	6.8e+22	1.0e+26	2.6e+28
$n_\omega = 1000$	1.9e+13	3.6e+15	4.6e+18	1.1e+21	2.7e+23	4.1e+26	1.0e+29
$n_\omega = 2000$	7.5e+13	1.4e+16	1.8e+19	4.4e+21	1.1e+24	1.6e+27	4.1e+29
$n_\omega = 5000$	4.7e+14	8.9e+16	1.1e+20	2.7e+22	6.8e+24	1.0e+28	2.6e+30

Table 1: Number of evaluations of ρ required to compute the 3D algorithm. The non-evanescent portion of the wavefield has been evaluated numerically using a background medium velocity $c_0 = 1500m/s$, a time sampling interval $dt = 0.004s$, and a space sampling interval $dx = 10m$.

	$n_k = 10$	$n_k = 20$	$n_k = 50$	$n_k = 100$	$n_k = 200$	$n_k = 500$	$n_k = 1000$
$n_\omega = 100$	4.7e+07	6.7e+08	2.4e+10	3.8e+11	5.9e+12	2.3e+14	3.7e+15
$n_\omega = 200$	1.9e+08	2.6e+09	9.6e+10	1.5e+12	2.4e+13	9.1e+14	1.5e+16
$n_\omega = 500$	1.2e+09	1.6e+10	6.0e+11	9.3e+12	1.5e+14	5.7e+15	9.1e+16
$n_\omega = 1000$	4.7e+09	6.6e+10	2.4e+12	3.7e+13	5.8e+14	2.3e+16	3.6e+17
$n_\omega = 2000$	1.9e+10	2.6e+11	9.5e+12	1.5e+14	2.3e+15	9.1e+16	1.4e+18
$n_\omega = 5000$	1.2e+11	1.6e+12	5.9e+13	9.2e+14	1.5e+16	5.7e+17	9.0e+18

Table 2: Number of evaluations of ρ required to compute the 2D algorithm. The non-evanescent portion of the wavefield has been evaluated numerically using a background medium velocity $c_0 = 1500m/s$, a time sampling interval $dt = 0.004s$, and a space sampling interval $dx = 10m$.

2.2 Memory requirements

We now estimate the the amount of computer memory required by the 3D internal multiple prediction algorithm. Expression (4) clearly shows that, for a fixed value of k_{xg}, k_{yg}, k_{xs} and k_{ys} and ω, the integrations along k_{x1}, k_{y1}, k_{x2}, k_{y2} and z, still span the entire 5-dimensional extent of b_1. Moreover, the rapid variation of indices corresponding to variables k_{x1}, k_{y1}, k_{x2}, k_{y2} and z in Algorithm (4) suggests the necessity that data be available for random access.

Assuming each spectral coefficient of b_1 is described by an 8-byte variable, an estimate of the amount of memory effectively required by the 3D algorithm, evaluated for a range of typical data sizes, is given in Table (3).

An inspection of Table (3) shows that current computing equipment would support the 3D case only in the smallest data configurations. To overcome that issue, the algorithm ought to be further decomposed into parts dependent on smaller portions of the input b_1, each manageable within the memory built into a single compute node. On the other hand, each of the spatial integrals in Expression (4) samples b_1 along mutually perpendicular directions and an efficient data logistics scheme seems to be hard to devise.

A rational and efficient data-handling strategy can only be achieved thanks to the observation of

	$n_k = 10$	$n_k = 20$	$n_k = 50$	$n_k = 100$	$n_k = 200$	$n_k = 500$	$n_k = 1000$
$n_z = 128$	10 Mb	163 Mb	6 Gb	102 Gb	1 Tb	64Tb	1 Pb
$n_z = 256$	20 Mb	327 Mb	12 Gb	204 Gb	3 Tb	128Tb	2 Pb
$n_z = 512$	40 Mb	655 Mb	25 Gb	409 Gb	6 Tb	256Tb	4 Pb
$n_z = 1024$	81 Mb	1 Gb	51 Gb	819 Gb	13 Tb	512Tb	8 Pb
$n_z = 2048$	163 Mb	2 Gb	102 Gb	1 Tb	26 Tb	1 Pb	16 Pb
$n_z = 4096$	327 Mb	5 Gb	204 Gb	3 Tb	52 Tb	2 Pb	32 Pb

Table 3: Determining memory requirements. Estimate of memory requirement for one realization of function ρ (Equation 7) for various data sizes.

	$n_k = 10$	$n_k = 20$	$n_k = 50$	$n_k = 100$	$n_k = 200$	$n_k = 500$	$n_k = 1000$
$n_z = 128$	102 kb	409 kb	2 Mb	10 Mb	40 Mb	256 Mb	1 Gb
$n_z = 256$	204 kb	819 kb	5 Mb	20 Mb	81 Mb	512 Mb	2 Gb
$n_z = 512$	409 kb	1 Mb	10 Mb	40 Mb	163 Mb	1 Gb	4 Gb
$n_z = 1024$	819 kb	3 Mb	20 Mb	81 Mb	327 Mb	2 Gb	8 Gb
$n_z = 2048$	1 Mb	6 Mb	40 Mb	163 Mb	655 Mb	4 Gb	16 Gb
$n_z = 4096$	3 Mb	13 Mb	81 Mb	327 Mb	1 Gb	8 Gb	32 Gb

Table 4: Determining memory requirements. Estimate of memory requirement for one realization of function ρ in the 2D case for various data sizes.

symmetries in the effective data b_1 Kaplan et al. (2005). It is in fact straightforward to demonstrate that the wave-number domain reciprocity relation:

$$f(k_g, k_s) = f^*(k_s, k_g) \tag{23}$$

holds for any real valued function $f(x_g, x_s)$, where k_g and k_s are the Fourier conjugates of x_g and x_s. The wave-number reciprocity property can then be applied to the effective data b_1 and used to rationalize the data requirements of the prediction algorithm.

Specifically, the wave-number reciprocity relationship allows Expression (7) to be rewritten as:

$$\begin{aligned} b_3^{IM}(k_{xg}, k_{yg}, k_{xs}, k_{ys}, \omega) = \frac{1}{(2\pi)^4} \int\int\int\int_{-\infty}^{+\infty} & dk_{x1} dk_{y1}\ e^{-iq_1(z_g - z_s)}\ dk_{x2} dk_{y2}\ e^{iq_2(z_g - z_s)} \\ & \times \int_{-\infty}^{+\infty} dz_1\ b_1(k_{x1}, k_{y1}, k_{x2}, k_{y2}, z_1) e^{-i(q_1+q_2)z_1} \\ & \times \int_{z_1+\epsilon}^{+\infty} dz_2\ b_1(k_{xg}, k_{yg}, k_{x1}, k_{y1}, z_2) e^{i(q_g+q_1)z_2} \\ & \times \int_{z_1+\epsilon}^{+\infty} dz_2\ b_1^*(k_{xs}, k_{ys}, k_{x2}, k_{y2}, z_2) e^{i(q_2+q_s)z_2} \end{aligned} \tag{24}$$

$$\rho(k_{xg},k_{yg},k_{x1},k_{y1},k_{x2},k_{y2},k_{xs},k_{ys},\omega) = \int_{-\infty}^{+\infty} dz_1\ b_1(k_{x1},k_{y1},k_{x2},k_{y2},z_1)e^{-i(q_1+q_2)z_1} \times \int_{z_1+\epsilon}^{+\infty} dz_2\ b_1(k_{xg},k_{yg},k_{x1},k_{y1},z_2)e^{i(q_g+q_1)z_2} \times \int_{z_1+\epsilon}^{+\infty} dz_2\ b_1^*(k_{xs},k_{ys},k_{x2},k_{y2},z_2)e^{i(q_2+q_s)z_2} \quad (25)$$

where the instance of $b_1(k_{x2},k_{y2},k_{xs},k_{ys},z_2)$ has been replaced by $b_1^*(k_{xs},k_{ys},k_{x2},k_{y2},z_2)$. That way, any requirement for source wave-number gather is converted to a requirement for a receiver wavenumber gather.

It is now important to notice how a relatively large number of calculations can be performed using a data base of just three receiver wave-number gathers $b_1(k_{xg},k_{yg},:,:)$, $b_1(k_{xs},k_{ys},:,:)$ and $b_1(k_{x1},k_{y1},:,:)$ in the computer's local memory. It is therefore convenient to design the process such that the integration along the innermost spatial variables k_{x2} and k_{y2} is executed under the assumption that the computer has enough memory to store those three gathers locally. At the end of that task, the computer will only need to load a different realization of the gather $b_1(k_{x1},k_{y1},:,:)$ to continue the integration along k_{x1} and k_{y1}.

3 Work plan: develop 3D functionality based on the existing Blugene implementation

During 2004, a version of the 2D internal multiple prediction algorithm was written to run on largely distributed cluster systems such as the IBM Blugene/L (Kaplan et al., 2005) (Perrone, 2007). The code was designed to use a large number of nodes (thousands) with small local memory resources.

The stringent restrictions on node resources led to the memory-saving solution outlined in Section 2.2 and to a very effective parallelization strategy based on task specialization. The code is composed of specialized procedures for nodes assigned to *compute*, *data distribution* and *data collection* tasks.

The compute nodes are responsible for a set of realizations of ρ required to evaluate the algorithm. These nodes also request and receive the subsets of the effective data relevant for those computations from the data nodes.

Conversely, the data nodes hold the effective data b_1 in memory and communicate parts of them to the compute nodes when needed. Since the size of the data may be larger than the node's memory, a group of two or more nodes may be necessary to administer data distribution. Thanks to the wave-number reciprocity property, any data gather requested by a compute node can be mapped to a gather that is entirely contained in one of the data node's memory.

The collection nodes are in charge of receiving the realizations of ρ from the compute nodes and of accruing them to construct the output prediction. Since the size of the output prediction b_3^{IM} is

similar to the size of the effective data b_1, a similar number of nodes should be used for collection as used for input.

Because of its characteristic of scalability and parsimonious memory management, the Blugene code constitutes a very convenient starting point for the development of the 3D case, where both data size and the computational effort are expected several orders of magnitude larger then for the 2D case. From the point of view of cost, the parallelization of the data distribution and collection processes allows the code to run on a virtually unlimited number of nodes, provided that an appropriate ratio is maintained between those dedicated to computing and those dedicated to the distribution and collection of the data. The parallel backbone of the existing Blugene code may also handle the large input 3D data by simply using by an adequate number of data distribution and collection nodes.

4 Conclusions

These notes mark the onset of a new coding project, aimed at prducing a 3D implementation of the inverse scattering internal multiple prediction algorithm. Our quantitative estimates indicate that the 3D approach implies a computational effort several orders of magnitude higher than in the 2D case. Such a sharp increase clearly depends on both larger input data size and higher theoretical complexity with respect to the 2D algorithm.

Those extreme characteristics further emphasize the need for a scalable and efficient parallel programming scheme, whose aims are not limited to expediting the computations. We recognize in fact that only a very refined parallel infrastructure may be capable of performing the calculations using the resources offered by the distributed computing system currently in use.

Most of that infrastructure is already functioning in the 2D version of the algorithm specifically written for the IBM Blue Gene cluster. Therefore we identify that implementation and several solutions therein as an excellent starting point for the new task.

5 Acknowledgements

The information contained in these notes were largely taken from Sam Kaplan's reports and code documentation. The authors wish to express gratitude for the extraordinary efforts dedicated to putting the inverse scattering theory to work in practice.

References

Araújo, Fernanda V. *Linear and non-linear methods derived from scattering theory: backscattered tomography and internal multiple attenuation.* PhD thesis, Universidade Federal da Bahia, 1994.

Kaplan, S. T., K. A. Innanen, and A. B. Weglein. "Updates to M-OSRP internal and free surface multiple coding projects." *Mission-Oriented Seismic Research Program (M-OSRP) Annual Report*. 2005.

Kaplan, Sam T., Kristopher A. Innanen, Einar Otnes, and Arthur Weglein. "Internal multiple attenuation code-development and implementation." *Mission-Oriented Seismic Research Program (M-OSRP) Annual Report*. 2004, 83–102.

Kaplan, Sam T., Billy Robinson, and Kristopher A. Innanen. "Optimizing internal multiple attenuation algorithms for large distributed computing systems." *Mission-Oriented Seismic Research Program (M-OSRP) Annual Report*. 2005.

Perrone, Michael. "A Processor Performance Comparison of the Internal Multiple Attenuation Algorithm." *Public presentation slides* (2007).

Weglein, A. B., F. A. Gasparotto, P. M. Carvalho, and R. H. Stolt. "An Inverse-Scattering Series Method for Attenuating Multiples in Seismic Reflection Data." *Geophysics* 62 (November-December 1997): 1975–1989.

Addressing the bandlimited nature of seismic source and rapid lateral variations of the Earth: source regularization and cascaded imaging operator

Fang Liu and Arthur B. Weglein

Abstract

In the inverse scattering series (ISS), the seismic data processing can be catagorized as five major tasks: (1) the elimination of free surface multiples, (2) the elimination of internal multiples, (3) imaging the primaries to their actual depth, (4) Q compensation and, (5) inverting for parameter changes across geological boundaries. This article focuses on the third task of the aforementioned procedure: imaging primaries to their correct spatial location without knowing and using the actual subsurface velocity. The major objective of this article is to accommodate the most imminent challenges for M-OSRP future field imaging test: the multiparameter and multidimensional nature of the Earth. The first segment studies the source signature regularization for multiparameter imaging and the second segment is the progress in one parameter imaging for multidimensional medium with rapid lateral variation. Compared with our previous work, the progresses include the following: (1) cross-communication between data from different angles are studied and a stable and velocity independent regularization procedure is proposed and demonstrated with numerical examples and, (2) the polynomial expansion of many seismic operators are identified and the relationship between the seismic imaging operator to calculate α_1 and α_2 is studied. A cascaded application of the seismic imaging operators is formulated to capture more imaging capability for models with rapid lateral variations.

1 Introduction

After its initial proposal in Weglein et al. (2000; 2002), seismic imaging subseries was further developed in Shaw et al. (2003); Weglein et al. (2003); Innanen (2004); Liu et al. (2004); Shaw (2005); Liu (2006). The velocity perturbation is defined as:

$$\alpha(x,z) = 1 - \frac{c_0^2}{c^2(x,z)}, \tag{1}$$

and calculated from the data on the measurement surface as:

$$\alpha(x,z) = \alpha_1(x,z) + \alpha_2(x,z) + \alpha_3(x,z) + \cdots, \tag{2}$$

where α_1 is the first term in the inverse series and is the part of the velocity perturbation that is linear in terms of measured data. In our case, it is the same as migration inversion with constant water speed, Clayton and Stolt (1981). The first imaging subseries being identified is the leading

order imaging subseries (LOIS) (Shaw et al., 2003; Shaw, 2005). It was extended higher order imaging suberies (HOIS) (Liu et al., 2004; Liu, 2006) to incorporate models with large contrast. Both LOIS and HOIS are constructed from the linear image α_1. The intuitive leap from LOIS to HOIS is based on the physical interpretation which serves as our guiding principle for many years: *in geological models without lateral variation, we should not incorporate information from deeper layers to determine the spatial location of a reflector.*

Compared with the current seismic imaging methods, the inverse scattering imaging subseries allow the seismic events to communicate among themselves nonlinearly to further image primaries to their correct spatial locations with a constant unchanged and often highly inaccurate reference velocity. Since one of the major challenges in seismic imaging is to obtain a working velocity field for geological targets with rapid lateral variations, our seismic imaging problem in M-OSRP focuses on the acoustic medium with lateral velocity variation but without density variation.

In Shaw (2005); Liu (2006), the nonlinear communication between seismic data is restricted within data from a single incidence angle. It is easy to imagine the issue for this restriction: *if the Earth has multiple types of changing properties, the data from a certain fixed incidence angle will not have enough freedom to incorporate any change beyond velocity.*[1] Naturally, the cross-communication between data from different angles are necessary.

Extending the one-parameter result of Shaw et al. (2003); Shaw (2005), the parameter inversion subseries in Zhang and Weglein (2003; 2004); Zhang et al. (2005); Zhang (2006); Jiang et al. (2008); Li and Weglein (2010) are formulated as communications between seismic data with different incidence angles. Following the strategy of divide and conquer, the problem is formulated in the simplest scenario where the parameter inversion problem exists and the task is focused on the complicated process of inverting for parameters from perfect data, i.e, the impulse response which has infinite bandwidth.

It is well known that the seismic data in the field is always bandlimited: it lacks low-frequency and high-frequency information. It is very important in ISS imaging research to accommodate bandlimited source in multiparameter imaging. This article will discuss the issue caused by a bandlimited source and formulate a regularization procedure to address this challenge. The procedure we proposed is stable and velocity independent, i.e., no subsurface information is needed, just like the multiple removal methods and seismic imaging algorithms from the M-OSRP.

Another important task in ISS imaging research is to handle geological models with rapid lateral variations. The Fourier transform techniques with interpolation documented in Liu and Weglein (2008) provide us with very accurate numerical values of many seismic imaging operators and pave the path towards quantitative understanding about their relationship. We study the seismic imaging operator in α_1 and α_2 calculation that has no 1D analogy. It is clear that there are lots of astonishingly simple relationships between the rapidly varying seismic imaging operators that have not been identified and these relationships will significantly contribute *both* to the effectiveness

[1] As an example, in 1D the seismic data from a single incidence angle is a function of time: $D(t)$, which has one degree of freedom that cannot be used to calculated two depth functions $c(z)$ (velocity) and $\rho(z)$ (density) simultaneously.

of the imaging algorithms to handle rapid lateral variation *and* the efficiency of the algorithms in terms of computational time.

Several interesting phenomena are worth reporting: (1) the family of seismic imaging operators $\eta_{m,n}$ (**where** $m > -2, n > -1$) are simpler and vanish completely in many areas and they are the composite function of Bessel functions of the first kind and the square root function, (2) the seismic imaging operator $\xi_{m,n}$ (**where** $n > -1$) can be very accurately approximated by $\eta_{n-1,m}$, and (3) the seismic imaging operator to calculate α_1 and α_2 are of the same family and the calculation of α_1 and α_2 are closely related.

Most of the inverse scattering tasks after the free surface multiple removal is cascaded, i.e., most of them are an infinite series containing terms that are by themselves an infinite series. For example, the internal multiple attenuation algorithm in Weglein et al. (1997) contains one term and the corresponding leading order elimitation subseries in Ramirez and Weglein (2005) contain an infinite number of terms. As another example, in order to accommodate a large velocity contrast, the simultaneous imaging and inversion series in Innanen (2004) and the higher order imaging subseries in Liu et al. (2004) have to include additional terms to extend the original leading order imaging subseries identified by Shaw et al. (2003). The cascaded nature of ISS is another guiding principle that has been emphasised in inverse scattering research for many years, which is demonstrated very helpful in the velocity independent imaging research.

Taking advantage of the cascaded nature of the inverse scattering series and the close relation between the seismic imaging in α_1 and α_2 calculation, we propose the cascaded application of the lateral varying part of the α_1 seismic imaging operator to represent the part of α_2 contribution that is linear in terms of the measured data. This cascaded operator is constructed from $\xi_{-2,2}$, a known structure previously identified. The cascaded operator consistently improves the image of geological models with rapid lateral variations: (1) more accurately image the reflectors at depth, both laterally and vertically, (2) produces images that is invisible in the linear image and turns unwanted diffractions in α_1 into geological boundaries and, (3) works constructively in all M-OSRP's imaging subseries. For example, the leading order imaging subseries (LOIS) and the higher order imaging subseries (HOIS).

2 Conventions, notations, and definitions

In this article we use c_0 to denote the constant unchanged reference velocity[2], ρ_0 is the reference density and denote $\mathbf{i} \triangleq \sqrt{-1}$. The function **sgn** is defined as:

$$\mathbf{sgn}(u) \triangleq \begin{cases} 1 & \mathbf{if}(u \geq 0), \\ -1 & \mathbf{if}(u < 0). \end{cases} \tag{3}$$

It is easy to verify the following identity:

[2]It is also called migration velocity since it is the constant velocity field inputted into our imaging algorithm.

$$\mathtt{sgn}(uv) = \mathtt{sgn}(u)\mathtt{sgn}(v). \tag{4}$$

We use H to denote the integral of Dirac δ-function or the Heaviside function:

$$H(u) \stackrel{\triangle}{=} \int_{-\infty}^{u} \delta(v)dv = \begin{cases} 0 & \textbf{if}(u < 0), \\ 1 & \textbf{if}(u \geq 0). \end{cases} \tag{5}$$

It is easy to verify the following identity:

$$H(uv) = H(u)H(v) \ + \ H(-u)H(-v). \tag{6}$$

The square root is used extensively in this article based on the symmetry of Green's function detailed in Liu and Weglein (2008), we define our special square root[3]:

$$\sqrt[?]{<u>^2 + v} \stackrel{\triangle}{=} \begin{cases} \mathtt{sgn}(u)\sqrt{u^2 + v} & \textbf{if}(u^2 + v \geq 0), \\ \mathbf{i}\sqrt{-u^2 - v} & \textbf{if}(u^2 + v < 0). \end{cases} \tag{7}$$

We insert an extra question mark to avoid confusion with the ordinary square root operator $\sqrt{\ }$. Note that in the definition above, we intensionally placed the argument u inside the bracket $<>$ to indicate our choice that when the argument inside the square root is positive, the sign of the answer is chosen to follow u. Consequently, the numbers inside the square root on the right-hand side of Equation (7) are always positive and we have chosen the square root to be positive. It is straightforward to verify the following properties of our specifically defined square root[4]:

$$\begin{aligned} \sqrt[?]{<-u>^2 + v} &= -\left(\sqrt[?]{<u>^2 + v}\right)^*, \\ \mathbf{i}\sqrt[?]{<-u>^2 + v} &= \left(\mathbf{i}\sqrt[?]{<u>^2 + v}\right)^*, \\ e^{\mathbf{i}\sqrt[?]{<-u>^2+v}} &= \left(e^{\mathbf{i}\sqrt[?]{<u>^2+v}}\right)^*. \end{aligned} \tag{8}$$

It is easy to prove by exhausting all possible cases that if both u and $w = \sqrt[?]{<u>^2 + v}$ are real, u can be inverted from w simply as:

$$u = \sqrt[?]{<w>^2 - v}. \tag{9}$$

[3]This square root is very useful in representing the vertical wavenumber calculated from the dispersion relation. For example, in the dispersion relation: $k^2 + q^2 = (\omega/c_0)^2$, according to our Fourier transform convention, q should be calculated as: $q = \sqrt[?]{<\omega/c_0>^2 - k^2}$.

[4]In Equation (8), the superscript * means complex conjugate.

The wide tilde sign $\widetilde{\ }$ is used above a function to denote its Fourier transform and the following Fourier transform conventions are used throughout this article.

We use t to denote time and ω to denote its Fourier conjugate (temporal frequency). The Fourier transform of a function $f(t)$ in the time domain into its spectrum in the frequency domain is defined as:

$$\widetilde{f}(\omega) = \int_{-\infty}^{\infty} f(t) e^{\mathbf{i}\omega t} dt. \tag{10}$$

The corresponding inverse Fourier transform is defined as:

$$f(t) = \frac{1}{2\pi} \int_{-\infty}^{\infty} \widetilde{f}(\omega) e^{-\mathbf{i}\omega t} d\omega. \tag{11}$$

We use z to denote depth (the vertical coordinate), its Fourier conjugate is denoted as vertical wavenumber k_z. The forward and inverse Fourier transform between z and k_z are respectively defined as:

$$\widetilde{f}(k_z) = \int_{-\infty}^{\infty} f(z) e^{\mathbf{i}k_z z} dz \quad , \quad f(z) = \frac{1}{2\pi} \int_{-\infty}^{\infty} \widetilde{f}(k_z) e^{-\mathbf{i}k_z z} dk_z. \tag{12}$$

On the other hand, the Fourier transform between x (the horizontal coordinate) and k_m (the horizontal wavenumber) is defined with a different sign convention:

$$\widetilde{f}(k_m) \triangleq \int_{-\infty}^{\infty} f(x) e^{-\mathbf{i}k_m x} dx \quad , \quad f(x) \triangleq \frac{1}{2\pi} \int_{-\infty}^{\infty} \widetilde{f}(k_m) e^{\mathbf{i}k_m x} dk_m. \tag{13}$$

3 Source regularization for acoustic multiparameter inversion

3.1 The incidence wave from a perfect impulsive source

In the frequency domain, a source located at $x_s = z_s = 0$ in a homogeneous acoustic medium with velocity c_0 and density ρ_0 will produce a steady wave that satisfies:

$$\left(\frac{\partial^2}{\partial x^2}+\frac{\partial^2}{\partial z^2}+\frac{\omega^2}{c_0^2}\right)G_0(x,z,\omega)=\rho_0\delta(x)\delta(z). \tag{14}$$

Following the physical interpretation immediately after Equation (74) in Appendix A, we apply a Radon transform with constant slope $p=\frac{\sin\theta}{c_0}<\frac{1}{c_0}$, or an equivalently forward Fourier transform $\int_{-\infty}^{\infty} dx e^{-\mathbf{i}kx}$ on the equation above where the wavenumber k is proportional to the frequency: $k=\omega p$, the original 2D Helmholtz equation is transformed into a 1D Helmholtz equation[5]:

$$\left(\frac{\partial^2}{\partial z^2}+\omega^2\left[c_0^{-2}-p^2\right]\right)G_0(p,z,\omega)=\rho_0\delta(z).$$

With the Fourier transform from time to frequency defined as: $\widetilde{f}(\omega)=\int_{-\infty}^{\infty} f(t)e^{\mathbf{i}\omega t}dt$, the causal solution of the 1D wave equation above is obviously (Weglein et al., 2003, Equation 64)[6]:

$$G_0(p,z,\omega)=\rho_0\frac{e^{\mathbf{i}q|z|}}{2\mathbf{i}q} \qquad \texttt{where} \qquad q=\sqrt[?]{<\omega/c_0>^2-k^2}=\omega\sqrt{c_0^{-2}-p^2}. \tag{15}$$

Equation (15) can be transformed from the ω-domain into the τ-domain as[7]:

$$\begin{aligned}
G_0(p,z,\tau)&=\frac{1}{2\pi}\int_{-\infty}^{\infty}\rho_0\frac{e^{\mathbf{i}q|z|}}{2\mathbf{i}q}e^{-\mathbf{i}\omega\tau}d\omega=\frac{\rho_0}{2\pi}\int_{-\infty}^{\infty}\frac{e^{\mathbf{i}\omega[\sqrt{c_0^{-2}-p^2}|z|-\tau]}}{2\mathbf{i}\omega\sqrt{c_0^{-2}-p^2}}\\
&=\frac{\rho_0}{2\pi\sqrt{c_0^{-2}-p^2}}\int_{-\infty}^{\infty}\frac{e^{-\mathbf{i}\omega[\tau-|z|\sqrt{c_0^{-2}-p^2}]}}{2\mathbf{i}\omega}d\omega\\
&=-\frac{\rho_0}{2\sqrt{c_0^{-2}-p^2}}H\left(\tau-|z|\sqrt{c_0^{-2}-p^2}\right),
\end{aligned} \tag{16}$$

where H is the Heaviside function defined in Equation (5). This solution is essentially Equation (7.3.16) of Morse and Feshbach (1953). Note that the Heaviside function conserves shape after applying an arbitrary stretch factor, for example, $H(x)=H(x/5)=H(9x)$.

[5] The same notation G_0 is used for the Green's function for both before and after the transform. This will not cause much confusion since the domain of G_0 can be identified by the arguments inside the parenthesis immediately after.

[6] It is essentially Equation (7.2.19) of Morse and Feshbach (1953).

[7] If p, the ratio between k and ω, is fixed, then the inverse Fourier transform from ω will obtain a result in the vertical time τ domain. The detail can be found in Appendix A, Equation (75), and the physical interpretation immediately after.

3.2 The incidence wave from a bandlimited source

The Green's function can be viewed as the wave caused by an ideal impulsive source, where in Equation (14) the source signature can be viewed as $\widetilde{w}(\omega) = 1$ (in the frequency domain) or $w(t) = \delta(t)$ (in the time domain). If the source is not ideally implusive and has a wavy or tapering signature (in the frequency domain) $\widetilde{w}(\omega) \neq 1$, the incidence wave P_0 satisfies the following Equation:

$$\left(\frac{\partial^2}{\partial x^2} + \frac{\partial^2}{\partial z^2} + \frac{\omega^2}{c_0^2}\right) P_0(x, z, \omega) = \rho_0 \delta(x)\delta(z)\widetilde{w}(\omega). \tag{17}$$

Obviously, Equation (17) can be obtained by simply multiplying Equation (14) with a factor $\widetilde{w}(\omega)$. Hence, in the frequency domain, it's solution P_0 is simply G_0 multiplying $\widetilde{w}(\omega)$:

$$P_0(x, z, \omega) = G_0(x, z, \omega)\widetilde{w}(\omega). \tag{18}$$

Since a multiplication in the ω-domain corresponds to a convolution in the conjugate τ-domain after Radon transform with slope $p = \frac{\sin\theta}{c_0}$, the incidence wave in the homogeneous medium is the convolution of the source signature $w(t)$ with the Green's operator in Equation (16):

$$P_0(p, z, \tau) = \int_{-\infty}^{\infty} G_0(p, z, u) w(\tau - u) du = A\left(\tau - |z|\sqrt{c_0^{-2} - p^2}\right), \tag{19}$$

where the function A is defined as:

$$A(t) = -\frac{\rho_0}{2\sqrt{c_0^{-2} - p^2}} \int_{-\infty}^{t} w(u) du = -\frac{c_0\rho_0}{2\cos\theta} \int_{-\infty}^{t} w(u) du. \tag{20}$$

We denote the portion of $A(t)$ that depends only on the wavelet as:

$$W(t) = \int_{-\infty}^{t} w(u) du. \tag{21}$$

Re-writing the amplitude term as $-\frac{\rho_0}{2\sqrt{c_0^{-2}-p^2}} = -\frac{c_0\rho_0}{2\cos\theta}$, the direct arrival is:

$$P_0(p, z, \tau) = A\left(\tau - |z|\sqrt{c_0^{-2} - p^2}\right) = A\left(\tau - \frac{|z|\cos\theta}{c_0}\right). \tag{22}$$

Following the principal of divide and conquer, let us consider the simplest geological model where the bandlimited source will cause communication issues between data from different incidence angles: an acoustic model with constant velocity where there is no seismic imaging problem; for example, a simple geological model with homogeneous velcoity $c(z) \equiv c_0$ and variable density as the following:

$$\rho(z) = \begin{cases} \rho_0 & \texttt{if}(z < d_0), \\ \rho_1 & \texttt{if}(d_0 \le z \le d_1), \\ \rho_2 & \texttt{if}(z > d_1). \end{cases}$$

In the medium specified by the equation above, the steady wave satisfies the following Helmholtz equation:

$$\left(\frac{\partial^2}{\partial x^2} + \frac{\partial^2}{\partial z^2} + \frac{\omega^2}{c^2(z)}\right) P_0(x, z, \omega) = \rho\delta(x)\delta(z)\widetilde{w}(\omega). \tag{23}$$

Applying the Radon transform with fixed p or Fourier transform over x with the conjugate variable fixed as $k = \omega p$, Equation (23) becomes:

$$\frac{\partial^2}{\partial z^2} + \omega^2 \left[c^{-2}(z) - p^2\right] P_0(p, z, \omega) = \rho\delta(z)\widetilde{w}(\omega). \tag{24}$$

Equation (24) can be transformed into τ by applying the inverse Fourier transform: $\frac{1}{2\pi}\int_{-\infty}^{\infty} d\omega e^{-\mathrm{i}\omega\tau}$ on both sides to have:

$$\frac{\partial^2}{\partial z^2} - \left[c^{-2}(z) - p^2\right] \frac{\partial^2 P_0(\tau, p, z)}{\partial \tau^2} = \rho\delta(z)w(\tau). \tag{25}$$

Equation (25), is a 1D wave equation with propagation velocity $\left[c^{-2}(z) - p^2\right]^{-1/2}$. It is obvious that in the τ-p domain, the original 2D wave equation becomes a 1D wave equation with propagation velocity $\left[c^{-2}(z) - p^2\right]^{-1/2}$ and density ρ is kept the same. A well-known result concerning the reflection coefficient of a 1D wave equation states:

In 1D, a two-layered acoustic medium with velocity and densities being (c_0, ρ_0) for the first layer, (c_1, ρ_1) for the second layer, and the reflector depth is at $z = h$, the reflection coefficient and two way travel time (for coincident source and receiver at depth $z = 0$) are $R = \frac{c_1\rho_1 - c_0\rho_0}{c_1\rho_1 + c_0\rho_0}$, and $t = 2h/c_0$.

Consequently, in multi-D medium without lateral variation, if:

1. the medium property of the first layer is (c_0, ρ_0),
2. the second layer is (c_1, ρ_1), and
3. the reflector depth is at $z = h$,

after Radon transform with constant slope p, the problem can be regarded as a 1D problem with the apparent velocity of the first layer being $1/\sqrt{c_0^{-2} - p^2}$ and the apparent velocity of the second layer being $1/\sqrt{c_1^{-2} - p^2}$. As a result, for this problem the reflection coefficient and vertical travel time (for coincident source and receiver at depth $z = 0$) can be calculated as:

$$R = \frac{I_1 - I_0}{I_1 + I_0} \qquad , \qquad \tau = 2h\sqrt{c_0^{-2} - p^2} \tag{26}$$

where $I_0 = \rho_0/\sqrt{c_0^{-2} - p^2}$, $I_1 = \rho_1/\sqrt{c_1^{-2} - p^2}$. It is straightforward to verify the following facts:

1. If velocity does not change across the boundary, i.e., $c_0 = c_1$, we have that in Equation (26) all terms that varies with angle are equal: $(c_0^{-1} - p^2)^{-1/2}$=$(c_1^{-1} - p^2)^{-1/2}$. In Equation (26), they perfectly cancel each other in the division to calculate R. In this case, the reflection coefficient R does not vary with angle. Our logic can easily derive one of the most important benchmarks in M-OSRP parameter inversion.
2. Equation (26) also agrees perfectly with Equation (3.13) from Zhang (2006). The proof is as follows: since $p = \sin(\theta)/c_0$, $c_0^{-2} - p^2 = c_0^{-2}\cos^2(\theta)$, and $c_1^{-2} - p^2 = c_1^{-2}\left[1 - (c_1^2/c_0^2)\sin^2(\theta)\right]$ We have:

$$\begin{aligned} R = \frac{I_1 - I_0}{I_1 + I_0} &= \frac{\rho_1 c_1/\sqrt{1 - (c_1^2/c_0^2)\sin^2(\theta)} \;\; - \;\; \rho_0 c_0/\cos(\theta)}{\rho_1 c_1/\sqrt{1 - (c_1^2/c_0^2)\sin^2(\theta)} \;\; + \;\; \rho_0 c_0/\cos(\theta)} \\ &= \frac{(\rho_1/\rho_0)(c_1/c_0)\sqrt{1 - \sin^2\theta} - \sqrt{1 - (c_1^2/c_0^2)\sin^2(\theta)}}{(\rho_1/\rho_0)(c_1/c_0)\sqrt{1 - \sin^2\theta} + \sqrt{1 - (c_1^2/c_0^2)\sin^2(\theta)}}, \end{aligned} \tag{27}$$

   which is exactly the same as Equation (3.13) from Zhang (2006).

Consequently, in the $\tau - p$ domain, using the incidence wave from Equation (22), the reflected data (ignoring internal multiples) from the model above is:

$$\hat{D}(\tau, p) = R_1 A(\tau - t_1) + R_2' A(\tau - t_2),$$

where:

$$\begin{array}{lll} t_1 = 2d_0\sqrt{c_0^{-2}-p^2} & , & t_2 = 2d_1\sqrt{c_0^{-2}-p^2}, \\ R_1 = \frac{\rho_1-\rho_0}{\rho_1+\rho_0} & , & R_2' = \frac{\rho_2-\rho_1}{\rho_2+\rho_1}(1-R_1^2). \end{array}$$

If we define: $b = 2\sqrt{c_0^{-2}-p^2} = \frac{2\cos(\theta)}{c_0}$ (the conversion scale factor from the vertical time τ to the pseudo-depth z), the transformed data in the pseudo-depth domain for the multiparameter inversion framework in our group is[8]:

$$\begin{aligned} D(z,p) = -\frac{b}{\rho_0}\hat{D}(zb,p) &= R_1 W(zb-t_1) + R_2' W(zb-t_2) \\ &= R_1 W\left(b\left[z-d_0\right]\right) + R_2' W\left(b\left[z-d_1\right]\right). \end{aligned} \tag{28}$$

Just as dicussed in Equation (78) and the paragraph immediately after, the data in τ-p domain is stretched and squeezed by the same factor $b = \frac{2\cos(\theta)}{c_0}$. Note that:

- Compared with the discussion after Equation (78), an extra factor ρ_0 is introduced to incorporate density. Another factor $\cos(\theta)$ is necessary because in the τ-p domain, the data satisfy a 1D wave equation with velocity $\frac{c_0}{\cos(\theta)}$.
- The strectch factor b is angle dependent; in other words, data from different angle will be stretched by different factors and this is the reason why data from different angle have a communication issue.
- As detailed in Equation (31), the strectch factor b does not depend on the actual velocity c, or the location of the reflector.
- From the equation above, it is clear that both reflectors are correctly imaged to their actual depth at d_0 and d_1. In other words, since the reference velocity c_0 equals to the actual velocity, there is no imaging issues and we do not need to move the reflectors any further.

If we want to remove the density contribution to the reflection coefficient as detailed in X. Li and Weglein (2008); Li and Weglein (2010); Jiang et al. (2008); Wang et al. (2009); Liang et al. (2009), we need to calculate the difference between data from two different incidence angles p.

[8] An extra factor of $-\frac{b}{\rho_0} = -\frac{2\cos\theta}{c_0\rho_0}$ is multiplied to tailor it to the convention of data used by Zhang (2006); Jiang et al. (2008); X. Li and Weglein (2008); Li and Weglein (2010); Wang et al. (2009); Liang et al. (2009). Noting that $\frac{c_0}{2\cos\theta}$ is the conversion factor from the vertical time τ to the pseudo-depth z, its reciprocal, $\frac{2\cos\theta}{c_0}$ is naturally multiplied to the amplitude so the total area is conserved in the conversion from τ to pseudo-depth. The detail can be found in Appexdix B.

Let us first consider the ideal case with full bandwidth data where each event is of the form $W(t) = H(t)$. In this case, each event conserves shape after applying different stretch factors: $W(b[z-d_0]) = H(b[z-d_0]) = H(z-d_0)$ and $W(b[z-d_1]) = H(b[z-d_1]) = H(z-d_1)$, both are independent of angle and consequently the data is independent of the angle p:

$$D(z,p) = R_1 W(b[z-d_0]) + R_2' W(b[z-d_1]) = R_1 H(z-d_0) + R_2' H(z-d_1).$$

As a result, the difference between two sets of data (from two different angles) will vanish, so does the density contribution to the reflection coefficient. In conclusion, for ideal full bandwidth data there is no communication issue.

In the real world, we have bandlimited data where $W(t) \neq H(t)$. In this case, an event will not conserve shape after applying different stretch factors and $D(z,p)$ will depend on the angle p and the difference between the data from two different angles will not vanish. How can we solve this problem?

For simplicity, let us consider the data from two different angles, $p_1 < p_2$:

$$D(z,p_1) = R_1 W(b_1[z-d_0]) + R_2' W(b_1[z-d_1]), \tag{29}$$

and:

$$D(z,p_2) = R_1 W(b_2[z-d_0]) + R_2' W(b_2[z-d_1]), \tag{30}$$

where $b_1 = 2\sqrt{c_0^{-2} - p_1^2}$, $b_2 = 2\sqrt{c_0^{-2} - p_2^2}$.

It is obvious that $b_1 > b_2$. As a result, each packet $W(b_1[z-\cdots])$ has a broader frequency content than $W(b_2[z-\cdots])$, the convolution procedure to change each $W(b_1[z-\cdots])$ to $W(b_2[z-\cdots])$ (at the same pseudo depth) is stable and does not depend on the actual location of the wave packet. After the regularization, the data in Equations (29) and (30) should be equal and we have a clean subtraction.

This simplest multiparameter inversion problem suggests a source signature regularization procedure described in this section to benefit the algorithms to get rid of the density contribution to reflection coefficients.

For a joint inversion problem with two different angles: $\theta_1 < \theta_2$, $b_1 = \frac{\cos\theta_1}{c_0} > b_2 = \frac{\cos\theta_2}{c_0}$. We want a source regularization operation that will change the data in Equation (29) to the data in Equation (30). Our idea is to change the packet $W(b_1[z-d])$ located at the pseudodepth d to $W(b_2[z-d])$ at the same pseudodepth. If we define: $\lambda = \frac{b_1}{b_2}$, this can be done in the τ-domain by converting every packet $W(\tau - d)$ in Equation (29) to $W(\lambda[\tau - d])$. Let us look at the ratio between these two wave packets:

$$\gamma(\omega,\theta_1,\theta_2)=\frac{\int_{-\infty}^{\infty}W(\lambda[z-d])e^{\mathbf{i}\omega t}dt}{\int_{-\infty}^{\infty}W(t-d)e^{\mathbf{i}\omega t}dt}=\frac{\frac{1}{\lambda}\widetilde{W}(\omega/\lambda)e^{\mathbf{i}\omega d}}{\widetilde{W}(\omega)e^{\mathbf{i}\omega d}}$$
$$=\frac{\frac{1}{\lambda}\widetilde{W}(\omega/\lambda)}{\widetilde{W}(\omega)},\qquad \texttt{where}:\quad \lambda=\frac{b_1}{b_2}=\frac{\cos\theta_1}{\cos\theta_2}<1. \tag{31}$$

Note that in Equation (31), the contribution from the depth d cancel with each other in the division and consequently the factor $\gamma(\omega,\theta_1,\theta_2)$ does not depend on the location d of the reflector. Since $W(t)$ is the integral of $w(t)$, $\widetilde{W}(\omega)=\widetilde{w}(\omega)/(\mathbf{i}\omega)$, and factor $\gamma(\omega,\theta_1,\theta_2)$ can be further simplified as:

$$\gamma(\omega,\theta_1,\theta_2)=\frac{\widetilde{w}\left(\frac{\omega}{\lambda}\right)}{\widetilde{w}(\omega)} \tag{32}$$

Note that the factor $\gamma(k_z,\theta_1,\theta_2)$ does not depend on the subsurface geology.

3.3 Regularization of Gaussian type wavelet

$$a=100$$
$$w(t)=\frac{\partial}{\partial t}\frac{ae^{-a^2t^2/4}}{2\sqrt{\pi}}=-\frac{a^3t}{4\sqrt{\pi}}e^{-a^2t^2/4}\qquad \widetilde{w}(\omega)=-\mathbf{i}\omega e^{-\omega^2/a^2} \tag{33}$$
$$A(t)=-\frac{c_0\rho_0}{2\cos(\theta)}\int_{-\infty}^{t}w(u)du=\frac{c_0\rho_0a^3}{8\cos(\theta)\sqrt{\pi}}\int_{-\infty}^{t}ue^{-a^2u^2/4}du=-\frac{c_0\rho_0a}{4\cos(\theta)\sqrt{\pi}}e^{-a^2t^2/4}$$

In this case, the wavelet can be recovered to Gaussian through a simple integration. In Equation (32), we can calculate the factor γ using the frequency-domain expression of a Gaussian function:

$$\widetilde{w}(\omega)=e^{-\omega^2/a^2}\quad,\quad \gamma(\omega,\theta_1,\theta_2)=\exp\left(-\frac{\omega^2}{a^2}\left[\frac{\cos^2\theta_1}{\cos^2\theta_2}-1\right]\right)\le 1 \tag{34}$$

In Equation (34), $\gamma\le 1$ and the source regularization procedure (multiplying γ in the frequency domain) is very stable.

As an example, let us consider the geological model listed in Table (3.3). The source wavelet is the first derivative of Gaussian shown in Figure (1). The input data is τp domain is shown in Figure (2). The effects of regularization are demonstrated in Figures (3)$\sim$(5).

Depth Range (m)	Velocity (m/s)	Density (g/cm^3)
$-\infty < z < 500$	1500.0	1.0
$500 < z < 1000$	1500.0	1.1
$1000 < z < \infty$	1500.0	1.2

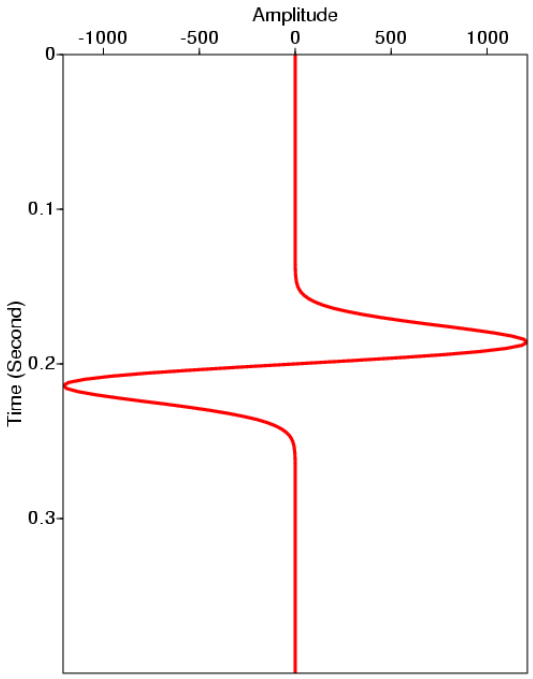

Figure 1: The source signature (in time domain) is the first derivative of Gaussian that lacks zero and high frequency unformation.

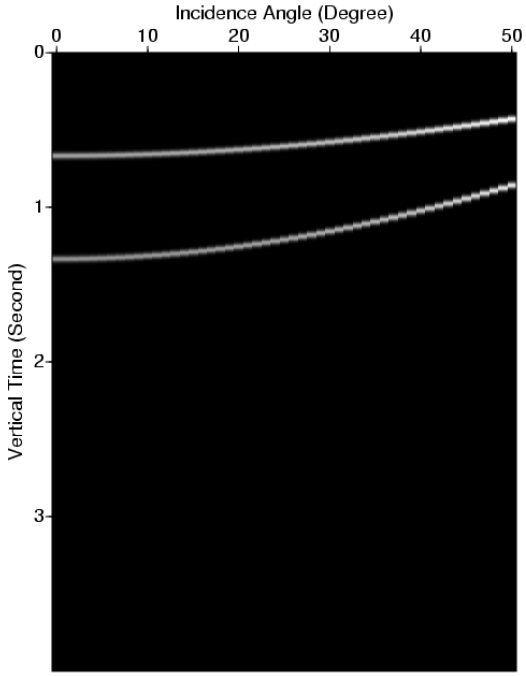

Figure 2: The data after Radon transform. The elliptical events are two primaries and internal multiples are absent.

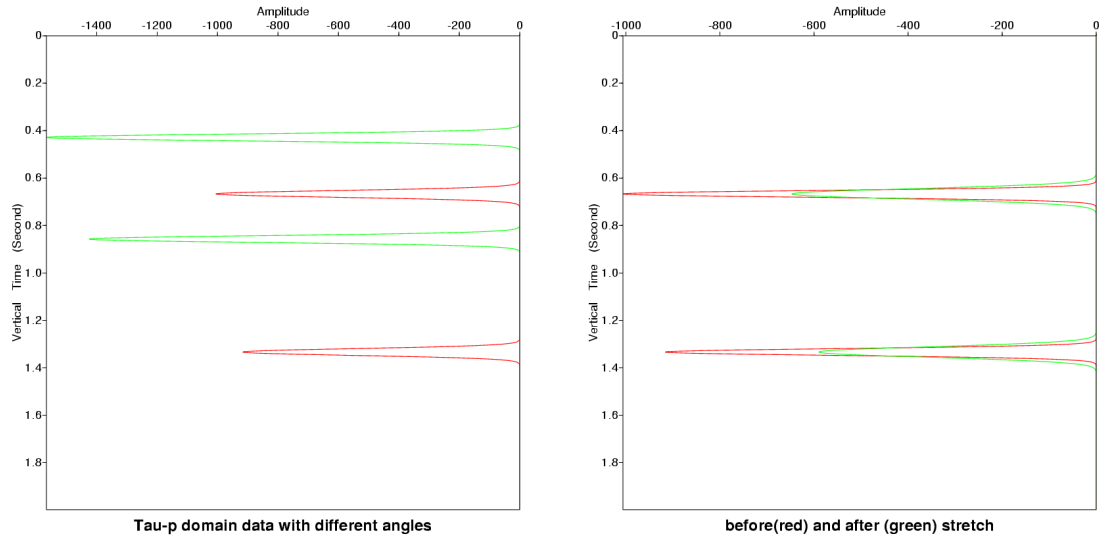

Figure 3: Regularization results: on the left is the input data in the τ-p domain. On the right is data after regularization. The red curves signify data from zero angle and the green curves signify data from $\theta = 50°$. In the τ-p domain, an event has the same width but different amplitude and arrival time. In the pseudodepth domain, an event has the same depth but different depth.

4 Source regularization for elastic inversion

In the homogeneous or piecewise homogeneous medium, the P-wave or the S-wave equation looks very similar to the acoustic equation. This is the reason why the acoustic results in the previous section can be extended to PP data in the elastic model.

Just as in the acoustic case, after Radon transform the elastic data is a function of veritcal time τ.

In parameter inversion; for example, Zhang (2006); X. Li and Weglein (2008); Li and Weglein (2010); Jiang et al. (2008); Liang et al. (2009), the seismic data was conveniently considered as a function of (pseudo) depth. A linear transforms are used to map the seismic data in the $\tau - p$ domain to the seismic data conveniently used by aforementioned articles. These transform is actually the "stretch and squeeze" discussed in Equation (78) and the paragraph immediately after.

5 The seismic imaging operator $\xi_{m,n}$ and $\eta_{m,n}$

There is an integration operator for every term in the inverse scattering series. For an ISS term, its seismic imaging operator is the integration operator used in its calculation. In the calculation of terms of inverse scattering series, we find it is very convient to introduce the concept of a seismic imaging operator. For velocity only inverse series with lateral variation, the seismic imaging

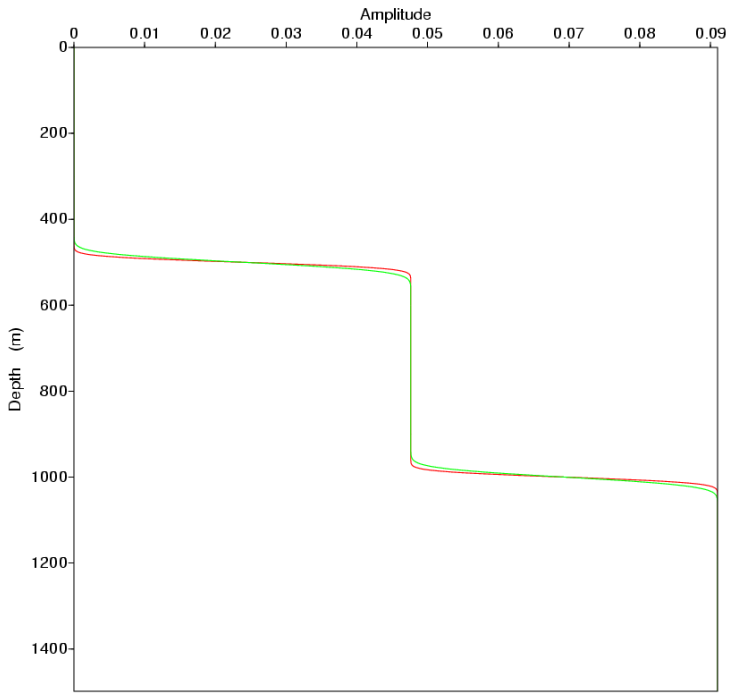

Figure 4: Data from two different angles: the red curve shows data from zero angle. The green curve shows data from $\theta = 50°$. It is obvious that the wave packet in the red curve are thinner than that of green curve.

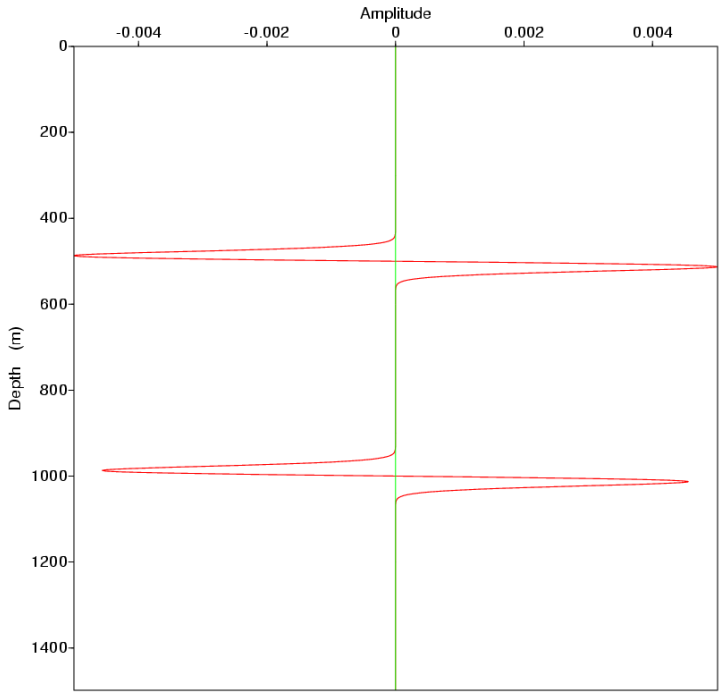

Figure 5: The difference between data from 0° and 50°: "red" (without regularization) and "green" (with regularization). It is obvious that: (1) the data difference does not vanish without regularization as desired by this benchmark, (2) the benchmark is satisfied after regularization where the data difference vanishes.

operators[9] for the linear term α_1 and the quadratic term α_2 along with their various derivatives, with respect to depth, can generally be expressed as the Fourier transform of the function:

$$\mathbf{i}^m(-\mathbf{i})^n k_z^n \left[\sqrt[?]{<k_z>^2 \pm 1}\right]^m e^{\mathbf{i}u\sqrt[?]{<k_z>^2 \pm 1}}, \tag{35}$$

where $n > -1$ and m are two integers[10].

Use the symbol v to denote the Fourier conjugate of k_z and define two sets of operators as the following Fourier transform:

$$\xi_{m,n}(u,v) \stackrel{\triangle}{=} \frac{1}{2\pi}\int_{-\infty}^{\infty} \mathbf{i}^m(-\mathbf{i})^n k_z^n \left[\sqrt[?]{<k_z>^2 + 1}\right]^m e^{\mathbf{i}(u\sqrt[?]{<k_z>^2+1} - vk_z)} dk_z. \tag{36}$$
$$\texttt{where}: \ -\infty < u, v < \infty \ , \ m = 0, \pm 1, \pm 2, \cdots \ , \ n = 0, 1, 2, \cdots$$

$$\eta_{m,n}(u,v) \stackrel{\triangle}{=} \frac{1}{2\pi}\int_{-\infty}^{\infty} \mathbf{i}^m(-\mathbf{i})^n k_z^n \left[\sqrt[?]{<k_z>^2 - 1}\right]^m e^{\mathbf{i}(u\sqrt[?]{<k_z>^2-1} - vk_z)} dk_z. \tag{37}$$
$$\texttt{where}: \ -\infty < v < \infty \ , \ u \geq 0 \ , \ m = -1, 0, 1, 2, \cdots \ , \ n = 0, 1, 2, \cdots$$

$$\begin{aligned}\psi_{m,n}(u,v) &\stackrel{\triangle}{=} \frac{1}{2\pi}\int_{-1}^{1} \mathbf{i}^m(-\mathbf{i})^n k_z^n \left[\sqrt[?]{<k_z>^2 - 1}\right]^m e^{\mathbf{i}(u\sqrt[?]{<k_z>^2-1} - vk_z)} dk_z \\ &= \frac{1}{2\pi}\int_{-1}^{1} (-\mathbf{i}k_z)^n \left[-\sqrt{1-k_z^2}\right]^m e^{-u\sqrt{1-k_z^2}} e^{-\mathbf{i}vk_z} dk_z\end{aligned} \tag{38}$$
$$\texttt{where}: \ -\infty < v < \infty \ , \ u \geq 0 \ , \ m = -1, 0, 1, 2, \cdots \ , \ n = 0, 1, 2, \cdots$$

The seimic imaging operators defined in equations (36)$\sim$(38) can cover not only all the structures in calculating α_1 and α_2, but will also be extensively used in computing later terms such as α_3, α_4, $\cdots$. We use the superscript $^{\mathbf{Reg}}$ to denote the regular part of a corresponding operator.

To be more specific, $\xi_{-2,2}^{\mathbf{Reg}}$ is used to construct the cascaded imaging operator: $\xi_{-1,0}^{\mathbf{Reg}}$, $\eta_{-1,0}^{\mathbf{Reg}}$, $\xi_{-1,2}^{\mathbf{Reg}}$, and $\eta_{1,2}^{\mathbf{Reg}}$ are used to calculate the α_{23} term in Equation (2.22) of Liu (2006). From Equation (60),

[9] A very similar definition can be found in § 7 of Liu and Weglein (2008), but we now use a totally new different set of notations.

[10] We require m and n to be selected to make sure the integrand is Riemann integrable at $k_z = 0$ and $k_z = \pm 1$.

(69), and(70) it is clear that they are all composites of Bessel functions of the first kind and the square root function.

Note that when k_z varies from $-\infty$ to ∞, the k_z^2+1 term inside the square roots of the integrand in Equation (36) is always positive and consequently this integral conatains no evanescent integrand. On the other hand, in Equation (37) the term k_z^2-1 inside the square root will be negative when $|k_z|<1$ and this integral contains evanescent integrand.

Let us consider the special case where $m=n=0$:

$$\xi_{0,0}(u,v)=\frac{1}{2\pi}\int_{-\infty}^{\infty} e^{\mathbf{i}(u\sqrt[?]{<k_z>^2+1}-vk_z)}dk_z,$$
$$\eta_{0,0}(u,v)=\frac{1}{2\pi}\int_{-\infty}^{\infty} e^{\mathbf{i}(u\sqrt[?]{<k_z>^2-1}-vk_z)}dk_z.$$

Using the third property in Equation (8) after flipping the sign of k_z we have:

$$e^{\mathbf{i}(u\sqrt[?]{<-k_z>^2\pm1}-v[-k_z])}=e^{\mathbf{i}u\sqrt[?]{<-k_z>^2\pm1}}e^{\mathbf{i}vk_z}=\left[e^{\mathbf{i}u\sqrt[?]{<k_z>^2\pm1}}\right]^*\left[e^{-\mathbf{i}vk_z}\right]^*$$
$$=\left[e^{\mathbf{i}u\sqrt[?]{<k_z>^2\pm1}}e^{-\mathbf{i}vk_z}\right]^*=\left[e^{\mathbf{i}(u\sqrt[?]{<k_z>^2\pm1}-vk_z)}\right]^*.$$

$$\xi_{0,0}(u,v)=\frac{1}{2\pi}\int_{-\infty}^{\infty} e^{\mathbf{i}(u\sqrt[?]{<k_z>^2+1}-vk_z)}dk_z$$
$$=\frac{1}{2\pi}\int_{0}^{\infty}\left[e^{\mathbf{i}(u\sqrt[?]{<k_z>^2+1}-vk_z)}+e^{\mathbf{i}(u\sqrt[?]{<-k_z>^2+1}-v[-k_z])}\right]dk_z,$$
$$=\frac{1}{\pi}\int_{0}^{\infty}\mathbf{RE}\left[e^{\mathbf{i}(u\sqrt[?]{<k_z>^2+1}-vk_z)}\right]dk_z \qquad \texttt{is real}$$

$$\eta_{0,0}(u,v)=\frac{1}{2\pi}\int_{-\infty}^{\infty} e^{\mathbf{i}(u\sqrt[?]{<k_z>^2-1}-vk_z)}dk_z.$$
$$=\frac{1}{2\pi}\int_{0}^{\infty}\left[e^{\mathbf{i}(u\sqrt[?]{<k_z>^2-1}-vk_z)}+e^{\mathbf{i}(u\sqrt[?]{<-k_z>^2-1}-v[-k_z])}\right]dk_z,$$
$$=\frac{1}{\pi}\int_{0}^{\infty}\mathbf{RE}\left[e^{\mathbf{i}(u\sqrt[?]{<k_z>^2-1}-vk_z)}\right]dk_z \qquad \texttt{is real}$$

Consequently, the function $\xi_{0,0}(u,v)$ and $\eta_{0,0}(u,v)$ are all real:

$$[\xi_{0,0}(u,v)]^* = \xi_{0,0}(u,v),$$

and as a result if the signs of u and v are flipped simultaneously we have:

$$\begin{aligned}\xi_{0,0}(-u,-v) &= \frac{1}{2\pi}\int_{-\infty}^{\infty} e^{\mathbf{i}(-u\sqrt[?]{<k_z>^2+1}+vk_z)}dk_z = \frac{1}{2\pi}\int_{-\infty}^{\infty}\left[e^{\mathbf{i}(u\sqrt[?]{<k_z>^2+1}-vk_z)}\right]^* dk_z \\ &= \left[\frac{1}{2\pi}\int_{-\infty}^{\infty} e^{\mathbf{i}(u\sqrt[?]{<k_z>^2+1}-vk_z)}dk_z\right]^* = [\xi_{0,0}(u,v)]^* = \xi_{0,0}(u,v)\end{aligned}$$

Using similar argument for arbitrary m and $n > -1$ we have:

$$\xi_{m,n}(-u,-v) = (-1)^{m+n}\xi_{m,n}(u,v). \tag{39}$$

Ignoring $\psi_{m,n}$ (the evanescent portion of the integral that becomes negligible even for the depth value beyond several meters), $\eta_{m,n}$ can be expressed by [11] $\xi_{n-1,m+1}$. The proof is as follows: if $|k_z| > 1$ we can change the integration variables to $\lambda = \sqrt[?]{<k_z>^2 - 1}$. In this case, both k_z and λ are real and the condition in Equation (9) is satisfied and consequently we have: $k_z = \sqrt[?]{<\lambda>^2 + 1}$

$$\begin{aligned}&\eta_{m,n}(u,v) - \psi_{m,n}(u,v) \\ &= \frac{1}{2\pi}\int_{|k_z|\geq 1} \mathbf{i}^m(-\mathbf{i})^n k_z^n \left[\sqrt[?]{<k_z>^2-1}\right]^m e^{\mathbf{i}(u\sqrt[?]{<k_z>^2-1}-vk_z)}dk_z \\ &= \int_{-\infty}^{\infty} \mathbf{i}^m(-\mathbf{i})^n \left[\sqrt[?]{<\lambda>^2+1}\right]^n \lambda^m e^{\mathbf{i}(u\lambda - v\sqrt[?]{<\lambda>^2+1})}\frac{\lambda}{\sqrt[?]{<\lambda>^2+1}}d\lambda \\ &= \int_{-\infty}^{\infty} \mathbf{i}^m(-\mathbf{i})^n \left[\sqrt[?]{<\lambda>^2+1}\right]^{(n-1)} \lambda^{m+1} e^{\mathbf{i}(u\lambda - v\sqrt[?]{<\lambda>^2+1})}d\lambda \\ &= (-1)^{m+n-1}\int_{|\lambda|\geq 1} \mathbf{i}^{n-1}(-\mathbf{i})^{m+1}\left[\sqrt[?]{<\lambda>^2+1}\right]^{n-1}\lambda^{m+1}e^{\mathbf{i}(u\lambda - v\sqrt[?]{<\lambda>^2+1})}d\lambda \\ &= (-1)^{m+n-1}\xi_{n-1,m+1}(-v,-u).\end{aligned} \tag{40}$$

[11] The accuracy of the approximation improves very quickly as the value of u increases.

Combining the relationship in Equation (39) and Equation (40) we have:

$$\eta_{m,n}(u,v) \approx (-1)^{m+n-1}\xi_{n-1,m+1}(-v,-u) = -\xi_{n-1,m+1}(v,u). \tag{41}$$

Note that in approximate relation to Equation (41) there is always a negative sign.

In other words, the seismic imaging operator $\xi_{m,n}$ that has no evanescent integrand that can be well approximated by a seismic imaging operator $\eta_{n-1,m+1}$ that contains the evanescent integrand. The approximation can be summarized as follows, for $u > 0$:

$$\begin{aligned}\xi_{m,n}(u,v) &\approx \begin{cases} (-1)^{m+n-1}\eta_{n-1,m+1}(-v,-u) & \texttt{If}(v<0), \\ -\eta_{n-1,m+1}(v,u) & \texttt{If}(v\geq 0). \end{cases} \\ &= \begin{cases} 0 & \texttt{If}(v<0), \\ -\eta_{n-1,m+1}(v,u) & \texttt{If}(v\geq 0). \end{cases}\end{aligned} \tag{42}$$

The corresponding exact relation is:

$$\begin{aligned}\xi_{m,n}(u,v) &= \begin{cases} (-1)^{m+n-1}\left[\eta_{n-1,m+1}(-v,-u) - \psi_{n-1,m+1}(-v,-u)\right] & \texttt{If}(v<0), \\ -\eta_{n-1,m+1}(v,u) + \psi_{n-1,m+1}(v,u) & \texttt{If}(v\geq 0). \end{cases} \\ &= \begin{cases} (-1)^{m+n}\psi_{n-1,m+1}(-v,-u) & \texttt{If}(v<0), \\ -\eta_{n-1,m+1}(v,u) + \psi_{n-1,m+1}(v,u) & \texttt{If}(v\geq 0). \end{cases}\end{aligned} \tag{43}$$

5.1 Well-defined discontinuities

As detailed in Liu and Weglein (2008), after expanding the integrand in an infitine series in terms of various powers k_z:

$$\mathbf{i}^m(-\mathbf{i})^n k_z^n \left[\sqrt[?]{<k_z>^2 \pm 1}\right]^m e^{\mathbf{i}u\left[\sqrt[?]{<k_z>^2\pm 1}-k_z\right]} = \sum_{j=-\infty}^{m+n} a_j(u)\left(\mathbf{i}k_z\right)^j, \tag{44}$$

where each coefficient is written as $a_j(u)$ since it is a function of u the seismic imaging operators $\xi_{m,n}$ and $\eta_{m,n}$ contains two portions:

1. The linear combinations of the following well-understood Dirac δ-functions:

$$\sum_{j=0}^{m+n} a_j(u)\delta^{(j)(u-v)}$$

2. A rapidly varying function with well-defined discontinuity at $u = v$. In this article, it will be denoted by adding a superscript $^{\mathbf{Reg}}$ to the corresponding operator.

$$\begin{aligned}\xi_{m,n}(u,v) &= \sum_{j=0}^{j\leq n+m} a_j(u)\delta^{(n+m-j)}(u-v) + \xi_{m,n}^{\mathbf{Reg}}(u,v),\\ \eta_{m,n}(u,v) &= \sum_{j=0}^{j\leq n+m} a_j(u)\delta^{(n+m-j)}(u-v) + \eta_{m,n}^{\mathbf{Reg}}(u,v),\end{aligned} \tag{45}$$

where in the right-hand side of the Equation (45) the coefficients a_j are all functions of u, and are specific to each $\xi_{m,n}$ or $\eta_{m,n}$. The first part is the linear combination of $\delta(u-v)$, $\delta'(u-v)$, $\delta''(u-v)$, $\cdots$, the second part is a Riemann integral which is finite at every depth and denoted as[12] $\xi_{m,n}^{\mathbf{Reg}}(u,v)$ and $\eta_{m,n}^{\mathbf{Reg}}(u,v)$ can be calculated via:

$$\xi_{m,n}^{\mathbf{Reg}}(u,v) = \frac{1}{2\pi}\int_{-\infty}^{\infty}\left\{\begin{array}{l}\mathbf{i}^m(-\mathbf{i})^n k_z^n\left[\sqrt[?]{<k_z>^2+1}\right]^m e^{\mathbf{i}(u\sqrt[?]{<k_z>^2+1}-vk_z)}\\ -\sum_{j=0}^{m+n} a_j(u)(\mathbf{i}k_z)^j e^{\mathbf{i}(u-v)k_z}\end{array}\right\}dk_z, \tag{46}$$

and

$$\eta_{m,n}^{\mathbf{Reg}}(u,v) = \frac{1}{2\pi}\int_{-\infty}^{\infty}\left\{\begin{array}{l}\mathbf{i}^m(-\mathbf{i})^n k_z^n\left[\sqrt[?]{<k_z>^2+1}\right]^m e^{\mathbf{i}(u\sqrt[?]{<k_z>^2+1}-vk_z)}\\ -\sum_{j=0}^{m+n} a_j(u)(\mathbf{i}k_z)^j e^{\mathbf{i}(u-v)k_z}\end{array}\right\}dk_z, \tag{47}$$

Although the functions $\xi_{m,n}^{\mathbf{Reg}}(u,v)$ and $\eta_{m,n}^{\mathbf{Reg}}(u,v)$ are finite, they are also discontinuous when $u = v$ which is the unique location where the δ-function becomes active.

Since we have covered the δ-function produced by $(\mathbf{i}k_z)^0$, $(\mathbf{i}k_z)^1$, $(\mathbf{i}k_z)^2$, $\cdots$, it is natural to look at the highest power among the remaining expansion: $(\mathbf{i}k_z)^{-1}$. Indeed this term produces discontinuities; however, the proof is as follows for an arbitrarily chosen number $\mathbf{\Xi} \geq 1$, the integral below:

$$\int_{|k_z|\geq\mathbf{\Xi}} \frac{e^{\mathbf{i}(u-v)k_z}}{\mathbf{i}k_z}dk_z = 2\int_{\mathbf{\Xi}}^{\infty}\frac{\sin\left[(u-v)k_z\right]}{k_z}dk_z$$

[12] Due to the fact that it is the regularized portion of the original integral, it is denoted with a superscript $^{\mathbf{Reg}}$.

is an odd function of $(u-v)$. We only need to study its behavior for positive $(u-v)$ to understand its properties in the entire space. If we assume $u-v>0$ and change the integration variable to $y \stackrel{\triangle}{=} k_z * (u-v)$. The expression above reduces to the sine integral defined in Equation (5.2.1) of Abramowitz and Stegun (1965):

$$\begin{aligned}\int_{\Xi}^{\infty} \frac{\sin\left[(u-v)k_z\right]}{k_z} dk_z &= 2 \int_{(u-v)\Xi}^{\infty} \frac{\sin\left[y\right]}{y} dy \\ =2\left(\frac{\pi}{2} - \int_{0}^{(u-v)\Xi} \frac{\sin[y]}{y} dy\right) &= 2 * \left(\frac{\pi}{2} - \mathtt{Si}([u-v]\Xi)\right).\end{aligned}$$

Obviously, according to Figure (5.6) from Abramowitz and Stegun (1965) we have:

$$\lim_{(u-v)\to 0^+} \mathtt{Si}([u-v]\Xi) = 0 \qquad (\mathtt{For\ any\ finite}\ \Xi).$$

Consequently,

$$\lim_{(u-v)\to 0^+} \int_{\Xi}^{\infty} \frac{\sin\left[(u-v)k_z\right]}{k_z} dk_z = 2 * \left(\frac{\pi}{2} - 0\right) = \pi \qquad (\mathtt{For\ any\ finite}\ \Xi).$$

The function converges to π from the right $(u-v=0^+)$. Since the function above is an odd function of $(u-v)$ it will converge to $-\pi$ from the left $(u-v=0^-)$:

$$\lim_{(u-v)\to 0^-} \int_{\Xi}^{\infty} \frac{\sin\left[(u-v)k_z\right]}{k_z} dk_z = -2 * \left(\frac{\pi}{2} - 0\right) = -\pi \qquad (\mathtt{For\ any\ finite}\ \Xi).$$

Since this expansion converges to different limits from the left and right, it is discontinuous when $u-v=0$. This is the only discontinuity in the entire expansion[13]. Note that if we change the value of Ξ, the size of the discontinuity will not change since it is not a function of Ξ. This independency with Ξ is reasonable since Ξ is only artificially chosen and should not affect the size of the discontinuities. In summary, the discontinuity at $u=v$ is:

$$\lim_{u=v+0^+} \xi^{\mathbf{Reg}}_{m,n}(u,v) - \lim_{u=v+0^-} \xi^{\mathbf{Reg}}_{m,n}(u,v) = a_{-1}(u)\frac{\pi-(-\pi)}{2\pi} = a_{-1}(u) \tag{48}$$

[13] The integral in the finite range $\int_{-\Xi}^{\Xi} dk_z$ will be continuous. Also, the $\int_{|k_z|\geq\Xi} dk_z$ integral for $(\mathbf{i}k_z)^{-2}$, $(\mathbf{i}k_z)^{-3}$, $\cdots$ are all well-defined exponential integrals and will all be continuous.

Note that in Equation (48), $a_{-1}(u)$ is the coefficients of k_z^{-1} in the expansion of

$$\mathbf{i}^m(-\mathbf{i})^n k_z^n \left[\sqrt[?]{<k_z>^2 \pm 1}\right]^m e^{\mathbf{i}u[\sqrt[?]{<k_z>^2 \pm 1}-k_z]}$$

at the point $k_z = +\infty$; hence, a_{-1} will be a polynomial of u. At the diagonal where the mountaintop expansion happens we have $\breve{r} = u = v$. Consequently, we can simply rewrite it as a function of $\breve{r}$, i.e., $a_{-1}(\breve{r})$.

5.2 Properties of the seismic imaging operator and its impact on the structure of our imaging algorithm

1. Well-defined discontinuity.

   As demonstrated in §5.1, the functions $\xi_{m,n}$ and $\eta_{m,n}$ are discontinuous. This discontinuity always happens at $u = v$ where the Dirac δ function becomes active and this discontinuity can be derived by simply collecting the highest power $(\mathbf{i}k_z)^{-1}$, which is the final result that is listed in Equation (48).

2. Flat ocean half, rapidly varying mountain half, and easily predicted beachhead and mountaintop.

   The distribution $\xi_{m,n}$ behaves very differently in the region where $u < v$ and the region $u > v$. We call the first region "ocean half" because with the increase of u and v, our distribution becomes more flat and smooth and much closer to zero. We call the second region the "mountain half" because the distribution shows more and more rapid oscillations for greater u and v. For a fixed u, the most rapid variation always occurs at the limit $v = u$. We define the "beachhead" and "mountaintop" in the (u, v) plane as the lines that satisfy $u = v + 0^-$ and $u = v + 0^+$ because the beachhead is as flat and smooth as the ocean half. For large u, we can safely predict the value at this location as 0 (to be exact, the prediction error will decrease exponentially with the increase of u). Consequently, we can predict the mountaintop using the well-defined discontinuity in Equation (48).

   On the other hand, the distribution $\eta_{m,n}$ also behaves very different in the region where $u > v$ and the region $u < v$. We call the first region "ocean half" because with the increase of u and v, our distribution completely vanishes to become zero. We call the second region the "mountain half" because the distribution shows more and more rapid oscillations with increase in u and v. For a fixed u, the most rapid variation always occurs at the limit $v = u$.

   We define the "beachhead" and "mountaintop" in the (u, v) plane as the lines that satisfy $u = v + 0^+$ and $u = v + 0^-$ because the beachhead is constantly zero. For any u, we can safely predict the value at this location as exactly being 0. Consequently, we can predict the mountaintop using the well-defined discontinuity in Equation (48).

3. Infinite expansion at the discontinuity.

Although $\xi^{\mathbf{Reg}}_{m,n}$ and $\eta^{\mathbf{Reg}}_{m,n}$ are highly transcendental functions with daunting complexities far beyond the functions well-studied in the literature, their behavior at the diagonal region $u = v$ is highly predictable and the greater the u, the better the predictability.

A Taylor expansion of a 2D function gives:

$$f(u,v) = f(u_0,v_0) + \sum_{j=1}^{\infty} \frac{1}{j!} \left[\left(\frac{\partial}{\partial u}\Delta u + \frac{\partial}{\partial v}\Delta v \right)^j f(u,v) \right]_{u=u_0, v=v_0}. \tag{49}$$

In our case for an arbitrary location (u,v), the closest location with good approximation[14] of f (and its derivatives) happens at the beachhead location $(\breve{r},\breve{r})$ where $\breve{r} \overset{\triangle}{=} \frac{u+v}{2}$. Using Equation (49), we have the closest point to start the expansion: $u_0 = v_0 = \breve{r} = \frac{u+v}{2}$, $\Delta u = \Delta v = \frac{1}{\sqrt{2}}\frac{u-v}{2} = \frac{\breve{a}}{\sqrt{2}}$ where $\breve{a} \overset{\triangle}{=} \frac{u-v}{2}$. We have the mountaintop expansion; for example, $\xi_{-2,2}(u,v)$ is essentially the seismic imaging operator γ_1 that is used to calculate α_1 and it can be very accurately approximated by the following expansion:

$$\begin{aligned}
\xi_{-2,2}(u,v) = \delta(u-v) &- \frac{1}{2}(\breve{r}) + \frac{1}{2\sqrt{2}}\left(3+\frac{1}{2}\breve{r}^2\right)\breve{a} - \frac{1}{4}\left(\frac{3}{2}\breve{r}+\frac{1}{12}\breve{r}^3\right)\breve{a}^2 + \frac{1}{4\sqrt{2}}\left(\frac{2}{3}+\frac{1}{4}\breve{r}^2+\frac{1}{144}\breve{r}^4\right)\breve{a}^3 \\
&- \frac{1}{8}\left(\frac{1}{6}\breve{r}+\frac{1}{48}\breve{r}^3+\frac{1}{2880}\breve{r}^5\right)\breve{a}^4 + \frac{1}{8\sqrt{2}}\left(\frac{1}{30}+\frac{1}{60}\breve{r}^2+\frac{1}{960}\breve{r}^4+\frac{1}{86400}\breve{r}^6\right)\breve{a}^5 \\
&- \frac{1}{16}\left(\frac{1}{180}\breve{r}+\frac{1}{1080}\breve{r}^3+\frac{1}{28800}\breve{r}^5+\frac{1}{3628800}\breve{r}^7\right)\breve{a}^6 + \cdots
\end{aligned} \tag{50}$$

$$\begin{aligned}
&\cdots + \frac{1}{16\sqrt{2}}\left(\frac{1}{1260}+\frac{\breve{r}^2}{2520}+\frac{\breve{r}^4}{30240}+\frac{\breve{r}^6}{1209600}+\frac{\breve{r}^8}{203212800}\right)\breve{a}^7 \\
&- \frac{1}{32}\left(\frac{\breve{r}}{10080}+\frac{\breve{r}^3}{60480}+\frac{\breve{r}^5}{1209600}+\frac{\breve{r}^7}{67737600}+\frac{\breve{r}^9}{14631321600}\right)\breve{a}^8 \\
&+ \frac{1}{32\sqrt{2}}\left(\frac{1}{90720}+\frac{\breve{r}^2}{181440}+\frac{\breve{r}^4}{2177280}+\frac{\breve{r}^6}{65318400}+\frac{\breve{r}^8}{4877107200}+\frac{\breve{r}^{10}}{1316818944000}\right)\breve{a}^9 \\
&- \frac{1}{64}\left(\frac{\breve{r}}{907200}+\frac{\breve{r}^3}{5443200}+\frac{\breve{r}^5}{108864000}+\frac{\breve{r}^7}{4572288000}+\frac{\breve{r}^9}{438939648000}+\frac{\breve{r}^{11}}{144850083840000}\right)\breve{a}^{10} \\
&+ \cdots
\end{aligned} \tag{51}$$

First, let us look at the highest-order term (in terms of $\breve{r}$) in each expansion.The ratio between the coefficients of consecutive terms are: $2 = 1 \times 2$, $6 = 2 \times 3$, $12 = 3 \times 4$, $20 = 4 \times 5$, $30 = 5 \times 6$, $42 = 6 \times 7$, $56 = 7 \times 8$, $72 = 8 \times 9$, $90 = 9 \times 10$, $110 = 10 \times 11$, $\cdots$.

Collecting the highest power in each term, we can guess the following closed-form:

[14] The approximation is reached by three steps: (1) approximate the beachhead value of $f(\breve{r},\breve{r})$ as zero, (2) calculate the discontinuity by Equation (48) and, (3) add the discontinuity to the beachhead value to get the value of mountaintop.

$$-\frac{1}{2}\breve{r}\sum_{n=0}^{\infty}\frac{(-\breve{r}\breve{a}/\sqrt{2})^n}{(n!)\,(n+1)!}. \tag{52}$$

It is obvious that the second highest term in each expansion follows the same ratio rule. We can also similarly guess the closed-form for the second highest term:

$$\frac{3}{2\sqrt{2}}\breve{a}\sum_{n=0}^{\infty}\frac{(-\breve{r}\breve{a}/\sqrt{2})^n}{(n!)\,(n+1)!}. \tag{53}$$

The partial derivatives of $\widetilde{\gamma}_1$ taken to $69^{\mathtt{th}}$-order derivatives results in the following pattern:

$$\begin{aligned}\xi_{-2,2}(u,v)-\delta(u-v) &= -\sum_{\imath=0}^{\infty}\sum_{\ell=0}^{\ell\le\left[\frac{\imath+1}{2}\right]}\breve{a}^{\imath}\breve{r}^{\imath+1-2\ell}\cdot\begin{cases}\frac{(-1)^{\imath}}{\imath!(\imath+1)!} & (\ell=0)\\ \frac{(-1)^{\imath}3}{\imath!(\imath-1)!} & (\ell=1)\\ \frac{(-1)^{\imath}4}{\imath!(\imath+1-2\ell)!} & (\ell>1)\end{cases}\\ &= -\sum_{\imath=0}^{\infty}\frac{(-\breve{a})^{\imath}}{\imath!}\sum_{\ell=0}^{\ell\le\left[\frac{\imath+1}{2}\right]}\frac{\breve{r}^{\imath+1-2\ell}}{(\imath+1-2\ell)!}\cdot\begin{cases}1 & (\ell=0)\\ 3 & (\ell=1)\\ 4 & (\ell>1)\end{cases}\end{aligned} \tag{54}$$

where $\breve{r}=\frac{u+v}{2}$ and $\breve{a}=\frac{u-v}{2}$, $\imath$ is the power of $\breve{a}$, ℓ is index of diagonal ($\ell=0$ corresponding to the uppermost diagonal). Equation (54) is an expansion according to $\imath$, the coefficient for each power $\breve{a}^{\imath}$ by itself is a finite sum over the powers of $\breve{r}$. If we define $\jmath=\imath+1-2\ell$ which is the power of $\breve{r}$.

$$\jmath=\imath+1-2\ell \quad\Longrightarrow\quad \imath=2\ell-1+\jmath \quad\Longrightarrow\quad \imath\in\{\jmath-1,\jmath+1,\jmath+3,\cdots\}$$

For all $\jmath\ge 1$, we have $\jmath-1=|\jmath-1|$ which is positive and is a legitimate power for $\breve{a}$. For the only special case of $\jmath=0$, $\jmath-1=-1$ is not a legitimate power for $\breve{a}$ and its minimal value should be the next odd integer 1. In conclusion, we have:

$$\imath\ge|\jmath-1|. \tag{55}$$

With index range determined in Equation (55), the expansion in Equation (54) can be written according to $\breve{r}^{\jmath}$ as follows:

$$\begin{aligned}\xi_{-2,2}(u,v) &= \delta(u-v)+\xi_{-2,2}^{\mathbf{Reg}}(u,v)\\ &\approx \delta(u-v)-H(\breve{a})\sum_{\jmath=0}^{\infty}\left(\sum_{\imath\ge|\jmath-1|}^{\imath+=2}\frac{\breve{a}^{\imath}(-\breve{r})^{\jmath}}{\imath!\jmath!}\cdot\begin{cases}1 & (\imath=\jmath-1)\\ 3 & (\imath=\jmath+1)\\ 4 & (\imath>\jmath+1)\end{cases}\right).\end{aligned} \tag{56}$$

Equation (56) can be used to prove the absolute convergence of the expansion,

$$\begin{aligned}
&\sum_{\jmath=0}^{\infty}\left(\sum_{\imath\geq|\jmath-1|}^{\imath+=2}\left|\frac{\breve{a}^{\imath}(-\breve{r})^{\jmath}}{\imath!\jmath!}\cdot\begin{cases}1 & (\imath=\jmath-1)\\ 3 & (\imath=\jmath+1)\\ 4 & (\imath>\jmath+1)\end{cases}\right|\right)\\
\leq&\sum_{\jmath=0}^{\infty}\left(\sum_{\imath\geq|\jmath-1|}^{\imath+=2}\frac{4\breve{a}^{\imath}\breve{r}^{\jmath}}{\imath!\jmath!}\right)\leq 4\sum_{\jmath=0}^{\infty}\left(\sum_{\imath\geq|\jmath-1|\%2}^{\imath+=2}\frac{\breve{a}^{\imath}\breve{r}^{\jmath}}{\imath!\jmath!}\right)=4\sum_{\jmath=0}^{\infty}\frac{\breve{r}^{\jmath}}{\jmath!}\sum_{\imath\geq|\jmath-1|\%2}^{\imath+=2}\frac{\breve{a}^{\imath}}{\imath!}\\
=&4\sum_{\jmath=0}^{\infty}\frac{\breve{r}^{\jmath}}{\jmath!}\sinh^{(\jmath)}(\breve{a})=4\sinh(\breve{a}+\breve{r}).
\end{aligned}\tag{57}$$

The absolute convergence of Equation (57) guarantees that this series converges to a unique value regardless whatever sequence it is summed.

Due to the fact that $\breve{r}\breve{a}=\frac{u^2-v^2}{4}=\left(\frac{\sqrt{u^2-v^2}}{2}\right)^2$:

$$(-\breve{r}\breve{a})^{\imath}=(-1)^{\imath}\left(\frac{\sqrt{u^2-v^2}}{2}\right)^{2\imath+1}\frac{2}{\sqrt{u^2-v^2}}=(-1)^{\imath}\left(\frac{\sqrt{u^2-v^2}}{2}\right)^{2\imath+1}\frac{1}{\sqrt{\breve{r}\breve{a}}}.\tag{58}$$

We can also expand using ℓ as the outmost index:

$$(3\breve{a}-\breve{r})\sum_{\imath=0}^{\infty}\frac{(-\breve{a}\breve{r})^{\imath}}{\imath!(\imath+1)!}\qquad-\qquad 4\sum_{\ell=2}^{\infty}\breve{a}^{2\ell-1}\sum_{\imath\geq 2\ell-1}\frac{(-\breve{a}\breve{r})^{\imath+1-2\ell}}{\imath!(\imath+1-2\ell)!}.\tag{59}$$

Using the relation in Equation (58), the first term in Equation (59) can be expressed as Bessel function of the first kind:

$$\begin{aligned}
(3\breve{a}-\breve{r})\sum_{\imath=0}^{\infty}\frac{(-\breve{a}\breve{r})^{\imath}}{\imath!(\imath+1)!}&=\left(3\sqrt{\frac{\breve{a}}{\breve{r}}}-\sqrt{\frac{\breve{r}}{\breve{a}}}\right)\sum_{\imath=0}^{\infty}\frac{(-1)^{\imath}\left(\sqrt{u^2-v^2}/2\right)^{2\imath+1}}{\imath!(\imath+1)!}\\
&=\left(3\sqrt{\frac{\breve{a}}{\breve{r}}}-\sqrt{\frac{\breve{r}}{\breve{a}}}\right)J_1\left(\sqrt{u^2-v^2}\right).
\end{aligned}\tag{60}$$

Similarly, the second term in Equation (59) can also be expressed as Bessel functions:

$$
\begin{aligned}
&4\sum_{\ell=2}^{\infty}\breve{a}^{2\ell-1}\sum_{\imath\geq 2\ell-1}\frac{(-\breve{a}\breve{r})^{\imath+1-2\ell}}{\imath!(\imath+1-2\ell)!}=4\sum_{\ell=2}^{\infty}\breve{a}^{2\ell-1}\sum_{\ell=0}^{\infty}\frac{(-1)^{\ell}\left[(u^2-v^2)/4\right]^{\ell}}{\ell!(\ell+2\ell-1)!}\\
=&4\sum_{\ell=2}^{\infty}\breve{a}^{2\ell-1}\sum_{\ell=0}^{\infty}\frac{(-1)^{\ell}\left[\sqrt{u^2-v^2}/2\right]^{2\ell}}{\ell!(\ell+2\ell-1)!}=4\sum_{\ell=2}^{\infty}\left(\frac{2\breve{a}}{\sqrt{u^2-v^2}}\right)^{2\ell-1}\sum_{\ell=0}^{\infty}\frac{(-1)^{\ell}\left[\sqrt{u^2-v^2}/2\right]^{2\ell+2\ell-1}}{\ell!(\ell+2\ell-1)!}\\
=&4\sum_{\ell=2}^{\infty}\left(\sqrt{\breve{a}/\breve{r}}\right)^{2\ell-1}J_{2\ell-1}\left(\sqrt{u^2-v^2}\right),
\end{aligned}
$$

where in the last step of the equation above, we use the Taylor expansion of $J_{2\ell-1}$, i.e, Equation (9.1.10) in $\mathbf{P_{360}}$ of Abramowitz and Stegun (1965).

6 The seismic imaging operator for α_1

In the (k_m, z) domain with the constraint of $k_h = p_h = 0$, α_1 can be expressed as[15]:

$$\begin{aligned}
&\widetilde{\alpha}_1(k_m, z) = -\frac{8}{c_0}\int_{-\infty}^{\infty} \widetilde{D}\left(k_m, \frac{2z'}{c_0}\right)\widetilde{\gamma}_1(k_m, z, z')dz', \\
&\texttt{where} \quad : \quad \widetilde{\gamma}_1(k_m, z, z') = \frac{1}{2\pi}\int_{-\infty}^{\infty} dk_z \frac{k_z^2}{k_z^2 + k_m^2} e^{\mathbf{i}(z'\sqrt{k_z^2+k_m^2} - zk_z)}, \\
&\texttt{and} \quad : \quad \widetilde{D}(k_m, \tau) = \int_{-\infty}^{\infty} dx_m e^{-\mathbf{i}k_m x_m} \int_{-\infty}^{\infty} dx_h D\left(x_m + \frac{x_h}{2}, x_m - \frac{x_h}{2}, \tau\right).
\end{aligned} \tag{61}$$

Note that:

1. Although $\widetilde{\gamma}_1$ has three arguments it can be expressed by the distribution $\xi_{-2,2}$ which has only two degrees of freedom.
2. Due to the fact that in seismic exploration both z and z' can reach several kilometers, the seismic imaging algorithm in Equation (61) needs the value of the distribution $\xi_{-2,2}$ at very large depths.
3. For a fixed k_m, the larger the depth the bigger the argument required in $\xi_{-2,2}$.
4. For a fixed pair of depths (z, z'), the higher the k_m (horizontal wavenumber) the more demanding the algorithm becomes in terms of information from $\xi_{-2,2}$.

In Equation (61), D is the original data in the space and time domain: $D = D(x_g, x_s, t)$, and $\widetilde{D}(k_m, \tau)$ is the data after Radon transform in a **CMP** gather with $p_h = 0$. Changing the integration variable to $\kappa \triangleq k_z/k_m$ and using Equation (36), the distribution $\widetilde{\gamma}_1$ can be further expressed as:

[15] This equation is the same as Equation (2.22) of Liu (2006).

$$
\begin{aligned}
\widetilde{\gamma}_1(k_m, z, z') &= \frac{1}{2\pi} \int_{-\infty}^{\infty} dk_z \frac{k_z^2}{k_z^2 + k_m^2} e^{\mathbf{i}(z'\sqrt{k_z^2+k_m^2} - zk_z)} \\
&= \frac{|k_m|}{2\pi} \int_{-\infty}^{\infty} d\kappa \frac{\kappa^2}{\kappa^2+1} e^{\mathbf{i}(k_m z'\sqrt{\kappa^2+1} - k_m z\kappa)} = |k_m| \xi_{-2,2}(k_m z', k_m z) \\
&= |k_m| \xi_{-2,2}(|k_m| z', |k_m| z) \\
&= |k_m| \left[\delta(|k_m|[z'-z]) + \xi_{-2,2}^{\mathbf{Reg}}(|k_m| z', |k_m| z) \right] \\
&= \delta(z'-z) + |k_m| \xi_{-2,2}^{\mathbf{Reg}}(|k_m| z', |k_m| z)
\end{aligned}
\tag{62}
$$

Substituting the $\widetilde{\gamma}_1$ expression in Equation (62) into Equation (61) we have:

$$
\begin{aligned}
\widetilde{\alpha}_1(k_m, z) = &- \frac{8}{c_0} \widetilde{D}\left(k_m, \frac{2z}{c_0}\right) \\
&- \frac{8}{c_0} |k_m| \int_{-\infty}^{\infty} \widetilde{D}\left(k_m, \frac{2z'}{c_0}\right) \xi_{-2,2}^{\mathbf{Reg}}(|k_m| z', |k_m| z)
\end{aligned}
\tag{63}
$$

In this article, the cascaded modification to $\widetilde{\gamma}_1$ used prior to HOIS is:

$$
\breve{\gamma}_1(k_m, z', z) = \delta(z'-z) + |k_m| \xi_{-2,2}^{\mathbf{Reg}}(|k_m| z', |k_m| z) + |k_m| f(|k_m| z', |k_m| z), \tag{64}
$$

where the operator f is the cascaded application of the previously defined operator $\xi_{-2,2}^{\mathbf{Reg}}$, the portion of the α_1 imaging operator that vanishes for Earth without lateral variation:

$$
f(z', z) = \int_{-\infty}^{\infty} \xi_{-2,2}^{\mathbf{Reg}}(z', u) \xi_{-2,2}^{\mathbf{Reg}}(u, z) du. \tag{65}
$$

The cascaded modification to $\widetilde{\gamma}_1(k_m, z', z)$ has the following features:

- The modification is entirely invisible to Earth without lateral variation and its effects will be less significant for models with less lateral variations. Its contribution is significant for models with rapid lateral variations.

- Since the cascaded application of several linear operators is still linear[16], the cascaded operator is linear in terms of measured data. In the hierarchy of the inverse series, it is of the order of α_1. We think this is the reason why the result is compatible with the current closed-form solutions that formulated from the linear image α_1, i.e., LOIS and HOIS.
- Due to the similarity between the seismic imaging operator to calculate α_{23} and the operator used in the cascaded scheme: they are all Bessel functions composite with the square root function. This cascaded term seems have extracted some benefits from α_{23} term detailed in Equation (2.27) of Liu (2006).
- It is very likely that a better modification based on the relationship in the inverse series will give further improvement for imaging through rapid lateral variations.

The cascaded linear image is:

$$\begin{aligned}\widetilde{\alpha}_1^{\texttt{cascaded}}(k_m,z) = &-\frac{8}{c_0}\widetilde{D}\left(k_m,\frac{2z}{c_0}\right)\\ &-\frac{8}{c_0}|k_m|\int_{-\infty}^{\infty}\widetilde{D}\left(k_m,\frac{2z'}{c_0}\right)\xi_{-2,2}^{\mathbf{Reg}}(|k_m|z',|k_m|z)\\ &-\frac{8}{c_0}|k_m|\int_{-\infty}^{\infty}\widetilde{D}\left(k_m,\frac{2z'}{c_0}\right)f(|k_m|z',|k_m|z)\\ =\widetilde{\alpha}_1(k_m,z) &-\frac{8}{c_0}|k_m|\int_{-\infty}^{\infty}\widetilde{D}\left(k_m,\frac{2z'}{c_0}\right)f(|k_m|z',|k_m|z).\end{aligned} \tag{66}$$

[16] In terms of ordinary functions, it can be understood as follows: the composite of two linear functions are linear; for example, the composite of $y = f(u) = 5u + 7$ and $u = g(x) = 3x + 5$ is $f(g(x)) = 5(3x + 5) + 7 = 15x + 32$, a linear function in terms of x.

7 The Seismic imaging operator for α_2

In 2D, α_2 can be rewritten in the (k_m, z) domain as[17]:

$$\widetilde{\alpha}_2(k_m,z)=\frac{1}{4\pi}\int_{-\infty}^{\infty}dk'_m\int_{-\infty}^{\infty}dz'\widetilde{\alpha}_1(0.5k_m-k'_m,z')\int_{-\infty}^{\infty}dz''\widetilde{\alpha}_1(0.5k_m+k'_m,z'')\\ \widetilde{\gamma}_2\left(k_m,k'_m,z-\frac{z'+z''}{2},\frac{z'-z''}{2}\right). \tag{67}$$

In Equation (67), the function $\widetilde{\gamma}_2$ is defined with the sign convention for square-root specified in Equation (7):

$$\widetilde{\gamma}_2\left(k_m,k'_m,\varepsilon_0,\varepsilon_1\right)=H(\varepsilon_1)\frac{1}{2\pi}\int_{-\infty}^{\infty}dk_z\mathbf{i}\frac{k_z^2+k_m^2}{u_1}e^{\mathbf{i}(\varepsilon_1u_1-\varepsilon_0k_z)},\\ \texttt{where}:\quad u_1=\sqrt[?]{<k_z>^2+k_m^2-4k_m'^2}. \tag{68}$$

Given that k_z ranges from $-\infty$ to ∞, the square root in Equation (68) will have very different behavior if the sign of $k_m^2-4k_m'^2$ is different. If $k_m^2-4k_m'^2\geq 0$, the quantity $k_z^2+k_m^2-4k_m'^2$ which is inside the square root will always be positive for every $k_z\in(-\infty,\infty)$; otherwise, $k_z^2+k_m^2-4k_m'^2$ will be negative for small k_z.

1. First case: $k_m^2-4k_m'^2\geq 0$, we define $a\stackrel{\triangle}{=}\sqrt{k_m^2-4k_m'^2}$ and consequently $u_1=\sqrt{k_z^2+k_m^2-4k_m'^2}=\sqrt{k_z^2+a^2}$. Changing the integration variable to $\kappa\stackrel{\triangle}{=}k_z/a$ and using the function defined in Equation (36) we can convert Equation (68) to:

$$\begin{aligned}\widetilde{\gamma}_2\left(k_m,k'_m,\varepsilon_0,\varepsilon_1\right)&=\frac{1}{2\pi}H(\varepsilon_1)\int_{-\infty}^{\infty}dk_z\mathbf{i}\frac{k_z^2+k_m^2}{\sqrt[?]{<k_z>^2+a^2}}e^{\mathbf{i}(\varepsilon_1\sqrt[?]{<k_z>^2+a^2}-\varepsilon_0k_z)}\\ &=\frac{a^2}{2\pi}H(\varepsilon_1)\int_{-\infty}^{\infty}d\kappa\mathbf{i}\frac{\kappa^2e^{\mathbf{i}(a\varepsilon_1\sqrt[?]{<\kappa>^2+1}-a\varepsilon_0k_z)}}{\sqrt[?]{<\kappa>^2+1}}+\frac{k_m^2}{2\pi}H(\varepsilon_1)\int_{-\infty}^{\infty}d\kappa\mathbf{i}\frac{e^{\mathbf{i}(a\varepsilon_1\sqrt[?]{<\kappa>^2+1}-a\varepsilon_0k_z)}}{\sqrt[?]{<\kappa>^2+1}}\\ &=a^2H(\varepsilon_1)\xi_{-1,2}(a\varepsilon_1,a\varepsilon_0)-k_m^2H(\varepsilon_1)\xi_{-1,0}(a\varepsilon_1,a\varepsilon_0)\\ &\approx -a^2H(\varepsilon_1)\eta_{1,0}(a\varepsilon_0,a\varepsilon_1)+k_m^2H(\varepsilon_1)\eta_{-1,0}(a\varepsilon_0,a\varepsilon_1)\end{aligned} \tag{69}$$

[17] Note that in Equation (68), this definition of $\widetilde{\gamma}_2$ is the same as that of Equation (36) in Liu and Weglein (2008), but different from the $\widetilde{\gamma}_2$ of Equation (A.29) in Liu (2006), they differ by $\frac{1}{2\pi}$. Currently we feel it is better to put the $\frac{1}{2\pi}$ factor in the definition of $\widetilde{\gamma}_2$ since it belongs to the inverse Fourier transform over k_z. In Equation (67), the upper limit of the dz'' integral is changed to be z', which will introduce another factor of 2.

In the last step of the derivation above, we use the approximation relation in Equation (41).

2. Second case: $k_m^2-4k_m'^2<0$, we define $a\triangleq\sqrt{4k_m'^2-k_m^2}$ and consequently $u_1=\sqrt{k_z^2+k_m^2-4k_m'^2}=\sqrt[?]{<k_z>^2-a^2}$. Note that in this case, $k_z^2-a^2$ will change sign as k_z varies from $-\infty$ to ∞.

   Changing the integration variable to $\kappa\triangleq k_z/a$ and using the function relation in Equation (37), this integral can be expressed as:

$$
\begin{aligned}
\widetilde{\gamma}_2 &= \frac{1}{2\pi}H(\varepsilon_1)\int_{-\infty}^{\infty} dk_z \mathbf{i}\frac{k_z^2+k_m^2}{\sqrt[?]{<k_z>^2-a^2}}e^{\mathbf{i}(\varepsilon_1\sqrt[?]{<k_z>^2-a^2}-\varepsilon_0 k_z)} \\
&= \frac{a^2}{2\pi}H(\varepsilon_1)\int_{-\infty}^{\infty} d\kappa \mathbf{i}\frac{\kappa^2 e^{\mathbf{i}(a\varepsilon_1\sqrt[?]{<\kappa>^2-1}-a\varepsilon_0\kappa)}}{\sqrt[?]{<\kappa>^2-1}} + \frac{k_m^2}{2\pi}H(\varepsilon_1)\int_{|\kappa|\geq 1} d\kappa \mathbf{i}\frac{e^{\mathbf{i}(a\varepsilon_1\sqrt[?]{<\kappa>^2-1}-a\varepsilon_0\kappa)}}{\sqrt[?]{<\kappa>^2-1}} \\
&= \frac{a^2}{2\pi}H(\varepsilon_1)\int_{-\infty}^{\infty} d\kappa \frac{(\mathbf{i}\kappa)^2 e^{\mathbf{i}(a\varepsilon_1\sqrt[?]{<\kappa>^2-1}-a\varepsilon_0\kappa)}}{\mathbf{i}\sqrt[?]{<\kappa>^2-1}} - \frac{k_m^2}{2\pi}H(\varepsilon_1)\int_{-\infty}^{\infty} d\kappa \frac{e^{\mathbf{i}(a\varepsilon_1\sqrt[?]{<\kappa>^2-1}-a\varepsilon_0\kappa)}}{\mathbf{i}\sqrt[?]{<\kappa>^2-1}} \\
&= a^2 H(\varepsilon_1)\eta_{-1,2}(a\varepsilon_1, a\varepsilon_0) - k_m^2 H(\varepsilon_1)\eta_{-1,0}(a\varepsilon_1, a\varepsilon_0)
\end{aligned}
\tag{70}
$$

For the regular portion of $\widetilde{\gamma}_2$, the calculation scheme is as follows:

$$
\begin{aligned}
&= \frac{1}{8\pi^2}\int_{-\infty}^{\infty} dk_1 e^{\mathbf{i}k_1 x}\int_{-\infty}^{\infty} dk_2 e^{\mathbf{i}k_2 x}\int_{-\infty}^{\infty} dz_1 \widetilde{\alpha}_1(k_1, z_1+z)\int_{-\infty}^{\infty} dz_2 \widetilde{\alpha}_1(k_2, z_2+z) \\
&\quad \mathtt{sgn}(k_1k_2)H(k_1k_2z_1)H(z_1-z_2)H(-z_1-z_2) \\
&\quad \left\{ \begin{array}{l} 2(z_1^2+z_2^2)\sum\limits_{m=0}^{\infty}\frac{[-(\mathbf{i}k_1)(\mathbf{i}k_2)]^{m+2}[z_1z_2]^m}{m!(m+2)!} \\ +\left[(\mathbf{i}k_1)^2+(\mathbf{i}k_2)^2\right]\sum\limits_{m=0}^{\infty}\frac{[-(\mathbf{i}k_1)(\mathbf{i}k_2)z_1z_2]^m}{[m!]^2} \end{array} \right\}
\end{aligned}
\tag{71}
$$

8 Numerical examples for cascaded imaging operators

In this section we present the numerical examples of the three geological models with rapid lateral variation and big velocity contrast:

- The sphere model.

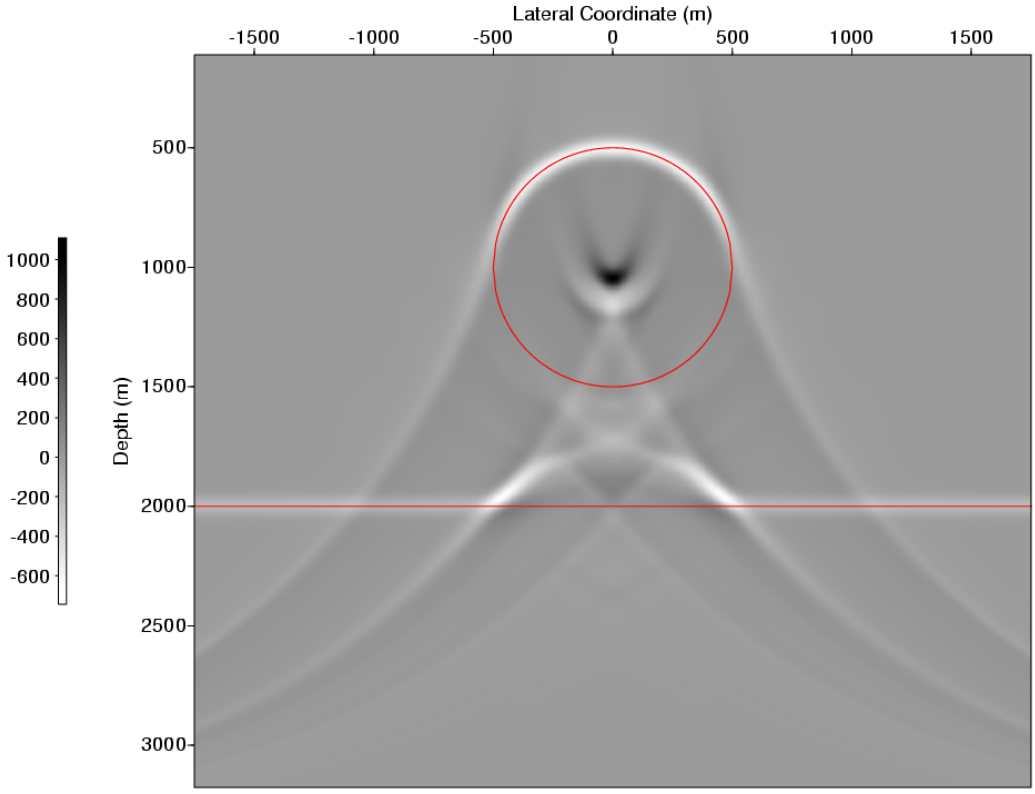

Figure 6: The linear image α_1 for the sphere model (i.e., without cascaded operation). Although the top of the sphere is correctly imaged, the bottom of the sphere is too narrow compared with the benchmark.

- The fault model.
- The salt model.

In all the images in this section:

- The red lines are benchmarks indicating the correct spatial location of the subsurface reflectors.
- The partial derivatives over z is taken to better show the locations of the reflectors.

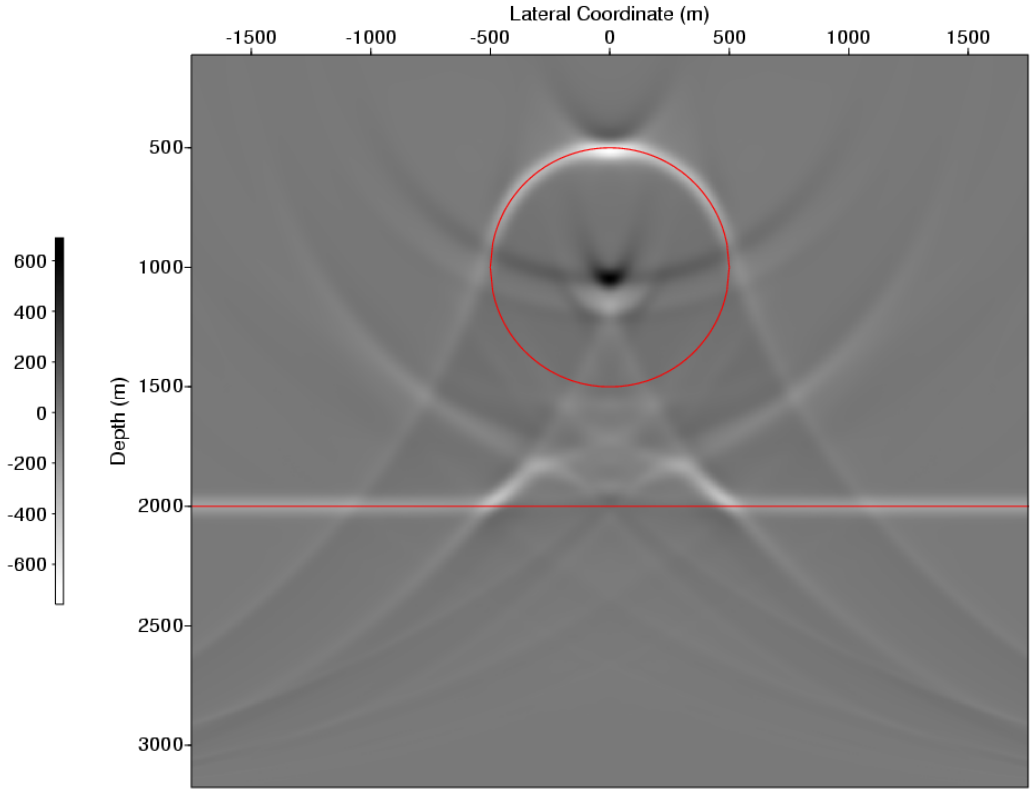

Figure 7: The cascaded image $\alpha_1^{\text{cascaded}}$ of the sphere model. The cascaded operation extends the image of the sphere bottom laterally to its full geological extent.

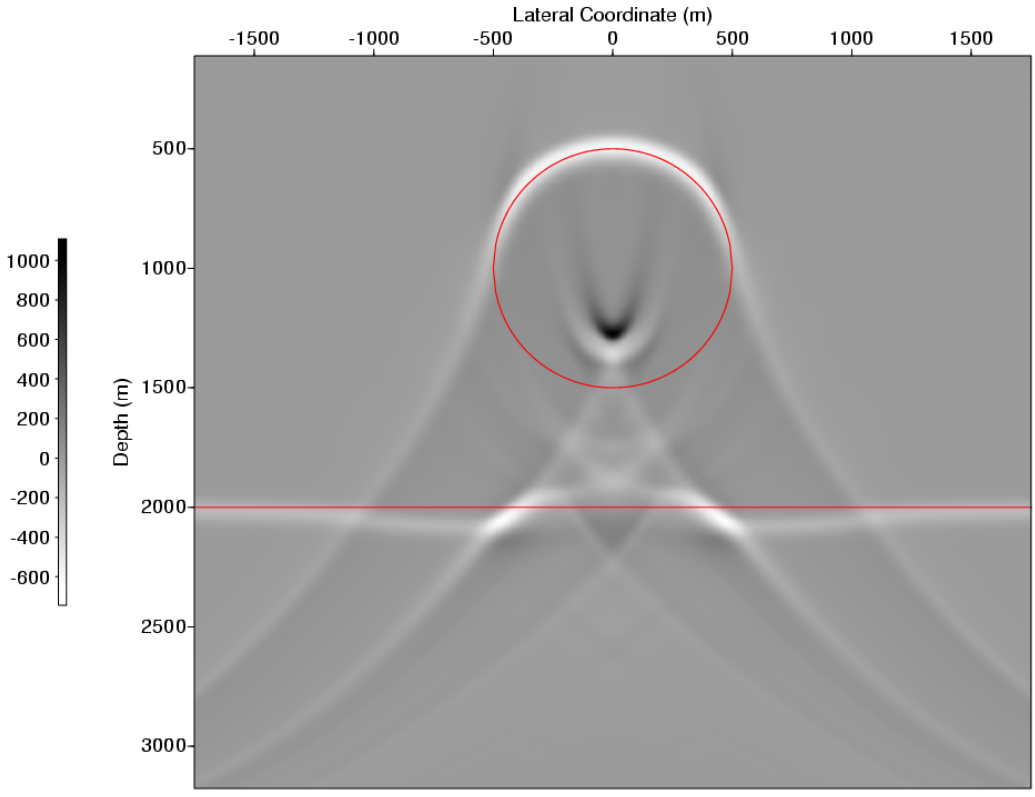

Figure 8: The sphere model, the HOIS image without cascaded operation.

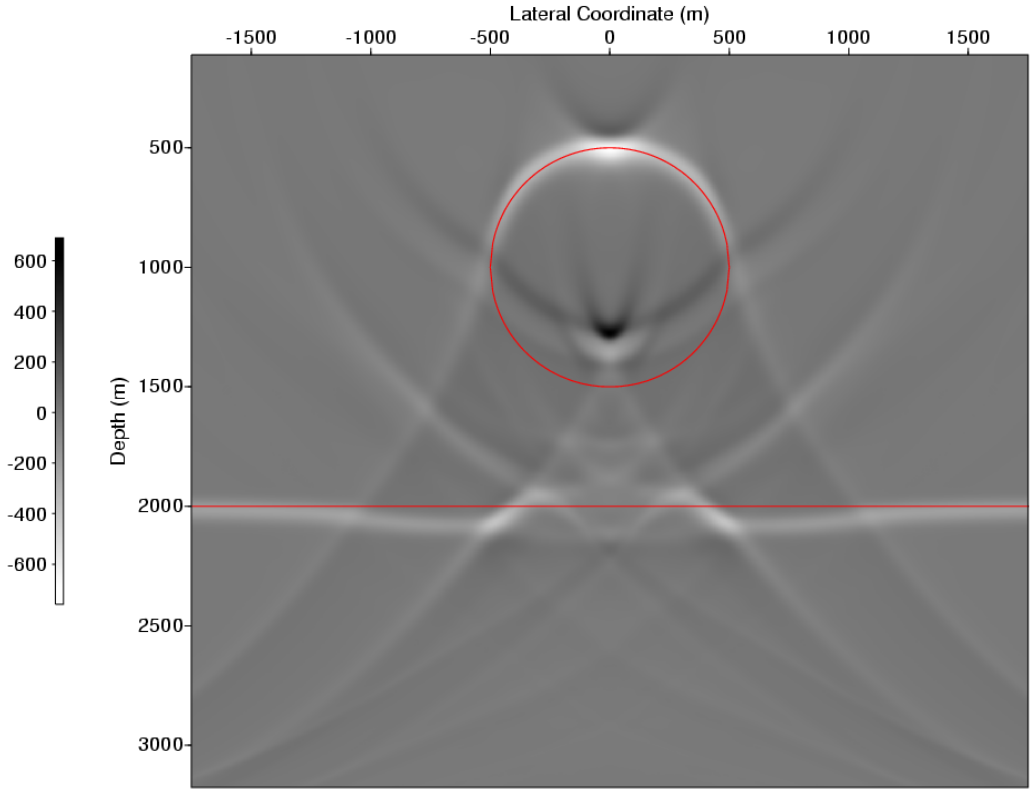

Figure 9: The sphere model, the HOIS with cascaded operation. The lateral location of the bottom of the sphere is much improved.

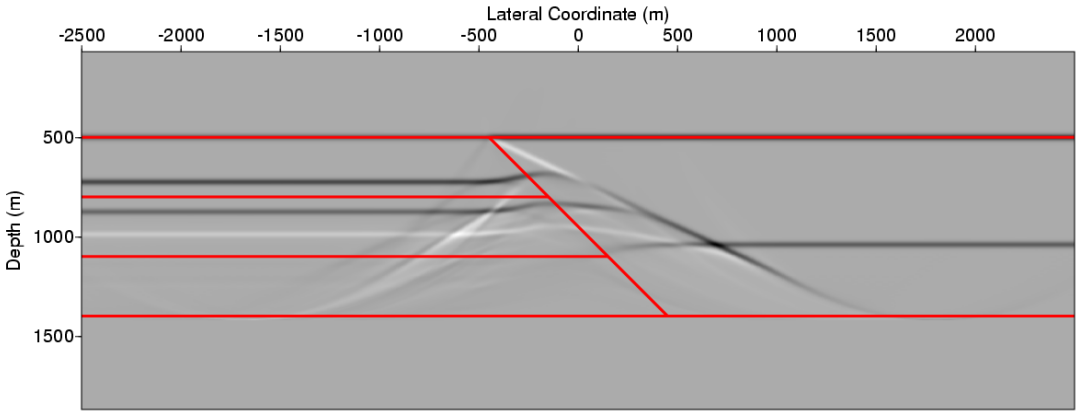

Figure 10: The linear image α_1 of the fault mode (without cascaded operation).

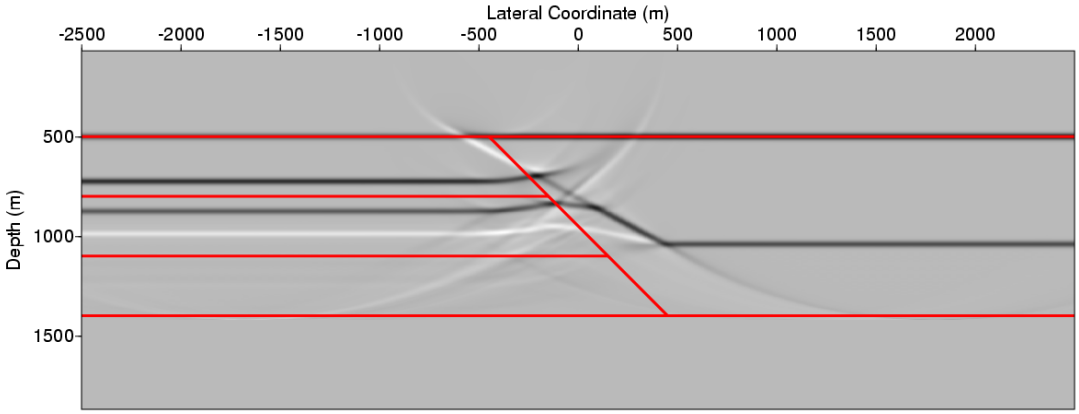

Figure 11: The cascaded image $\alpha_1^{\texttt{cascaded}}$ of the fault model.

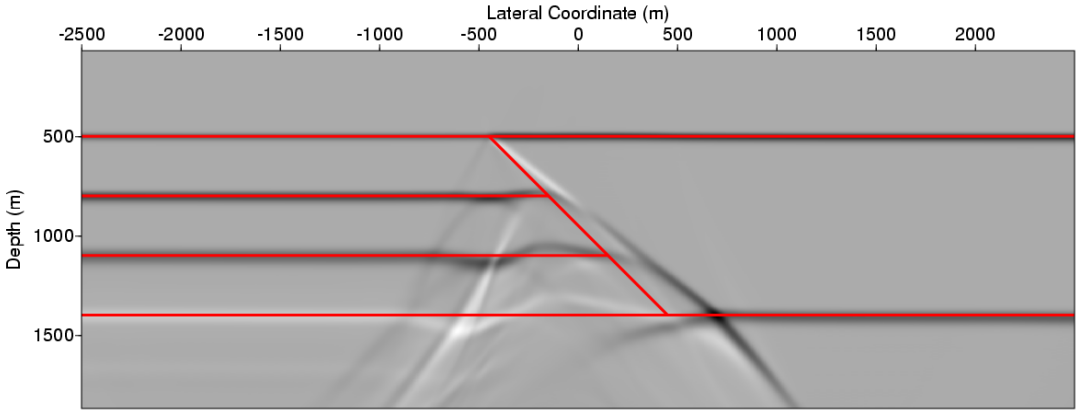

Figure 12: The fault model, the HOIS image without cascaded operation.

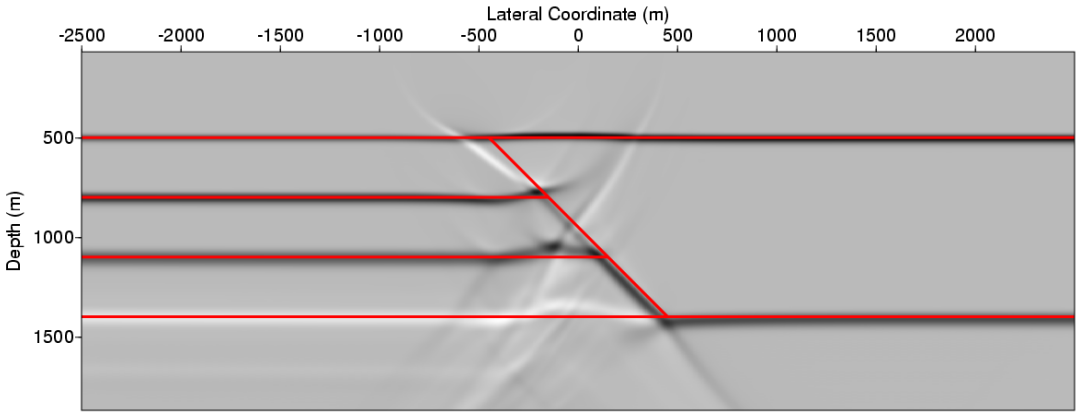

Figure 13: The fault model, the HOIS image with cascaded operation. Both the lateral and vertical location of the fault is much improved.

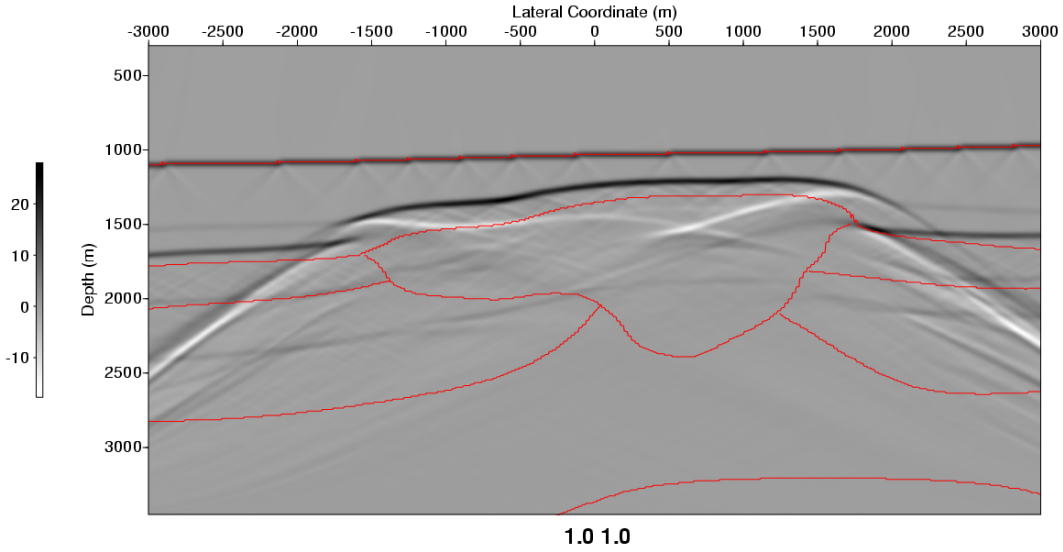

Figure 14: The linear image α_1 for the salt model (without ascaded operation).

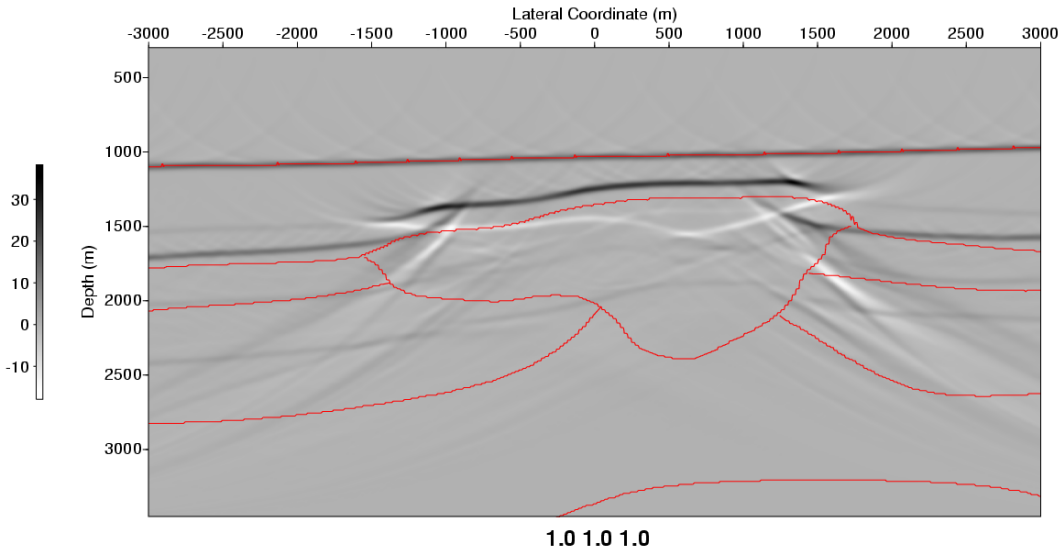

Figure 15: The cascaded image $\alpha_1^{\text{cascaded}}$ for the salt model. The image of the subsalt reflector becomes clearer.

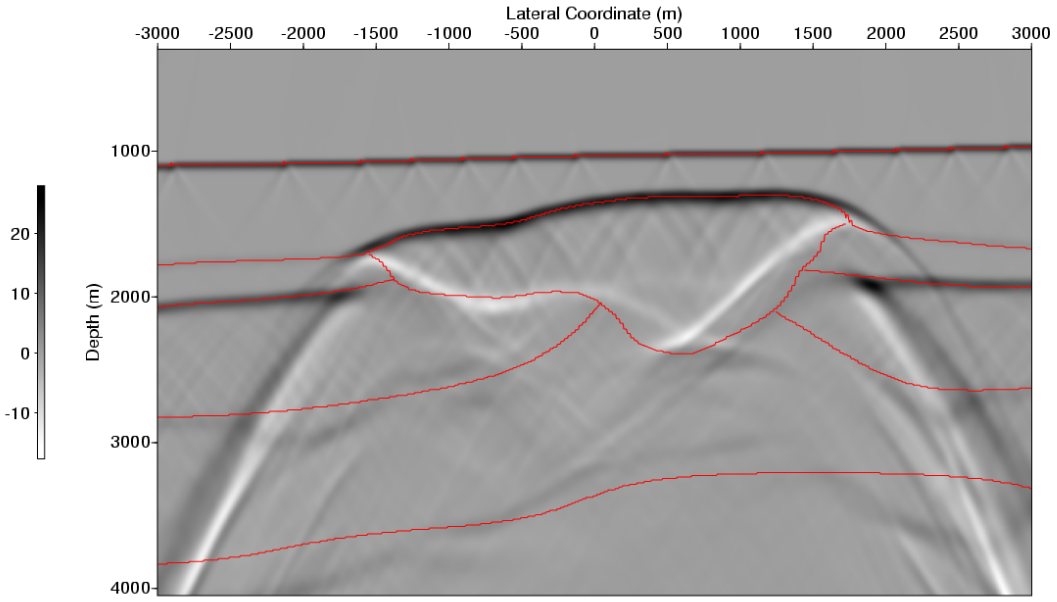

Figure 16: The salt model, the HOIS image without cascaded operation.

9 Conclusions and discussions

Towards more realism to accomodate the multiparameter nature of the Earth, a stable and velocity independent regularization algorithm is developed to harmonize the communication between bandlimited seismic data from different angles, a crucial step towards the goal of excluding the density contribution to the reflection coefficients. To address the multidimensional nature of the Earth with rapid lateral variation, accurate calculation of the seismic imaging operators for a laterally varying Earth has been developed for α_1 and α_2 and their relationship studied. The cascaded application of the α_1 imaging operator had been studied and demonstrated to provide added value for geological models with rapid lateration variations.

Acknowledgements

The authors would like to thank all M-OSRP members and sponsors. This work has been partially funded by NSFCMG award DMS-0327778 and DOE Basic Energy Sciences Award DE-FG02-05ER15697.

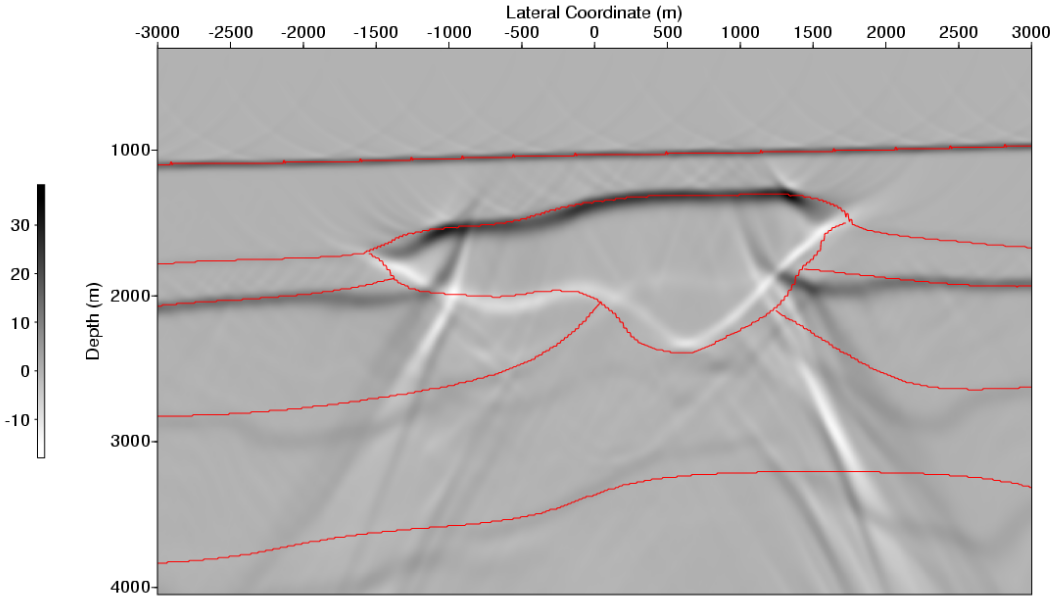

Figure 17: The salt model, the HOIS image without cascaded operation. The subsalt reflector is imaged to its correct location as indicated by the benchmark.

References

Abramowitz, Milton and Irene A. Stegun. *Handbook of Mathematical Functions.* New York: Dover, 1965.

Clayton, R. W. and R. H. Stolt. "A Born-WKBJ inversion method for acoustic reflection data." *Geophysics* 46 (1981): 1559–1567.

Innanen, Kristopher. A. *Reflector location using high-order inverse scattering series terms.* PhD thesis, 2004.

Jiang, S., A. B. Weglein, and S. A. Shaw. "Depth imaging without the velocity cares about the phase and amplitude information of events: Focusing on the use of the angle dependent amplitude information of events." *M-OSRP Annual Report* (2008).

Li, X. and A. B. Weglein. "ISS imaging for type 1 and type 2 AVO targets: analysis of forward and inverse series for target identification, part I." *2009 M-OSRP Annual Report* (2010).

Liang, H., A. B. Weglein, and X. Li. "Initial tests for the impact of matching and mismatching between the earth model and the processing model for ISS imaging and parameter estimation." *2009 M-OSRP Annual Report* (2009).

Liu, F. and A. B. Weglein. "Inverse scattering series velocity independent imaging in laterally verying media: analysis of transcendental integrals in the mathematics of multidimensional imaging." *M-OSRP Annual Report* (2008): 129–178.

Liu, F., A. B. Weglein, B. G. Nita, and K. A. Innanen. "Inverse scattering series for vertically and laterally varying media: application to velocity independent depth imaging." *M-OSRP Annual Report* 4 (2004).

Liu, Fang. *Multi-dimensional depth imaging without an adequate velocity model.* PhD thesis, University of Houston, 2006.

Morse, Philip M. and Herman Feshbach. *Methods of theoretical physics.* McGraw-Hill Book Co., 1953.

Ramirez, Adriana C. and Arthur B. Weglein. "An inverse scattering internal multiple elimination method: Beyond attenuation, a new algorithm and initial tests." *M-OSRP Annual Report* 4 (2005).

Shaw, S. A., A. B. Weglein, D. J. Foster, K. H. Matson, and R. G. Keys. "Isolation of a leading order depth imaging series and analysis of its convergence properties." *M-OSRP Annual Report* 2 (2003): 157–195.

Shaw, Simon. A. *An inverse scattering series algorithm for depth imaging of reflection data fro m a layered acoustic medium with an unknown velocity model.* PhD thesis, University of Houston, 2005.

Wang, Z., A. B. Weglein, and X. Li. "New capture of direct velocity independent depth imaging in a one-dimensional two-parameter acoustic earth." *2009 M-OSRP Annual Report* (2009).

Weglein, A. B., F. V. Araújo, P. M. Carvalho, R. H. Stolt, K. H. Matson, R. T. Coates, D. Corrigan, D. J. Foster, S. A. Shaw, and H. Zhang. "Inverse scattering series and seismic exploration." *Inverse Problems* 19 (2003): R27–R83.

Weglein, A. B., D. J. Foster, K. H. Matson, S. A. Shaw, P. M. Carvalho, and D. Corr igan. "Predicting the correct spatial location of reflectors without knowing or determining the precise medium and wave velocity: initial concept, algorithm and analytic and numerical e xample." *Journal of Seismic Exploration* 10 (2002): 367–382.

Weglein, A. B., F. A. Gasparotto, P. M. Carvalho, and R. H. Stolt. "An inverse-scattering series method for attenuating multiples in seismic reflection data." *Geophysics* 62 (1997): 1975–1989.

Weglein, A. B., K. H. Matson, D. J. Foster, P. M. Carvalho, D. Corrigan, and S. A. Shaw. "Imaging and inversion at depth without a velocity model: Theory, concepts a nd initial evaluation." *70th Annual Internat. Mtg., Soc. Expl. Geophys., Expanded Abstracts.* . Soc. Expl. Geophys., 2000. 1016–1019.

X. Li, S. Jiang,F. Liu and A. B. Weglein. "Depth imaging without the velocity cares about the phase and amplitude information of events: Focusing on the use of the angle dependent amplitude information of events." *M-OSRP Annual Report* (2008).

Zhang, H. *Direct non-linear acoustic and elastic inversion: Towards fundamentally new comprehensive and realistic target identification.* PhD thesis, University of Houston, 2006.

Zhang, H. and A. B. Weglein. "Target identification using the inverse scattering series: inversion of large-contrast, variable velocity and density acoustic media." *M-OSRP Annual Report* 2 (2003).

Zhang, H. and A. B. Weglein. "Target identification using the inverse scattering series: data requirements for the direct inversion of large-contrast, inhomogeneous elastic media." *M-OSRP Annual Report* 3 (2004).

Zhang, H., A. B. Weglein, and R. G. Keys. "Velocity independent depth imaging and non-linear direct target identification for 1D elastic media: testing and evaluation for application to non-linear AVO, using only PP data." *M-OSRP Annual Report* 4 (2005).

10 Appendix A: Some basic notations and conventions of Radon transform

Radon transform, or slant stacking, is commonly called $\tau - p$ transform in seismic exploration where τ is the vertical time and p is the slope. The Radon transform of a function $f(x,t)$ into (τ,p) domain, denoted as $F(\tau,p)$, is:

$$F(\tau,p) = \int_{-\infty}^{\infty} f(x,\tau+px)dx. \tag{72}$$

Note that for $p \neq 0$, $\tau + px$ may occur somewhere in between the original sampling grids. In other words, interpolation between grids may become necessary. This interpolation can be done via Fast Fourier transform:

$$f(x,\tau+px) = \frac{1}{2\pi}\int_{-\infty}^{\infty} \widetilde{f}(x,\omega)e^{-\mathbf{i}\omega(\tau+px)}d\omega \qquad \texttt{where} \qquad \widetilde{f}(x,\omega) = \int_{-\infty}^{\infty} f(x,t)e^{\mathbf{i}\omega t}. \tag{73}$$

Consequently, the Radon transform in Equation (72) can be written as:

$$F(\tau,p) = \int_{-\infty}^{\infty} f(x,\tau+px)dx = \frac{1}{2\pi}\int_{-\infty}^{\infty} e^{-\mathbf{i}\omega\tau}\int_{-\infty}^{\infty} dx\widetilde{f}(x,\omega)e^{-\mathbf{i}\omega px}. \tag{74}$$

Note that the last in Equation (74) is actually a Fourier transform over x: $\int_{-\infty}^{\infty} dx\widetilde{f}(x,\omega)e^{-\mathbf{i}kx}$ in the frequency domain where the wavenumber k is set to be proportional to the frequency, $k = \omega p$.

If in Equation (74) the last integral is denoted as $\widetilde{\widetilde{f}}(p,\omega) \triangleq \int_{-\infty}^{\infty} dx\widetilde{f}(x,\omega)e^{-\mathbf{i}\omega px}$, the Radon transform can be implemented as:

$$\begin{aligned} F(\tau,p) &= \int_{-\infty}^{\infty} f(x,\tau+px)dx = \frac{1}{2\pi}\int_{-\infty}^{\infty} e^{-\mathbf{i}\omega\tau}\int_{-\infty}^{\infty} dx\widetilde{f}(x,\omega)e^{-\mathbf{i}\omega px} \\ &= \int_{-\infty}^{\infty} f(x,\tau+px)dx = \frac{1}{2\pi}\int_{-\infty}^{\infty} e^{-\mathbf{i}\omega\tau}\widetilde{\widetilde{f}}(p,\omega). \end{aligned} \tag{75}$$

Note that in Equation (75), if p is fixed, the last integral is an inverse Fourier transform from ω to the vertical time τ domain.

11 Appendix B: The seismic data in pseudo-depth domain

In this appendix, we present our best understanding of the seismic data in inverse scattering series parameter inversion, i.e., the data described by Zhang (2006); Jiang et al. (2008); X. Li and Weglein (2008); Li and Weglein (2010); Wang et al. (2009); Liang et al. (2009).

For simplicity, let's consider a 1D case where the recorded data is a function of time $d(t)$[18], but the data used in Zhang (2006); Jiang et al. (2008); X. Li and Weglein (2008); Li and Weglein (2010); Wang et al. (2009); Liang et al. (2009) are all a function of depth $D(z)$[19]. How are they connected?

First of all, an event in the time domain, its arrival time; for example, t is converted to pseudo depth $z = \frac{c_0}{t}$ where c_0 is the reference velocity. This can be achieved by letting them be equal in the Fourier domain $\widetilde{D}(k_z) = \widetilde{D}(2\omega/c_0) = \widetilde{d}(\omega)$, where their definition in the Fourier domain are:

$$\widetilde{d}(\omega) = \int_{-\infty}^{\infty} dt e^{\mathbf{i}\omega t} d(t), \tag{76}$$

and

$$\widetilde{D}(k_z) = \int_{-\infty}^{\infty} dz e^{\mathbf{i}k_z z} D(z). \tag{77}$$

Consequently, $D(z)$ can be linked to $d(t)$ as follows $z = c_0 t/2$, $t = 2z/c_0$:

$$\begin{aligned} D(z) &= \frac{1}{2\pi}\int_{-\infty}^{\infty} dk_z e^{-\mathbf{i}k_z z}\widetilde{D}(k_z) = \frac{1}{2\pi}\int_{-\infty}^{\infty} e^{-\mathbf{i}(2\omega/c_0)z}\widetilde{D}(2\omega/c_0)d(2\omega/c_0) \\ &= \frac{2}{c_0}\frac{1}{2\pi}\int_{-\infty}^{\infty} e^{-\mathbf{i}\omega(2z/c_0)}\widetilde{D}(2\omega/c_0)d\omega = \frac{2}{c_0}\frac{1}{2\pi}\int_{-\infty}^{\infty} e^{-\mathbf{i}\omega(2z/c_0)}\widetilde{d}(\omega)d\omega \\ &= \frac{2}{c_0}d(2z/c_0) \end{aligned} \tag{78}$$

From Equation (78), the data in the depth domain can be obtained from data in the time domain by stretching the argument by a factor $\frac{c_0}{2}$ and squeezed by its reciprocal $\frac{2}{c_0}$. Consequently, the total area remain the same: $\int_{-\infty}^{\infty} d(t)dt = \int_{-\infty}^{\infty} D(z)dz$.

[18] We used the lower-case d to denote data in the time domain.
[19] We use the upper-case D to denote data in depth.

12 Appendix C: General relation of $\eta_{m,n}(u,v)$

This section contains analytic results of $\eta_{-1,0}$, $\eta_{-1,2}$ and $\eta_{1,0}$ obtained by mountain top expansion. For $u>0$, $-\infty<v<\infty$:

$$\begin{aligned}\eta_{-1,0}(u,v)&=\frac{1}{2\pi}\int_{-\infty}^{\infty}dk_z\frac{e^{\mathbf{i}[u\sqrt[?]{<k_z>^2-1}-vk_z]}}{\mathbf{i}\sqrt[?]{<k_z>^2-1}}=-H(v-u)J_0\left(\sqrt{v^2-u^2}\right)\\&=-H(v-u)\sum_{m=0}^{\infty}\frac{1}{[m!]^2}\left(\frac{u^2-v^2}{4}\right)^m\end{aligned}\tag{79}$$

$$\begin{aligned}&\eta_{-1,2}(u,v)=\frac{1}{2\pi}\int_{-\infty}^{\infty}dk_z\frac{(-\mathbf{i}k_z)^2e^{\mathbf{i}[u\sqrt[?]{<k_z>^2-1}-vk_z]}}{\mathbf{i}\sqrt[?]{<k_z>^2-1}}=\frac{\partial^2\eta_{-1,0}(u,v)}{\partial v^2}\\&=-\delta'(v-u)+\frac{v}{2}\delta(v-u)\\&\quad-H(v-u)\left[\frac{u^2+v^2}{4}\sum_{m=0}^{\infty}\frac{[(u^2-v^2)/4]^m}{m!(m+2)!}-\frac{1}{2}\sum_{m=0}^{\infty}\frac{[(u^2-v^2)/4]^m}{[m!]^2}\right]\\&=-\delta'(v-u)+\frac{v}{2}\delta(v-u)-H(v-u)\left[\frac{u^2+v^2}{u^2-v^2}J_2\left(\sqrt{u^2-v^2}\right)-\frac{1}{2}J_0\left(\sqrt{u^2-v^2}\right)\right]\end{aligned}\tag{80}$$

$$\begin{aligned}&\eta_{1,0}(u,v)=\frac{1}{2\pi}\int_{-\infty}^{\infty}dk_z\left[\mathbf{i}\sqrt[?]{<k_z>^2-1}\right]e^{\mathbf{i}[u\sqrt[?]{<k_z>^2-1}-vk_z]}=\frac{\partial^2\eta_{-1,0}(u,v)}{\partial u^2}\\&=-\delta'(v-u)+\frac{u}{2}\delta(v-u)\\&\quad-H(v-u)\left[\frac{u^2+v^2}{4}\sum_{m=0}^{\infty}\frac{[(u^2-v^2)/4]^m}{m!(m+2)!}+\frac{1}{2}\sum_{m=0}^{\infty}\frac{[(u^2-v^2)/4]^m}{[m!]^2}\right]\\&=-\delta'(v-u)+\frac{v}{2}\delta(v-u)-H(v-u)\left[\frac{u^2+v^2}{u^2-v^2}J_2\left(\sqrt{u^2-v^2}\right)+\frac{1}{2}J_0\left(\sqrt{u^2-v^2}\right)\right]\end{aligned}\tag{81}$$

Note: A derivation of the HOIS closed form

Z. Wang, A. B. Weglein and F. Liu

Abstract

The high order imaging subseries closed form (HOIS, Liu (2006)) is a critical advancement for imaging using inverse scattering series (ISS) (Weglein et al., 2002) from the leading order imaging subseries closed form (LOIS, Shaw et al. (2004)). It not only captures more terms than the LOIS closed form, but also avoids the misusing of the deeper events for the location of the shallow ones (Zhang et al. (2006)). However, the HOIS closed form is mainly a conjecture from intuition and there is no clear derivation. It is hard to go further from HOIS closed form for 1D medium to more general cases, e.g., medium with lateral variations or acoustic/elastic medium with not only velocity variations. In this note, we show a clear derivation of the HOIS closed form, which proves this conjecture and provides a method for future research.

1 Introduction

Conventional imaging algorithms use the velocity underneath to do imaging, which is a big challenge especially when the medium is complex. The inverse scattering series aims to perform imaging without the subsurface information. In an Earth model that only allows variations in velocity, two different inverse scattering imaging subseries with different degrees of imaging capture and capability closed forms have been identified and tested in M-OSRP: LOIS in Shaw et al. (2004) with a detail derivation:

$$\alpha^{LOIS}(z) = \alpha_1\left(z - \frac{1}{2}\int_{-\infty}^{z}\alpha_1(u)du\right) \tag{1}$$

and HOIS in Liu (2006) without a derivation, and mainly conjectured from the intuition:

$$\alpha^{HOIS}\left(z + \frac{1}{2}\int_{-\infty}^{z}du\frac{\alpha_1(u)}{1-0.25\alpha_1(u)}\right) = \alpha_1(z). \tag{2}$$

The HOIS closed form not only captures more terms in ISS than LOIS, it also avoids the misusing of the deeper events for the shift of the shallow ones (Zhang et al. (2006)) which can be explained as following:

(1). In LOIS, the value of α^{LOIS} at depth z equals the value of α_1 at depth $z-\frac{1}{2}\int_{-\infty}^{z}\alpha_1(u)du = z_b'$, if $z > z_b'$ which often is true, $\frac{1}{2}\int_{-\infty}^{z}\alpha_1(u)du$ means it needs to use events from $-\infty$ to z (deeper than z_b') to help the location of event at z_b' (shown in the left panel of Fig. 1);

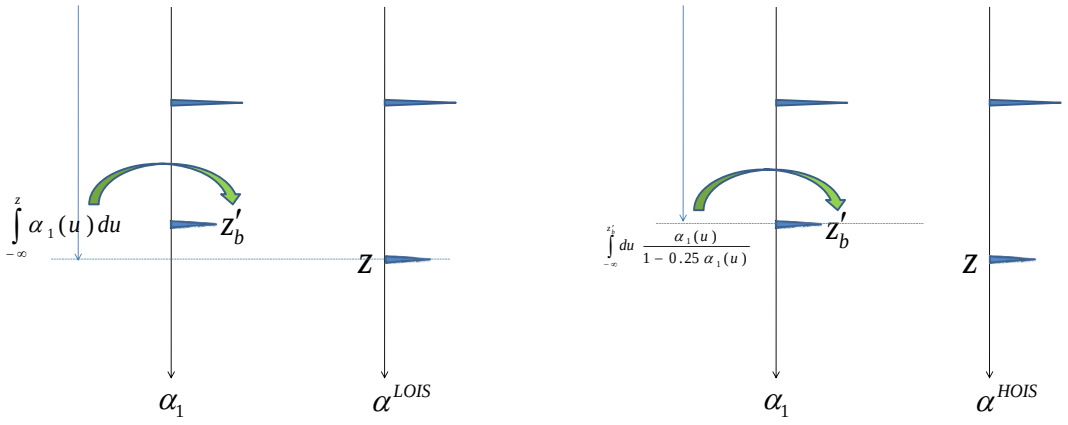

Figure 1: A schematic of the relationships between the locations of an event and the events used to do the shift in LOIS (left panel) and HOIS (right panel).

(2). While for the HOIS, the value of α^{HOIS} at depth $z = z'_b + \frac{1}{2}\int_{-\infty}^{z'_b} du \frac{\alpha_1(u)}{1-0.25\alpha_1(u)}$ equals the value of α_1 at depth z'_b, so it uses events from $-\infty$ to z'_b to help the location of event at z'_b (shown in the right panel of Fig. 1).

In this note, we derived the HOIS closed form in two steps: the first step, by capturing more terms than LOIS, we derived the Shifted LOIS closed form (SLOIS) (Zhang et al. (2006)):

$$\alpha^{SLOIS}\left(z + \frac{1}{2}\int_{-\infty}^{z} \alpha_1(u)du\right) = \alpha_1(z); \tag{3}$$

The second step was deriving HOIS.

2 Review of deriving the LOIS closed form

In Shaw et al. (2004), $\alpha_2(z)$ and $\alpha_3(z)$ for the 1D constant density variable velocity acoustic medium were calculated:

$$\begin{aligned} \alpha_2(z) &= -\frac{1}{2}\left(\alpha_1^2(z) + \left[\frac{d\alpha_1(z)}{dz}\right]\int_{-\infty}^{z} \alpha_1(u)du\right) \\ \alpha_3(z) &= \frac{3}{16}\alpha_1^3(z) + \frac{3}{4}\alpha_1(z)\left[\frac{d\alpha_1(z)}{dz}\right]\left(\int_{-\infty}^{z} \alpha_1(u)du\right) \\ &\quad + \frac{1}{8}\left[\frac{d^2\alpha_1(z)}{dz^2}\right]\left(\int_{-\infty}^{z} \alpha_1(u)du\right)^2 \end{aligned} \tag{4}$$

$$-\frac{1}{8}\left[\frac{d\alpha_1(z)}{dz}\right]\left(\int_{-\infty}^{z}\alpha_1^2(u)du\right)$$
$$-\frac{1}{16}\int_{-\infty}^{z}\int_{-\infty}^{z}\left[\frac{d\alpha_1(u)}{du}\right]\left[\frac{d\alpha_1(v)}{dv}\right]\alpha_1(u+v-z)dudv \quad (5)$$

The leading-order terms were taken out and the LOIS closed form was derived:

$$\begin{aligned}\alpha^{LOIS}(z) &= \alpha_1(z)-\frac{1}{2}\left[\frac{d\alpha_1(z)}{dz}\right]\left(\int_{-\infty}^{z}\alpha_1(u)du\right)\\ &\quad+\frac{1}{8}\left[\frac{d^2\alpha_1(z)}{dz^2}\right]\left(\int_{-\infty}^{z}\alpha_1(u)du\right)^2+\cdots\\ &= \sum_{n=0}^{\infty}\frac{1}{n!}\left[\frac{d^n\alpha_1(z)}{dz^n}\right]\left(-\frac{1}{2}\int_{-\infty}^{z}\alpha_1(u)du\right)^n\\ &= \alpha_1\left(z-\frac{1}{2}\int_{-\infty}^{z}\alpha_1(u)du\right) \quad (6)\end{aligned}$$

Here the n^{th} term comes from the n^{th} order term $\alpha_n(z)$.

3 Derivation of the Shifted LOIS closed form

Next, we will show the derivation of SLOIS:

$$\alpha^{SLOIS}\left(z+\frac{1}{2}\int_{-\infty}^{z}\alpha_1(u)du\right)=\alpha_1(z). \quad (7)$$

If expanding L.H.S. of Equation 7 in the same way as for the LOIS closed form, we will get:

$$\begin{aligned}\alpha_1(z) &= \alpha^{LOIS}\left(z+\frac{1}{2}\int_{-\infty}^{z}\alpha_1(u)du\right)\\ &= \sum_{n=0}^{\infty}\left(\frac{1}{n!}\right)\left[\frac{d^n\alpha^{LOIS}(z)}{dz^n}\right]\left(\frac{1}{2}\int_{-\infty}^{z}\alpha_1(u)du\right)^n\\ &= \alpha^{LOIS}(z)+\sum_{n=1}^{\infty}\left(\frac{(1/2)^n}{n!}\right)\left[\frac{d^n[\alpha_1(z)+\alpha_2(z)+\alpha_3(z)+\cdots]}{dz^n}\right]\left(\int_{-\infty}^{z}\alpha_1(u)du\right)^n \quad (8)\end{aligned}$$

$$\alpha^{LOIS}(z)=\alpha_1(z)-\sum_{n=1}^{\infty}\left(\frac{(1/2)^n}{n!}\right)\left[\frac{d^n[\alpha_1(z)+\alpha_2(z)+\alpha_3(z)+\cdots]}{dz^n}\right]\left(\int_{-\infty}^{z}\alpha_1(u)du\right)^n \quad (9)$$

This gives us an indication that maybe we should keep the terms with the derivative of $\alpha_i(i\geq 2)$, instead of expanding it into α_1. For example, the equation for α_3 is:

$$G_0k_0^2\alpha_3G_0=-G_0k_0^2\alpha_2G_0k_0^2\alpha_1G_0-G_0k_0^2\alpha_1G_0k_0^2\alpha_2G_0-G_0k_0^2\alpha_1G_0k_0^2\alpha_1G_0k_0^2\alpha_1G_0, \quad (10)$$

and separate it into parts $\alpha_{31},\ \alpha_{32}$ and α_{33}, which are:

$$G_0k_0^2(\alpha_{31}+\alpha_{32})G_0 = -G_0k_0^2\alpha_2G_0k_0^2\alpha_1G_0 - G_0k_0^2\alpha_1G_0k_0^2\alpha_2G_0, \tag{11}$$

$$G_0k_0^2\alpha_{33}G_0 = -G_0k_0^2\alpha_1G_0k_0^2\alpha_1G_0k_0^2\alpha_1G_0. \tag{12}$$

The parts with $\frac{d\alpha_i}{dz}$ $(i \geq 2)$ are $\alpha_{31}+\alpha_{32}$, which has the solution:

$$\alpha_{31}+\alpha_{32} = -\alpha_1(z)\alpha_2(z) - \frac{1}{2}\left[\frac{d\alpha_1(z)}{dz}\right]\int_{-\infty}^{z}\alpha_2(u)du - \frac{1}{2}\left[\frac{d\alpha_2(z)}{dz}\right]\int_{-\infty}^{z}\alpha_1(u)du. \tag{13}$$

Expand α_2 into α_1 except $\frac{d\alpha_2}{dz}$ and then α_3 will become:

$$\begin{aligned}
\alpha_3(z) &= \alpha_{31}+\alpha_{32}+\alpha_{33} \\
&= \frac{3}{16}\alpha_1^3(z) - \frac{1}{2}\left[\frac{d\alpha_2(z)}{dz}\right]\int_{-\infty}^{z}\alpha_1(u)du \\
&\quad -\frac{1}{8}\left[\frac{d^2\alpha_1(z)}{dz^2}\right]\left(\int_{-\infty}^{z}\alpha_1(u)du\right)^2 - \frac{1}{8}\left[\frac{d\alpha_1(z)}{dz}\right]\left(\int_{-\infty}^{z}\alpha_1^2(u)du\right) \\
&\quad -\frac{1}{16}\int_{-\infty}^{z}\int_{-\infty}^{z}\left[\frac{d\alpha_1(u)}{du}\right]\left[\frac{d\alpha_1(v)}{dv}\right]\alpha_1(u+v-z)dudv
\end{aligned} \tag{14}$$

Do the same for the i^{th} order term:

$$G_0k_0^2(\alpha_{i1}+\alpha_{i2})G_0 = -G_0k_0^2\alpha_1G_0k_0^2\alpha_{i-1}G_0 - G_0k_0^2\alpha_{i-1}G_0k_0^2\alpha_1G_0. \tag{15}$$

In the solution:

$$\alpha_{i1}(z)+\alpha_{i2}(z) = -\alpha_1(z)\alpha_{i-1}(z) - \frac{1}{2}\left[\frac{d\alpha_1(z)}{dz}\right]\int_{-\infty}^{z}\alpha_{i-1}(u)du - \frac{1}{2}\left[\frac{d\alpha_{i-1}(z)}{dz}\right]\int_{-\infty}^{z}\alpha_1(u)du, \tag{16}$$

keep $\frac{d\alpha_{i-1}}{dz}$, not expanding it into $\alpha_1(z)$.

The terms:

$$-\frac{1}{2}\left[\frac{d\alpha_{i-1}(z)}{dz}\right]\int_{-\infty}^{z}\alpha_1(u)du$$

are similar to the second order term in LOIS and if summing them up, we can get:

$$\begin{aligned}
-\frac{1}{2}\sum_{i=1}^{\infty}\left[\frac{d\alpha_i(z)}{dz}\right]\int_{-\infty}^{z}\alpha_1(u)du &= -\frac{1}{2}\left[\frac{d\sum_{i=1}^{\infty}\alpha_i(z)}{dz}\right]\int_{-\infty}^{z}\alpha_1(u)du \\
&= -\frac{1}{2}\left[\frac{d\alpha(z)}{dz}\right]\int_{-\infty}^{z}\alpha_1(u)du
\end{aligned} \tag{17}$$

Do the same for the other terms in the LOIS:

For n^{th} term $\frac{(1/2)^n}{n!}\left[\frac{d^n\alpha_1(z)}{dz^n}\right]\left(\int_{-\infty}^{z}\alpha_1(u)du\right)^n$ $(n\geq 1)$ in LOIS, we solve equations as following:

$$G_0k_0^2[\alpha_m]_{part}G_0 = -\sum G_0k_0^2\Theta_1G_0\cdots k_0^2\Theta_{n+1}G_0 \qquad (m\geq n+1) \tag{18}$$

Here, in $\theta_1,\theta_2,\cdots,\theta_{n+1}$, only one of them equals α_{m-n} and the others are all α_1. The $\sum$ is summing over all the different combinations and $[\alpha_m]_{part}$ means it is a part of α_m. Then summing up the following terms:

$$-\frac{(1/2)^n}{n!}\left[\frac{d^n\alpha_i(z)}{dz^n}\right]\left(\int_{-\infty}^{z}\alpha_1(u)du\right)^n \qquad (i=m-n\geq 1)$$

over all m (which is the same as summing over i):

$$\begin{aligned}-\frac{(1/2)^n}{n!}\sum_{i=1}^{\infty}\left[\frac{d^n\alpha_i(z)}{dz^n}\right]\left(\int_{-\infty}^{z}\alpha_1(u)du\right)^n &= -\frac{(1/2)^n}{n!}\left[\frac{d^n\sum_{i=1}^{\infty}\alpha_i(z)}{dz^n}\right]\left(\int_{-\infty}^{z}\alpha_1(u)du\right)^n \\ &= -\frac{(1/2)^n}{n!}\left[\frac{d^n\alpha(z)}{dz^n}\right]\left(\int_{-\infty}^{z}\alpha_1(u)du\right)^n \end{aligned} \tag{19}$$

It is the n^{th}-order term in SLOIS and is from summing over the terms similar to n^{th}-order term in LOIS. So the SLOIS is:

$$\begin{aligned}\alpha^{LOIS}(z) &= \alpha_1(z)-\frac{1}{2}\left[\frac{d\alpha(z)}{dz}\right]\left(\int_{-\infty}^{z}\alpha_1(u)du\right) \\ &\quad -\frac{1}{8}\left[\frac{d^2\alpha(z)}{dz^2}\right]\left(\int_{-\infty}^{z}\alpha_1(u)du\right)^2-\cdots\end{aligned} \tag{20}$$

Notice that, different from the LOIS, the n^{th}-order term of SLOIS α_n^{SLOIS} is contributed by not only α_n but also terms $\alpha_m(m>n)$.

The terms, except the leading-order, would contribute to the $\alpha^{SLOIS}(z)$, so we would remove the others and just keep the leading-order terms in α on the right hand side:

$$\begin{aligned}\alpha^{SLOIS}(z) &= \alpha_1(z)-\frac{1}{2}\left[\frac{d\alpha^{SLOIS}(z)}{dz}\right]\left(\int_{-\infty}^{z}\alpha_1(u)du\right) \\ &\quad -\frac{1}{8}\left[\frac{d^2\alpha^{SLOIS}(z)}{dz^2}\right]\left(\int_{-\infty}^{z}\alpha_1(u)du\right)^2-\cdots\end{aligned} \tag{21}$$

$$\begin{aligned}\alpha_1(z) &= \alpha^{SLOIS}(z)+\frac{1}{2}\left[\frac{d\alpha^{SLOIS}(z)}{dz}\right]\left(\int_{-\infty}^{z}\alpha_1(u)du\right) \\ &\quad +\frac{1}{8}\left[\frac{d^2\alpha^{SLOIS}(z)}{dz^2}\right]\left(\int_{-\infty}^{z}\alpha_1(u)du\right)^2+\cdots \\ &= \sum_{n=0}^{\infty}\left(\frac{(1/2)^n}{n!}\right)\left[\frac{d^n\alpha^{SLOIS}(z)}{dz^n}\right]\left(\int_{-\infty}^{z}\alpha_1(u)du\right)^n\end{aligned}$$

$$= \alpha^{SLOIS}\left(z + \frac{1}{2}\int_{-\infty}^{z}\alpha_1(u)du\right) \tag{22}$$

This is the SLOIS closed form. As we mentioned in the beginning, it avoids the misuse of the deeper events for the location of the shallow ones.

4 Derivation of the HOIS closed form

Next, we will derive the HOIS closed form:

$$\alpha^{HOIS}\left(z + \frac{1}{2}\int_{-\infty}^{z} du\frac{\alpha_1(u)}{1-0.25\alpha_1(u)}\right) = \alpha(z). \tag{23}$$

In the previous section, we have already shown that if we keep all the terms with $\frac{d\alpha_i}{dz}(i \geq 2)$, then the expressions for α_2 and α_3 are:

$$\alpha_2(z) = -\frac{1}{2}\left(\alpha_1^2(z) + \left[\frac{d\alpha_1(z)}{dz}\right]\int_{-\infty}^{z}\alpha_1(u)du\right) \tag{24}$$

$$\begin{aligned}\alpha_3(z) = {} & \frac{3}{16}\alpha_1^3(z) - \frac{1}{2}\left[\frac{d\alpha_2(z)}{dz}\right]\int_{-\infty}^{z}\alpha_1(u)du \\ & -\frac{1}{8}\left[\frac{d^2\alpha_1(z)}{dz^2}\right]\left(\int_{-\infty}^{z}\alpha_1(u)du\right)^2 - \frac{1}{8}\left[\frac{d\alpha_1(z)}{dz}\right]\left(\int_{-\infty}^{z}\alpha_1^2(u)du\right) \\ & -\frac{1}{16}\int_{-\infty}^{z}\int_{-\infty}^{z}\left[\frac{d\alpha_1(u)}{du}\right]\left[\frac{d\alpha_1(v)}{dv}\right]\alpha_1(u+v-z)dudv\end{aligned} \tag{25}$$

For α_3, the first term is inversion-only and the fifth term is for the multiple. The second and third terms are for imaging and have already been included in the SLOIS closed form. Now we consider the fourth term the same as we have shown before. Regarding the differential part, there will be higher terms to compute α_1 to α in the derivative part, that is:

$$-\frac{1}{8}\left[\frac{d\alpha(z)}{dz}\right]\left(\int_{-\infty}^{z}\alpha_1^2(u)du\right).$$

which and the second term in LOIS:

$$-\frac{1}{2}\left[\frac{d\alpha(z)}{dz}\right]\int_{-\infty}^{z}\alpha_1(u)du$$

are the first two terms of:

$$-\frac{1}{2}\left[\frac{d\alpha(z)}{dz}\right]\int_{-\infty}^{z} du\frac{\alpha_1(u)}{1-0.25\alpha_1(u)} = -\frac{1}{2}\left[\frac{d\alpha(z)}{dz}\right]\int_{-\infty}^{z} du\alpha_1(u)\left(1 + \frac{1}{4}\alpha_1(u) + \frac{1}{16}\alpha_1^2(u) + \cdots\right)$$

We can imagine that the higher order terms here would be provided by the higher terms $\alpha_4, \alpha_5 \cdots$.

Then we get the HOIS:

$$\begin{aligned}\alpha^{HOIS}(z) &= \alpha_1(z) - \frac{1}{2}\left[\frac{d\alpha(z)}{dz}\right]\int_{-\infty}^{z} du\frac{\alpha_1(u)}{1-0.25\alpha_1(u)} \\ &\quad -\frac{1}{8}\left[\frac{d^2\alpha(z)}{dz^2}\right]\left(\int_{-\infty}^{z} du\frac{\alpha_1(u)}{1-0.25\alpha_1(u)}\right)^2 - \cdots \end{aligned} \tag{26}$$

The same as the LOIS closed form, terms except the higher-order would contribute to the $\alpha^{HOIS}(z)$, keep higher-order terms in α on the right-hand side:

$$\begin{aligned}\alpha^{HOIS}(z) &= \alpha_1(z) - \frac{1}{2}\left[\frac{d\alpha^{HOIS}(z)}{dz}\right]\int_{-\infty}^{z} du\frac{\alpha_1(u)}{1-0.25\alpha_1(u)} \\ &\quad -\frac{1}{8}\left[\frac{d^2\alpha^{HOIS}(z)}{dz^2}\right]\left(\int_{-\infty}^{z} du\frac{\alpha_1(u)}{1-0.25\alpha_1(u)}\right)^2 - \cdots \end{aligned} \tag{27}$$

$$\begin{aligned}\alpha_1(z) &= \alpha^{HOIS}(z) + \frac{1}{2}\left[\frac{d\alpha^{HOIS}(z)}{dz}\right]\int_{-\infty}^{z} du\frac{\alpha_1(u)}{1-0.25\alpha_1(u)} \\ &\quad +\frac{1}{8}\left[\frac{d^2\alpha^{LOIS}(z)}{dz^2}\right]\left(\int_{-\infty}^{z} du\frac{\alpha_1(u)}{1-0.25\alpha_1(u)}\right)^2 + \cdots \\ &= \sum_{n=0}^{\infty}\left(\frac{(1/2)^n}{n!}\right)\left[\frac{d^n\alpha^{HOIS}(z)}{dz^n}\right]\left(\int_{-\infty}^{z} du\frac{\alpha_1(u)}{1-0.25\alpha_1(u)}\right)^n \\ &= \alpha^{HOIS}\left(z + \frac{1}{2}\int_{-\infty}^{z} du\frac{\alpha_1(u)}{1-0.25\alpha_1(u)}\right) \end{aligned} \tag{28}$$

This is the HOIS closed form we are trying to get.

5 Discussions and conclusions

In this note, a clear derivation of the HOIS closed form is given. It proves the correctness of the HOIS closed form and provides a tool for further captures in the case of a medium with lateral variations or multi-parameters. Wang et al. (2009) used a similar analysis for the two-parameter acoustic medium and captured more terms beyond the conjecture.

6 Acknowledgements

All M-OSRP sponsors are gratefully appreciated for their support in the research. This work has been partially funded by NSF-CMG (award DMS-0327778) and U.S. DOE-BES (Grant No. DOE-De-FG02-05ER15697).

References

Liu, F. *Multi-dimensional depth imaging without an adequate velocity model.* PhD thesis, University of Houston, 2006.

Shaw, S. A., A. B. Weglein, D. J. Foster, K. H. Matson, and R. G. Keys. "Isolation of a leading order depth imaging series and analysis of its convergence properties." *Journal of Seismic Exploration* 2 (November 2004): 157–195.

Wang, Z., A. B. Weglein, and X. Li. "New capture of direct velocity independent depth imaging in a one-dimension two-parameter acoustic earth." *Mission-Oriented Seismic Research Program (M-OSRP) Annual Report.* 2009.

Weglein, A. B., D. J. Foster, K. H. Matson, S. A. Shaw, P. M. Carvalho, and D. Corrigan. "Predicting the correct spatial location of reflectors without knowing or determining the precise medium and wave velocity: initial concept, algorithm and analytic and numerical example." *Journal of Seismic Exploration* 10 (2002): 367–382.

Zhang, J., F. Liu, Kristopher Innanen, and Arthur B. Weglein. "Comprehending and analyzing the leading order and higher order imaging closed forms derived from inverse scattering series." *Mission-Oriented Seismic Research Program Annual Report* (2006): 149–159.

Note: Evaluations of the HOIS closed form and its two variations

Z. Wang, A. B. Weglein., and F. Liu

Abstract

For any imaging algorithm it is important to know the following properties:

1. Assumptions: Can we use the algorithm to solve our problem?
2. Efficiency: How much does the algorithm cost if we use it?
3. Performance: How good is the result?

For people developing algorithms, they design new algorithms or improve existing algorithms by removing the assumptions or revising the preprocessing to satisfy the assumptions, enhancing the efficiency, or improving the performance. For people utilizing algorithms, they decide which algorithm to use by comparing these properties with the problems they are trying to solve, the resources they have, and the aims they are trying to achieve.
Higher-order imaging subseries (HOIS, Liu et al. (2005)), derived from inverse scattering series (ISS), does not need the subsurface velocity and very fast (a little more than constant velocity FK migration). In this work, we will focus on evaluating the performance of the HOIS and two of its variations. One variation is designed for a very large contrast medium and another one is similar to HOIS and shows up in the process of developing imaging algorithm for multip-parameter Earth (Wang et al., 2009).

1 Introduction

For complex media, velocity analysis has difficulties and the requirement for velocity-dependent algorithms is violated. Inverse scattering series (ISS) provides another choice: imaging without subsurface information. There are two different imaging subseries proposed by M-OSRP for one-parameter medium (constant density): leading-order imaging subseries (LOIS, Shaw and Weglein (2004)) and higher-order imaging subseries(HOIS, Liu et al. (2005)). The HOIS captures more terms than the LOIS and comparations have been made in Liu et al. (2005). But neither of them captures all of the terms. Zhang et al. (2006) shows that HOIS is able to accurately shift the second interface to the correct location but not the deeper interfaces. In this note, from the analytic calculation, we gave evaluations of HOIS and its two other variation forms. One variation is designed for a very large contrast medium and another one is similar to HOIS and shows up in the process of developing imaging algorithm for multip-parameter Earth (Wang et al., 2009).

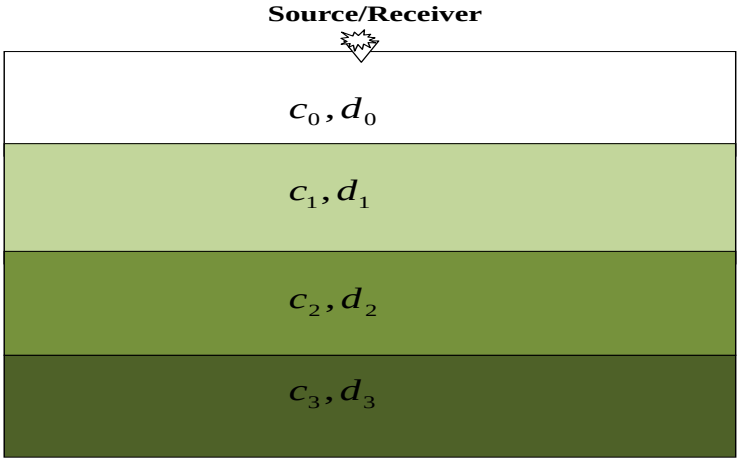

Figure 1: A 1D four-layer model with velocities c_0, c_1, c_2, c_3 and thicknesses d_0, d_1, d_2, ∞.

2 The model being used

Our aim is to give clear evaluations of HOIS:

$$\alpha^{HOIS}\left(z+\frac{1}{2}\int_{-\infty}^{z}du\frac{\alpha_1(u)}{1-0.25\alpha_1(u)}\right)=\alpha_1(z) \tag{1}$$

and two other closed forms:

$$\alpha^{HHOIS}\left(z+\frac{1}{2}\int_{-\infty}^{z}du\frac{\alpha_1(u)+0.0625\int_{-\infty}^{u-\Delta}dv\alpha_1'(v)\alpha_1^2(v-\Delta)}{1-0.25\alpha_1(u)+0.015625\int_{-\infty}^{u-\Delta}dv\alpha_1'(v)\alpha_1(v-\Delta)[1-\alpha_1(v-\Delta)]}\right)=\alpha_1(z); \tag{2}$$

$$\alpha^{HOIS}(z)=\alpha_1\left(z-\frac{1}{2}\int_{-\infty}^{z}du\frac{\alpha(u)}{1+0.25\alpha(u)}\right), \tag{3}$$

here Δ in Equation 2 is a constant ususally just choosing it as the wavelength.

A 1D four-layer constant-density acoustic model (Fig. 1) would be simple but sufficient to indicate the accuracies of these algorithms. In this model, the layers have velocities c_0, c_1, c_2, c_3 and thicknesses d_0, d_1, d_2, ∞.

Supposing that both the source and receiver are located at depth zero and if there is a spike from the source at $t = 0$, some data D would be received at the receiver (just primaries):

$$D(t)=R_1\delta(t-t_1)+\hat{R}_2\delta(t-t_2)+\hat{R}_3\delta(t-t_3) \tag{4}$$

where the amplitudes and arrival times have the relationship as below:

$$R_1 = \frac{c_1 - c_0}{c_1 + c_0}, \quad R_2 = \frac{c_2 - c_1}{c_2 + c_1}, \quad R_3 = \frac{c_3 - c_2}{c_3 + c_2},$$

$$T_{01} = 1 - R_1, \quad T_{10} = 1 + R_1, \quad T_{12} = 1 - R_2, \quad T_{21} = 1 + R_2,$$

$$\hat{R_2} = T_{01}T_{10}R_2 = (1 - R_1^2)R_2,$$

$$\hat{R_3} = T_{01}T_{10}T_{12}T_{21}R_3 = (1 - R_1^2)(1 - R_2^2)R_3,$$

$$t_1 = 2 * \frac{d_0}{c_0}, \quad t_2 = 2 * (\frac{d_0}{c_0} + \frac{d_1}{c_1}), \quad t_3 = 2 * (\frac{d_0}{c_0} + \frac{d_1}{c_1} + \frac{d_2}{c_2}).$$

Using the equation for α_1 (constant velocity FK migration) we can get:

$$\alpha_1(z) = 4R_1H(z - z_1') + 4R_2(1 - R_1^2)H(z - z_2') + 4R_3(1 - R_2^2)(1 - R_1^2)H(z - z_3') \tag{5}$$

$$\alpha_1'(z) = 4R_1\delta(z - z_1') + 4R_2(1 - R_1^2)\delta(z - z_2') + 4R_3(1 - R_2^2)(1 - R_1^2)\delta(z - z_3') \tag{6}$$

where z_i' is the pseudo depth for the ith interface. They are imaged for the events using reference velocity c_0:

$$z_1' = d_0, \quad z_2' = d_0 + \frac{c_0 d_1}{c_1}, \quad z_3' = d_0 + \frac{c_0 d_1}{c_1} + \frac{c_0 d_2}{c_2}$$

3 Evaluation of the HOIS closed form

By using Equation 5:

$$\alpha_1(z) = 4R_1H(z - z_1') + 4R_2(1 - R_1^2)H(z - z_2') + 4R_3(1 - R_2^2)(1 - R_1^2)H(z - z_3')$$

into HOIS:

$$\alpha^{HOIS}\left(z + \frac{1}{2}\int_{-\infty}^{z} du \frac{\alpha_1(u)}{1 - 0.25\alpha_1(u)}\right) = \alpha_1(z).$$

we will get the locations of the interfaces:

$$z_1^{HOIS} = z_1' + \frac{1}{2}\int_{-\infty}^{z_1'} du \frac{\alpha_1(u)}{1 - 0.25\alpha_1(u)} = d_0, \tag{7}$$

$$\begin{aligned} z_2^{HOIS} &= z_2' + \frac{1}{2}\int_{-\infty}^{z_2'} du \frac{\alpha_1(u)}{1 - 0.25\alpha_1(u)} \\ &= d_0 + \frac{c_0 d_1}{c_1} + \frac{c_0 d_1}{c_1} * \frac{2R_1}{1 - R_1} = d_0 + d_1, \end{aligned} \tag{8}$$

$$\begin{aligned} z_3^{HOIS} &= z_3' + \frac{1}{2}\int_{-\infty}^{z_3'} du \frac{\alpha_1(u)}{1 - 0.25\alpha_1(u)} \\ &= z_2' + \frac{1}{2}\int_{-\infty}^{z_2'} du \frac{\alpha_1(u)}{1 - 0.25\alpha_1(u)} + (z_3' - z_2') + \frac{1}{2}\int_{z_2'}^{z_3'} du \frac{\alpha_1(u)}{1 - 0.25\alpha_1(u)} \end{aligned}$$

$$
\begin{aligned}
&= d_0 + d_1 + \frac{c_0 d_2}{c_2} * \frac{1 + R_1 + R_2(1 - R_1^2)}{1 - R_1 - R_2(1 - R_1^2)} \\
&= d_0 + d_1 + d_2 * \frac{(1 - R_1)(1 - R_2)}{(1 + R_1)(1 + R_2)} * \frac{(1 + R_1)(1 + R_2 - R_1 R_2)}{(1 - R_1)(1 - R_2 - R_1 R_2)} \\
&= d_0 + d_1 + d_2 + d_2 * \frac{2R_1 R_2^2}{1 - R_1 R_2 - R_2^2 - R_1 R_2^2} \qquad (9)
\end{aligned}
$$

Comparing with the correct locations, z_1^{HOIS} and z_2^{HOIS} give the exact value, while z_3^{HOIS} has a deviation from the exact which is:

$$\Delta d_2^{HOIS} = d_2 * \frac{2R_1 R_2^2}{1 - R_1 R_2 - R_2^2 + R_1 R_2^2}. \qquad (10)$$

It is in the third order of the reflectivity and first order of the thickness, which is related to the size of the differences between the actual and reference media and the duration of this differences. Usually, this deviation is not large. For example, if $R_1 = R_2 = 0.1$ and $d_2 = 0.5mi$, $\Delta d_2^{HOIS} \approx 1(meters)$. This can be ignored. But when the differences between the actual and reference medium are big and/or the duration of these differences are large, for example $R_1 = R_2 = 0.5$ and $d_2 = 1mi$, the deviation would be $\Delta d_2^{HOIS} \approx 250(meters)$ and can not be neglected.

4 Evaluation of the HHOIS closed form

Equation 10 shows that the deviation from the correct location would be obvious by using HOIS closed form when the size and duration of the differences between actual and reference medium are large. So we proposed HHOIS closed form to solve this problem:

$$\alpha^{HHOIS}(z + \frac{1}{2}\int_{-\infty}^{z} du \frac{\alpha_1(u) + 0.0625\int_{-\infty}^{u-\Delta} dv \alpha_1'(v)\alpha_1^2(v-\Delta)}{1 - 0.25\alpha_1(u) + 0.0625\int_{-\infty}^{u-\Delta} dv \alpha_1'(v)\alpha_1(v-\Delta)[1 - 0.25\alpha_1(v-\Delta)]}) = \alpha_1(z).$$

Also using

$$\alpha_1(z) = 4R_1 H(z - z_1') + 4R_2(1 - R_1^2)H(z - z_2') + 4R_3(1 - R_2^2)(1 - R_1^2)H(z - z_3')$$

$$\alpha_1'(z) = 4R_1 \delta(z - z_1') + 4R_2(1 - R_1^2)\delta(z - z_2') + 4R_3(1 - R_2^2)(1 - R_1^2)\delta(z - z_3'),$$

the locations of the interfaces are:

$$
\begin{aligned}
z_1^{HHOIS} &= z_1' + \frac{1}{2}\int_{-\infty}^{z_1'} du \frac{\alpha_1(u) + 0.0625\int_{-\infty}^{u-\Delta} dv \alpha_1'(v)\alpha_1^2(v-\Delta)}{1 - 0.25\alpha_1(u) + 0.0625\int_{-\infty}^{u-\Delta} dv \alpha_1'(v)\alpha_1(v-\Delta)[1 - 0.25\alpha_1(v-\Delta)]} = d_0 \\
z_2^{HHOIS} &= z_2' + \frac{1}{2}\int_{-\infty}^{z_2'} du \frac{\alpha_1(u) + 0.0625\int_{-\infty}^{u-\Delta} dv \alpha_1'(v)\alpha_1^2(v-\Delta)}{1 - 0.25\alpha_1(u) + 0.0625\int_{-\infty}^{u-\Delta} dv \alpha_1'(v)\alpha_1(v-\Delta)[1 - 0.25\alpha_1(v-\Delta)]}
\end{aligned}
$$

$$
\begin{aligned}
&= z_1' + \frac{1}{2}\int_{-\infty}^{z_1'} du \frac{\alpha_1(u) + 0.0625\int_{-\infty}^{u-\Delta} dv\alpha_1'(v)\alpha_1^2(v-\Delta)}{1 - 0.25\alpha_1(u) + 0.0625\int_{-\infty}^{u-\Delta} dv\alpha_1'(v)\alpha_1(v-\Delta)[1-0.25\alpha_1(v-\Delta)]} \\
&\quad + z_2' - z_1' + \frac{1}{2}\int_{z_1'}^{z_2'} du \frac{\alpha_1(u) + 0.0625\int_{-\infty}^{u-\Delta} dv\alpha_1'(v)\alpha_1^2(v-\Delta)}{1 - 0.25\alpha_1(u) + 0.0625\int_{-\infty}^{u-\Delta} dv\alpha_1'(v)\alpha_1(v-\Delta)[1-0.25\alpha_1(v-\Delta)]} \\
&= d_0 + \frac{c_0 d_1}{c_1} + \frac{1}{2}\int_{z_1'}^{z_2'} du \frac{\alpha_1(u) + 0.0625 * R_1 * 0}{1 - 0.25\alpha_1(u) + 0.0625 * R_1 * 0 * 1} \\
&= d_0 + \frac{c_0 d_1}{c_1} + \frac{c_0 d_1}{c_1} * \frac{2R_1}{1-R_1} \\
&= d_0 + d_1 \qquad (11)
\end{aligned}
$$

$$
\begin{aligned}
z_3^{HHOIS} &= z_3' + \frac{1}{2}\int_{-\infty}^{z_3'} du \frac{\alpha_1(u) + 0.0625\int_{-\infty}^{u-\Delta} dv\alpha_1'(v)\alpha_1^2(v-\Delta)}{1 - 0.25\alpha_1(u) + 0.0625\int_{-\infty}^{u-\Delta} dv\alpha_1'(v)\alpha_1(v-\Delta)[1-0.25\alpha_1(v-\Delta)]} \\
&= z_2' + \frac{1}{2}\int_{-\infty}^{z_2'} du \frac{\alpha_1(u) + 0.0625\int_{-\infty}^{u-\Delta} dv\alpha_1'(v)\alpha_1^2(v-\Delta)}{1 - 0.25\alpha_1(u) + 0.0625\int_{-\infty}^{u-\Delta} dv\alpha_1'(v)\alpha_1(v-\Delta)[1-0.25\alpha_1(v-\Delta)]} \\
&\quad + z_3' - z_2' + \frac{1}{2}\int_{z_2'}^{z_3'} du \frac{\alpha_1(u) + 0.0625\int_{-\infty}^{u-\Delta} dv\alpha_1'(v)\alpha_1^2(v-\Delta)}{1 - 0.25\alpha_1(u) + 0.0625\int_{-\infty}^{u-\Delta} dv\alpha_1'(v)\alpha_1(v-\Delta)[1-0.25\alpha_1(v-\Delta)]} \\
&= d_0 + d_1 + d_2' + \int_{z_2'}^{z_3'} du \frac{2R_1 + 2R_2(1-R_1^2) + 0.0625\int_{-\infty}^{u-\Delta} dv\alpha_1'(v)\alpha_1^2(v-\Delta)}{1 - R_1 - R_2(1-R_1^2) + 0.0625\int_{-\infty}^{u-\Delta} dv\alpha_1'(v)\alpha_1(v-\Delta)[1-0.25\alpha_1(v-\Delta)]} \\
&= d_0 + d_1 + d_2' + \int_{z_2'}^{z_3'} du \frac{2R_1 + 2R_2(1-R_1^2) + 2R_1^2R_2(1-R_1^2)}{1 - R_1 - R_2(1-R_1^2) + R_2(1-R_1^2)R_1(1-R_1)} \\
&= d_0 + d_1 + d_2 * \frac{(1-R_1)(1-R_2)}{(1+R_1)(1+R_2)} * \frac{1 + R_1 + R_2(1-R_1^2) + R_2(1-R_1^2)R_1(1+R_1)}{1 - R_1 - R_2(1-R_1^2) + R_2(1-R_1^2)R_1(1-R_1)} \\
&= d_0 + d_1 + d_2 + d_2 * \frac{2R_1^3R_2^2}{1 - R_2^2 - R_1^3R_2 - R_1^3R_2^2} \qquad (12)
\end{aligned}
$$

Comparing with the correct locations, z_1^{HHOIS} and z_2^{HHOIS} give the exact value while z_3^{HHOIS} has a deviation from the exact, which is:

$$\Delta d_2^{HHOIS} = d_2 * d_2 * \frac{2R_1^3R_2^2}{1 - R_2^2 - R_1^3R_2 - R_1^3R_2^2}. \qquad (13)$$

Comparing with the result of HOIS:

$$\Delta d_2^{HOIS} = d_2 * \frac{2R_1R_2^2}{1 - R_1R_2 - R_2^2 + R_1R_2^2}. \qquad (14)$$

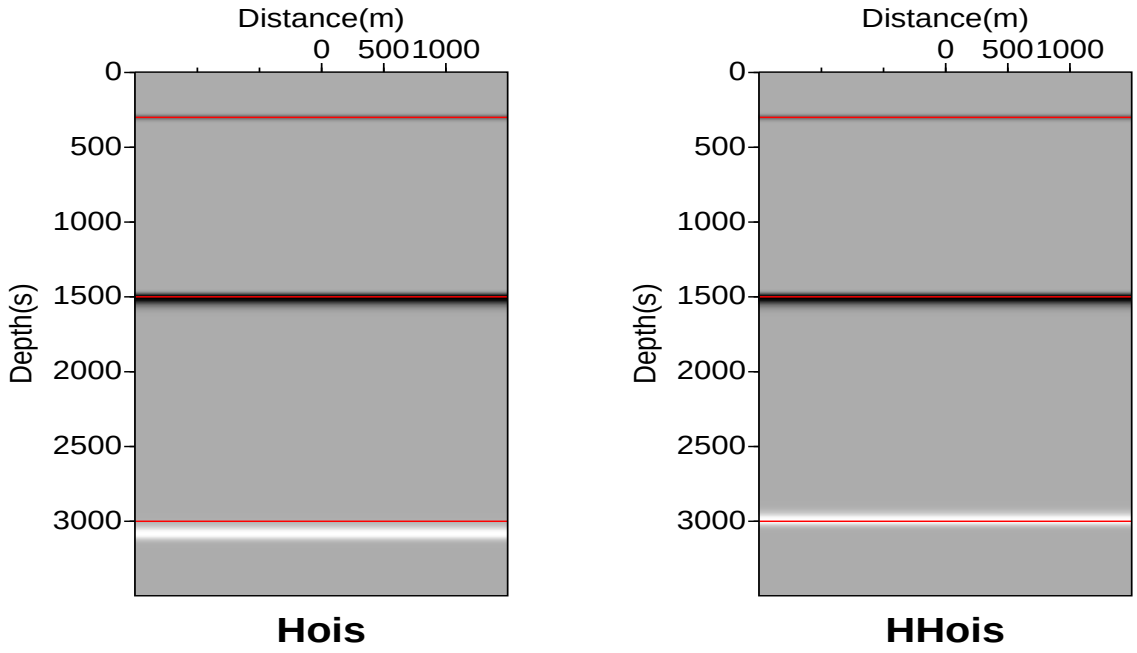

Figure 2: HOIS and HHOIS results of a four-layer model with properties: $v_0 = 1500m/s,\ v_1 = 2000m/s,\ v_2 = 5000m/s,\ v_3 = 3000m/s$ and interfaces at $300m, 1500m, 3000m$.

We can see that the deviation is still proportionate to the thickness but now in fifth order of the reflectivity. Because the reflectivity is always smaller than 1, often very small, HHOIS would always have a smaller deviation than HOIS as long as the input value of α_1 is accurate.

Figure 2 shows the numerical testing results. The left panel is the result using the HOIS and the right panel is the result using HHOIS. We can see that the result of HHOIS shows a big improvement over that of HOIS.

5 Evaluation of recursive HOIS

In Wang et al. (2009), for the multi-parameter acoustic medium, instead of getting HOIS-based 'imaging conjecture', we could only get the recursive HOIS (RHOIS) based algorithm directly. Here, the RHOIS is:

$$\alpha^{RHOIS}(z) = \alpha_1 \left(z - \frac{1}{2} \int_{-\infty}^{z} du \frac{\alpha(u)}{1 + 0.25\alpha(u)} \right). \tag{15}$$

Next we will show the recursive HOIS closed form would be equal to the normal HOIS closed form.

The expression for α_1 is:

$$\alpha_1(z) = 4R_1 H(z - z_1') + 4R_2(1 - R_1^2)H(z - z_2') + 4R_3(1 - R_2^2)(1 - R_1^2)H(z - z_3').$$

and suppose α^{HOIS} is:

$$\alpha(z) = 4R_1 H(z - z_1^{HOIS}) + 4R_2(1 - R_1^2)H(z - z_2^{HOIS}) + 4R_3(1 - R_2^2)(1 - R_1^2)H(z - z_3^{HOIS}).$$

These two should be compatible with each other.

For the first interface, it requires:

$$z_1' = z_1^{HOIS} - \frac{1}{2} \int_{-\infty}^{z_1^{HOIS}} du \frac{\alpha(u)}{1 + 0.25\alpha(u)} \Rightarrow z_1^{HOIS} = z_1' = d_0. \tag{16}$$

For the second interface, it requires:

$$z_2' = z_2^{HOIS} - \frac{1}{2} \int_{-\infty}^{z_2^{HOIS}} du \frac{\alpha(u)}{1 + 0.25\alpha(u)}, \tag{17}$$

$$d_0 + \frac{c_0 d_1}{c_1} = d_0 + d_1^{HOIS} - d_1^{HOIS} * \frac{2R_1}{1 + R_1}, \tag{18}$$

$$\Rightarrow d_1^{HOIS} = \frac{c_0 d_1}{c_1} * \frac{1 + R_1}{1 - R_1} = d_1. \tag{19}$$

For the third interface, it requires:

$$z_3' = z_3^{HOIS} - \frac{1}{2} \int_{-\infty}^{z_3^{HOIS}} du \frac{\alpha(u)}{1 + 0.25\alpha(u)}, \tag{20}$$

$$z_2' + \frac{c_0 d_2}{c_2} = z_2^{HOIS} + d_2^{HOIS} - \frac{1}{2}\int_{-\infty}^{z_2^{HOIS}} du \frac{\alpha(u)}{1+0.25\alpha(u)} - d_2^{HOIS} * \frac{2R_1 + 2R_2(1-R_1^2)}{1+R_1+R_2(1-R_1^2)}, \quad (21)$$

$$\Rightarrow d_2^{HOIS} = \frac{c_0 d_2}{c_2} * \frac{1+R_1+R_2(1-R_1^2)}{1-R_1-R_2(1-R_1^2)} = d_2 * \frac{2R_1R_2^2}{1-R_1R_2-R_2^2-R_1R_2^2}. \quad (22)$$

The HOIS closed form and the recursive HOIS closed form have the same result when α has the same amplitudes but different locations comparing with α_1.

In practice, the R.H.S. of Equation 15 requires $\alpha(z)$ which we do not have. But a recursive method could be used to solve this problem which is: At first, we use $\alpha_1(z)$ for $\alpha(z)$ on the R.H.S. of Equation 15 and then use the result of $\alpha(z)$ back to Equation 15 again. Repeating this process until the result is stable (not changing any more when repeating). This is also why we call it recursive HOIS.

Because an algorithm similar to equation 15 is had in the two-parameter case, a numerical test shown below is carried out in the two-parameter case using that algorithm instead of RHOIS. But the logic behind this is the same. The model we are using is 1D two-parameter and has three layers with properties $v_0 = 1500m/s, \rho_0 = 1.0g/cm^3$; $v_1 = 1600m/s, \rho_1 = 1.1g/cm^3$; $v_2 = 1700m/s, \rho_2 = 1.2g/cm^3$. Figure 3 and Figure 4 are the results using the HOIS-based 'imaging conjecture' and the RHOIS-based algorithm with two iterations. The figures show that the results from these two algorithms are nearly the same which supports the analytical caculation.

6 Discussion and conclusions

In this report, the imaging results of HOIS, HHOIS, and recursive HOIS for a 1D four-layer medium are calculated. The HHOIS showed obvious improvements while consuming little more calculation when the size and duration of the differences between the actual and reference medium are large. The recursive HOIS is the same with HOIS but requires iterations. This conclusion is important in the multi-parameter case for the leap from the direct calculation to the two-parameter 'imaging conjecture'.

7 Acknowledgements

All M-OSRP sponsors are gratefully acknowledged for their support in the research. This work has been partially funded by NSF-CMG (award DMS-0327778) and U.S. DOE-BES (Grant No. DOE-De-FG02-05ER15697).

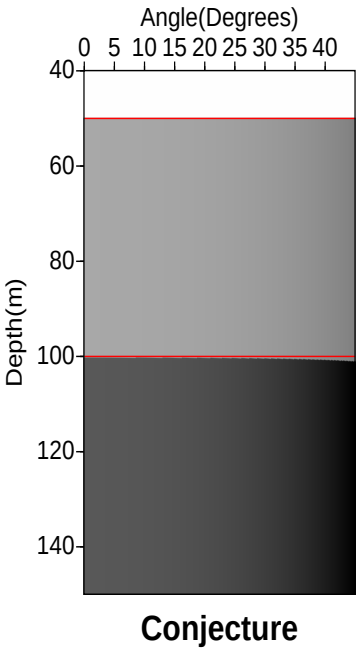

Figure 3: The result of HOIS-based 'imaging conjecture' for a three-layer model with properties: $v_0 = 1500m/s, \rho_0 = 1.0g/cm^3$; $v_1 = 1600m/s, \rho_1 = 1.1g/cm^3$; $v_2 = 1700m/s, \rho_2 = 1.2g/cm^3$.

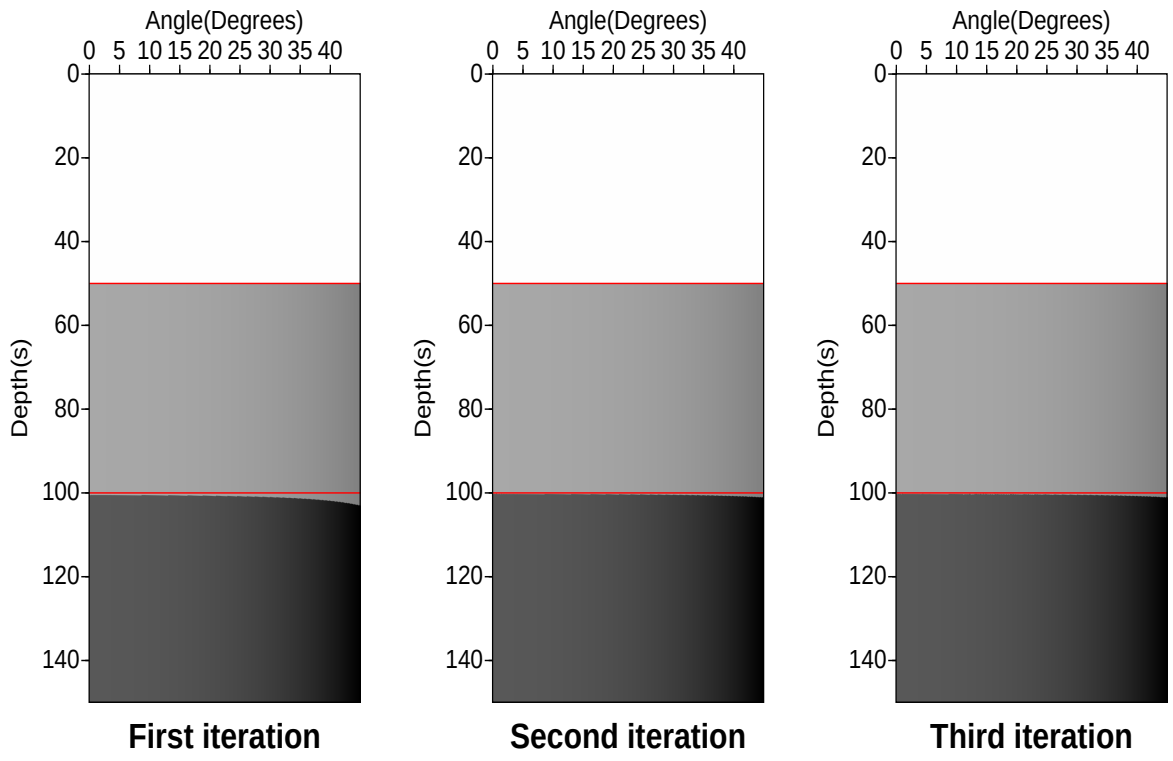

Figure 4: The results of recursive HOIS-based two-parameter algorithm for a three-layer model with properties: $v_0 = 1500m/s, \rho_0 = 1.0g/cm^3$; $v_1 = 1600m/s, \rho_1 = 1.1g/cm^3$; $v_2 = 1700m/s, \rho_2 = 1.2g/cm^3$.

References

Liu, F., A. B. Weglein, B. G. Nita, and K. A. Innanen. "Investigating the Grouping of Inverse Scattering Series Terms: Simultaneous Imaging and Inversion I(Theory)." *Mission-Oriented Seismic Research Program (M-OSRP) Annual Report.* 2005.

Shaw, S. A. and A. B. Weglein. "A leading order imaging series for prestack data acquired over a laterally invariant acoustic medium. Part I: Derivation and preliminary analysis." *M-OSRP Annual Report* 3 (2004).

Wang, Z., A. B. Weglein, and X. Li. "New capture of direct velocity independent depth imaging in a one-dimension two-parameter acoustic earth." *Mission-Oriented Seismic Research Program (M-OSRP) Annual Report.* 2009.

Zhang, J., F. Liu, Kristopher Innanen, and Arthur B. Weglein. "Comprehending and analyzing the leading order and higher order imaging closed forms derived from inverse scattering series." *Mission-Oriented Seismic Research Program Annual Report* (2006): 149–159.

New capture of direct velocity independent depth imaging in a one-dimension two-parameter acoustic Earth

Z. Wang, A. B. Weglein, and X. Li

Abstract

Among the challenges that the inverse scattering series (ISS) has to address in direct depth imaging without the velocity are:

1. The size of the difference between the actual and reference velocity,
2. The duration of the difference,
3. The number of parameters to describe the medium,
4. The number of dimensions of the medium, and
5. The incident angles where the reflection events occur.

Each of these challenges has its own requirements for the imaging algorithms and many times they are coupled together. It means even if one imaging algorithm can solve several challenges seperately it may fail when these challenges happen together.
In this report, we will focus on extending the previous capability of the ISS imaging for a multi-parameter Earth to accommodate larger differences between actual and reference velocity.

1 Introduction

Current migration algorithms have the assumption that the velocity is known which is obtained from a procedure called "velocity analysis". For complex media in which the velocity analysis has difficulties, the assumption is not satisfied and the performances of the algorithms are affected. One way to avoid these is to improve the performance of the velocity analysis and the other is to develop algorithms which do not require the actual velocity. The inverse scattering series (ISS) has been used to derive candidate direct nonlinear imaging algorithms following the latter route (Weglein et al., 2002) . Shaw and Weglein (2004a) and Shaw and Weglein (2004b) successfully isolated the leading order imaging subseries (LOIS) in the one-parameter (velocity only variations) medium. It works well when the differences between actual and reference velocity are small. When the differences are large, we need to use the higher order imaging subseries (HOIS, Liu et al. (2005)), which has a better imaging capability than LOIS. When going from one-parameter medium to two-parameter medium (both velocity and density variations), an extension was required and proposed

in what is called the 'imaging conjecture' (Weglein (2008), Pages 1-8). The 'imaging conjecture' has a multi-parameter front-end (sitting on top of a Fang Liu type of HOIS imaging algorithm engine) that excludes density only reflections and outputs reflectivity. It can deal with very big contrast one-parameter medium (constant density case, it will be the same as HOIS) and small contrast two-parameter medium (Jiang et al. (2008); Li et al. (2008)). In this report, we showed the limited capabiltiy of the 'imaging conjecture' for a large contrast two-parameter medium where these two challenges happen together. Upon that, an imaging algorithm 'beyond capture' is provided and tested.

2 The 'imaging conjecture' for two-parameter medium

Zhang (2006) and Jiang and Weglein (2007) derived the equation for α_1, β_1:

$$D(z,\theta) = -\frac{\rho_0}{4}\left[\frac{1}{cos^2\theta}\alpha_1(z) + (1-tan^2\theta)\beta_1(z)\right], \tag{1}$$

and defined an new "imaging composite" $\mathscr{D}(z,\theta)$ as following:

$$\mathscr{D}(z,\theta) = \frac{1}{cos^2\theta}\alpha_1(z) + (1-tan^2\theta)\beta_1(z) = -\frac{4}{\rho_0}D(z,\theta). \tag{2}$$

It is a quantity related to the reflectivity. They also derived the equations for α_2, β_2 and α_3, β_3. Here we rearrange the terms by grouping them as the expressions of $(\alpha_1 - \beta_1)$ and $\mathscr{D}(z,\theta)$ whenever possible:

$$\begin{aligned} & \frac{1}{cos^2\theta}\alpha_2(z) + (1-tan^2\theta)\beta_2(z) \\ = \; & -\frac{1}{2}\frac{1}{cos^2\theta}\mathscr{D}(z,\theta)[\alpha_1(z)-\beta_1(z)] - \frac{1}{2}\frac{1}{cos^2\theta}\frac{d\mathscr{D}(z,\theta)}{dz}\int_{-\infty}^{z} dz'[\alpha_1(z')-\beta_1(z')] \end{aligned} \tag{3}$$

$$\begin{aligned} & \frac{1}{cos^2\theta}\alpha_3(z) + (1-tan^2\theta)\beta_3(z) \\ = \; & -\frac{1}{cos^4\theta}[\alpha_1(z)-\beta_1(z)][\alpha_2(z)-\beta_2(z)] + \frac{1}{4}\frac{1}{cos^2\theta}\beta_1^2(z)[\alpha_1(z)-\beta_1(z)] \\ & +\frac{1}{8}\frac{1}{cos^4\theta}[\alpha_1(z)-\beta_1(z)]^2 - \frac{5}{16}\frac{1}{cos^6\theta}[\alpha_1(z)-\beta_1(z)]^3 \\ & -\frac{1}{2}\frac{1}{cos^2\theta}\frac{d\mathscr{D}(z,\theta)}{dz}\int_{-\infty}^{z} dz'[\alpha_2(z')-\beta_2(z')] \qquad (4) \\ & +\frac{1}{8}\frac{1}{cos^4\theta}\frac{d^2\mathscr{D}(z,\theta)}{dz}\left[\int_{-\infty}^{z} dz'[\alpha_1(z')-\beta_1(z')]\right]^2 \qquad (5) \\ & -\frac{1}{8}\frac{1}{cos^4\theta}\frac{d\mathscr{D}(z,\theta)}{dz}\int_{-\infty}^{z} dz'[\alpha_1(z')-\beta_1(z')]^2 \qquad (6) \end{aligned}$$

$$+\frac{1}{2}\frac{1}{cos^2\theta}\beta_1(z)\frac{d\mathscr{D}(z,\theta)}{dz}\int_{-\infty}^{z}dz'[\alpha_1(z')-\beta_1(z')] \tag{7}$$

$$+\frac{1}{2}\frac{1}{cos^4\theta}[\alpha_1+(3tan^2\theta-1)\beta_1]\frac{d\beta_1}{dz}\int_{-\infty}^{z}dz'[\alpha_1(z')-\beta_1(z')] \tag{8}$$

Next, We will use the same method for deriving HOIS closed form (Wang et al., 2009a) to show how the 'imaging conjecture' (equation 9)is derived:

$$\mathscr{D}^{HOIS}\left(z+\frac{1}{2}\int_{-\infty}^{z}dz'\frac{\alpha_1(z')-\beta_1(z')}{cos^2\theta-0.25[\alpha_1(z')-\beta_1(z')]},\theta\right)=\mathscr{D}(z,\theta). \tag{9}$$

1. For term (4), it can combine with the second term in Equation 3:

$$-\frac{1}{2}\frac{1}{cos^2\theta}\frac{d\mathscr{D}(z,\theta)}{dz}\int_{-\infty}^{z}dz'[\alpha_1(z')-\beta_1(z')]-\frac{1}{2}\frac{1}{cos^2\theta}\frac{d\mathscr{D}(z,\theta)}{dz}\int_{-\infty}^{z}dz'[\alpha_2(z')-\beta_2(z')]$$

   and we could imagine there will be more terms including $\int_{-\infty}^{z}dz'[\alpha_3(z')-\beta_3(z')]$, $\int_{-\infty}^{z}dz'[\alpha_4(z')-\beta_4(z')]$ and so on in the higher-order terms. So the second term in equation 3 would become $-\frac{1}{2}\frac{1}{cos^2\theta}\frac{d\mathscr{D}(z,\theta)}{dz}\int_{-\infty}^{z}dz'[\alpha(z')-\beta(z')]$. It happens the same for terms including $\alpha_1-\beta_1$ or β_1, for example, terms (5)-(8). They are all changed from $\alpha_1-\beta_1$ to $\alpha-\beta$ and β_1 to β.

2. For term (5), it provides the third term in the series:

$$\mathscr{D}(z,\theta)-\frac{1}{2}\frac{1}{cos^2\theta}\frac{d\mathscr{D}(z,\theta)}{dz}\int_{-\infty}^{z}dz'[\alpha_1(z')-\beta_1(z')]+\frac{1}{8}\frac{1}{cos^4\theta}\frac{d^2\mathscr{D}(z,\theta)}{dz}\left[\int_{-\infty}^{z}dz'[\alpha_1(z')-\beta_1(z')]\right]^2+\cdots$$

   and this series can be writen as the LOIS closed form:

$$\mathscr{D}^{LOIS}(z,\theta)=\mathscr{D}\left(z-\frac{1}{2}\frac{1}{cos^2\theta}\int_{-\infty}^{z}dz'[\alpha_1(z')-\beta_1(z')],\theta\right). \tag{10}$$

3. For term (6), combined with the second term in Equation 3 and the other terms from higher orders, it would provide:

$$\begin{aligned}&-\frac{1}{2}\frac{1}{cos^2\theta}\frac{d\mathscr{D}(z,\theta)}{dz}\int_{-\infty}^{z}dz'[\alpha_1(z')-\beta_1(z')]-\frac{1}{8}\frac{1}{cos^4\theta}\frac{d\mathscr{D}(z,\theta)}{dz}\int_{-\infty}^{z}dz'[\alpha_1(z')-\beta_1(z')]^2-\cdots\\ =\;&-\frac{1}{2}\frac{1}{cos^2\theta}\frac{d\mathscr{D}(z,\theta)}{dz}\int_{-\infty}^{z}dz'\frac{\alpha_1(z')-\beta_1(z')}{1+0.25[\alpha_1(z')-\beta_1(z')]/cos^2\theta}\end{aligned} \tag{11}$$

   Collecting all the terms mentioned in 1, 2, and 3 we would get the HOIS closed form as:

$$\mathscr{D}^{HOIS}(z,\theta)=\mathscr{D}\left(z-\frac{1}{2}\int_{-\infty}^{z}dz'\frac{\alpha(z')-\beta(z')}{cos^2\theta+0.25[\alpha(z')-\beta(z')]},\theta\right). \tag{12}$$

In Wang et al. (2009b), it has been shown that this form of HOIS is equal to take the moving part to the left-hand side of the equation, which is:

$$\mathscr{D}^{HOIS}\left(z+\frac{1}{2}\int_{-\infty}^{z}dz'\frac{\alpha_1(z')-\beta_1(z')}{cos^2\theta-0.25[\alpha_1(z')-\beta_1(z')]},\theta\right)=\mathscr{D}(z,\theta). \tag{13}$$

This is exactly the 'imaging conjecture' from Professor Weglein. The middle panels of Figure 1 and Figure 2 show the results of the 'imaging conjecture' for a small and large contrast medium. The model used in Figure 1 has a smaller velocity contrast (about 6.7%) and the one used in Figure 2 has a bigger velocity contrast (about 23.3%). We see that for the small contrast medium the 'imaging conjecture' corrects locations of the mislocated reflectors in FK constant velocity migration, while for the big contrast medium the second interface is still mislocated especially at large angles. This indicates that there are more challenges to address for large contrast media.

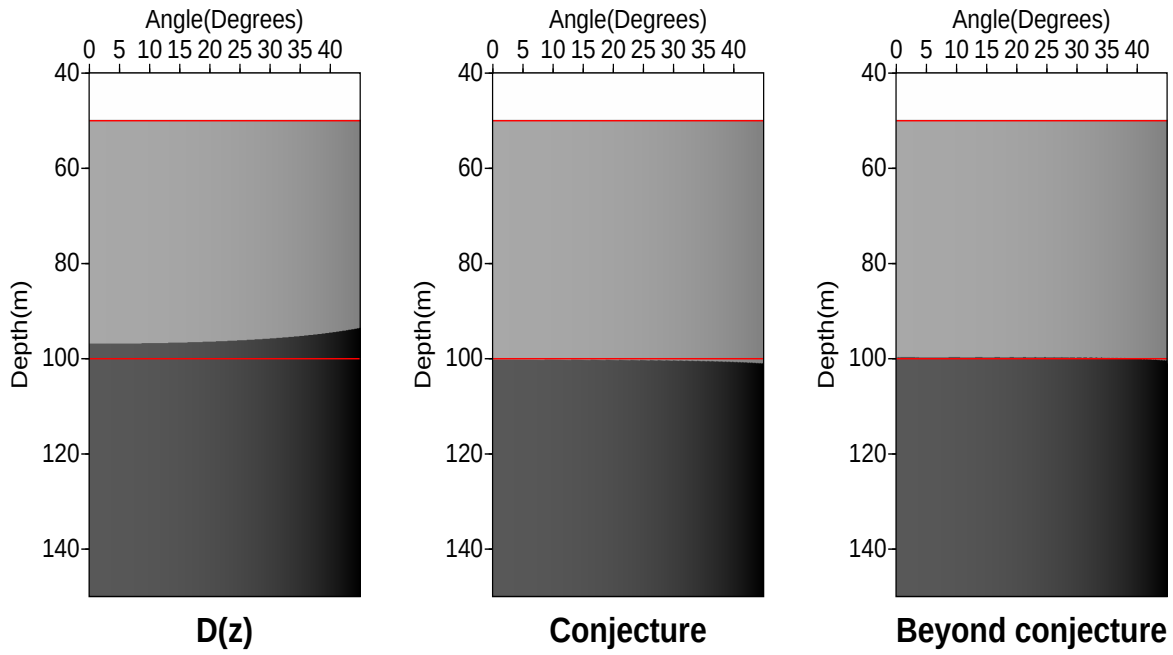

Figure 1: The comparison of 'the conjecture' and 'beyond conjecture' using a three-layer model with small contrasts in properties: $v_0 = 1500m/s,\ \rho_0 = 1.0g/cm^3$; $v_1 = 1600m/s,\ \rho_1 = 1.1g/cm^3$; $v_2 = 1700m/s,\ \rho_2 = 1.2g/cm^3$. The left panel is the imaging result of $D(z,\theta)$ using FK constant velocity migration, the middle panel is the result of 'the conjecture', and the right panel is the result of 'beyond conjecture' imaging capture.

3 The capture 'beyond conjecture'

We notice that there are still imaging terms (term (7) and term (8)) not included in the 'imaging conjecture'. We do not know how to deal with term (8) at the present; however, for term (7), if we combine it with the second term in equation 3:

$$\begin{aligned} & -\frac{1}{2}\frac{1}{cos^2\theta}\frac{d\mathscr{D}(z,\theta)}{dz}\int_{-\infty}^{z}dz'[\alpha_1(z')-\beta_1(z')]+\frac{1}{2}\frac{1}{cos^2\theta}\beta_1(z)\frac{d\mathscr{D}(z,\theta)}{dz}\int_{-\infty}^{z}dz'[\alpha_1(z')-\beta_1(z')] \\ = \quad & -\frac{1}{2}\frac{1}{cos^2\theta}[1-\beta_1(z)]\frac{d\mathscr{D}(z,\theta)}{dz}\int_{-\infty}^{z}dz'[\alpha_1(z')-\beta_1(z')]. \end{aligned} \tag{14}$$

So the closed form including all terms similar to (7) would become:

$$\mathscr{D}^{HOIS}\left(z+\frac{1}{2}[1-\beta_1(z)]\int_{-\infty}^{z}dz'\frac{\alpha_1(z')-\beta_1(z')}{cos^2\theta-0.25[\alpha_1(z')-\beta_1(z')]},\theta\right)=\mathscr{D}(z,\theta). \tag{15}$$

It captures more terms than the 'imaging conjecture' and has a better capability. The testing results for the two models stated above are shown in the right panels of Figure 1 and Figure 2. Note that comparing with 'imaging conjecture', it improves the location of the second reflector and the range of angles where the image is reliable.

4 Discussion and conclusions

In this report, the multi-parameter imaging conjecture is reached by analysing and combining the ISS terms which proves its rationality and correctness. Also, a new capture beyond conjecture is proposed and tested. Since it includes more imaging terms, the results show good improvements in both the location of the second reflector and the range of angles where the image is reliable. This will be extended to elastic media before field data imaging application/test. There is still one more imaging term in the third order of ISS not included in the new capture and our next aim is to get it included and provides a better imaging algorithm.

5 Acknowledgements

All M-OSRP sponsors are gratefully appreciated for their support in the research. We would like to show our further appreciation to Dr. Fang Liu for his encouragements and helpful suggestions. This work has been partially funded by NSF-CMG (award DMS-0327778) and U.S. DOE-BES (Grant No. DOE-De-FG02-05ER15697).

References

Jiang, S. and A. B. Weglein. "Deriving an imaging algorithm for a laterally invariant multi-parameter acoustic medium from the inverse scattering series." *Mission-Oriented Seismic Research Program (M-OSRP) Annual Report*. 2007.

Jiang, S., A. B. Weglein, and S. Shaw. "Progressing multiparameter imaging using the inverse scattering series." *Mission-Oriented Seismic Research Program (M-OSRP) Annual Report*. 2008.

Li, X., F. Liu, S. Jiang, and A. B. Weglein. "Deriving an imaging algorithm for a laterally invariant multi-parameter acoustic medium from the inverse scattering series." *Mission-Oriented Seismic Research Program (M-OSRP) Annual Report*. 2008.

Liu, F., A. B. Weglein, B. G. Nita, and K. A. Innanen. "Investigating the Grouping of Inverse Scattering Series Terms: Simultaneous Imaging and Inversion I(Theory)." *Mission-Oriented Seismic Research Program (M-OSRP) Annual Report*. 2005.

Shaw, S. A. and A. B. Weglein. "A leading order imaging series for prestack data acquired over a laterally invariant acoustic medium. Part I: Derivation and preliminary analysis." *M-OSRP Annual Report* 3 (2004).

Shaw, S. A. and A. B. Weglein. "A leading order imaging series for prestack data acquired over a laterally invariant acoustic medium. Part II: Analysis for data missing low frequencies." *M-OSRP Annual Report* 3 (2004).

Wang, Z., A. B. Weglein, and F. Liu. "Note: A derivation of the HOIS closed form." *Mission-Oriented Seismic Research Program (M-OSRP) Annual Report*. 2009.

Wang, Z., A. B. Weglein, and F. Liu. "Note: Evaluations of the HOIS closed form and its two variations." *Mission-Oriented Seismic Research Program (M-OSRP) Annual Report*. 2009.

Weglein, A. B. "Introduction and preface." *Mission-Oriented Seismic Research Program (M-OSRP) Annual Report*. 2008.

Weglein, A. B., D. J. Foster, K. H. Matson, S. A. Shaw, P. M. Carvalho, and D. Corrigan. "Predicting the correct spatial location of reflectors without knowing or determining the precise medium and wave velocity: initial concept, algorithm and analytic and numerical example." *Journal of Seismic Exploration* 10 (2002): 367–382.

Zhang, H. *Direct non-linear aoustic and elastic inversion: Towards fundamentally new comprehensive and realistic target identification*. PhD thesis, University of Houston, 2006.

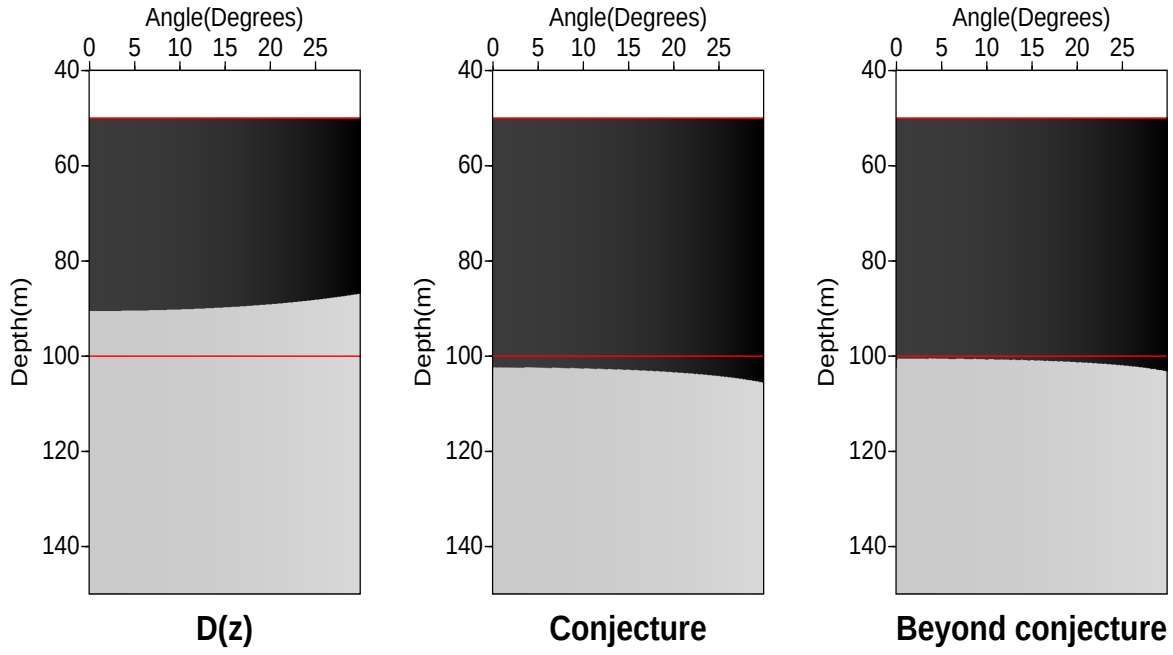

Figure 2: The comparison of 'the conjecture' and 'beyond conjecture' using a three-layer model with large contrasts in properties: $v_0 = 1500m/s,\ \rho_0 = 1.0g/cm^3$; $v_1 = 1850m/s,\ \rho_1 = 1.1g/cm^3$; $v_2 = 1350m/s,\ \rho_2 = 1.2g/cm^3$. The left panel is the imaging result of $D(z,\theta)$ using FK constant velocity migration, the middle panel is the result of 'the conjecture', and the right one is the result of 'beyond conjecture' imaging capture.

Analysis of forward and inverse series for target identification

X. Li and A. B. Weglein

Abstract

A key objective of seismic inversion is to determine the mechanical properties of subsurface targets towards identifying hydrocarbon resources in the earth. The inverse scattering series can achieve many distinct traditional processing objectives within a single framework but without the traditional need for subsurface information. The simplest and prototype inverse problem (for parameter estimation) is to determine the changes in physical properties across a single isolated interface from reflected data. We study, and progress our understanding of, the forward and inverse series for that specific acoustic case. Matson (1996) showed that if the upper half-space and lower half-space have velocities c_0 and c_1, respectively, then convergence occurs if $c_1 > c_0/\sqrt{2}$ and divergence occurs if $c_1 < c_0/\sqrt{2}$. Therefore, for smaller reflection coefficients (R.C.) (< -0.1716) the forward series diverges but for larger reflection coefficients the forward series converges. How can that make any sense? First, we show how that surprising result 'makes sense'.

Then we examine the corresponding inverse problem and for the first time show that: (1) the ISS converges for all values of R; (2) the series is a term by term improvement towards determining c_1, when the R.C. < 0.625; (3) when the R.C. > 0.625, the series converges, but will get worse before it gets better; and (4) for this example the inverse series has better convergence properties than the forward series. This analysis is a first and important step towards understanding how the inverse scattering series addresses the actual target identification problem for determining changes in elastic properties and density in a complex multi-D earth.

1 Introduction

The objective of seismic exploration is to determine the location and mechanical properties of potential hydrocarbon resources in the earth using recorded data. The recorded data is nonlinearly related to the change of the medium properties across a reflector. Current methods for inversion either assume a linear relationship between the amplitude of a primary and the mechanical property change across the reflector, which can be violated in practice and result in erroneous predictions; or assume a nonlinear relationship but use an indirect model-matching method to seek the solution, which often has a significant computation effort and also has reported ambiguity issues. The inverse scattering series developed by Weglein

et al. (2003) realizes and honors the nonlinear relationship between the perturbation and the scattered wave field. It is the only multi-D and multi-dimensional direct nonlinear formulasm. In this extremely complicated framework, there are task specific subseries that can achieve all the seismic processing objectives, such as multiple removal, depth imaging, direct nonlinear target identification and Q compensasion using only recorded data and reference medium through the same manner.

A very reasonable question to ask is, when we have an algorithm which is a subseries of inverse scattering series, how to determine the value of a term or a collection of terms in that task specific subseries? How many terms would be required in practice to achieve a certain level of effectiveness? And when does added terms improve the specific task associated with that subseries? These issues has been addressed for the isolated subseries for free surface multiple removal and internal multiple removal by understanding specifically what each term in that subseries is designed to accomplish. For example, in SRME, D^2 adds to D to remove all the first order free surface multiples, and to alter all higher order free surface multiples. When this is done, the second order free surface multiples look even worse than before, until D^3 sets in and takes care of them. If the second order free surface multiples did not get worse in preparation for higher terms, when D^3 adds up, it will not be able to eliminate the unaltered second order free surface multiples. This is an illustration of purposeful perturbation which is defined as knowledge of precisely what each term within a given task-specific subseries is designed to achieve.

We notice from the previous example that each term in inverse scattering series has its own purpose as part of the series working towards the goal associated with that subset. This same logic is true for target identification subseries too. For inversion purpose, it is reasonable that we would expect when the second order α_2 added to the first order α_1, the estimation will move towards the actual value. But an added-value second term is what we want instead of what the series promised to provide. The direct non-linear inversion for multi-parameter elastic case even for 1D is complicated. Dr. Haiyan Zhang did a lot of work to get the terms without integral to the 2nd order (Zhang, 2006). In this report, we analyze and understand the value of terms in this subseries for target identification by studying a simpler accoustic problem first. These new results from the accoustic example will affect how we define the issues we are going to focus our attention on.

In this report, we extended the previous work on understanding the inverse scattering series multiple removal method to direct nonlinear target identification. We present a first step study and examples of such understanding. In the first section we give a brief description of the inverse scattering series. In the second section, the convergence properties of the direct nonlinear inversion subseries are analyzed and also compared with the forward series in Matson (1996). For the 1D one parameter acoustic case with single reflector, the inverse scattering series has better convergence properties than the forward series. In the third section, by studying the analytic examples, we look at the value of terms for the direct nonlinear target identification, which provide us a guideline when we move to the more complicated elastic world.

2 Inverse scattering series

Starting from the two basic differential equations, (Weglein et al., 2003)

$$LG = \delta, \tag{1}$$

$$L_0 G_0 = \delta. \tag{2}$$

where L and L_0 are the differential operators that describe the wave propagation in the actual and reference medium, respectively; G and G_0 are the corresponding Green's functions.
The perturbation and the scattered field are defined as follows (Weglein et al., 2002):

$$V = L_0 - L, \tag{3}$$

$$\psi_s \equiv G - G_0, \tag{4}$$

The Lippmann-Schwinger equation which relates to G, G_0 and V (Taylor, 1972) is the fundamental eqation of the scattering theory:

$$G = G_0 + G_0 V G, \tag{5}$$

Iterating the above equation back to itself generates the Born series

$$G = G_0 + G_0 V G_0 + G_0 V G_0 V G_0 + \cdots \tag{6}$$

The scattered field ψ_s can be written as

$$\psi_s = G_0 V G_0 + G_0 V G_0 V G_0 + \cdots = (\psi_s)_1 + (\psi_s)_2 + \cdots \tag{7}$$

where the $(\psi_s)_n$ is the portion of ψ_s that is n^{th} order in V. The measured values of ψ_s are the data D

$$D = (\psi_s)_{ms} = (\psi_s)_{\texttt{onthemeasurementsurface.}} \tag{8}$$

Expanding V as a series in orders of measured data (Weglein et al., 1997)

$$V = V_1 + V_2 + V_3 + \cdots, \tag{9}$$

Substituting the inverse form 9 into the forward 7

$$\begin{aligned} D &= G_0(V_1 + V_2 + \cdots)G_0 \\ &+ G_0(V_1 + V_2 + \cdots)G_0(V_1 + V_2 + \cdots)G_0 + \cdots \end{aligned} \tag{10}$$

Evaluating both sides on the measurement surface and set terms of equal order in the data equal, and we have the set of equations determining V_1, V_2,... and hence V in terms of D and G_0.

$$D = [G_0 V_1 G_0]_{ms}, \tag{11}$$

$$0 = [G_0 V_2 G_0]_{ms} + [G_0 V_1 G_0 V_1 G_0]_{ms}, \tag{12}$$

$$\begin{aligned} 0 &= [G_0 V_3 G_0]_{ms} + [G_0 V_1 G_0 V_2 G_0]_{ms} \\ &+ [G_0 V_2 G_0 V_1 G_0]_{ms} + [G_0 V_1 G_0 V_1 G_0 V_1 G_0]_{ms}, \end{aligned} \tag{13}$$

$$\vdots$$

3 The inverse scattering subseries for target identification

Consider a 1D constant density variable velocity acoustic medium where the propagation of the wave field P is governed by:

$$\left(\frac{d^2}{dz^2} + \frac{\omega^2}{c^2(z)}\right) P = 0 \tag{14}$$

where ω is the angular frequency, $c(z)$ is the local acoustic velocity, and z is the field point of the wavefield. If the reference medium is chosen to be an acoustic wholespace with velocity c_0, then the perturbation can be written as:

$$V(z) = \frac{\omega^2}{c_0^2} - \frac{\omega^2}{c^2(z)} = k_0^2 \alpha(z) \tag{15}$$

where $\alpha(z) = 1 - c_0^2/c^2(z)$ and $k_0 = \omega/c_0$. And $\alpha(z)$ can be expanded as a series in terms of data,

$$\alpha(z) = \alpha_1(z) + \alpha_2(z) + \alpha_3(z) + \cdots . \tag{16}$$

3.1 Convergence properties of the direct nonlinear target identification subseries

In the previous imaging work, (Shaw et al., 2004) isolated the leading order imaging subseries and analyzed its convergence properties. Meanwhile, a direct non-linear inversion subseries was also isolated. Here let us move forward and study the convergence properties of the inversion subseries. The inversion only terms are:

$$\alpha^{AO}(z) = \alpha_1(z) - \frac{1}{2}\alpha_1^2(z) + \frac{3}{16}\alpha_1^3(z) + \cdots . \tag{17}$$

We assume that a plane wave propagates in the medium, and the medium consists of two half-spaces in contact, with acoustic velocities c_0 and c_1 and a interface located at $z = a$ as shown in Figure 1. If the incidence angle is θ, Zhang (2006) showed that α_1 can be expressed as

$$\alpha_1(z) = 4R(\theta)\cos^2\theta H(z-a),$$

where R is the reflection coefficient. For normal incidence case $R = \frac{c_1 - c_0}{c_1 + c_0}$. When $z > a$

$$\alpha_1 = 4R.$$

Substituting α_1 into equation (17), the direct non-linear inversion subseries above can be written as follows:

$$\alpha^{AO} = 4R - 8R^2 + 12R^3 - 16R^4 + \cdots = 4R(\sum_{n=0}(n+1)(-1)^n R^n). \tag{18}$$

For this simplest example, we can prove this general form for the series from the close form that R and α has. Since we have a general form now, we can examine the convergence of this subseries through the ratio test as follws:

$$\left|\frac{\alpha_{n+1}}{\alpha_n}\right| = \left|\frac{(-1)^{n+1}(n+2)R^{n+1}}{(-1)^n(n+1)R^n}\right| = \left|\frac{n+2}{n+1}R\right|. \tag{19}$$

We know if $\lim_{n\to\infty}\left|\frac{\alpha_{n+1}}{\alpha_n}\right| < 1$, this series converges absolutely. That is

$$|R| < \lim_{n\to\infty}\frac{n+1}{n+2} = 1. \tag{20}$$

Thus, the direct non-linear inversion subseries converges when the reflection coefficient $|R|$ is less than 1, which is always true. Hence, for this example, the inverse series will converge under any velocity contrasts between the two media. Compared to the forward series which is convergent for a certain range of relative medium velocites, the inverse series has better convergence properties. We will discuss this in the subsection about the forward scattering series studied in Matson (1996).

3.2 Analytic examples

Now, back to the inverse subseries for target identification, we know that for the model described previously with 1D earth single reflector, it converges for all values of R. For this well-converging subseries, there are other issues we want to know: How about the rate of convergence? Is it a term-by-term added value improvement towards determining the actual medium properties? In this section, we study these issues by looking at three analytic examples with different velocity contrasts. Considering the examples shown in Figures 2, 3 and 4. In these three pictures, the horizontal axis shows the number of terms added in the estimation. For example, the corresponding points on the red line of n^{th} term means the n^{th} order estimation of α, which is $\sum_{i=1}^{n}\alpha_i$. The green line represents the actual value of α, the red line represents the estimation value of α, and the blue line represents the error between the estimation and the actual value.

We now examine the convergence properties of the inversion subseries to the velocity contrast. From Figure 2 to Figure 4, we notice: 1, The smaller the contrast, the faster the series will converge. When the velocity contrast is getting bigger, the error of α_1 esitmation is getting bigger, so it takes more terms and efforts to deal with the issue; 2, Analytic tests for this 1D acoustic layered model shows that when the reflection coefficient R is smaller than 0.625, this series is always a term-by-term added value improvement towards determining c_1. For example, in Figure 2, as more terms are captured and added up, the error is approaching zero, which means the estimation is getting closer to the actual value of α; when the reflection coefficient is larger than 0.625 as in the other two cases, the series is still convergent, but the

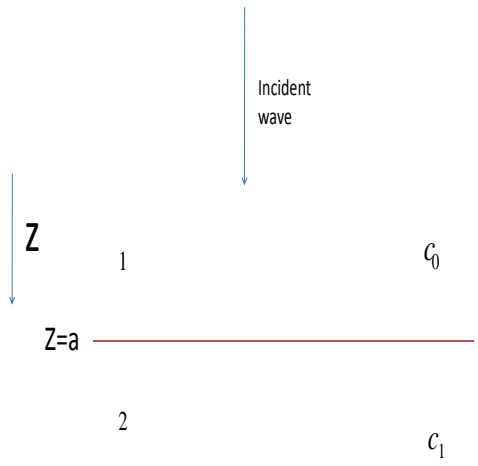

Figure 1: Plane wave incident on a planar interface. 1D accoustic medium with velocites in the two layers as c_0 and c_1.

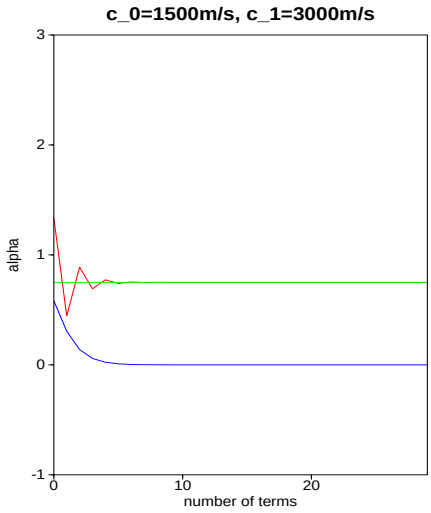

Figure 2: In this case, $c_0 = 1500m/s, c_1 = 3000m/s, \alpha = 0.75$, $R = 0.3333$, where R is the reflection coefficient. The green line represents the actual value of parameter α, the red line shows the n^{th} order estimation, the blue line is the absolute error between the actual value and the estimation.

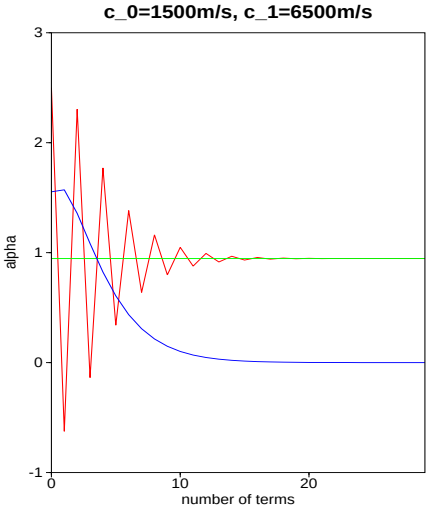

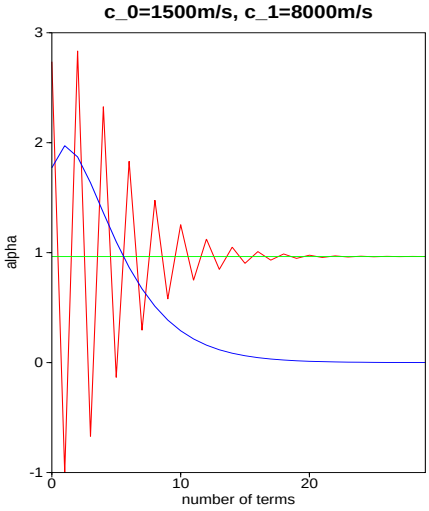

Figure 3: This one shows the case of $c_0 = 1500m/s, c_1 = 6500m/s, \alpha = 0.946746$, $R = 0.625$.

Figure 4: $c_0 = 1500m/s, c_1 = 8000m/s, \alpha = 0.964844$, $R = 0.6842$.

estimation will get worse before it gets better; 3, Each term works towards the final goal, for example, the higher order terms always correct towards the right direction; 4, Sometimes when more terms in the series are included, the estimation looks worse locally (for example, in Figure 3, when α_2 is included, the estimation is worse than α_1; and in Figure 4, when α_3 is included, the estimation is still worse than α_1), as soon as it starts to improve the estimation at a certain order, the results never get worse again, every single term after that order will produce an improved estimation. As we can see from these examples, each term is a team player towards a collective goal, and specific intended function for that term does not depend on what we expect. These favorable properties of target identification are consequences of directness and purposefulness of the entire series, same as the free surface multiple removal algorithms illustrated in Weglein et al. (2003) and depth imaging illustrated in Weglein et al. (2008). This first step study and new results have very important conceptual and practicle implication for direct nonlinear inversion.

3.3 Analysis of forward scattering series

Forward scattering takes the reference medium, the reference wavefield and the perturbation operator as input and outputs the actual wavefield. Matson (1996) showed for a layered model with only velocity variation, the reflection coefficient (R) and transmission coefficient

(T) produced from this scattering model are series in terms of perturbation. When the reference velocity is less than $\sqrt{2}$ times the lowest velocity in the scattering region, the R and T are consistant with the classic results. For the simple example described in previous section, the forward scattering series gives R in terms of $\alpha = 1 - c_0^2/c_1^2$ as follows:

$$R = \frac{1}{4}\alpha + \frac{1}{8}\alpha^2 + \frac{5}{64}\alpha^3 + \cdots . \tag{21}$$

This series will converge if $c_1 > c_0/\sqrt{2}$ (or $R > -0.1716$), and will diverge if $c_1 < c_0/\sqrt{2}$ (or $R < -0.1716$). This result seems a little surprising: for bigger reflection coefficient the series will converge, while for smaller reflection coefficient it will not converge regardless of the velocity contrast between the two layers. In order to better understand the physical meaning behind the simple math, let us rewrite α as follows:

$$\alpha = \frac{c_1^2 - c_0^2}{c_1^2} = \frac{c_1 - c_0}{c_1 + c_0}\frac{(c_1 + c_0)^2}{c_1^2}. \tag{22}$$

The transmission coefficient T from layer 1 to layer 2 is defined as $T = 1 + R$, we have

$$\alpha = 4R/T^2.$$

We notice that the perturbation α is related to the combination of R and T. The convergence of the forward series requires $|\alpha|$ to be less than 1, which means $|4R/T^2|$ should be less than 1. As we find out from last subsection, for the inverse series to be convergent, all it needs is $|R|$ to be less than 1. We have a clear idea about the difference between the convergence conditions for the forward and inverse series. Let us take a closer look at the forward series: Suppose c_0 is fixed and c_1 is at some value that is bigger than $c_0/\sqrt{2}$, when c_1 increases, $4R/T^2$ increases. From equation 22, we can see when c_1 goes to infinity, α goes to 1 but smaller than 1, the convergence of the series always holds; when c_1 decreases, so does $4R/T^2$, but when c_1 is small enough, R starts to change sign and T can be very small, at some point $4R/T^2$ will reach -1 and go beyond that, then this series will diverge.

4 Conclusions

In conclusion, we have analyzed the convergence properties and extended the prevous work on understanding the term-by-term value of ISS multiple removal method to the direct nonlinear target identification. From the analytic examples, we notice that the smaller the contrast the faster the series will converge. For the first time it is shown: for this example, inverse series has more favorable convergence properties than forward series; the inverse series for target identification is convergent for all values of reflection coefficient (R.C.); when R.C. is smaller than 0.625, the series is a term-by-term added value improvement towards determining the unknown lower half-space velocity, otherwise, the estimation will get worse before it gets better. This first step provides us a guideline and will affect our efforts in direct nonlinear inversion as we move to the more complicated elastic world.

5 ACKNOWLEDGMENTS

We are grateful to all M-OSRP sponsors for long-term encouragement and support in this research. All members in M-OSRP are thanked for the help of finishing this paper and valuable discussions in this research program. Dr. Robert Keys from Conocophilips is thanked for providing the important type I AVO parameters.

References

Matson, K. H. "The relationship between scattering theory and the primaries and multiples of reflection seismic data." *Journal of Seismic Exploration* 5 (1996): 63–78.

Shaw, S. A., A. B. Weglein, D. J. Foster, K. H. Matson, and R. G. Keys. "Isolation of a leading order depth imaging series and analysis of its convergence properties." *Journal of Seismic Exploration* 2 (November 2004): 157–195.

Taylor, J. R. *Scattering theory: the quantum theory of nonrelativistic collisions.* John Wiley & Sons, Inc., 1972.

Weglein, A. B., F. V. Araújo, P. M. Carvalho, R. H. Stolt, K. H. Matson, R. T. Coates, D. Corrigan, D. J. Foster, S. A. Shaw, and H. Zhang. "Inverse Scattering Series and Seismic Exploration." *Inverse Problems* (2003): R27–R83.

Weglein, A. B., D. J. Foster, K. H. Matson, S. A. Shaw, P. M. Carvalho, and D. Corrigan. "Predicting the correct spatial location of reflectors without knowing or determining the precise medium and wave velocity: initial concept, algorithm and analytic and numerical example." *Journal of Seismic Exploration* 10 (2002): 367–382.

Weglein, A. B., F. A. Gasparotto, P. M. Carvalho, and R. H. Stolt. "An Inverse-Scattering Series Method for Attenuating Multiples in Seismic Reflection Data." *Geophysics* 62 (November-December 1997): 1975–1989.

Weglein, A. B., A. C. Ramirez, K. A. Innanen, F. Liu, J. E. Lira, and S. Jiang. "The underlying unity of distinct processing algorithms for: (1) the removal of free surface and internal multiples, (2) Q compensation (without Q), (3) depth imaging, and (4) nonlinear AVO, that derive from the inverse scattering series." *SEG Technical Program Expanded Abstracts* 27 (2008): 2481–2486.

Zhang, H. *Direct non-linear acoustic and elastic inversion: Towards fundamentally new comprehensive and realistic target identification.* PhD thesis, University of Houston, 2006.

An unanticipated and immediate AVO by-product (responding to pressing type I and type II AVO challenges) delivered within the ISS imaging program

X. Li, A. B. Weglein, and H. Liang

Abstract

Depth imaging through a complicated geologic overburden is an important and long standing challenge in exploration seismology. Inverse scattering series (ISS) depth imaging subseries has the potential of producing an image of earth directly using only recorded data and reference medium. An 'imaging conjecture' for multi-parameter was proposed by Weglein (2009), pages 1-8, to extend the single parameter imaging algorithm of Shaw et al. (2004) and Liu et al. (2005). A single collective image of a reflectivity like quantity as a function of angle is output as part of the imaging conjecture. We examine this unanticipated AVO by-product for type I and type II AVO targets and applications. In the previous reports (Li et al., 2009; Jiang et al., 2009), we analyzed and tested the 1D analytic example for a two-parameter (velocity and density) acoustic medium. In this report, we follow up the multi-parameter imaging study and show initial elastic results where ISS imaging conjecture not only produces a flat common image gather at correct depth without needing the velocity but also preserve the zero crossing information in reflection coefficient.

1 Introduction

The ISS can achieve all seismic processing objectives (including depth imaging) directly and without subsurface information. The ISS direct depth imaging without the velocity algorithm describes a non-linear relationship between data and the wavefield. Since the goal of our imaging project was to use the ISS for locating structure without knowing any subsurface information, it was reasonable to begin with an earth model that only allowed unknown velocity variations. There are different ISS imaging subseries with different degrees of imaging capture and capability. For example, (Weglein et al., 2000; 2002; 2003), LOIS (Shaw et al., 2003a;b; Innanen, 2003) and HOIS (Liu, 2006) were developed for earth models where only the velocity was variable and was assumed to be initially unknown and remained unknown. LOIS and HOIS refer to the leading and higher order imaging subseries.

In reality, the earth can have rapid and unknown variations in both velocity and density. We want a minimally complicated model that is adequate to achieve our predictive purposes but

not too simple to be unrealistic, nor too complicated to be more than necessary to reach E&P goals. So we need a multi-parameter ISS to study how the depth imaging task is performed in this more realistic and much more complicated earth model. With all current leading-edge imaging methods which require an accurate velocity, only the phase of the reflection data is needed to locate a reflector. In contrast, all ISS objectives can be achieved in the same way that the free surface multiples are removed by using both the amplitude and phase of the events in reflection data. However, the reflections caused by only rapid density variations play no role in the ISS imaging subseries. To eliminate reflections due to density changes only required a generalization of imaging theories developed for modles that only accomodate velocity changes. The ISS imaging method which is called the 'imaging conjecture' (Weglein (2009), pages 1-8) generalizes the velocity only methods by excluding density only changing reflections. Imaging conjecture uses strength and avoids the daunting issues of the multi-parameter inverse series from the multiplicative conversations of events - instead of searching for several separate images for each parameter, it automatically produces a single collective image of a reflectivity like quantity at depth without the velocity.

This unexpected AVO by-product resulted from the imaging conjecture. It automatically produced a reflectivity-like output as a function of angle at the correct depth and with a flat common image gather (CIG) without needing either a velocity model or a trim mean filter to force the flat CIG. In AVO methods there are two steps: (1) create a flat CIG which is an intermediate result before AVO analysis and (2) use $R(\theta)$ for subsequent parameter estimation to determine changes in mechanical properties. In traditional and current AVO work, seeking a flat CIG requires knowledge of the velocity. In practice, the zero crossing information can be damaged through Step 1 by the combination of velocity analysis and "ironing". A serious issue arises for identifying type I and type II AVO targets which have a sign change in reflection coefficient at certain angles. Since ISS imaging can produce a flat CIG without knowing the velocity, is it possible to preserve zero crossing information in reflection coefficient for cases where we have a sensitive issue? Yes, this opportunity and tool developed from the imaging conjecture for automatic flat common image gathers of a reflectivity-like output without the need for ironing and without ironing away polarity reversals. Doug Foster suggested examining the ISS to produce a flat CIG for type I and type II AVO targets. Early tests of that possibility are encouraging.

The development of this new velocity and density varying imaging theory progresses from simple 1D to complex multi-D tests. In this report, we show the ISS imaging results for 1D elastic data which preserve zero crossing information in reflection coefficient at depth without needing the velocity. This AVO by-product of the imaging conjecture will be delivered along with our first imaging field data tests.

2 ISS multi-parameter imaging algorithm

For an earth model with unknown velocity variation only, closed forms of the imaging subseries known as the leading order imaging series (LOIS) (Shaw et al., 2003a) and the higher order imaging series (HOIS) (Liu, 2006) are developed as different degrees of imaging capture and capability:

$$\alpha^{LOIS}(z) = \alpha_1(z - \frac{1}{2}\int_0^z \alpha_1(z')dz'); \tag{1}$$

$$\alpha^{HOIS}(z + \frac{1}{2}\int_0^z \frac{\alpha_1(z')}{1 - 0.25\alpha(z')}dz') = \alpha_1(z). \tag{2}$$

The ISS imaging algorithm has been extended to multi-parameter cases for both acoustic and elastic media. In the following subsections, we will give a brief review of the conjectured imaging algorithm. The effectiveness of the conjecture has been extended to include ISS imaging terms beyond that initial imaging capability within a multi-parameter acoustic world (Wang et al., 2010).

2.1 Imaging conjecture for multi-parameter acoustic

In previous reports (Li et al., 2009; Jiang et al., 2009), imaging conjecture for acoustic data has been analyzed and tested. Let us review the extended imaging algorithm for an 1D two parameter acoustic earth model first (e.g. bulk modulus and density or velocity and density). Starting with the 3D acoustic wave equations for reference and actual medium:

$$[\frac{\omega^2}{K_0(r)} + \nabla \cdot \frac{1}{\rho_0(r)}\nabla]G_0(\mathbf{r}, \mathbf{r_s}; \omega) = \delta(\mathbf{r} - \mathbf{r_s}), \tag{3}$$

$$[\frac{\omega^2}{K(r)} + \nabla \cdot \frac{1}{\rho(r)}\nabla]G(\mathbf{r}, \mathbf{r_s}; \omega) = \delta(\mathbf{r} - \mathbf{r_s}). \tag{4}$$

where G_0 and G are the reference and actual Green's functions respectively. $K = c^2\rho$, is P-bulk modulus, c is P-wave velocity, and ρ is density. The subscript 0 represents those variables in the reference medium.

The perturbation is:

$$V = L_0 - L = \frac{\omega^2\alpha}{K_0} + \nabla \cdot \frac{\beta}{\rho_0}\nabla, \tag{5}$$

where $\alpha = 1 - \frac{K_0}{K}$ and $\beta = 1 - \frac{\rho_0}{\rho}$ are the two parameters we are going to use. $V(z, \nabla)$, $\alpha(z)$ and $\beta(z)$ can be expanded in terms of recorded data (Weglein et al., 2003) respectively as:

$$V(z, \nabla) = V_1(z, \nabla) + V_2(z, \nabla) + \cdots, \tag{6}$$

$$\alpha(z) = \alpha_1(z) + \alpha_2(z) + \cdots, \tag{7}$$

$$\beta(z) = \beta_1(z) + \beta_2(z) + \cdots. \tag{8}$$

Based on inverse scattering series, the second order approximation for the parameters was calculated in Zhang and Weglein 2005 for a layered acoustic media with both velocity and density changes, the imaging-only term in the second order ISS equation was identified as:

$$-\frac{1}{2}\frac{1}{\cos^2\theta}[\frac{1}{\cos^2\theta}\alpha_1'(z) + (1-\tan^2\theta)\beta_1'(z)]\int_{-\infty}^{z}[\alpha_1(z') - \beta_1(z')]dz'. \tag{9}$$

Substituting $\alpha_1(z)$ of one parameter case shown in Eq.(2) with $\alpha_1(z)-\beta_1(z)$ of multiparameter case, we have the conjectured imaging algorithm for the latter one as:

$$\mathscr{D}^{HOIS}(z + \int_{-\infty}^{z}\frac{[\alpha_1(z') - \beta_1(z')]dz'}{\cos^2\theta - 0.25\cdot[\alpha_1(z') - \beta_1(z')]}, \theta) = D(z,\theta), \tag{10}$$

where:

$$D(z,\theta) = -\frac{\rho_0}{4}(\frac{1}{\cos^2\theta}\alpha_1(z) + (1-\tan^2\theta)\beta_1(z)), \tag{11}$$

which is a composite dataset rescaled from the data after a constant velocity migration $\mathscr{D}^{HOIS}(z,\theta) = -\frac{4}{\rho_0}D(z,\theta)$.

2.2 Imaging conjecture for multi-parameter elastic

Based on the imaging conjecture proposed by Weglein, the multi-parameter acoustic imaging closed-form has been extended to multi-parameter elastic (Jiang et al., 2009).

For a 1D three-parameter elastic, PP data only:

$$\mathscr{D}^{HOIS}(z + \frac{1}{2}\int_{-\infty}^{z}\frac{a_\gamma^{(1)}(z') - a_\rho^{(1)}(z')}{\cos^2\theta - 0.25(a_\gamma^{(1)}(z') - a_\rho^{(1)}(z'))}dz') = D^{PP}(z,\theta) \tag{12}$$

where:

$$D^{PP}(z,\theta) = -\frac{1}{4}(1+\tan^2\theta)a_\gamma^{(1)}(z) - \frac{1}{4}(1-\tan^2\theta)a_\rho^{(1)}(z) + 2\frac{\beta_0^2\sin^2\theta}{\alpha_0^2}a_\mu^{(1)}(z). \tag{13}$$

The composite dataset output from the imaging conjecture is $\mathscr{D}^{HOIS}(z,\theta) = -4D^{PP}(z,\theta)$.

2.3 Multi-parameter AVO front end

In the conjectured imaging algorithm for acoustic data, the two parameters (velocity and density) will be imaged as a composite form, which means instead of distinguishing the details of the changed information (velocity change or density change), the imaging task recognizes them as a combined form linear in the recorded data. The next step is to preprocess the amplitude information for $\alpha_1 - \beta_1$ which is called the multi-parameter front end for imaging. From the first order ISS equation for 1D two-parameter acoustic case, choosing two different angles to solve for $\alpha_1 - \beta_1$ (Zhang, 2006):

$$\alpha_1(z) - \beta_1(z) = 4\frac{D(z,\theta_1) - D(z,\theta_2)}{\tan^2\theta_1 - \tan^2\theta_2}. \tag{14}$$

The extended imaging conjecture for elastic follows the same logic and avoids seeking for three separate images for bulk modulus, shear modulus, and density. If only given D^{PP}, there are three unknowns but only one equation, see in Eq. (13). So we choose three angles to solve for $a_\gamma^{(1)} - a_\rho^{(1)}$ (Zhang, 2006).

3 Analytic examples: Polarity reversals in a reflection from an elastic interface

Polarity reversals in seismic reflection provide information of an important type of AVO targets. To obtain the flat common image gather as well as preserve this information is necessary. We talked about polarity reversals for an acoustic interface in Li et al. (2009). Now we extend this study to an elastic model. The following two models are analyzed to show the ISS imaging results have presesrved the zero crossing information for reflection coefficient at depth without needing the velocity. In these two elastic models, the data is prestack PP data. $D(x,t)$ is the shot record and the reference P wave velocity depth image is $D(z,\theta)$, where z is depth and $\theta = \sin^{-1}(\frac{k_x}{\omega/c_0})$, where k_x and ω are the conjugates of x and t and c_0 is the constant reference P wave velocity.

There is only an imaging contribution required of the ISS if the actual velocity varies and the input velocity is assumed to be constant. In the first model (Figure 1), the velocities V_p and V_s in the first and second layers do not change. The velocity above the first reflector is the reference velocity. For this model, when we use the reference velocity which is the correct velocity, there is no imaging issues for the second reflector. The reference P wave velocity image (left) will give the correct location of the reflectors. We can see in Figure 2, ISS imaging conjecture (right) still provides the result which agrees with the constant velocity image (red line represents the correct location). To look at the detailed amplitude information at depth, $\frac{\partial D}{\partial z}$ is shown for model I in Figure 3. We only focus on the second interface at which the reflection coefficient as a function of angle experiences a zero crossing. The part that we

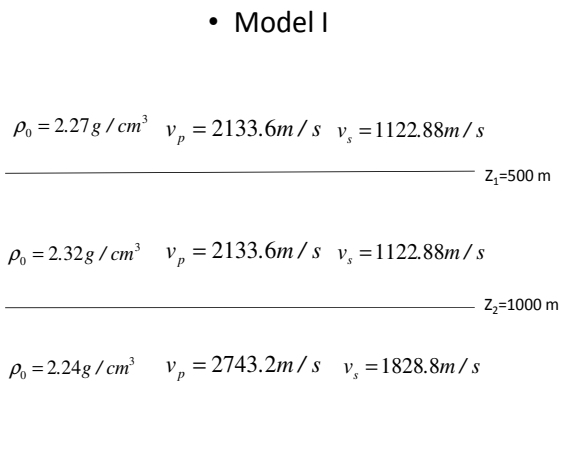

Figure 1: Elastic model I with type I AVO at the second reflector and zero crossing in reflection coefficient happens at $\theta = 28.45°$. V_p and V_s do not change, only density change across the first reflector.

are interested in has been enlarged. Notice that the zero crossing information for the second reflector has been preserved. For the second model (in Figure 4) where ρ, V_p and V_s all change. When we image the data using the reference velocity above the first reflector, we are using a wrong velocity, there is a mislocation for the second interface as shown in Figure 5 ISS imaging conjecture moves the second reflector to correct location (red line represents the correct location). Figure 6 displays the zero crossing information for model II and again we notice that the imaging result preserves zero crossing information in AVO targets at depth without needing the velocity.

4 Conclusions

In conclusion, this report follows up on the previous work regarding multi-parameter acoustic study. We tested the more complicated elastic case where the ISS imaging results preserve zero crossing information and signs in reflection coefficient at depth without needing the velocity. To get a flat common image gather and to identify type I and type II AVO targets is an intermediate step towards parameter estimation. We are providing an important results under the circumstances that even this intermediate step is difficult to achieve. This AVO by-product resulted from imaging conjecture will be delivered along with our first imaging field data test.

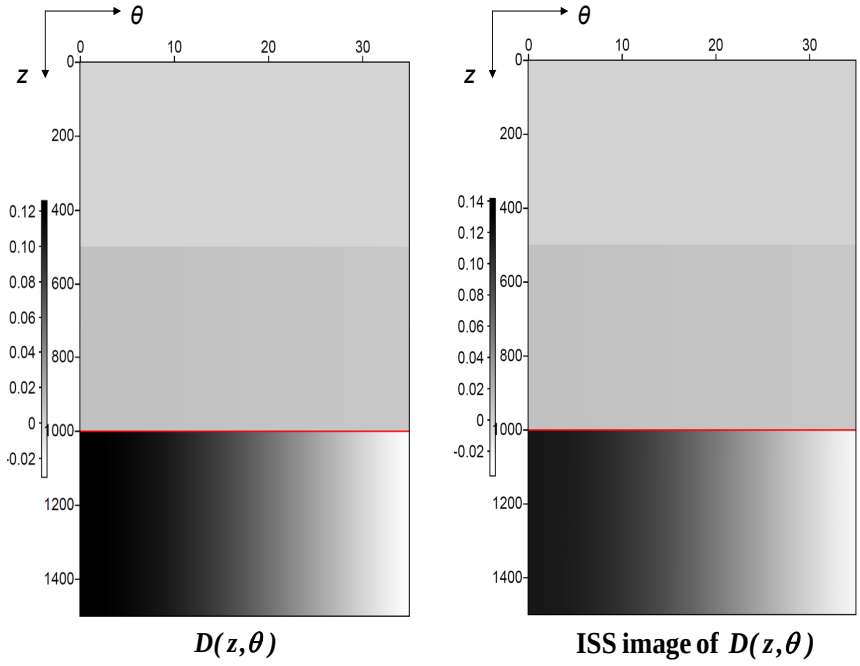

Figure 2: The figure on the left shows data $D(z, \theta)$ imaged with reference P wave velocity for model I, and the figure on the right shows the HOIS image of $D(z, \theta)$.

5 ACKNOWLEDGMENTS

We are grateful to all M-OSRP sponsors for long-term encouragement and support in this research. All members in M-OSRP are thanked for the help of finishing this paper and valuable discussions in this research program. Dr. Robert Keys from Conocophilips is thanked for providing the important type I AVO parameters.

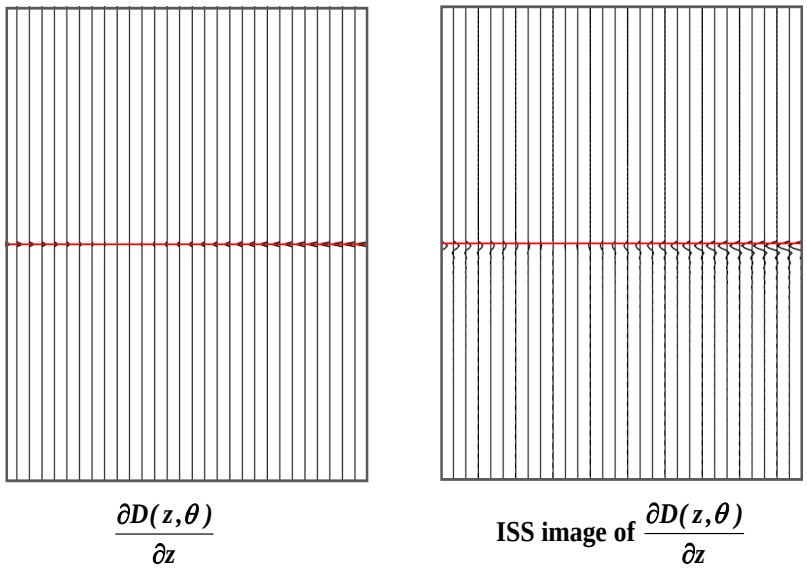

Figure 3: The figure on the left shows $\frac{\partial D(z,\theta)}{\partial z}$ imaged with reference P wave velocity, and the figure on the right shows the HOIS iamge of $\frac{\partial D(z,\theta)}{\partial z}$. We only enlarge the part at second reflector that has the information of zero crossing. We notice that the zero crossing information is preserved after HOIS.

References

Innanen, Kristopher. A. *Methods for the treatment of acoustic and absorptive/dispersive wave field measurements*. PhD thesis, University of British Columbia, 2003.

Jiang, S., A. B. Weglein, and S. A. Shaw. "Progressing multiparameter imaging using the inverse scattering series: An initial analytic test of the leading order imaging subseries (LOIS) closed form and its extended higher order imaging subseries (HOIS) closed form for a laterally invariant two-parameter acoustic medium." *2008 M-OSRP Annual Report* (2009): 91–113.

Li, X., F. Liu, S. Jiang, and A. B. Weglein. "Depth imaging without the velocity cares about the phase and amplitude information of events: Focusing on the use of the angle dependent amplitude information of events." *2008 M-OSRP Annual Report* (2009): 114–128.

Liu, F. *Multi-dimensional depth imaging without an adequte velocity model*. PhD thesis, University of Houston, 2006.

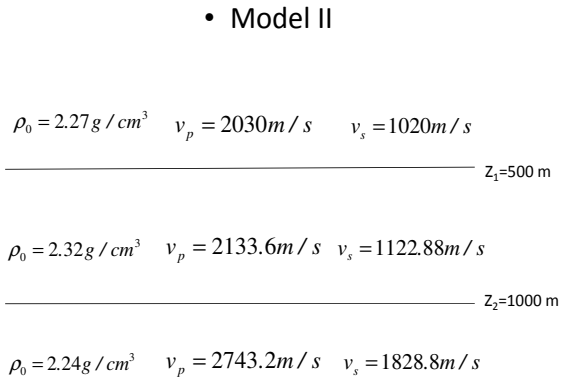

Figure 4: Elastic model II with type I AVO at the second reflector and zero crossing in reflection coefficient happens at $\theta = 26.95°$. V_p and V_s and density all change across the first reflector.

Liu, F., A.B. Weglein, K.A. Innanen, and B.G Nita. "Extension of the non-linear depth imaging capability of the inverse scattering series to multidimensional media: strategies and numerical results." 2005.

Shaw, S. A., A. B. Weglein, D. J. Foster, K. H. Matson, and R. G. Keys. "Convergence properties of a leading order depth imaging series." *73rd Annual Internat. Mtg., Soc. Expl. Geophys., Expanded Abstracts*. . Soc. Expl. Geophys., 2003. 937–940.

Shaw, S. A., A. B. Weglein, D. J. Foster, K. H. Matson, and R. G. Keys. "Isolation of a leading order depth imaging series and analysis of its convergence properties." *2002 M-OSRP Annual Report* 2 (2003): 157–195.

Shaw, S. A., A. B. Weglein, D. J. Foster, K. H. Matson, and R. G. Keys. "Isolation of a leading order depth imaging series and analysis of its convergence properties." *Journal of Seismic Exploration* 2 (November 2004): 157–195.

Weglein, A. B. "M-OSRP 2008 Introduction and Preface." *2008 M-OSRP Annual Report* (2009): 1–8.

Weglein, A. B., F. V. Araújo, P. M. Carvalho, R. H. Stolt, K. H. Matson, R. T. Coates, D. Corrigan, D. J. Foster, S. A. Shaw, and H. Zhang. "Inverse scattering series and seismic exploration." *Inverse Problems* 19 (2003): R27–R83.

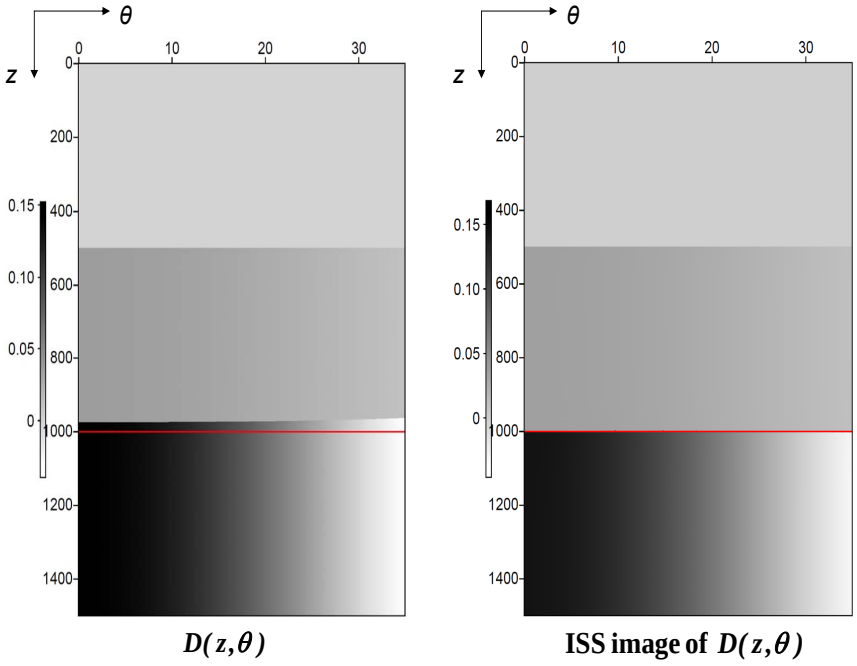

Figure 5: The figure on the left shows data $D(z,\theta)$ imaged with reference P wave velocity for model II, and the figure on the right shows the HOIS image of $D(z,\theta)$.

Weglein, A. B., F. V. Araújo, P. M. Carvalho, R. H. Stolt, K. H. Matson, R. T. Coates, D. Corrigan, D. J. Foster, S. A. Shaw, and H. Zhang. "Inverse Scattering Series and Seismic Exploration." *Inverse Problems* (2003): R27–R83.

Weglein, A. B., D. J. Foster, K. H. Matson, S. A. Shaw, P. M. Carvalho, and D. Corrigan. "Predicting the correct spatial location of reflectors without knowing or determining the precise medium and wave velocity: initial concept, algorithm and analytic and numerical example." *Journal of Seismic Exploration* 10 (2002): 367–382.

Weglein, A. B., K. H. Matson, D. J. Foster, P. M. Carvalho, D. Corrigan, and S. A.Shaw. "Imaging and inversion at depth without a velocity model: Theory, concepts and initial evaluation." *70th Annual Internat. Mtg., Soc. Expl. Geophys., Expanded Abstracts.* . Soc. Expl. Geophys., 2000. 1016–1019.

Zhang, H. *Direct non-linear acoustic and elastic inversion: Towards fundamentally new comprehensive and realistic target identification.* PhD thesis, University of Houston, 2006.

Zhang, H. and A.B. Weglein. "The inverse scattering series for tasks associated with primaries: depth

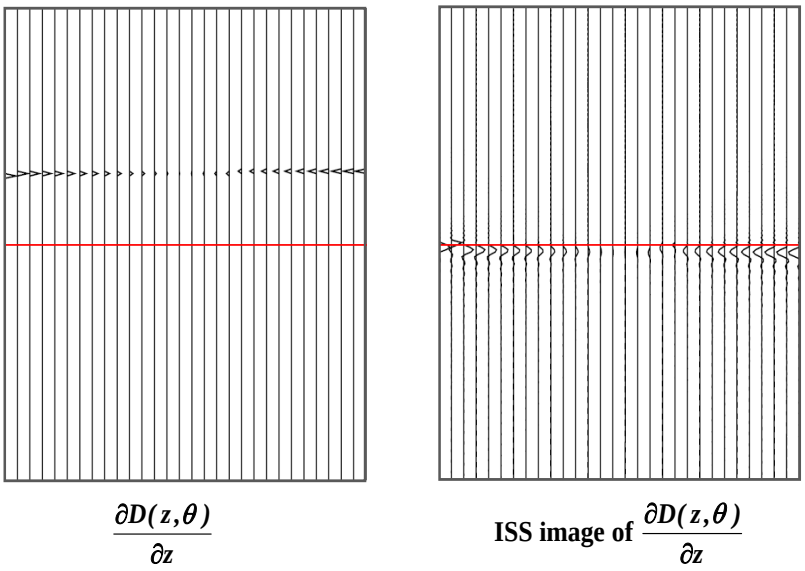

Figure 6: The figure on the left shows $\frac{\partial D(z)}{\partial z}$ imaged with reference P wave velocity, and the figure on the right shows the HOIS iamge of $\frac{\partial D(z,\theta)}{\partial z}$. We only enlarge the part at second reflector that has the information of zero crossing. We notice that the zero crossing information is preserved after HOIS.

imaging and direct non-linear inversion of 1D variable velocity and density acoustic media." *SEG Technical Program Expanded Abstracts*. 2005, 1705–1708.

Initial tests for the impact of matching and mismatching between the earth model and the processing model for the ISS imaging and parameter estimation

H. Liang, A. B. Weglein and X. Li, M-OSRP, University of Houston

Abstract

The objective of seismic processing is to determine the structure and the properties of the subsurface from the recorded wavefield. To invert for medium properties requires the specification of the parameters to be identified. The choice of the type and number of the parameters defines an earth model type (e.g., acoustic, elastic, isotropic, anisotropic) (Weglein et al., 2003). In both current conventional seismic processing and the new platform inverse scattering series (ISS) imaging and parameter estimation, there are significant implications for having a mismatch between the model that generates the data and the model assumed in the processing algorithms. In this report, we focus on examining the effect of such a mismatch for the ISS approaches. The numerical tests of the 1D three-parameter analytic elastic data, using the ISS imaging conjecture and inversion for both acoustic and elastic media, confirm that it is important to match the processing algorithm's model type to the data model for ISS imaging and inversion application.

1 Introduction

All inversion methods for identifying subsurface properties require specification of the assumed earth model that generates the data. In this report, 'model type' indicates the choice of the type and number of the medium properties which describe how the waves propagate in the subsurface. Choosing medium parameters depends on: (1) processing goal and (2) the algorithm to achieve that goal. For instance, regarding the goal of depth imaging, the conventional imaging algorithms need both the arrival time and velocity to locate reflectors; whereas, the ISS imaging algorithms take advantage of both the time and amplitude information without knowing the velocity. In the context of seismic exploration, we especially investigate the consequences of having a mismatch between the model that generate the data and the model assumed in the processing algorithms for ISS imaging and parameter estimation.

The inverse scattering series has the potential to perform all tasks associated with inversion without knowing the subsurface information (Weglein et al., 2003). Within the overall series,

certain subseries each performs one specific task and acts as if no other tasks exist. The order of the tasks performed using the inverse scattering series is: (1) free surface multiple removal, (2) internal multiple removal, (3) depth imaging, and (4) parameter estimation. The first two tasks are model type independent, i.e., the algorithms for achieving these two tasks are precisely the same for a very big class of earth model types. For imaging primaries, a model type independent ISS depth imaging algorithm is not yet developed. There will never be a model type independent parameter estimation algorithm since we need to determine which parameters to invert in order to predict the medium and target properties.

For locating structures using the ISS, the procedure begins with an earth model with velocity variation only. The single-parameter ISS leading order (LOIS) (Shaw et al., 2002) and extended higher order (HOIS) (Liu, 2006) imaging algorithms can achieve the imaging objective to a certain degree. However, these algorithms would fail if the medium has important density variations. Then a multi-parameter imaging 'conjecture' was proposed by Weglein to accommodate that special case. The leading order closed form imaging conjecture was validated by Jiang and Weglein (2008) and an extended higher order closed form was tested in the 2008 M-OSRP annual reports (Li et al., 2009; Jiang and Weglein, 2009). This imaging conjecture has also been extended to accommodate the 1D three-parameter elastic earth model with P wave velocity, S wave velocity, and density all varying.

In a context where the choice of model type is of fundamental importance, it is reasonable to ask how the adequacy of such choice could be assessed. From our point of view, a model is adequate if a less complicated model would decrease its drilling success and a more complicated model would not improve its efficacy of drilling. In this report, we use the minimally realistic earth model to achieve our processing goals, the isotropic elastic model.

In this report we consider analytic data examples. For linear estimation of parameters, the elastic data are first run through the acoustic two-parameter inversion and then run through elastic three-parameter inversion; as for locating structure, a three-layer elastic data model is first assumed as acoustic and imaged using acoustic imaging conjecture, then the results are compared with the elastic imaging conjecture results. Section 1 briefly introduces the model type issues within the overall inverse scattering series and the history of the inverse scattering imaging algorithms. In Section 2, we describe the inverse scattering series in general. Section 3 gives the background for both direct inversion and multi-parameter conjectured imaging algorithms, providing numerical test results for the issue of mismatching. Section 4 is our conclusions.

2 Inverse scattering series

Consider the two differential equations which describe how waves propagate in actual medium and reference medium:

$$LG = \delta \tag{1}$$

$$L_0 G_0 = \delta \tag{2}$$

where L, L_0 and G, G_0 are respectively the differential operators and Green functions in the actual and reference medium. We define the perturbation $V = L_0 - L$. The Lippmann-Schwinger equation is:

$$G = G_0 + G_0 V G \tag{3}$$

Iterating Equation (3) back into itself produces the Born series:

$$G = G_0 + G_0 V G_0 + G_0 V G_0 V G_0 + \cdots \tag{4}$$

The scattered field $\psi_s = G - G_0$ can be defined as:

$$\begin{aligned} \psi_s &= G_0 V G_0 + G_0 V G_0 V G_0 + G_0 V G_0 V G_0 V G_0 + \cdots \\ &= (\psi_s)_1 + (\psi_s)_2 + (\psi_s)_3 + \cdots \end{aligned} \tag{5}$$

where $(\psi_s)_n$ is the portion of ψ_s that is n^{th} order in V. The measured value of ψ_s is the data D, where $D = (\psi_s)_{ms} = (\psi_s)_{\text{on the measurement surface}}$. Expanding V as a series in orders of D yields:

$$V = V_1 + V_2 + V_3 + \cdots \tag{6}$$

where V_n is n^{th} order in D. Substituting the Equation (6) into the Equation (5) evaluating and setting the same order of the data equal on both sides of equation on the measurement surface yields:

$$D = [G_0 V_1 G_0]_{ms} \tag{7}$$

$$0 = [G_0 V_2 G_0]_{ms} + [G_0 V_1 G_0 V_1 G_0]_{ms} \tag{8}$$

$$\begin{aligned} 0 =& [G_0 V_3 G_0]_{ms} + [G_0 V_1 G_0 V_2 G_0]_{ms} \\ &+ [G_0 V_2 G_0 V_1 G_0]_{ms} + [G_0 V_1 G_0 V_1 G_0 V_1 G_0]_{ms} \end{aligned} \tag{9}$$

$$\vdots$$

The inverse scattering series provides a direct method for obtaining the subsurface information by inverting the series order by order to solve for the perturbation operator V using only the measured data D and a reference wave field G_0.

3 Direct inversion and multi-parameter imaging conjecture algorithms

3.1 Multi-parameter direct inversion

In this section, we review the linear estimation of parameters using ISS for 1D acoustic and elastic media (Zhang, 2006). It is assumed that the aoucstic medium varies in two parameters (velocity and density); whereas, the elastic medium varies in three parameters (P wave velocity, S wave velocity, and density).

3.1.1 Two parameter acoustic inversion

We begin with the 3D acoustic wave equations in the actual and reference medium (Clayton and Stolt, 1981; Weglein et al., 1997):

$$[\frac{\omega^2}{K(\mathbf{r})} + \bigtriangledown \cdot \frac{1}{\rho(\mathbf{r})} \bigtriangledown] G(\mathbf{r}, \mathbf{r}_s; \omega) = \delta(\mathbf{r} - \mathbf{r}_s) \tag{10}$$

$$[\frac{\omega^2}{K_0(\mathbf{r})} + \bigtriangledown \cdot \frac{1}{\rho_0(\mathbf{r})} \bigtriangledown] G_0(\mathbf{r}, \mathbf{r}_s; \omega) = \delta(\mathbf{r} - \mathbf{r}_s) \tag{11}$$

where $G(\mathbf{r}, \mathbf{r}_s; \omega)$ and $G_0(\mathbf{r}, \mathbf{r}_s; \omega)$ are respectively the free-space causal Green's functions which describe wave propagation in the actual and reference mediums. $K = c^2\rho$ is P-wave bulk modulus, c is P-wave velocity, and ρ is density. The quantities with subscript 0 are for the reference medium and those without the subscript are for the actual medium.

The perturbation operator is therefore defined as:

$$V = L_0 - L = \frac{\omega^2 \alpha}{K_0} + \bigtriangledown \cdot \frac{\beta}{\rho_0} \bigtriangledown \tag{12}$$

where $\alpha = 1 - \frac{K}{K_0}$ and $\beta = 1 - \frac{\rho}{\rho_0}$ are the two parameters we choose to invert. For the 1-D case, the perturbation V has the following form:

$$V(z, \bigtriangledown) = \frac{\omega^2 \alpha(z)}{K_0} + \frac{1}{\rho_0}\beta(z)\frac{\partial^2}{\partial x^2} + \frac{1}{\rho}\frac{\partial}{\partial z}\beta(z)\frac{\partial}{\partial z} \tag{13}$$

$V(z, \bigtriangledown)$, $\alpha(z)$ and $\beta(z)$ can be expanded as:

$$V(z, \bigtriangledown) = V_1(z, \bigtriangledown) + V_2(z, \bigtriangledown) + V_3(z, \bigtriangledown) + \cdots \tag{14}$$

$$\alpha(z) = \alpha_1(z) + \alpha_2(z) + \alpha_3(z) + \cdots \tag{15}$$
$$\beta(z) = \beta_1(z) + \beta_2(z) + \beta_3(z) + \cdots \tag{16}$$

Then the linear term in V is:

$$V_1(z, \bigtriangledown) = \frac{\omega^2 \alpha_1(z)}{K_0} + \frac{1}{\rho_0}\beta_1(z)\frac{\partial^2}{\partial x^2} + \frac{1}{\rho}\frac{\partial}{\partial z}\beta_1(z)\frac{\partial}{\partial z} \tag{17}$$

Substituting Equation (17) into Equation (7), we can obtain the linear solution for α_1 and β_1 in frequency domain:

$$\tilde{D}(q_g, \theta, z_g, z_s) = -\frac{\rho_0}{4} e^{-iq_g(z_s+z_g)} \left[\frac{1}{\cos^2\theta} \tilde{\alpha_1}(-2q_g) + (1 - \tan^2\theta)\tilde{\beta}_1(-2q_g) \right] \tag{18}$$

where the subscripts s and g denote source and receiver quantities respectively, θ is the incidence angle, q_g is the receiver vertical wave number, and $q_g = \frac{\omega}{c}\cos\theta$. For a one-interface case, it is assumed the interface surface is at depth $z = a$ and suppose $z_g = z_s = 0$. Using the analytic data:

$$\tilde{D}(q_g, \theta) = \rho_0 R(\theta) \frac{e^{2iq_g a}}{4\pi i q_g} \tag{19}$$

After Fourier transform over $2q_g$, for fixed θ we get:

$$\frac{1}{\cos^2\theta}\alpha_1(z) + (1 - \tan^2\theta)\beta_1(z) = 4R(\theta)H(z - a) \tag{20}$$

Choosing two different angles, α_1 and β_1 can be solved. The linear estimation of the relative change in P-wave velocity is (Zhang, 2006):

$$\left(\frac{\triangle c}{c}\right)_1 = \frac{1}{2}(\alpha_1 - \beta_1) \tag{21}$$

3.1.2 Three parameter elastic inversion

In this section we consider the linear estimation of parameters for 1D elastic medium. In the PS domain (Weglein et al., 1997), the perturbation is given by $\hat{V} = \begin{pmatrix} \hat{V}^{PP} & \hat{V}^{PS} \\ \hat{V}^{SP} & \hat{V}^{SS} \end{pmatrix}$, the Green's operator by $\hat{G}_0 = \begin{pmatrix} \hat{G}_0^P & 0 \\ 0 & \hat{G}_0^S \end{pmatrix}$, and data by $\hat{D} = \begin{pmatrix} \hat{D}^{PP} & \hat{D}^{PS} \\ \hat{D}^{SP} & \hat{D}^{SS} \end{pmatrix}$. Three parameters are chosen to be inverted: $a_\rho = \frac{\rho}{\rho_0} - 1$, $a_\gamma = \frac{\gamma}{\gamma_0} - 1$ and $a_\mu = \frac{\mu}{\mu_0} - 1$, where:

$$\rho = \text{density}$$

γ = bulk modulus $\rho\alpha^2$ (where α = P-wave velocity)

μ = shear modulus $\rho\beta^2$ (where β = S-wave velocity)

We consider only PP data in this report. Assuming source and receiver depths are zero, we can get the equation relating the linear components of the three elastic parameters and D^{PP} in the frequency domain (Zhang and Weglein, 2006):

$$\tilde{D}^{PP}(\nu_g,\theta) = -\frac{1}{4}(1-\tan^2\theta)\tilde{a}_\rho^{(1)}(-2\nu_g) - \frac{1}{4}(1+\tan^2\theta)\tilde{a}_\gamma^{(1)}(-2\nu_g) + \frac{2\beta_0^2}{\alpha_0^2}\sin^2\theta\tilde{a}_\mu^{(1)}(-2\nu_g) \quad (22)$$

Where θ is the incident angle and ν_g is the receiver vertical wave number, $\nu_g = \frac{\omega}{\alpha_0}\cos\theta$. Similar to the acoustic case, using the analytic data:

$$\tilde{D}^{PP}(\nu_g,\theta) = R^{PP}(\theta)\frac{e^{2i\nu_g a}}{4\pi i\nu_g} \quad (23)$$

After Fourier transform over $2\nu_g$, for fixed θ we have:

$$(1-\tan^2\theta)a_\rho^{(1)}(z) + (1+\tan^2\theta)a_\gamma^{(1)}(z) - 8\frac{\beta_0^2}{\alpha_0^2}\sin^2\theta a_\mu^{(1)}(z) = 4R^{pp}(\theta)H(z-a) \quad (24)$$

Choosing three different angles, $a_\rho^{(1)}$, $a_\gamma^{(1)}$, and $a_\mu^{(1)}$ can be solved. The linear estimation of the relative change in P-wave velocity is (Zhang, 2006):

$$\left(\frac{\triangle c}{c}\right)_1 = \frac{1}{2}(a_\gamma^{(1)} - a_\rho^{(1)}) \quad (25)$$

3.2 Numerical tests for acoustic and elastic inversion

In this section, a 1D two-layer elastic model to be tested is shown in Figure 1. We consider only one primary reflected from the reflector and assume that all the other seismic events (ghosts, free surface multiples, and internal multiples) have been removed. The analytic data has been shown in Equation (23). After Fourier transform over $2\nu_g$, we have:

$$D^{PP}(z,\theta) = R^{PP}(\theta)H(z-a) \quad (26)$$

where a is the depth of the reflector.

We first assume the data model is acoustic and use the acoustic inversion algorithm in Section 3.1.1 to obtain the linear estimation of P wave velocity change $(\frac{\triangle c}{c})_1 = \frac{1}{2}(\alpha_1 - \beta_1)$ from the inversion of elastic data. Then the elastic inversion algorithm is implemented and the linear

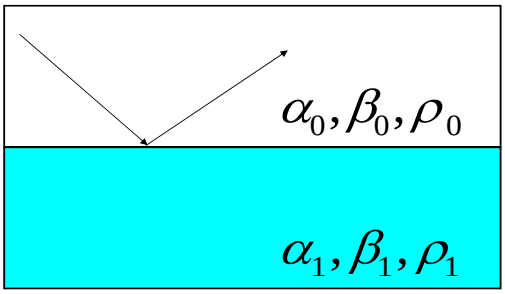

Figure 1: *A figure of a 1D two-layer elastic model with both P and S wave velocity change as well as density variation.*

estimation of P wave velocity change $(\frac{\triangle c}{c})_1 = \frac{1}{2}(a_\gamma^{(1)} - a_\rho^{(1)})$ is obtained. Then three examples are given and the numerical results for the two cases are compared.

From Figure 2, we notice that when the real value of P wave velocity change is 0.071, the two-parameter acoustic inversion of velocity changes range from -0.45 to -0.15; whereas, the elastic inversion result ranges from 0.06 to 0.074. The elastic inversion result is much closer to the exact value. In Figure 3, when the P wave velocity decreases the elastic inversion result is still better than the acoustic inversion. In Figure 4, when the change of the P wave velocity is zero, the elastic inversion result is significantly close to zero and it is still better than the acoustic inversion result.

3.3 Multi-parameter conjectured imaging algorithm

The ISS imaging subseries addresses depth imaging in a circumstantial nonlinear way (Weglein et al., 2009): if an accurate velocity model is given the ISS depth imaging is a linear problem; otherwise, the ISS would process depth imaging nonlinearly in terms of the data and without knowing the velocity. The first term in the ISS imaging subseries is the linear imaging result migrated using the reference velocity. The first nonlinear term in the subseries decides before it acts if there is a issue in the data. If so, it will light up and indicate that the higher order terms should go into action; otherwise, it will shut down immediately and signal to the higher order terms that there's nothing for them to do with the data. This is one of the intriguing properties that the inverse scattering series possesses.

With the above background, we can take a look at the first nonlinear term in the imaging subseries for the 1D two-parameter acoustic medium:

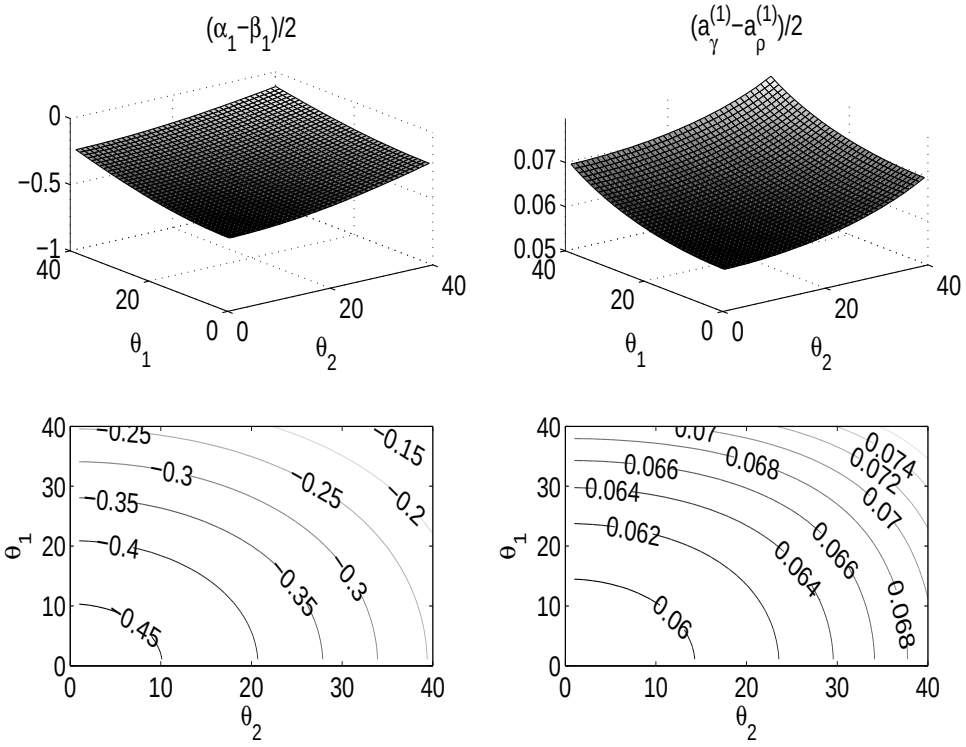

Figure 2: *Inversion comparison 1: the left two figures are the results of two-parameter acoustic inversion, the right figures are results using three-parameter elastic inversion, the lower figures are the contour of the upper figures. The parameters for the data model are:* ρ_0*=2.4g/cm*^{3}*,* ρ_1*=2.8g/cm*^{3}*;* c_{p0}*=2600m/s ,* c_{p1}*=2800m/s;* c_{s0}*=1500m/s,* c_{s1}*=1700m/s, with a exact value of velocity change 0.071.*

$$-\frac{1}{2}\frac{1}{\cos^2\theta}\left(\frac{1}{\cos^2\theta}\alpha_1'(z)+(1-\tan^2\theta)\beta_1'(z)\right)\int_{-\infty}^{z}[\alpha_1(z')-\beta_1(z')]dz'$$

The integral of $\alpha_1(z)-\beta_1(z)$ which only takes care of the velocity change will shut down if there is no velocity change in the medium. This means that there is no imaging task needed if the reference velocity is exactly the actual velocity. If and only if the reference velocity is different with the actual velocity, this term and the higher order terms will be turned on to move the reflector towards the correct location nonlinearly in terms of the data and without knowing the velocity.

Collecting the similar terms in the first nonlinear imaging term for the 1D three-parameter elastic mdium, we have:

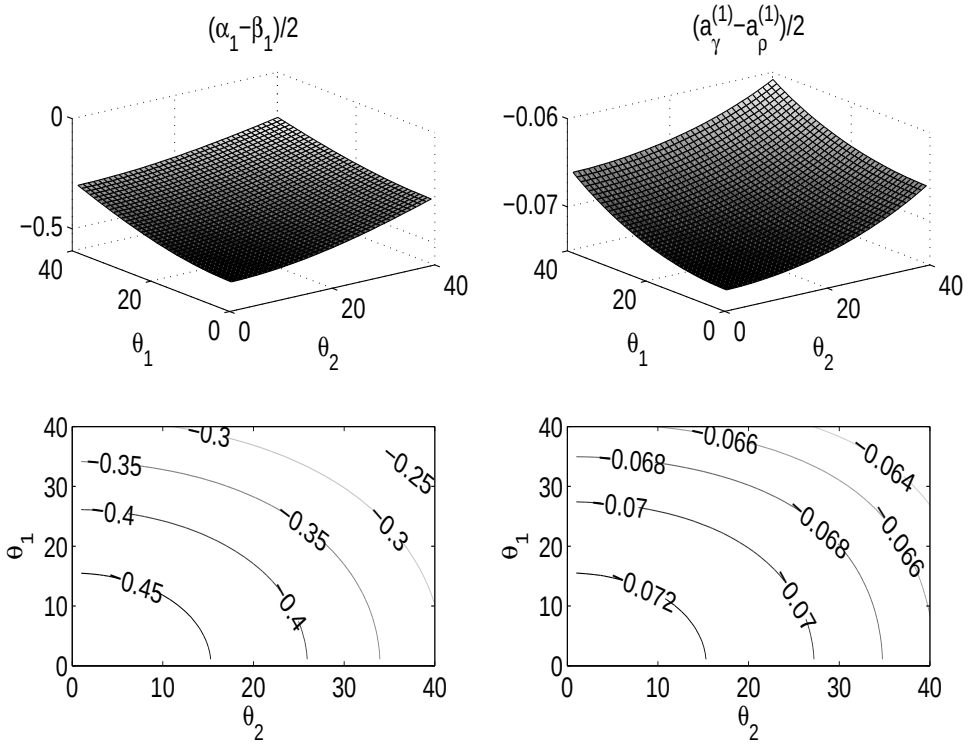

Figure 3: *Inversion comparison 2: the left two figures are the results of two-parameter acoustic inversion, the right figures are results using three-parameter elastic inversion, the lower figures are the contour of the upper figures. The parameters for the data model are:* ρ_0*=2.4 g/cm*^{3}*,* ρ_1*=2.8g/cm*^{3}*;* c_{p0}*=3000m/s,* c_{p1}*=2800m/s;* c_{s0}*=1500m/s,* c_{s1}*=1700m/s, with a exact value of velocity change -0.071.*

$$-\frac{1}{2}\frac{1}{\cos^2\theta}[\frac{1}{\cos^2\theta}a_\gamma^{(1)'}(z)+(1-\tan^2\theta)a_\rho^{(1)'}(z)-8\frac{\beta_0^2}{\alpha_0^2}\tan^2\theta a_\nu^{(1)'}(z)]\int_{-\infty}^{z}[a_\gamma^{(1)}(z')-a_\rho^{(1)}(z')]dz'$$

The logic and philosophy in the elastic case is similar as in the acoustic case. The integral of $a_\gamma^{(1)}(z)-a_\rho^{(1)}(z)$ which only takes care of the P wave velocity changes will be zero if only density changes in the medium.

Based on what has been discussed above and the one parameter HOIS imaging algorithm, the imaging conjecture for multi-parameter acoustic and elastic media has been proposed and confirmed. It has a multi-parameter front end which is a linear combination of the data and excludes density only reflections. The term related to the linear estimation of P wave velocity variations, $\alpha_1-\beta_1$ in the acoustic case, and $a_\gamma^{(1)}-a_\rho^{(1)}$ in the elastic case, are prepared through

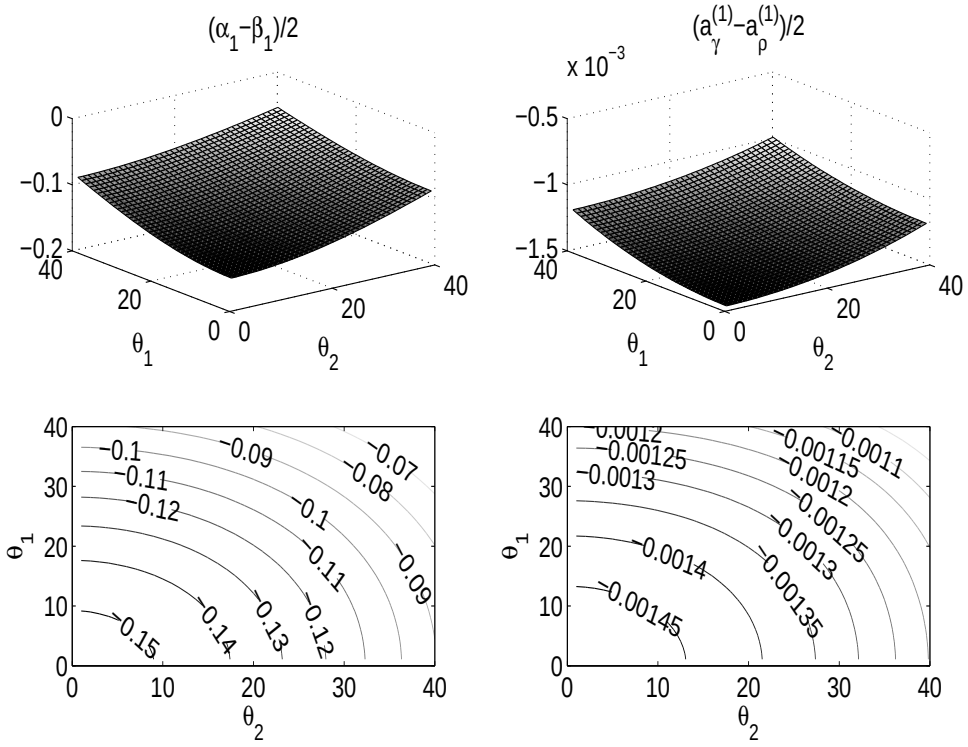

Figure 4: *Inversion comparison 3: the left two figures are the results of two-parameter acoustic inversion, the right figures are results using three-parameter elastic inversion, the lower figures are the contour of the upper figures. The parameters for the data model are:* ρ_0*=2.4g/cm*^{3}*,* ρ_1*=2.8g/cm*^{3}*;* c_{p0}*=3000m/s,* c_{p1}*=3000m/s;* c_{s0}*=1500m/s,* c_{s1}*=1500m/s, with a exact value of velocity change is 0.0*

the inversion of the first ISS term. Then they are imaged as a composite form in the imaging conjectures. The HOIS imaging conjecture for 1D two-parameter acoustic medium and 1D three-parameter elastic medium are as follow:

(1) for 1D two-parameter acoustic medium:

$$D^{HOIS}(z+\frac{1}{2}\int_{-\infty}^{\infty}\frac{\alpha_1(z')-\beta_1(z')}{\cos^2\theta-0.25(\alpha_1(z')-\beta_1(z'))}dz',\theta)=D(z,\theta) \tag{27}$$

(2) for 1D three-parameter elastic medium:

$$D^{HOIS}(z+\frac{1}{2}\int_{-\infty}^{\infty}\frac{a_\gamma^{(1)}(z')-a_\rho^{(1)}(z')}{\cos^2\theta-0.25(a_\gamma^{(1)}(z')-a_\rho^{(1)}(z'))}dz',\theta)=D^{PP}(z,\theta) \tag{28}$$

3.4 Numerical tests for multi-parameter imaging conjecture for acoustic and elastic media

In this section, a three-layer elastic model to be tested is shown in Figure 5. We consider only two primaries reflected from the reflectors and assume all the other events(ghosts, free surface multiples, and internal multiples)have been removed.

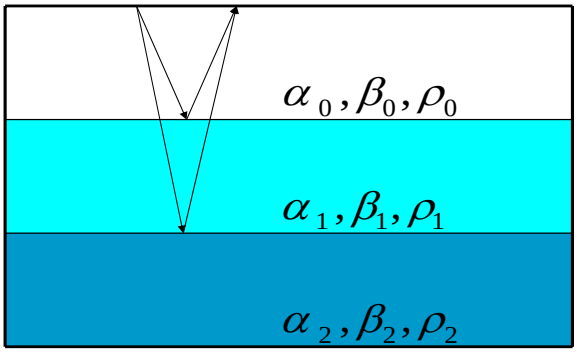

Figure 5: *A figure of a 1D three-layer elastic model with both P and S wave velocity change, as well as density variation.*

For this three-layer elastic model, the analytic data in the frequency domain can be written as:

$$\tilde{D}^{PP}(\nu_g, \theta) = R_{01}^{PP}(\theta)\frac{e^{2i\nu_g a}}{4\pi i\nu_g} + \hat{R}_{12}^{PP}\frac{e^{2i\nu_g a} + e^{2iq_g(b-a)}}{4\pi i\nu_g} \tag{29}$$

Where a and b are the exact depth of the two reflectors, ν_g and q_g are vertical wave numbers for P wave in the first two layers respectively and θ is the incident angle. Fourier transform over $2\nu_g$, we have:

$$D^{PP}(z, \theta) = R_{01}^{PP}(\theta)H(z-a) + \hat{R}_{12}^{PP}H(z-b') \tag{30}$$

This is the linear imaging result using the velocity in the first layer as the reference velocity. Since the reference velocity equals to the actual velocity above the first reflector, the depth of the first reflector is located correctly by the linear imaging. It is not the case for the second reflector, whose depth is located at a pseudo depth b', and $b'(\theta) = a + (b-a)\frac{q_g}{\nu_g}$.

The ISS conjectured imaging algorithms for two-parameter acoustic and three-parameter elastic media are tested respectively using the same elastic data model. We first assume the data model is acoustic and apply the acoustic imaging conjecture. Then the elastic imaging conjecture is implemented. The numerical results for the tests are shown below.

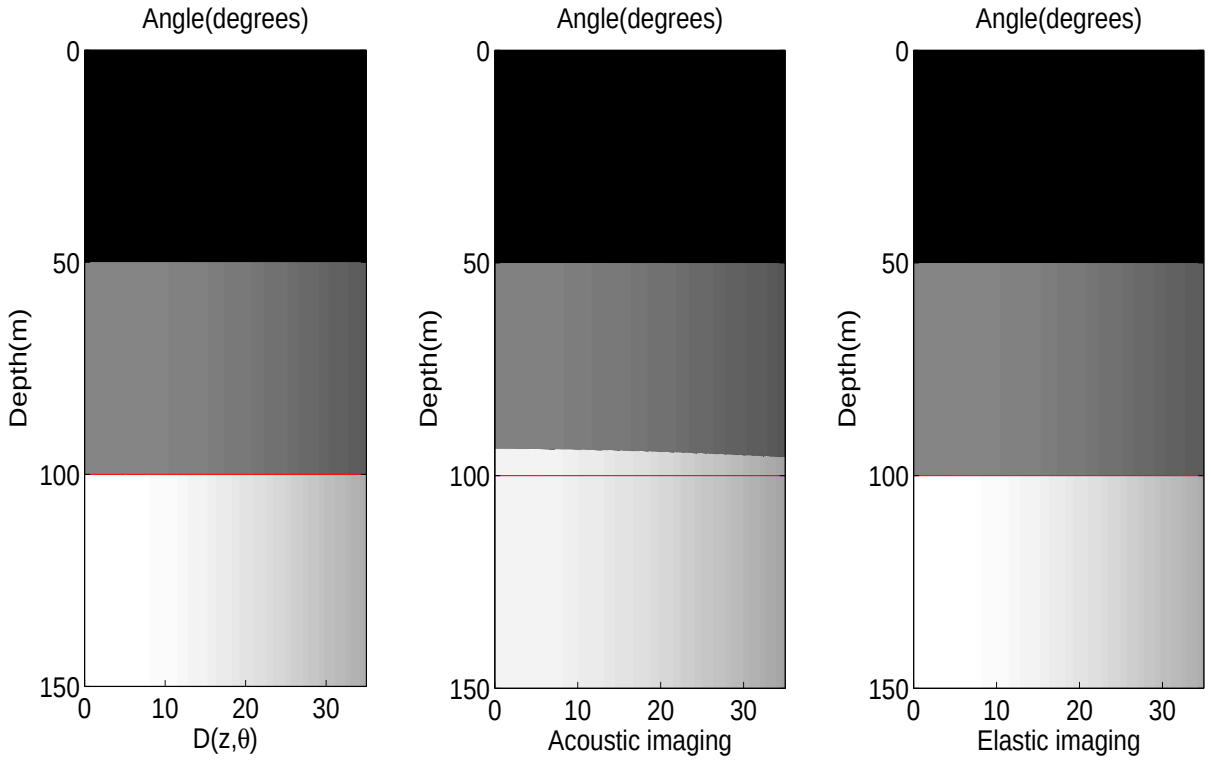

Figure 6: *Imaging comparison 1: the left figure is the result of constant velocity migration, the middle figure is acoustic imaging , and the right figure is the result of elastic imaging. The depth of the two reflectors are: a=50m and b=100m. The parameters for the data model are: ρ_0=2.1g/cm^3,ρ_1=2.4g/cm^3, ρ_2=2.7g/cm^3; v_{p0}=3000m/s, v_{p1}=3000m/s, v_{p2}=3000m/s; v_{s0}=1500m/s, v_{s1}=1500m/s, and v_{s2}=1500m/s*

In Figure 6, 7, and 8, are the results of constant velocity migration, acoustic imaging, and elastic imaging and the same analytic elastic data is used in each figure. In Figure 6, the P wave and S wave velocity keep constant, so there is no imaging issue in this example. From the results, we see that the elastic imaging do nothing; whereas, the acoustic imaging moves the deeper reflector to the wrong depth. In figure 7 and 8, the P wave velocity contrasts are the same. It is shown that compared with the constant velocity migration, the elastic imaging algorithm is better at locating the deeper reflectors, but it is not the case for the acoustic imaging algorithm.

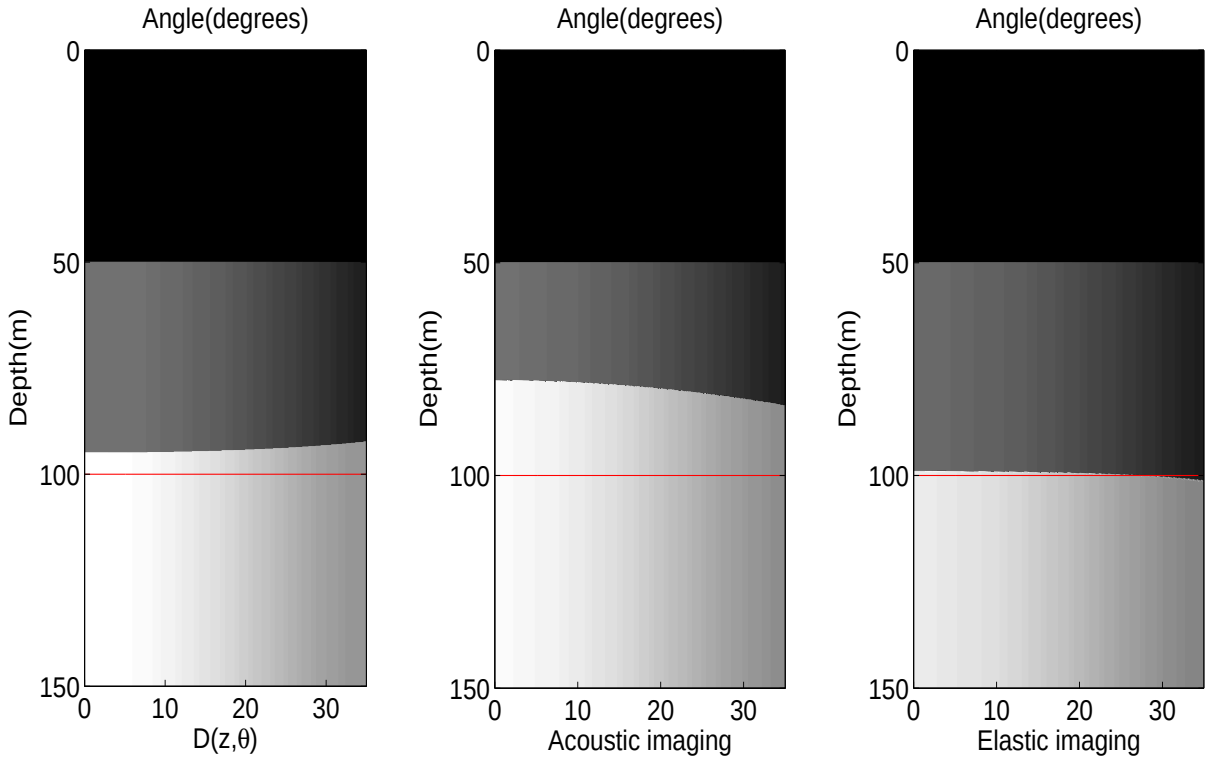

Figure 7: *Imaging comparison 2: the left figure is the result of constant velocity migration, the middle figure is acoustic imaging , and the right figure is the result of elastic imaging. The depth of the two reflectors are: a=50m and b=100m. The parameters for the data model are: ρ_0=2.1g/cm^3,ρ_1=2.3g/cm^3, ρ_2=2.5g/cm^3; v_{p0}=2700m/s, v_{p1}=3000m/s, v_{p2}=3500m/s; v_{s0}=1500m/s, v_{s1}=1800m/s, and v_{s2}=2000m/s*

After comparing the acoustic imaging results in Figure 7 and Figure 8, which have the same P wave velocity contrasts, we notice that the acoustic imaging result in Figure 8 improves significantly. From this, we may wonder if there is a case that acoustic imaging is better than elastic imaging for locating the deeper reflectors. After more numerical tests, we find that when the shear modulus in the elastic medium does not change the acoustic imaging algorithm is better at locating the deeper reflector. This can be illustrated by the following example.

In Figure 9, the shear modulus in the data model is constant. From the results, it is shown that acoustic imaging has better capability than elastic imaging in locating the deeper reflector. This is because the change of shear modulus is zero in the data model, and the model assumed in the acoustic inversion and imaging algorithm makes the change of the shear modulus zero, which is consistent with the data model. Instead, there is a leakage for the linear estimation of parameters when using the elastic inversion algorithms. The elastic inversion algorithm

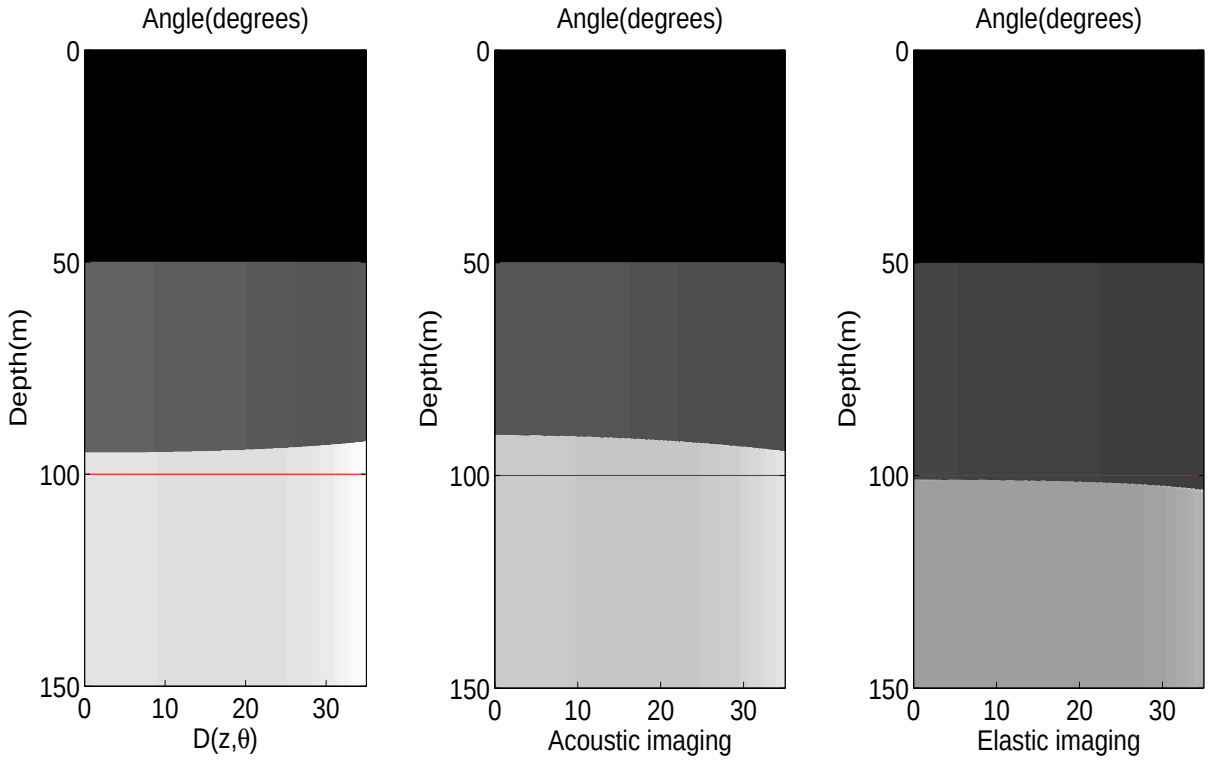

Figure 8: *Imaging comparison 3: the left figure is the result of constant velocity migration, the middle figure is acoustic imaging , and the right figure is the result of elastic imaging. The depth of the two reflectors are: a=50m and b=100m. The parameters for the data model are: ρ_0=2.1g/cm^3,ρ_1=2.2g/cm^3, ρ_2=2.3g/cm^3; v_{p0}=2700m/s, v_{p1}=3000m/s, v_{p2}=3500m/s; v_{s0}=1500m/s, v_{s1}=1600m/s, and v_{s2}=1700m/s*

would produce an nonzero linear estimation for the change of the shear modulus. Thus, under the special circumstances the acoustic imaging algorithm has better capability.

4 Conclusions

In this report, the consequences of using an inadequate model for the ISS imaging and parameter estimation have been studied. We first reviewed the direct inversion and multi-parameter imaging conjecture using the ISS. Then 1-D three-parameter elastic data models are tested numerically using the acoustic and elastic inversion and imaging algorithms. The imaging conjecture and inversion algorithms for acoustic medium treat the data as though only density and P wave velocity varied in the medium; whereas, the elastic algorithms allow the P wave velocity and S wave velocity and density to all vary. The numerical results show

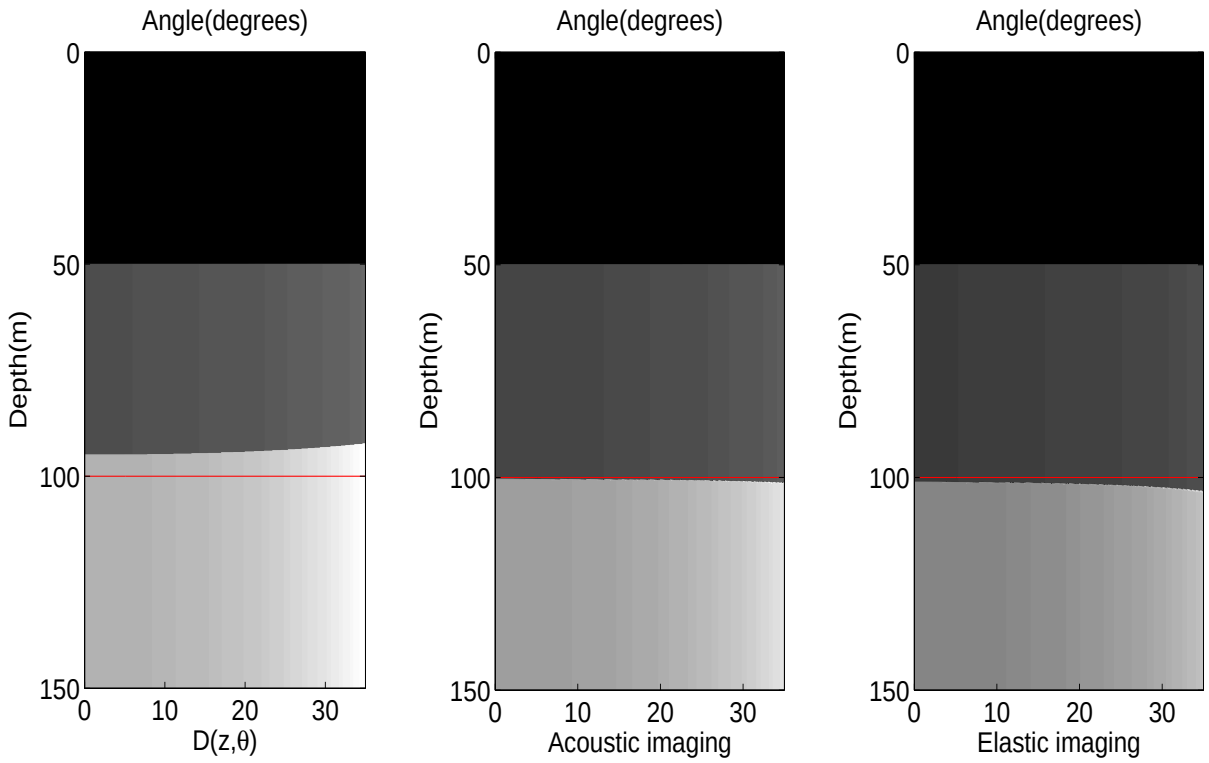

Figure 9: *Imaging comparison 4: the left figure is the result of constant velocity migration, the middle figure is acoustic imaging , and the right figure is the result of elastic imaging. The depth of the two reflectors are: a=50m and b=100m. The parameters for the data model are: ρ_0=2.1g/cm^3,ρ_1=2.3g/cm^3, ρ_2=2.5g/cm^3; v_{p0}=2700m/s, v_{p1}=3000m/s, v_{p2}=3500m/s; v_{s0}=1700m/s, v_{s1}=1624.4m/s, v_{s2}=1558.08m/s, and $\rho_0 v_{s0}^2 = \rho_1 v_{s1}^2 = \rho_2 v_{s2}^2$*

that when the processing algorithm's model type is matched with the data model, the ISS imaging and parameter estimation results are better than the case when the two models are mismatched. Thus, for ISS imaging and inversion application, it is important to match the processing's model type to the model that generates the data. What's more, the issue studied in this report dose not exclusively exist in the ISS approaches, others might also benefit from our lessons of matching and mismatching.

5 Acknowledgements

We are grateful to all M-OSRP sponsors for the long-term encouragement and support in our research. All members in M-OSRP are appreciated for their help in supporting the content generation of this paper and the valuable discussions presented in this research program.

References

Clayton, R. W. and R. H. Stolt. "A Born-WKBJ inversion method for acoustic reflection data." *Geophysics* (1981): 1559–1567.

Jiang, S. and A. B. Weglein. "Deriving an imaging algorithm for a laterally invariant multi-parameter acoustic medium from the inverse scattering series." *M-OSRP 2007 Annual meeting* (2008): 125–141.

Jiang, S. and A. B. Weglein. "Progressing multi-parameter imaging using the inverse scattering series: an initial analytic test on the Leading Order Imaging Subseries (LOIS) closed form and its extended Higher Order Imaging Subseries (HOIS) closed form for a laterally invariant two-parameter acoustic medium." *M-OSRP 2008 Annual meeting* (2009): 91–113.

Li, X., F. Liu, S. Jiang, and A. B. Weglein. "Depth imaging without the velocity cares about the phase and amplitude information of events: focusing on the use of angle dependent amplitude information of events." *M-OSRP 2008 Annual meeting* (2009): 114–128.

Liu, F. *Multi-dimensional depth imaging without an adequte velocity model.* PhD thesis, University of Houston, 2006.

Shaw, S., A. B. Weglein, K. H. Matson, and D. J. Foster. "Cooperation of the leading order terms in an inverse-scattering subseries for imaging: 1-D analysis and evaluation.." *SEG Technical Program Expanded Abstracts* (2002): 2277–2280.

Weglein, A. B., F. V. Araújo, P. M. Carvalho, R. H. Stolt, K. H. Matson, R. T. Coates, D. Corrigan, D. J. Foster, S. A. Shaw, and H. Zhang. "Inverse Scattering Series and Seismic Exploration." *Inverse Problems* (2003): R27–R83.

Weglein, A. B., F. A. Gasparotto, P. M. Carvalho, and R. H. Stolt. "An inverse-scattering series method for attenuating multiples in seismic reflection data." *Geophysics* (1997): 1975–1989.

Weglein, A. B., H. Zhang, A. Ramírez, F. Liu, and J. Lira. "Clarifying the underlying and fundamental meaning of the approximate linear inversion of seismic data." *Geophysics* (2009): WCD1–WCD13.

Zhang, H. *Direct nonlinear acoustic and elastic inversion: towards fundamentally new comprehensive and realistic target identification.* PhD thesis, University of Houston, 2006.

Zhang, H. and A. B. Weglein. "Direct non-linear inversion of multi-parameter 1D elastic media using the inverse scattering series." *SEG Technical Program Expanded Abstracts* (2006): 284–311.

Reverse-time migration and Green's theorem: A new and consistent theory that progresses and corrects current RTM concepts and methods

A. B. Weglein [(1)], R. H. Stolt [(2)] and J. D. Mayhan [(1)]

(1) M-OSRP, University of Houston, 617 Science & Research Bldg. 1, Houston, TX, 77004.

(2) ConocoPhillips, 600 North Dairy Ashford Road, Houston, TX 77079.

Abstract

In this paper we place Green's theorem based reverse-time migration (RTM), for the first time on a firm footing and technically consistent math-physics foundation. The required new Green function for RTM application is developed and provided, and is neither causal, anticausal, nor a linear combination of these prototype Green functions, nor these functions with imposed boundary conditions. We describe resulting fundamentally new RTM theory and algorithms, and provide a step-by-step prescription for application in 1D, 2D and 3D, the latter for an arbitrary laterally and vertically varying velocity field. The original RTM methods of running the wave equation backwards with surface reflection data as a boundary condition is not a wave theory method for wavefield prediction, neither in depth nor in reversed time. In fact that idea corresponds to the Huygens' principle idea (Huygens (1690)) which was changed and evolved into a wave theory predictor by George Green in 1826. The original RTM methods, where (1) 'running the wave equation backward in time', and then (2) employing a zero lag cross-correlation imaging condition, are in both of these ingredients less accurate and effective than the Green's theorem RTM method of this paper. Furthermore, all currently available Green's theorem methods for RTM make fundamental conceptual and algorithmic errors in their Green's theorem formulations. Consequently, even with an accurate velocity model, current Green's theorem RTM formulations can lead to image location errors and other reported artifacts. Addressing the latter problems is a principle goal of the new Green's theorem RTM method of this paper. Several simple analytic 1D examples illustrate the new RTM method. We also compare the general RTM methodology and philosophy, as the high water mark of current imaging concepts and application, with the next generation and emerging Inverse Scattering Series imaging concepts and methods.

1 Introduction

In this paper, we for the first time place Reverse Time Migration (RTM) on a firm theoretical footing derived from Green's theorem.

2 Overburden information for migration and migration-inversion

Green's theorem provides a useful framework for deriving algorithms to predict the wavefield at depth from surface measurements. There is much current interest and activity with RTM in exploration seismology.

The original RTM was pioneered, developed and applied by Dan Whitmore and his AMOCO colleagues in the 1980's (Whitmore (1983)), for exploration in the overthrust belt. The traditional seismic thinking that used a wave traveling from source down to the reflector and then up from the reflector to the receiver was extended to allow waves to move down and up from source to a reflector and down and then up from reflector to the receiver.

For one way wave propagation, a single step in depth corresponds to one step in time, with a fixed sign in the relationship between change in depth and change in time. Hence, for one way waves, you can equivalently go down the up wave in space or take a step backwards in time. For two way wave propagation, reversing time or extrapolating down an upcoming wave are not equivalent. And to image a reflector that reflected a turning wave requires a non-one way wave model that reversed time can satisfy.

In wave theoretic downward continuation migration, the source wavefield and receiver wavefield are extrapolated to the subsurface using one-way wave equations to obtain an experiment with coincident sources and receivers at depth.

The idea behind the two-way wave extrapolators (Whitmore (1983)) is to handle waves propagating in any direction, including overturning waves and prismatic waves. The most common implementation uses finite-difference techniques to solve the wave equation, which in the acoustic case is given by

$$\frac{1}{v^2}\frac{\partial^2 P}{\partial t^2} = \frac{\partial^2 P}{\partial x^2} + \frac{\partial^2 P}{\partial y^2} + \frac{\partial^2 P}{\partial z^2} \tag{1}$$

where P can be either source or receiver wavefield. To calculate the source wavefield, standard forward modeling injecting a user defined source signature into the model at the actual source position is done. For the receiver wavefield, the wave equation is run backwards in time and the recorded wavefield is injected into the model at the receiver positions as a boundary condition. The injection of the recorded wavefield is done starting with later times and finishing with the early times. That idea of using the measured values of the wavefield as the boundary conditions for a wave equation run backwards in time corresponds to Huygens'

principle (1690). The image, $I(\vec{x})$ is generated using a zero-lag cross-correlation imaging condition,

$$I(\vec{x}) = \int_0^{t_{max}} S(\vec{x}, t) R(\vec{x}, t_{max} - t) dt, \tag{2}$$

where the maximum recording time is t_{max}, $S(\vec{x}, t)$ is the modeled source wavefield and $R(\vec{x}, t_{max} - t)$ is the receiver wavefield (Fletcher et al. (2006)). Other imaging conditions can be used such as the deconvolution imaging condition (Zhang et al., 2007) but the cross-correlation is the most frequently used. The latter imaging principle is not equivalent to the downward continuation of sources and receivers at depth and seeking a zero time result from a coincident source-receiver experiment. One of the disadvantages of RTM is that it requires the availability of large amount of memory which increases with respect to the frequencies we want to migrate (Liu et al., 2009). As a consequence, memory availability has been a limitation to the application of this technology, especially to high resolution data from large 3D acquisitions. Nevertheless, recent improvements in computer hardware have enabled different implementations of RTM throughout the energy industry and there is a renewed interest in this technology due to its ability to accommodate and image in media where waves turn, as *e.g.* can occur in subsalt plays.

Several efforts have been aimed at improving the efficiency of the algorithm and dealing with the high storage cost for 3D implementation. For example, Toselli and Widlund (2000) used domain deconvolution which splits the computations across multiple nodes to improve the efficiency of the algorithm, and Symes (2007) introduced optimal checkpointing techniques to deal with the storage requirements, although, this type of techniques can increase the computation cost. These are examples of improvements directly related to the numerical implementation of the RTM algorithm.

Other efforts to deal with the practical limitations of RTM are based on changes in the theoretical approach to the problem. One example is the work of Luo and Schuster (2004) where a target oriented reverse-time datuming (RTD) technique based on Green's theorem is proposed. RTD can also be seen as a bottom-up shooting approach for RTM.

Using RTD's formulation, only the velocity model above the datum is used to calculate the Green function. No velocity under the datum is required, making the modeling more efficient. This formulation also allows for target oriented RTM and/or inversion. In target-oriented RTM, the idea is to redatum the data into a mathematical surface (referred to as the datum surface) within the earth's subsurface and use RTM below the datum surface to obtain a local RTM image of a given target area below the datum (Dong et al., 2009). In target-oriented inversion, the inversion is carried out only for a target area below the datum. Target-oriented inversion has also been proposed using the CFP domain.

The current formulation of RTD or bottom-up shooting for RTM, uses a high frequency approximation to Green's theorem (interferometry equation) and measurements at the measurement surface (above the earth) only. This formulation presents several approximations

which can impact the quality of the redatuming or the migration (if an imaging condition is applied after RTD): 1) The first approximation is related to the measurement surface. Green's theorem based algorithms, in principle, require measurements over a closed surface. The fact that we only measure the wavefield in a limited surface has an effect on the quality of the redatuming and can create artifacts in both the redatumed data and the migration. Directly addressing that issue is one of the principle aims of this paper. These measurements can be interchanged for sources at the surface using reciprocity principles. 2) The second approximation is the high frequency, one way-wave approximation commonly used in interferometry. This approximation allows to remove the need for the normal derivative of the pressure field at the measurement surface. These normal derivative is required by Green's theorem in its most common form, which is the one used by (Luo and Schuster, 2004) in their RTD formulation. As an analogy to interferometry, when used with two-way waves, this high frequency, one way wave approximation will create spurious multiples in the redatumed wavefield within the earth's subsurface (see *e.g.* Ramírez and Weglein (2009)).

Dong et al. (2009) deal with the effect of these approximations by smoothing the model, and, hence, reducing the effect of the one-way wave approximation. However, smoothing the model does not solve completely the problems created by the use of approximations. The redatumed wavefield will contain artifacts. Some of these artifacts will be imaged and stacking will not remove these artifacts completely.

In this paper, we show how to formulate and apply Green's theorem in an appropriate manner for two way propagating waves. We begin with a simple discussion of back propagating waves and imaging to illustrate how the type of *a priori* information needed above a target reflector depends on your goal and level of information extraction at the reflector. We show that only the velocity model above the reflector is needed to simply locate the reflector whereas all properties above the reflector are required if you want to determine both where any property has changed (structure imaging or migration) or what specific property has changed at the imaged reflector and by what amount (migration-inversion).

We begin by exemplifying how all traditional linear backpropagation methods for predicting waves at depth from surface reflection data need different types and degrees of *a priori* overburden subsurface information for different levels of ambition for subsurface target information extraction: migration versus migration-inversion

In traditional seismic processing, the spatial location of reflectors (migration) is determined by the velocity above the reflector while parameter estimation requires all properties above the depth image where changes in earth mechanical properties are to be determined. A very simple illustration of this idea can be obtained by using a 1D normal incident experiment using the model shown in Figure 1, where z_{ms} represents the depth of the source and receiver, and the depth of the first reflector is z_1, and the second reflector's depth is z_2, and z_2 is the location to be determined. The recorded data, $D(t)$, the wavefield at the coincident source and receiver position chosen as $z_{ms} = 0$, is given by

$$D(t, z_m = 0) = R_1\delta(t - 2t_1) + R_2'\delta(t - 2t_2) \tag{3}$$

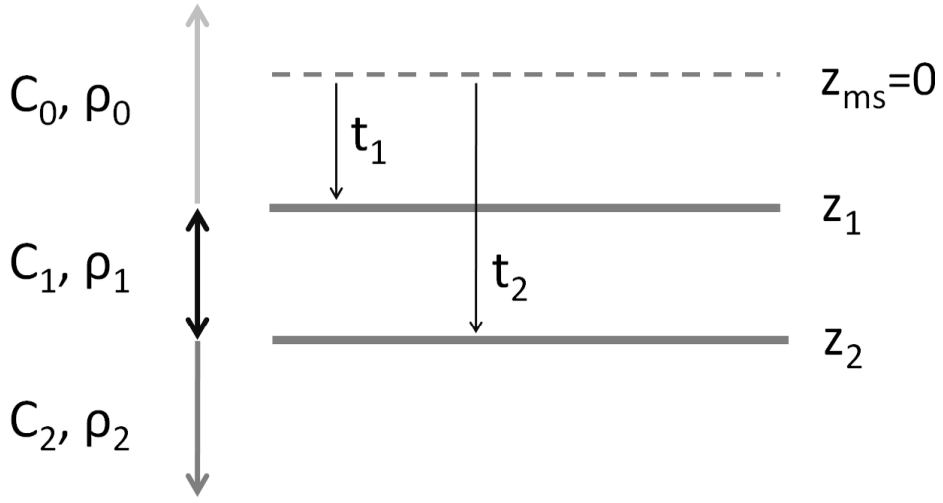

Figure 1: Zero-offset model. The velocity is denoted by c, and the density by ρ.

where $R_1 = R_{01}$ represents the reflection coefficient at the boundary between the first and second media, and $R_2' = T_{01}R_{12}T_{10}$ represents the amplitude of the second event and is the composite transmission and reflection coefficient in the second medium. The two-way travel times for the first and second events are given by $2t_1$ and $2t_2$, respectively.

Fourier transforming Equation (3) gives

$$D(\omega, z_m = 0) \quad = \quad R_1 e^{2i\omega t_1} + R_2' e^{2i\omega t_2} \tag{4}$$

where the first term on the right hand side is the primary from the first reflector (at $z = z_1$) and the second term is the primary from the second reflector (at $z = z_2$).

The next step is to locate the depth of the second reflector using the recorded data. To do so, we will call upon the simple solutions to the wave equation governing wave propagation in homogeneous media. In this example, that allows us to backpropagate separately the source and the receiver down reversing the actual propagation paths of the recorded upgoing waves. This step is known as downward continuation. Because, in traditional migration we assume that we know the velocity model above each reflector to be imaged, we will treat each primary separately, thus we write Equation (4) as

$$D(\omega, z_{ms} = 0) = D_1(\omega, z_{ms} = 0) + D_2(\omega, z_{ms} = 0). \tag{5}$$

The source and receiver corresponding to the first primary,

$$D_1(\omega, z_{ms} = 0) = R_1 e^{2i\omega t_1} \tag{6}$$

are downward continued in the first medium (above the shallower reflector at z_1), giving

$$D_1(\omega, z) \quad = \quad R_1 e^{2i\omega t_1} e^{-2i\frac{\omega}{c_0}z}. \tag{7}$$

In the downward continuation for the first primary, we use the medium properties (c_0, ρ_0) above that first reflector and the equation

$$\left(\frac{d^2}{dz^2} + \frac{\omega^2}{c_0^2}\right) D = 0 \tag{8}$$

and, hence, the receiver and the source each contribute a factor of $e^{-i(\omega/c_0)z}$.

The solution in Equation (7) simulates a coincident source and receiver reflection experiment at depth z. A non zero value of this coincident source and receiver experiment at depth at $t = 0^+$ indicates a reflector just below the coincident point in the medium. Hence, the next step in our example locates the reflectors by applying the imaging condition at $t = 0$ to the downward continued data. The latter is realized by integrating over all frequencies $\int d\omega\, D(\omega, z)$; in other words, we do an inverse Fourier transform evaluating the time in the exponential of the Fourier kernel with $t = 0$. Thus, we obtain

$$D_1(t = 0, z) = R_1 \delta(2t_1 - 2z/c_0), \tag{9}$$

corresponding to an image at $z = c_0 t_1$ at the depth of the first reflector.

The second primary,

$$D_2(\omega, z_{ms} = 0) = R_2' e^{2i\omega t_2}, \tag{10}$$

is downward continued in the medium above the first reflector using the path of an upgoing wave satisfying the differential equation (8) and for the medium between the first and second reflector the equation used is

$$\left(\frac{d^2}{dz^2} + \frac{\omega^2}{c_1^2}\right) D = 0, \tag{11}$$

which relates to the properties of the medium between z_1 and z_2. Therefore, taking the source and receiver to depth z in the medium below the first reflector

$$\begin{aligned} D_2(\omega, z) &= D_2(\omega, z_{ms} = 0) e^{-i\frac{2\omega}{c_0}z_1} e^{-i\frac{2\omega}{c_1}(z - z_1)} \\ &= R_2' e^{2i\omega t_2} e^{-i\frac{2\omega}{c_0}z_1} e^{-i\frac{2\omega}{c_1}(z - z_1)} \end{aligned} \tag{12}$$

and applying the imaging condition gives

$$D_2(t=0,z) \quad = \quad R_2'\delta(2t_2 - \frac{2z_1}{c_0} - \frac{2}{c_1}(z-z_1)). \tag{13}$$

The second primary images at $z = z_1 + c_1(t_2 - t_1)$, the depth of the second reflector, z_2. Therefore the location depends only on the velocity above each reflector (and not on the density).

However, to determine changes in mechanical properties across each reflector requires the reflection coefficients R_1 and R_{12} and the removal of $T_{01}T_{10}$ from R_2' to determine R_{12} where $R_2' = T_{01}R_{12}T_{10}$. To remove T_{01} and T_{10} we must know the changes in velocity and density at the first reflector. In other words, determining material property changes across each reflector requires the velocity and density (and absorption and all other property changes) above these two reflectors.

The latter amplitude issue can be viewed as a consequence of the properties of the R's and T's which come from continuity conditions (note: the pressure and its normal derivative are not continuous when the density and velocity change across a boundary). If the latter continuity of pressure and its normal derivative were the case, then amplitude would only care about velocity changes, in this simple acoustic example. To determine the amplitude of a reflection coefficient at depth requires knowledge of all material properties above the reflector and not only velocity. That's worth keeping in mind for those pursuing/promoting 'true amplitude' migration, especially if non linear target identification is the ultimate goal.

The general property of wavefield amplitude at depth from surface measurements follows from Green's theorem, where all medium properties are needed to provide the Green functions in the medium, and necessary for determining the wavefield at depth.

3 Overview on the evolution of migration concepts and goals: from NMOŨstack to AVO and migration to migration-inversion, the uncollapsed migration concept

As with all useful concepts, seismic migration has evolved and adapted to deal with ever more realistic and complex media and to allow higher and more ambitious goals for the imaged amplitudes. In seismic processing history the 'determine where anything changed' structure/migration people and their ideas/methods typically progressed totally independent from the 'what specifically changed' AVO people and their theories and methods. The AVO theorists and practitioners were never too concerned with locating the position in the earth of earth boundary changes, but rather focused on what specifically in detail was changing somewhere, and the migration people were not too interested in what was actually changing, after it was determined that something was changing at a point in the subsurface. Further,

AVO people assumed a simple 1D earth and asked difficult, complex, detailed questions; while the structure seeking migration people assumed a complex multi-D earth and asked a less ambitious structure question "where did anything change?" In the 1D world, NMO-stack evolved into AVO and multi-D migration evolved and was generalized into migration-inversion.

The components within migration are: a backpropagation of waves and an imaging condition, where the latter imaging condition enables the backpropagated waves to be used to locate and delineate reflectors. The uncollapsed migration imaging principle introduced by Stolt, Clayton, and Weglein in the mid-1980's (Clayton and Stolt (1981), Stolt and Weglein (1985)) extended and generalized the earlier Claerbout coincident source and receiver at depth at time equals imaging condition; that earlier Claerbout principle aimed at structure. This paper advances the propagation component theory of the propagation-imaging principle duet and incorporates the Stolt-Clayton-Weglein uncollapsed migration imaging condition. That uncollapsed imaging condition remains the high water mark of imaging conditions today, allowing automatic amplitude analysis at depth with respect to the normal of the imaged reflector, or imaging and inverting a point diffractor. We will not progress the imaging condition in this paper. That uncollapsed migration imaging condition has been reinvented (and relabeled), by among others Berkhout and Wapenaar (1988), de Bruin et al. (1990a), de Bruin et al. (1990b), Sava and Fomel (2006), and Sava and Vasconcelos (2009).

We begin by discussing the history and evolution of models for the volume beneath the measurement surface within which we backpropagate surface reflection data.

4 The infinite hemispherical migration model

The earliest wave equation migration pioneers viewed the backpropagation region as an infinite hemispherical half space with known mechanical properties, whose upper plane surface corresponded to the measurement surface, as in, *e.g.*, Schneider (1978) and Stolt (1978). Please see Figure 2.

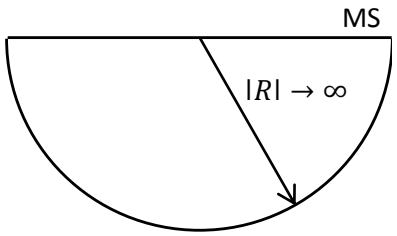

Figure 2: *The infinite hemispherical migration model. The measurement surface is denoted by MS.*

There are several problems with the infinite hemispherical migration model. That model assumes: (1) that all subsurface properties beneath the measurement surface (MS) are known,

and (2) that an anticausal Green function (*e.g.*, Schneider (1978)), with a Dirichlet boundary condition on the measurement surface, would allow measurements (MS) of the wavefield, P, on the upper plane surface of the hemisphere to determine the value of P within the hemispherical volume, V. The first assumption leads to the contradiction that you have not allowed for anything that is unknown to be determined in your model, since everything within the closed and infinite hemisphere is assumed to be known. Within the infinite hemispherical model there is nothing and/or nowhere below the measurement surface where an unknown scattering point or reflection surface can serve to produce reflection data whose generating reflectors are initially unknown and being sought by the migration process.

The second assumption, in early infinite hemispherical wave equation migration, assumes that Green's theorem with wavefield measurements on the upper plane surface and using an anticausal Green function satisfying a Dirichlet boundary condition can determine the wavefield within V. That conclusion assumes that the contribution from the lower hemispherical surface of S as the radius of the hemisphere goes to infinity vanishes. That is not the case, as we explicitly demonstrate below. To examine the various large radius hemispherical surface contributions to Green's theorem wave prediction in a volume, it is instructive to review the relationship between Green's theorem and the Lippmann-Schwinger scattering equation.

5 Green's theorem review (the Lippmann-Schwinger Equation and Green's theorem)

We begin with a space and time domain Green's theorem. Consider two wavefields P and G_0 that satisfy

$$(\nabla^2 - \frac{1}{c^2}\partial_t^2)P(\vec{r},t) = \rho(\vec{r},t) \tag{14}$$

$$\text{and } (\nabla^2 - \frac{1}{c^2}\partial_t^2)G_0(\vec{r},t,\vec{r}',t') \quad = \delta(\vec{r}-\vec{r}')\delta(t-t') \tag{15}$$

where we assume 3D wave propagation and c is a constant. ρ is a general source, *i.e.*, it represents both active sources (air guns, dynamite, vibrator trucks) and passive sources (heterogeneities in the earth). The causal solution to Equation (14) can be written

$$P(\vec{r},t) = \int_{-\infty}^{t^+} dt' \int_{\infty} d\vec{r}' G_0^+(\vec{r},t,\vec{r}',t')\rho(\vec{r}',t') \tag{16}$$

where G_0^+ is the causal whole space solution to Equation (15). The integral from t^+ to ∞ is zero due to the causality of G_0^+.

Equation (16) represents the linear superposition of causal solutions G_0^+ with weights $\rho(\vec{r}',t')$ summing to produce the physical causal wavefield solution to Equation (16). Equation (16) is called the scattering equation and represents an all space and all time causal solution for

$P(\vec{r},t)$. It explicitly includes all sources and produces the field at all points of space and time. No additional boundary or initial conditions are required in Equation (16).

Now consider the integral

$$\int_0^{t^+} dt' \int_V d\vec{r}'(P\nabla'^2 G_0 - G_0\nabla'^2 P) = \int_0^{t^+} dt' \int_V d\vec{r}'\nabla' \cdot (P\nabla' G_0 - G_0\nabla' P) \tag{17}$$

and we rewrite Equation (17) using Green's theorem

$$\int_0^{t^+} dt' \int_V d\vec{r}'\nabla' \cdot (P\nabla' G_0 - G_0\nabla' P) = \int_0^{t^+} dt' \int_S dS'(P\nabla' G_0 - G_0\nabla' P) \cdot \hat{n} \tag{18}$$

This is essentially an identity, within the assumptions on functions and surfaces, needed to derive Green's theorem. Now choose $P = P(\vec{r}',t')$ and $G_0 = G_0(\vec{r},t,\vec{r}',t')$ from Equations (14) and (15). Then replace $\nabla'^2 P$ and $\nabla'^2 G_0$ from the differential equations (14) and (15).

$$\nabla'^2 G_0 = \frac{1}{c^2}\partial_t'^2 G_0 + \delta(\vec{r}-\vec{r}')\delta(t-t') \tag{19}$$

$$\nabla'^2 P = \frac{1}{c^2}\partial_t'^2 P + \rho(\vec{r}',t') \tag{20}$$

and assume that the out variables $(\vec{r},t)$ are in the intervals of integration: $\vec{r}$ in V, $t > 0$. The left hand side of Equation (17) becomes:

$$\int_0^{t^+} dt' \int_V d\vec{r}' \frac{1}{c^2}(P\partial_{t'}^2 G_0 - G_0\partial_{t'}^2 P) + P(\vec{r},t) - \int_0^{t^+} dt' \int_V d\vec{r}'\rho(\vec{r}',t')G_0(\vec{r},t,\vec{r}',t') \tag{21}$$

The expression inside the first set of parentheses is a perfect derivative $\partial_{t'}(P\partial_{t'}G_0 - G_0\partial_{t'}P)$ integrated over t'.

The result is (for $\vec{r}$ in V and $t > 0$)

$$\begin{aligned} P(\vec{r},t) = &\int_V d\vec{r}' \int_0^{t^+} dt'\rho(\vec{r}',t')G_0(\vec{r},t,\vec{r}',t') - \frac{1}{c^2}\Big|_0^{t^+} \int_V d\vec{r}'[P\partial_{t'}G_0 - G_0\partial_{t'}P] \\ &+ \int_0^{t^+} dt' \int_S dS'(P\nabla G_0 - G_0\nabla P)\cdot\hat{n} \end{aligned} \tag{22}$$

We assumed differential equations (19) and (20) in deriving Equation (22) and G_0 can be any solution of Equation (19) in the space and time integrals in Equation (17), causal, anticausal, or neither. Each term on the right hand side of Equation (22) will differ with different choices of G_0, but the sum of the three terms will always be the same, $P(\vec{r},t)$.

If we now choose G_0 to be causal ($= G_0^+$) in Equation (22) and let the time interval be $[-\infty, t^+]$ and the volume, $V \to \infty$, rather than $[0,t^+]$ and V, respectively, then in the second term the upper limit gives zero because G_0^+ and $\partial_{t'}G_0^+$ are zero at $t' = t^+$ and $t' = -\infty$.

The causality of G_0^+ and $\partial_{t'} G_0^+$ causes only the lower limit $t' = 0$ to contribute in

$$-\frac{1}{c^2}\Big|_{t'=0}^{t^+} \int_V d\vec{r}'[P\partial_{t'} G_0^+ - G_0^+ \partial_{t'} P].$$

If we let the space and time limits in Equation (22) both become unbounded, *i.e.*, $V \to \infty$ and the t' interval becomes $[-\infty, 0]$ and choose $G_0 = G_0^+$, the whole space causal Green function, then by comparing Equations (16) and (22) we see that for $\vec{r}$ in V and $t > 0$ that

$$\int_{-\infty}^{t^+} dt' \int_S dS'(P\nabla G_0^+ - G_0^+ \nabla P) \cdot \hat{n} - \frac{1}{c^2}\Big|_{-\infty}^{t^+} \int_\infty d\vec{r}'[P\partial_{t'} G_0^+ - G_0^+ \partial_{t'} P] = 0.$$

$V = \infty$ means a volume that spans all space, and $\infty - V$ means all points in ∞ that are outside the volume V. For $\vec{r}$ in ∞ and any time t from Equation (16)

$$\begin{aligned} P(\vec{r}, t) = &\int_V d\vec{r}' \int_0^{t^+} dt' \rho(\vec{r}', t') G_0^+(\vec{r}, t, \vec{r}', t') \\ &+ \int_{\infty - V} d\vec{r}' \int_0^{t^+} dt' \rho(\vec{r}', t') G_0^+(\vec{r}, t, \vec{r}', t') \\ &+ \int_V d\vec{r}' \int_{-\infty}^0 dt' \rho(\vec{r}', t') G_0^+(\vec{r}, t, \vec{r}', t') \\ &+ \int_{\infty - V} d\vec{r}' \int_{-\infty}^0 dt' \rho(\vec{r}', t') G_0^+(\vec{r}, t, \vec{r}', t') \end{aligned} \tag{23}$$

This equation holds for any $\vec{r}$ and any t.

For $\vec{r}$ in V and $t > 0$ Equations (23) and (22) must agree and

$$\begin{aligned} &-\frac{1}{c^2}\Big|_0^{t^+} \int_V d\vec{r}'[P\partial_{t'} G_0^+ - G_0^+ \partial_{t'} P] \\ &= \int_V d\vec{r}' \int_{-\infty}^0 dt' \rho(\vec{r}', t') G_0^+(\vec{r}, t, \vec{r}', t') \\ &+ \int_{\infty - V} d\vec{r}' \int_{-\infty}^0 dt' \rho(\vec{r}', t') G_0^+(\vec{r}, t, \vec{r}', t') \end{aligned} \tag{24}$$

and

$$\begin{aligned} &\int_0^{t^+} dt' \int_S dS'[P\nabla G_0 - G_0 \nabla P] \cdot \hat{n} \\ &= \int_{\infty - V} d\vec{r}' \int_0^{t^+} dt' \rho(\vec{r}', t') G_0^+(\vec{r}, t, \vec{r}', t') \end{aligned} \tag{25}$$

The solution for $P(\vec{r}, t)$ in Equation (22) expresses the fact that if all of the factors that both create the wavefield (active sources) and that subsequently influence the wavefield (passive

sources, *e.g.*, heterogeneities in the medium) are explicitly included in the solution as in Equation (22), then the causal solution is provided explicitly and linearly in terms of those sources, as a weighted sum of causal solutions, and no surface, boundary or initial conditions are necessary or required.

From Equations (24) and (25) the role of boundary and initial conditions are clear. The contributions to the wavefield, P, at a point $\vec{r}$ in V and at a time, t in $[0, t^+]$ derives from three contributions: (1) a causal superposition over the sources within the volume V during the interval of time, say $[0, t^+]$ and (2) initial conditions of P and P_t over the volume V, providing all contributions due to sources earlier than time $t' = 0$, both inside and outside V, to the solution in V during $[0, t]$ and (3) a surface integral, enclosing V, integrated from $t' = 0$ to t^+ that gives the contribution from sources outside V during the time $[0, t^+]$ to the field, P, in V for times $[0, t^+]$.

Succinctly stated: initial conditions provide contributions from sources at earlier times and surface/boundary conditions provide contributions from outside the spatial volume to the field in the volume during the $[0, t]$ time interval. If all sources for all space and all time are explicitly included as in Equation (16), then there is no need for boundary or initial conditions to produce the physical/causal solution derived from a linear superposition of elementary causal solutions.

On the other hand, if you seek to find a physical causal solution for P in terms of a linear superposition of anticausal solutions, as you can arrange by choosing $G_0 = G_0^-$ in Equation (22), then the initial and surface integrals do <u>not</u> vanish when you let $V \to \infty$ and $[0, t] \to [-\infty, t]$. The vanishing of the surface integral contribution (as the radius of the surface $\to \infty$) to P with the choice $G_0 = G_0^+$ is called the Sommerfeld radiation condition, and is readily understood by the comparison with Equation (16).

We now examine, in the $\vec{r}, \omega$ domain Equations (14) and (15) become

$$(\nabla^2 + k^2)P = \rho(\vec{r}, \omega) \tag{26}$$

$$(\nabla^2 + k^2)G_0 = \delta(\vec{r} - \vec{r}') \tag{27}$$

and the causal all space and time solution analogous to Equation (16) is

$$P(\vec{r}, \omega) = \int_\infty d\vec{r}' \rho(\vec{r}', \omega) G_0^+(\vec{r}, \vec{r}', \omega)$$

and Green's second identity is

$$\int_V (P\nabla^2 G_0 - G_0 \nabla^2 P) d\vec{r}' = \oint_S (P\nabla G_0 - G_0 \nabla P) \cdot \hat{n}\, dS.$$

Substituting $\nabla^2 G_0 = -k^2 G_0 + \delta$ and $\nabla^2 P = -k^2 P + \rho$ in Green's theorem where $\int_{-\infty}^{\infty} P(\vec{r}, t) e^{i\omega t} dt = P(\vec{r}, \omega)$ we find

$$\int_V P(\vec{r}', \omega)\delta(\vec{r} - \vec{r}') d\vec{r}' = \int_V \rho(\vec{r}', \omega) G_0(\vec{r}, \vec{r}', \omega) d\vec{r}' + \oint_S (P\nabla' G_0 - G_0 \nabla' P) \cdot \hat{n} dS' \tag{28}$$

if $\vec{r}$ in V. There are no initial conditions, since in $\vec{r}, \omega$ you have already explicitly included all time in Fourier transforming from t to ω. All times of sources are included in the $\vec{r}, \omega$ domain. In $\vec{r}, \omega$ the issue is whether sources are inside or outside V. The Lippmann-Schwinger equation

$$P(\vec{r}, \omega) = \int_{\infty} d\vec{r}' G_0^+(\vec{r}, \vec{r}', \omega) \rho(\vec{r}', \omega). \tag{29}$$

provides the causal physical P for all $\vec{r}$. Equation (29) is the $\vec{r}, \omega$ version of Equation (16) and must choose $G_0 = G_0^+$ (causal) to have P as the physical solution built from superposition and linearity. In contrast, Equation (28) (as in Equation (22)) will produce the physical solution, P, with any solution for G_0 that satisfies Equation (27).

Equation (29) can be written as:

$$\int_V \rho G_0^+ + \int_{\infty - V} \rho G_0^+. \tag{30}$$

For $\vec{r}$ in V the second term on the right hand side of Equation (28) (with $G_0 = G_0^+$) equals the second term in Equation (30), *i.e.*,

$$\int_{\infty - V} \rho G_0^+ d\vec{r}' = \oint_S (P \nabla G_0^+ - G_0^+ \nabla P) \cdot \hat{n} dS'. \tag{31}$$

Thus, the first term in Equation (30) gives contribution to P, for $\vec{r}$ in V due to sources in V, and the second term in Equation (30) gives contribution to P, for $\vec{r}$ in V due to sources not in V.

With $G_0 = G_0^+$

$$\oint_S (P \nabla G_0^+ - G_0^+ \nabla P) \cdot \hat{n} \, dS$$

provides the contribution to the field, P, inside V due to sources outside the volume V.

What about the large $|\vec{r}|$ contribution of the surface integral to the field inside the volume?

We use Green's theorem to predict that the contribution to the physical/causal solution P in V from the surface integral in Green's theorem, in general, and also when $|\vec{r}| \to \infty$.

$$\oint_S \{P \frac{\partial G_0^+}{\partial n} - G_0^+ \frac{\partial P}{\partial n}\} dS \to 0 \text{ as } |\vec{r}| \to \infty$$

and in contrast the contribution to P in V from

$$\oint_S \{P \frac{\partial G_0^-}{\partial n} - G_0^- \frac{\partial P}{\partial n}\} dS$$

does not vanish as $|\vec{r}| \to \infty$.

We begin with Equation (28)

$$P(\vec{r},\omega) = \int_V G_0^{\pm}(\vec{r},\vec{r}',\omega)\rho(\vec{r}',\omega)\,d\vec{r}' + \oint_S \{P\frac{\partial G_0^{\pm}}{\partial n} - G_0^{\pm}\frac{\partial P}{\partial n}\}dS \qquad \vec{r} \text{ in V} \tag{32}$$

with G_0 either causal G_0^+ or anticausal G_0^-. When $|\vec{r}| \to \infty$, the contribution from

$$\oint_S \{P\frac{\partial G_0^{+}}{\partial n} - G_0^{+}\frac{\partial P}{\partial n}\}dS$$

to P in V must go to 0 since

$$P(\vec{r},\omega) = \int_\infty G_0^{+}(\vec{r},\vec{r}',\omega)\rho(\vec{r}',\omega)d\vec{r}'$$

(the Lippmann-Schwinger equation).

However, as $|\vec{r}| \to \infty$, with $G_0 = G_0^-$,

$$\oint_S \{P\frac{\partial G_0^{-}}{\partial n} - G_0^{-}\frac{\partial P}{\partial n}\}dS + \int_{V\to\infty} G_0^{-}(\vec{r},\vec{r}',\omega)\rho(\vec{r}',\omega)\,d\vec{r}' = \int_{V\to\infty} G_0^{+}(\vec{r},\vec{r}',\omega)\rho(\vec{r}',\omega)\,d\vec{r}' + 0 \tag{33}$$

so

$$\oint_S \{P\frac{\partial G_0^{-}}{\partial n} - G_0^{-}\frac{\partial P}{\partial n}\}dS = \int_\infty [G_0^{+}(\vec{r},\vec{r}',\omega) - G_0^{-}(\vec{r},\vec{r}',\omega)]\rho(\vec{r}',\omega)d\vec{r}' \neq 0 \qquad \text{for all time}$$

Hence, the large distance surface contribution to the physical field, P, within V with the physical field P and P_n and an anticausal Green function G_0^- will not vanish as $|\vec{r}| \to \infty$. As we mentioned earlier, this is one of the two problems with the infinite hemisphere model of seismic migration.

Although

$$P(\vec{r},\omega) = \int_\infty G_0^{-}(\vec{r},\vec{r}',\omega)\rho(\vec{r}',\omega)\,d\vec{r}'$$

would be a solution to Equations (14) and (26) for all $\vec{r}$, it would not be the causal/physical solution to Equations (14) and (26).

And hence, in summary the contribution to the causal/physical solution for $P(\vec{r},\omega)$ for $\vec{r}$ in V from

$$\int_S \left(P\frac{dG_0^{+}}{dn} - G_0^{+}\frac{dP}{dn}\right)dS \to 0$$

as $|R| \to \infty$ where P and dP/dn corresponds to physical/causal boundary values of P and dP/dn, respectively. Physical measurements of P and dP/dn on S are always causal/physical values. The integral

$$\int_S \left(P\frac{dG_0^{-}}{dn} - G_0^{-}\frac{dP}{dn}\right)dS$$

does not go to zero for anti-causal, G_0^-, and causal/physical P and dP/dn. The latter fact bumps up against a key assumption in the infinite hemisphere models of migration. That combined with the fact the infinite hemisphere model assumes the entire subsurface, down to 'infinite' depth is known, suggests the need for a different model. That model is the finite volume model.

6 Finite volume model for migration

The finite model for migration assumes that we know or can adequately estimate earth medium properties (velocity) down to the reflector we seek to image. The finite volume model assumes that beneath the sought after reflector the medium properties are and remain unknown. The 'finite volume model' corresponds to the volume within which we assume the earth properties are known and within which we predict the wavefield from surface measurements. We have moved away from the two issues of the infinite hemisphere model, *i.e.*, (1) the assumption we know the subsurface to all depths and (2) that the surface integral with an anticausal Green function has no contribution to the field being predicted in the earth.

The finite volume model takes away both assumptions. However, we are now dealing with a finite volume V, and with a surface S, consisting of upper surface S_U, lower surface S_L and walls, S_W. Please see Figure 3.

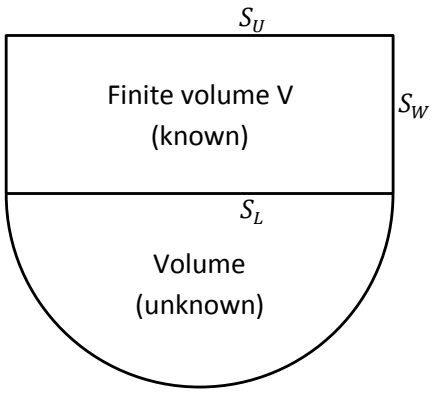

Figure 3: *The finite volume model*

We only have measurements on S_U. In the following sections on: (1) Green's theorem for one way propagation; and (2) Green's theorem for two way propagation we show how the choice of Green function allows the finite volume migration model to be realized.

The construction of the Green function that allows for two way propagation in V is the new and significant contribution of this paper. It puts RTM on a firm wave theoretical Green's theorem basis, for the first time, with algorithmic consequence and consistent and realizable

methods for RTM. The new Green function is neither causal, anticausal, nor a combination of causal and/or anticausal, Green functions.

7 Finite volume: one-way wave Green's theorem downward continuation

Consider a 1D up-going plane wavefield $P = Re^{-ikz}$ propagating upward through the 1D homogeneous volume without sources between $z = a$ and $z = b$.

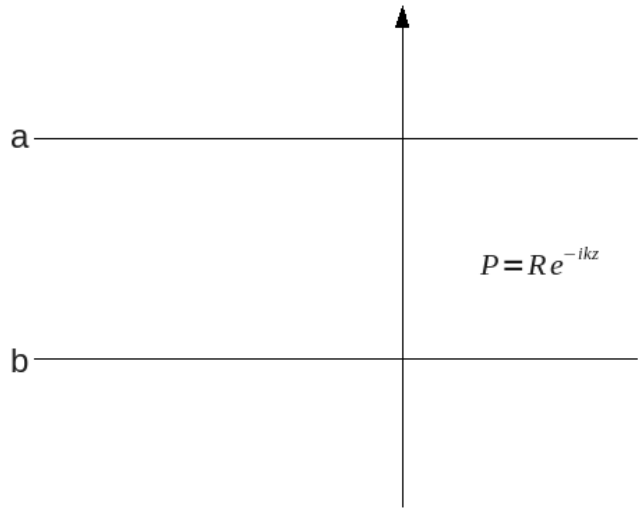

Figure 4: 1D upgoing plane wavefield.

The wave P inside V can be predicted from

$$P(z,\omega) \;=\; \Big|_{z'=a}^{b} \{P(z',\omega)\; \frac{dG_0}{dz'}(z,z',\omega) - G_0(z,z',\omega)\frac{dP}{dz'}(z',\omega)\} \tag{34}$$

with the Green function, G_0, that satisfies

$$\left(\frac{d^2}{dz'^2} + k^2\right)\; G_0(z,z',\omega) \;=\; \delta(z-z') \tag{35}$$

for z and z' in V.

We can easily show that for an upgoing wave, $P = Re^{-ikz}$, that if one chooses $G_0 = G_0^+$ (causal, $e^{ik|z-z'|}/(2ik)$), the lower surface (i.e. $z' = b$) constructs P in V and the contribution from the upper surface vanishes.

On the other hand, if we choose $G_0 = G_0^-$ (anticausal solution $e^{-ik|z-z'|}/(-2ik)$), then the upper surface $z = a$ constructs $P = Re^{-ikz}$ in V and there is no contribution from the lower surface $z' = b$. This makes sense since information on the lower surface $z' = b$ will move with the upwave into the region between a and b, with a forward propagating causal Green function, G_0^+. At the upper surface $z' = a$, the anticausal G_0^- will predict from an upgoing wave measured at $z' = a$, what the wave was previously and when it was moving up and deeper than $z' = a$.

Since in exploration seismology the reflection data is typically upgoing, once it is generated at the reflector, and we only have measurements at the upper surface $z' = a$, we choose an anticausal Green function G_0^- in one-way wave back propagation in the finite volume model. If in addition we want to rid ourselves of the need for dP/dz' at $z' = a$ we can impose a Dirichlet boundary condition on G_0^-, to vanish at $z' = a$.

The latter Green function is labeled G_0^{-D}.

$$G_0^{-D} = -\frac{e^{-ik|z-z'|}}{2ik} - \left(-\frac{e^{-ik|z^I-z'|}}{2ik}\right) \tag{36}$$

where z^I is the image of z through $z' = a$. It is easy to see that $z^I = 2a - z$ and that

$$P(z) = -\left(\frac{dG_0^{-D}}{dz'}(z, z', \omega)\right)_{z'=a} P(a) = e^{-ik(z-a)}P(a) \tag{37}$$

in agreement with a simple Stolt FK phase shift for back propagating an up-field.

Please note that $P(z,\omega) = -\left(\frac{dG_0^{-D}}{dz'}(z, z', \omega)\right)_{z'=a} P(a, \omega)$ back propagates $P(z' = a, \omega)$, not G_0^{-D}. The latter thinking that G_0^{-D} back propagates data is a fundamental mistake/flaw in many seismic back propagation migration and inversion theories.

The multidimensional 3D generalization for downward continuing both sources and receivers for an upgoing wavefield is as follows:

$$\begin{aligned} & \int \frac{dG_0^{-D}}{dz_s}(x'_s, y'_s, z'_s, x_s, y_s, z_s; \omega) \\ \times & \left[\int \frac{dG_0^{-D}}{dz_g}(x'_g, y'_g, z'_g, x_g, y_g, z_g; \omega) D(x_g, y_g, z_g, x_s, y_s, z_s; \omega) dx_g dy_g\right] dx_s dy_s \\ = & M(x'_s, y'_s, z'_s, x'_g, y'_g, z'_g; \omega) \end{aligned}$$

where $x'_g - x'_s = x'_h$, $x'_g + x'_s = x'_m$, $y'_g - y'_s = y'_h$, $y'_g + y'_s = y'_m$, $z'_g - z'_s = z'_h$, and $x'_g + z'_s = z'_m$. The uncollapsed migration is $M(x'_m, y'_m, z'_m, x'_h, y'_h, z'_h = 0; t = 0)$ and is ready for subsequent AVO analysis in a multi-D subsurface (see *e.g.* Clayton and Stolt (1981), Stolt and Weglein (1985), and Weglein and Stolt (1999)).

We now examine Green's theorem for two way RTM in a 1D earth.

8 Propagation for RTM in a one dimensional earth: Using Green functions to avoid the need for data at depth, new noncausal or causal Green functions

Green's theorem in 3D in the $(\vec{r}, \omega)$ domain to determine a wavefield, $P(\vec{r}, \omega)$ for $\vec{r}$ in V is given by

$$\begin{aligned} P(\vec{r}, \omega) &= \int_V d\vec{r}\,' G_0(\vec{r}, \vec{r}\,', \omega)\rho(\vec{r}\,', \omega) \\ &\quad + \oint_S dS'\, \vec{n} \cdot (P(\vec{r}\,', \omega)\nabla' G_0(\vec{r}, \vec{r}\,', \omega) - G_0(\vec{r}, \vec{r}\,', \omega)\nabla' P(\vec{r}\,', \omega)) \end{aligned} \tag{38}$$

In 1D in the slab $a \le z \le b$, Equation (38) becomes

$$\begin{aligned} P(z, \omega) &= \int_a^b dz'\, G_0(z, z', \omega)\rho(z', \omega) \\ &\quad + |_a^b \left(P(z', \omega)\frac{dG_0(z, z', \omega)}{dz'} - G_0(z, z', \omega)\frac{dP(z', \omega)}{dz'} \right) \end{aligned} \tag{39}$$

Assuming no sources in the slab, the 1D homogeneous wave equation is

$$\left(\frac{d^2}{dz'^2} + k^2 \right) P(z', \omega) = 0 \text{ for } z < z' < b \tag{40}$$

with general solution

$$P(z', \omega) = Ae^{ikz'} + Be^{-ikz'} \text{ for } z < z' < b \tag{41}$$

where $k = \omega/c$. Given the conventions positive z' increasing downward and time dependence $e^{-i\omega t}$ in Fourier transforming from ω to t, the first term in Equation (41) is a downgoing wave and the second term is an upgoing wave.

The equation for the corresponding Green function is

$$\left(\frac{d^2}{dz'^2} + k^2 \right) G_0 = \delta(z - z') \tag{42}$$

with causal and anticausal solutions

$$G_0^+(z,z',\omega) = \frac{1}{2ik}e^{ik|z-z'|} \tag{43}$$

$$G_0^-(z,z',\omega) = -\frac{1}{2ik}e^{-ik|z-z'|} \tag{44}$$

Equation (39) suggests the Green function we need is such that it and its derivative vanish at $z' = b$. Such a Green function "kills" the need for measurements at $z' = b$.

Equation (42) is an inhomogeneous differential equation with general solution $A_1 e^{ikz'} + B_1 e^{-ikz'} + G_0(z,z',\omega)$ where the first two terms are the general solution to the homogeneous differential equation and the third term is any particular solution to the inhomogeneous differential equation. The choice $G_0(z,z',\omega) = G_0^+(z,z',\omega)$ gives the following general solution of Equation (42);

$$G_0(z,z',\omega) = A_1 e^{ikz'} + B_1 e^{-ikz'} + \frac{1}{2ik}e^{ik|z-z'|} \tag{45}$$

Its derivative is

$$\begin{aligned}\frac{dG_0(z,z',\omega)}{dz'} &= A_1 e^{ikz'} ik + B_1 e^{-ikz'}(-ik) \\ &\quad + \frac{1}{2ik}e^{ik|z-z'|} ik \ \mathrm{sgn}(z-z')(-1)\end{aligned} \tag{46}$$

Now we impose boundary conditions in order to find A_1 and B_1. The requirement that Equations (45) and (46) vanish at $z' = b$ gives

$$0 = A_1 e^{ikb} + B_1 e^{-ikb} + \frac{1}{2ik} e^{ik\underbrace{|z-b|}_{b-z}}$$

$$0 = A_1 e^{ikb} ik + B_1 e^{-ikb}(-ik) + \frac{1}{2ik} e^{ik\underbrace{|z-b|}_{b-z}} ik \ \underbrace{\mathrm{sgn}(z-b)}_{-1}(-1)$$

$$\begin{aligned} A_1 e^{ikb} + B_1 e^{-ikb} &= -\frac{1}{2ik}e^{ik(b-z)} \\ A_1 e^{ikb} - B_1 e^{-ikb} &= -\frac{1}{2ik}e^{ik(b-z)} \\ 2A_1 e^{ikb} &= -2\frac{1}{2ik}e^{ik(b-z)} \\ A_1 &= -\frac{1}{2ik}e^{-ikz} \end{aligned} \tag{47}$$

$$\begin{aligned} 2B_1 e^{-ikb} &= 0 \\ B_1 &= 0 \end{aligned} \tag{48}$$

Substituting Equations (47) and (48) into (45) gives

$$\begin{aligned} G_0(z,z',\omega) &= -\frac{1}{2ik}e^{-ikz}e^{ikz'} + \frac{1}{2ik}e^{ik|z-z'|} \\ &= -\frac{1}{2ik}(e^{-ik(z-z')} - e^{ik|z-z'|}) \end{aligned} \tag{49}$$

Note the following about Equation (49):
(1) When $z' = b$ $G_0(z,b,\omega)$ vanishes:

$$\begin{aligned} G_0(z,b,\omega) &= -\frac{1}{2ik}(e^{-ik(z-b)} - e^{ik\underbrace{|z-b|}_{b-z}}) \\ &= -\frac{1}{2ik}(\underbrace{e^{-ik(z-b)} - e^{-ik(z-b)}}_{0}) \end{aligned}$$

(2) When $a < z' < b$ $G_0(z,z',\omega)$ is neither causal nor anticausal due to the presence of the term $-1/2ik\, e^{-ik(z-z')}$.
(3) When $z' = a$ $G_0(z,a,\omega)$ is the sum of anticausal and causal terms, but not in general or at any other depth.

$$\begin{aligned} G_0(z,a,\omega) &= -\frac{1}{2ik}(e^{-ik\underbrace{(z-a)}_{|z-a|}} - e^{ik|z-a|}) \\ &= \underbrace{-\frac{1}{2ik}e^{-ik|z-a|}}_{anticausal} + \underbrace{\frac{1}{2ik}e^{ik(z-a)}}_{causal} \end{aligned}$$

(4) Normally one uses Dirichlet or Neumann or Robin boundary conditions on the surface S (in our 1D case at both a and b). Constructing the Green function Equation (49) has enabled us to use both Dirichlet and Neumann boundary conditions on part of the surface S (in our 1D case only at a).

The Green function for two way propagation that will eliminate the need for data at the lower surface of the closed Green's theorem surface is found by finding a general solution to the Green function for the medium in the finite volume model and imposing both Dirichlet and Neumann boundary conditions at the lower surface. We confirm that the Green function Equation (49), when used in Green's theorem, will produce a two way wave for $a < z < b$ with only measurements on the upper surface. Substituting Equation (41), its derivative, Equation (49), and its derivative into Equation (39) gives $P(z,\omega) = Ae^{ikz} + Be^{-ikz}$, *i.e.*, we recover the original two way wavefield. The details are in Appendix A.

A and B can be derived from the measured data $P(a)$ and $P'(a)$:

$$P(a) = Ae^{ika} + Be^{-ika}$$

$$
\begin{aligned}
P'(a) &= Ae^{ika}ik + Be^{-ika}(-ik) \\
\frac{P'(a)}{ik} &= Ae^{ika} - Be^{-ika} \\
2Ae^{ika} &= P(a) + \frac{P'(a)}{ik} \\
A &= e^{-ika}\frac{ikP(a) + P'(a)}{2ik} \\
2Be^{-ika} &= P(a) - \frac{P'(a)}{ik} \\
B &= e^{ika}\frac{ikP(a) - P'(a)}{2ik}
\end{aligned}
$$

In a homogeneous medium the 3D equivalent of Equation (40) is

$$(\nabla'^{\,2} + k^2)P(x', y', z', \omega) = 0$$

where $k = \omega/c$. Fourier transforming over x' and y' gives

$$\left(\frac{d^2}{dz'^{\,2}} \underbrace{-k_{x'}^2 - k_{y'}^2 + \frac{\omega^2}{c^2}}_{\equiv k_{z'}^2}\right) P(k_{x'}, k_{y'}, z', \omega) = 0$$

which looks like the 1D problem

$$\left(\frac{d^2}{dz'^{\,2}} + k_{z'}^2\right) P(k_{x'}, k_{y'}, z', \omega) = 0$$

with general solution

$$P(k_{x'}, k_{y'}, z', \omega) = Ae^{ik_{z'}z'} + Be^{-ik_{z'}z'}$$

We illustrate, in the next section, a more complicated 1D example, where the finite volume contains a reflector.

9 RTM and Green's theorem: two way wave propagation in a 1D finite volume that contains a reflector

Consider a single reflector example:
z increases downward,
the source is located at depth z_s (where $0 < z_s < a$),
the receiver is located at depth z_g (where $z_s < z_g < a$),

for $0 \le z \le a$ the medium is characterized by c_0,
for $z > a$ the medium is characterized by c_1, and
the reflection coefficient R and transmission coefficient T at the interface ($z = a$) are given by

$$\begin{aligned} R &= \frac{c_1 - c_0}{c_0 + c_1} \\ T &= \frac{2c_1}{c_0 + c_1} \end{aligned} \tag{50}$$

Assume the source goes off at $t = 0$. Then the wavefield P for $z < a$ is given by

$$P = \frac{e^{ik|z-z_s|}}{2ik} + R\,\frac{e^{-ik(z-a)}}{2ik} e^{ik(a-z_s)} \tag{51}$$

Detail: In the time domain, the front of the plane wave travels with $\delta(t - |z - z_s|/c_0)$ out from the source. Hence, the first term in Equation (51) for P is the incident wavefield (an impulse) and for the second term in P

$$\delta\left(t - \underbrace{\frac{|a - z_s|}{c_0}}_{\text{from source to reflector}} - \underbrace{\frac{|z - a|}{c_0}}_{\text{from reflector to field point } z} \right)$$

Fourier transforming gives:

$$\begin{aligned} \int e^{i\omega t}\delta\left(t - \frac{|z - z_s|}{c_0}\right) dt &= e^{\left(i\omega\frac{|z-z_s|}{c_0}\right)} \\ & \qquad e^{\left(i\left(\frac{|a-z_s|}{c_0} + \frac{|z-a|}{c_0}\right)\omega\right)} \\ \text{for } z < a \qquad & \qquad e^{\left(i\left(\frac{a-z_s}{c_0} + \frac{a-z}{c_0}\right)\omega\right)} \\ &= e^{-ik(z-a)+ik(a-z_s)} \\ &= e^{-ik(z-(2a-z_s))} \end{aligned}$$

Therefore $2a - z_s - z$ is the travel path from the source to the reflector and up to the field point z.

If instead of an incident Green function we choose a plane wave, we drop the $1/(2ik)$ and set $z_s = 0$, and then the incident plane wave passes the origin $z = 0$ at $t = 0$.

The transmitted wave field is for $z > a$

$$P = \frac{1}{2ik} T e^{ik|a-z_s|} e^{ik_1(z-a)} \tag{52}$$

with R and T given by Equation (50) then Equations (51) and (52) provide the solution for the total wave field everywhere.

Now we introduce Green's theorem. The total wavefield P satisfies

$$\left\{\frac{d^2}{dz'^2}+\frac{\omega^2}{c^2(z')}\right\}P=\delta(z'-z_s)$$

The Green function G will satisfy

$$\left\{\frac{d^2}{dz'^2}+\frac{\omega^2}{c^2(z')}\right\}G=\delta(z-z')$$

where

$$c(z')=\begin{cases} c_0 & z'<a \\ c_1 & z'>a \end{cases}$$

The solution for P is given in Equations (51) and (52). The solution for G will be determined below. G_H and G_P are a homogeneous solution and particular solution, respectively, of the following differential equations:

$$\left\{\frac{d^2}{dz^2}+\frac{\omega^2}{c^2(z)}\right\}G_H=0$$
$$\left\{\frac{d^2}{dz^2}+\frac{\omega^2}{c^2(z)}\right\}G_P=\delta$$

A particular solution, G_P, can be given by Equations (51) and (52) with z_s replaced by

$$P(z,z_s,\omega) \;=\; \Big|_A^B\{P(z',z_s,\omega)\frac{dG}{dz'}(z,z',\omega)-G(z,z',\omega)\frac{dP}{dz'}(z',z_s,\omega)\}$$

where $A=z_g$, the depth of the MS, and $B>a$ is the lower surface of Green's theorem.

The "source", *i.e.*, z, is within $[A,B]$ and either above or below the reflector at $z=a$ and conditions will be placed on the solution, G, (for a source within the volume) for the field point of G, *i.e.*, z', to satisfy at B. That is

$$(G(z,z',\omega))_{z'=B}=0$$
$$\text{and}\quad\left(\frac{dG}{dz'}(z,z',\omega)\right)_{z'=B}=0$$

First pick the "source" in the Green function to be above the reflector, then Equations (51) and (52) provide a specific solution when you substitute for z_s in P, the parameter, z, and for z in P the parameter, z'. The latter allows a particular solution for G for the case that z in G is within $[A,B]$ but above $z=a$.

Please note: The physical source is outside the volume, but the "source" in the Green function is inside the volume. Also, note that for the case of the (output point, z) "source" in the Green

function to be below the reflector and within $[A, B]$ that a different solution for P other than what is given in Equations (51) and (52), would be needed for a particular solution of G. The latter would require a solution for P where the source is in the lower half space.

What about the general solution for G_H

$$\left\{ \frac{d^2}{dz'^2} + \frac{\omega^2}{c^2(z')} \right\} G_H = 0 \tag{53}$$

The general solution to Equation (53) is, for any incident plane wave, $A(k)$ for $[A, B]$

$$G_H = \begin{cases} A_1 e^{ikz'} + B_1 e^{-ikz'} & z' < a \\ C_1 e^{ik_1 z'} + D_1 e^{-ik_1 z'} & z' > a \end{cases}$$

The general solution to Equation (53) has to allow the possibility of an incident wave from either direction, that's what general solution means!

The general solution for G for the single reflector problem and the source, z, above the reflector is given by

$$G(z, z', \omega) = \begin{cases} \frac{e^{ik|z'-z|}}{2ik} + R\frac{e^{-ik(z'-a)}}{2ik} e^{ik(a-z)} + A_1 e^{ikz'} + B_1 e^{-ikz'} & z' < a \\ \frac{T}{2ik} e^{ik|a-z|} e^{ik_1(z'-a)} + C_1 e^{ik_1 z'} + D_1 e^{-ik_1 z'} & z' > a \end{cases} \tag{54}$$

for the source z being above the reflector and we choose C_1 and D_1 such that

$$G(z, B, \omega) = 0$$

$$\text{and } \left[\frac{dG}{dz'}(z, z', \omega) \right]_{z'=B} = 0$$

where for $z' > a$ G_P above is $1/(2ik) T e^{ik|a-z|} e^{ik_1(z'-a)}$.

Equation (54) will be the Green function needed in Green's theorem to propagate/predict above the reflector at $z' = a$ where P and its derivative are given by Equation (53). In practice, the deghosted scattered wave is upgoing (one way) and finding its vertical derivative is simply $ik_z \times P$. Deghosting precedes migration.

For downward continuing past the reflector, as previously stated, the P solution needed for the particular solution of the Green function starts with a source in the lower half space where $k_1 = \omega/c_1$. That's how it works. In practice for a $v(x, y, z)$ medium a modeling will be required that imposes a double vanishing boundary condition at depth to produce the Green function for RTM.

10 Multidimensional RTM

Consider a volume V inside a homogeneous medium; V is bounded on the left by $x' = A$, on the right by $x' = L_1$, on the top by $z' = B$, and on the bottom by $z' = L_2$. We want to use

Green's theorem to estimate the wavefield P in V which requires we measure P and $\partial P/\partial n$ on the boundary S of V. However, we can place receivers only at $z' = B$. Can we construct a Green function G such that it and its normal derivative $\partial G/\partial n$ vanish on three sides of V so that P can be estimated in V using only the measurements on $z' = B$?

G can be written as the sum of a homogeneous solution G_H and a particular solution G_P where G satisfies the partial differential equation $(\nabla^{'2} + k^2)G = \delta(\vec{r} - \vec{r}^{'})$ and G_H satisfies the partial differential equation $(\nabla^{'2} + k^2)G_H = 0$. We try solutions of the form:

$$G(\vec{r}^{'}, \vec{r}, \omega) = \sum_{m,n} A_{m,n}(\vec{r}) X_m(x') Z_n(z') + G_P(\vec{r}^{'}, \vec{r}, \omega) \tag{55}$$

$$G_H(\vec{r}^{'}, \vec{r}, \omega) = \sum_{m,n} A_{m,n}(\vec{r}) X_m(x') Z_n(z') \tag{56}$$

with the boundary conditions that G and $\partial G/\partial n$ vanish at $x' = A$, $z' = L_2$, and $x' = L_1$, *i.e.*,

$$\begin{aligned}
&\text{at } x' = A \; G = 0 \text{ and } -\frac{\partial G}{\partial x'} = 0, \\
&\text{at } z' = L_2 \; G = 0 \text{ and } \frac{\partial G}{\partial z'} = 0, \text{ and} \\
&\text{at } x' = L_1 \; G = 0 \text{ and } \frac{\partial G}{\partial x'} = 0.
\end{aligned}$$

Substituting Equation (56) into $(\nabla^{'2} + k^2)G_H = 0$ gives:

$$\begin{aligned}
0 &= \left(\frac{\partial^2}{\partial x^{'2}} + \frac{\partial^2}{\partial z^{'2}} + k^2\right) X_m(x') Z_n(z') \\
&= X_m''(x') Z_n(z') + X_m(x') Z_n''(z') + k^2 X_m(x') Z_n(z') \\
&= \frac{X_m''(x')}{X_m(x')} + \frac{Z_n''(z')}{Z_n(z')} + k^2 \\
\Longrightarrow \quad & \frac{Z_n''(z')}{Z_n(z')} = -\lambda^2 \\
0 &= Z_n''(z') + \lambda^2 Z_n(z') \\
Z_n(z') &= C_1 e^{i\lambda_n z'} + C_2 e^{-i\lambda_n z'} \qquad (57) \\
0 &= X_m''(x') + (\underbrace{k^2 - \lambda^2}_{\equiv \mu^2}) X_m(x') \\
X_m(x') &= C_3 e^{i\mu_m x'} + C_4 e^{-i\mu_m x'} \qquad (58)
\end{aligned}$$

where $\mu_m^2 \longrightarrow X_m(x')$ and $\lambda_n^2 \longrightarrow Z_n(z')$. We assume $X_m(x')$ and $Z_n(z')$ are orthonormal and complete.

The boundary conditions on the left are $G(A, z') = 0$, $G_{x'}(A, z') = 0$, on the right $G(L_1, z') = 0$, $G_{x'}(L_1, z') = 0$, and on the bottom $G(x', L_2) = 0$, $G_{z'}(x', L_2) = 0$. Substituting these

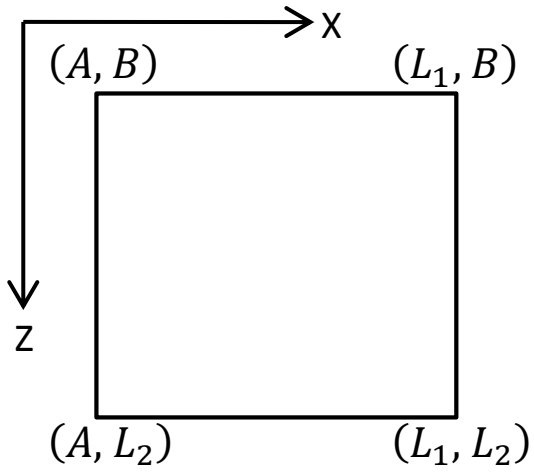

Figure 5: *Two dimensional finite volume model*

boundary conditions into Equation (55) gives:

$$0 = G(A, z', x, z) = \sum_{m,n} A_{m,n}(\vec{r}) X_m(A) Z_n(z') + G_P(A, z', x, z) \tag{59}$$

$$0 = G_{x'}(A, z', x, z) = \sum_{m,n} A_{m,n}(\vec{r}) X'_m(A) Z_n(z') + \frac{d}{dx'} G_P(A, z', x, z) \tag{60}$$

$$0 = G(L_1, z', x, z) = \sum_{m,n} A_{m,n}(\vec{r}) X_m(L_1) Z_n(z') + G_P(L_1, z', x, z) \tag{61}$$

$$0 = G_{x'}(L_1, z', x, z) = \sum_{m,n} A_{m,n}(\vec{r}) X'_m(L_1) Z_n(z') + \frac{d}{dx'} G_P(L_1, z', x, z) \tag{62}$$

$$0 = G(x', L_2, x, z) = \sum_{m,n} A_{m,n}(\vec{r}) X_m(x') Z_n(L_2) + G_P(x', L_2, x, z) \tag{63}$$

$$0 = G_{z'}(x', L_2, x, z) = \sum_{m,n} A_{m,n}(\vec{r}) X_m(x') Z'_n(L_2) + \frac{d}{dz'} G_P(x', L_2, x, z) \tag{64}$$

Equation (59) is:

$$-G_P(A, z', x, z) = \sum_{m,n} A_{m,n}(\vec{r}) X_m(A) Z_n(z')$$

Multiplying by $Z_s(z')$, integrating, and substituting Equations (57) and (58) give:

$$-\int_{L_2}^{B} G_P(A, z', x, z) Z_s(z')\, dz' = \sum_{m} A_{m,s}(\vec{r}) X_m(A)$$

$$
\begin{aligned}
& -\int_{L_2}^{B} G_P(A,z',x,z)(C_1 e^{i\lambda_s z'} + C_2 e^{-i\lambda_s z'})\,dz' \\
= & \sum_m A_{m,s}(\vec{r})(C_3 e^{i\mu_m A} + C_4 e^{-i\mu_m A})
\end{aligned}
$$

In similar fashion we get:

$$
\begin{aligned}
& -\int_{L_2}^{B} \frac{d}{dx'} G_P(A,z',x,z)(C_1 e^{i\lambda_s z'} + C_2 e^{-i\lambda_s z'})\,dz' \\
= & \sum_m A_{m,s}(\vec{r}) i\mu_m (C_3 e^{i\mu_m A} - C_4 e^{-i\mu_m A}) \\
& -\int_{L_2}^{B} G_P(L_1,z',x,z)(C_1 e^{i\lambda_s z'} + C_2 e^{-i\lambda_s z'})\,dz' \\
= & \sum_m A_{m,s}(\vec{r})(C_3 e^{i\mu_m L_1} + C_4 e^{-i\mu_m L_1}) \\
& -\int_{L_2}^{B} \frac{d}{dx'} G_P(L_1,z',x,z)(C_1 e^{i\lambda_s z'} + C_2 e^{-i\lambda_s z'})\,dz' \\
= & \sum_m A_{m,s}(\vec{r}) i\mu_m (C_3 e^{i\mu_m L_1} - C_4 e^{-i\mu_m L_1}) \\
& -\int_{A}^{L_1} G_P(x',L_2,x,z)(C_3 e^{i\mu_s x'} + C_4 e^{-i\mu_s x'})\,dz' \\
= & \sum_m A_{m,s}(\vec{r})(C_1 e^{i\lambda_n L_2} + C_2 e^{-i\lambda_n L_2}) \\
& -\int_{A}^{L_1} \frac{d}{dz'} G_P(x,L_2,x,z)(C_3 e^{i\mu_s x'} + C_4 e^{-i\mu_s x'})\,dz' \\
= & \sum_m A_{m,s}(\vec{r}) i\lambda_n (C_1 e^{i\lambda_n L_2} - C_2 e^{-i\lambda_n L_2})
\end{aligned}
$$

The $A_{m,s}$ coefficients are determined by the imposed Dirichlet and Neumann boundary conditions on the base and walls of the finite volume.

11 General Step-by-Step Prescription for RTM in a finite volume where the velocity configuration is $c(x,y,z)$

Step (1) For a desired downward continued/migration output point (x,y,z) for determining $P(x,y,z,\omega)$

$$
\left\{\nabla^2 + \frac{\omega^2}{c^2(x',y',z')}\right\} G_0(x',y',z',x,y,z,\omega) = \delta(x-x')\delta(y-y')\delta(z-z')
$$

for a source at (x, y, z) and P is the physical/causal solution satisfying

$$\left\{ \nabla'^{\,2} + \frac{\omega^2}{c^2(x', y', z')} \right\} P(x', y', z', x_s, y_s, z_s, \omega) = A(\omega)\delta(x' - x_s)\delta(y' - y_s)\delta(z' - z_s)$$

G_0 is the auxiliary or Green function satisfying

$$\left\{ \nabla'^{\,2} + \frac{\omega^2}{c^2(x', y', z')} \right\} G_0(x, y, z, x', y', z', \omega) = \delta(x - x')\delta(y - y')\delta(z - z')$$

for (x, y, z) in V and G_0 and $\nabla' G_0 \cdot \hat{n}'$ are both zero for (x', y', z') on the lower surface S_L and the walls S_W of the finite volume.

The solution for G_0 in V and on S can be found by a numerical modeling algorithm where the 'source' is at (x, y, z) and the field, G_0, at (x', y', z') and $\nabla G_0 \cdot \hat{n}$ are both imposed to be zero on S_L and S_W. Once that model is run for a source at (x, y, z) for $G_0(x', y', z', x, y, z, \omega)$ [for every eventual wave prediction point, (x, y, z), for P] where G_0 satisfies Dirichlet and Neumann conditions for (x', y', z') on S_L and S_W we output $G_0(x', y', z', x, y, z, \omega)$ for (x', y', z') on S_U (the measurement surface).

Step (2) Downward continue the receiver

$$P(x, y, z, x_s, y_s, z_s, \omega) = \int \left\{ \frac{\partial G_0}{\partial z'}(x, y, z, x', y', z', \omega) P(x', y', z', x_s, y_s, z_s, \omega) \right.$$
$$\left. - \frac{\partial P}{\partial z'}(x', y', z', x_s, y_s, z_s, \omega) G_0(x, y, z, x', y', z', \omega) \right\} dx' dy'$$

where z' = fixed depth of the cable and (x_s, y_s, z_s) = fixed location of the source. This brings the receiver down to (x, y, z), a point below the measurement surface in the volume V.

Step (3) Now downward continue the source

$$P(x_g, y_g, z, x, y, z, \omega) = \int \left\{ \frac{\partial G_0}{\partial z_s}(x, y, z, x_s, y_s, z_s, \omega) P(x_g, y_g, z, x_s, y_s, z_s, \omega) \right.$$
$$\left. - \frac{\partial P}{\partial z_s}(x_g, y_g, z, x_s, y_s, z_s, \omega) G_0(x, y, z, x_s, y_s, z_s, \omega) \right\} dx_s dy_s$$

$P(x_g, y_g, z, x, y, z, \omega)$ is a downward continued receiver to (x_g, y_g, z) and the source to (x, y, z) and change to midpoint offset $P(x_m, x_h, y_m, y_h, z_m, z_h = 0, \omega)$ and

$$\int d\omega \left\{ \frac{\partial G_0}{\partial z_s}(x, y, z, x_s, y_s, z_s, \omega) P(x_g, y_g, z, x_s, y_s, z_s, \omega) \right.$$
$$\left. - \frac{\partial P}{\partial z_s}(x_g, y_g, z, x_s, y_s, z_s, \omega) G_0(x, y, z, x_s, y_s, z_s, \omega) \right\}$$

and Fourier transform over x_m, x_h, y_m, y_h to find $\widetilde{P}(k_{x_m}, k_{x_h}, k_{y_m}, k_{y_h}, k_{z_m}, z_h = 0, t = 0)$ the RTM uncollapsed migration for a general $v(x, y, z)$ velocity configuration.

12 RTM and Inverse Scattering Series (ISS) imaging: now and the future

In practice, RTM is often applied using a wave equation that avoids reflections at reflectors above the target. Impedance matching at boundaries in the modeling, allows density and velocity to both have rapid variation at a reflector, but are arranged so that the normal incidence reflection coefficient will be zero. The result ia a smooth 'apparent velocity' that can support diving waves, but seeks to avoid the discontinuous velocity model commitment that including reflections would require. In RTM, including those reflections above the reflector to be imaged, drives a need for an accurate and discontinuous velocity model. The ISS imaging methods welcome (and require) all the reflectors above the one reflector being imaged, without implying a concomitant need for an accurate discontinuous velocity model.

One way to view the RTM to ISS imaging step is as removing reflectionless reflectors by an 'impedance matching' differential equation in RTM to avoid the need for a commitment to an accurate and discontinuous velocity. With ISS imaging we have the opposite situation: the welcome of all reflections to the imaging of any reflector, and without the need to know or determine the discontinuous velocity model. That's the next step, and our first field data tests with ISS imaging are underway. In the interim, we thought it useful to provide an assist to current best imaging RTM practice. We will be returning reflections to reflectors thereby turning the problem, observation, and obstacle in current RTM into the instrument of significant imaging progress, and without the need for a velocity model, discontinuous or otherwise.

13 Summary

- Migration and migration-inversion: required velocity information for location and beyond velocity only for amplitude analyses at depth.
- So when we say medium is 'known,' the meaning of known depends on the goal: migration or migration-inversion.
- Backpropagation and imaging: each evolved and then extended/generalized and merged into migration-inversion.

For one way wave propagation the double downward continued data, D is

$$D(\text{at depth}) = \int_{S_s} \frac{\partial G_0^{-D}}{\partial z_s} \int_{S_g} \frac{\partial G_0^{-D}}{\partial z_g} D \, dS_g \, dS_s$$

where D in the integrand $= D$(on measurement surface), $\partial G_0^{-D}/\partial z_s =$ anticausal Green function with Dirichlet boundary condition on the measurement surface, $s =$ shot, and $g =$ receiver.

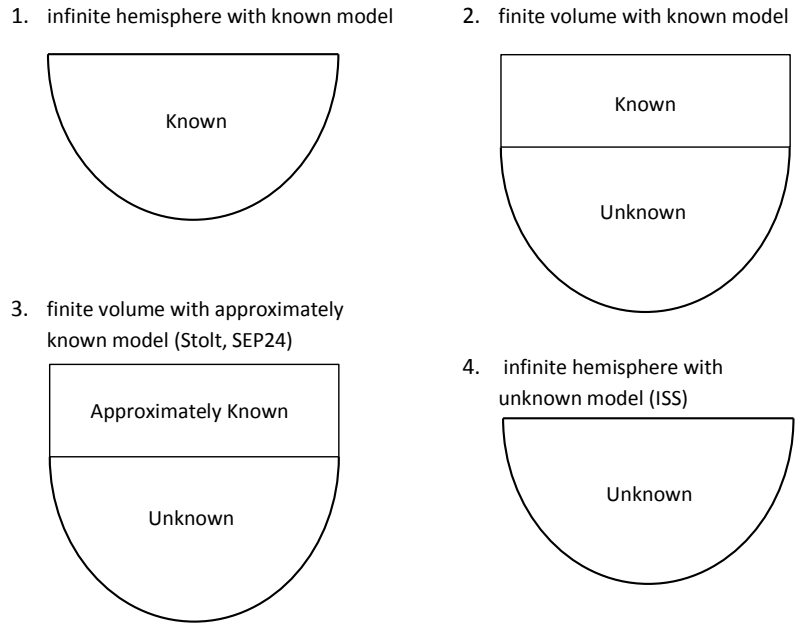

Figure 6: *Backpropagation model evolution*

For two way wave double downward continuation:

$$D(\text{at depth}) = \int_{S_s} \left[\frac{\partial G_0^{DN}}{\partial z_s} \int_{S_g} \left\{ \frac{\partial G_0^{DN}}{\partial z_g} D + \frac{\partial D}{\partial z_g} G_0^{DN} \right\} dS_g + G_0^{DN} \frac{\partial}{\partial z_s} \int_{S_g} \left\{ \frac{\partial G_0^{DN}}{\partial z_g} D + \frac{\partial D}{\partial z_g} G_0^{DN} \right\} dS_g \right] dS_s$$

where D in the integrands $= D$(on measurement surface). G_0^{DN} is neither causal nor anticausal. G_0^{DN} is not an anticausal Green function; it is not the inverse or adjoint of any physical propagating Green function. It is the Green function needed for Reverse Time Migration (RTM). G_0^{DN} is the Green function for the model of the finite volume that vanishes along with its normal derivative on the lower surface and the walls.

If you want to use the anticausal Green function of the two way propagation with Dirichlet boundary conditions at the measurement surface then you can do that, but you will need measurements at depth and on the vertical walls.

To have the Green function for two way propagation that doesn't need data at depth and on the vertical sides/walls, that requires a non-physical Green function that vanishes along with its derivative on the lower surface and walls.

In the Inverse Scattering Series (ISS) model sketch 4 in Figure 6 the Lippmann-Schwinger (LS) equation over all space, rather than Green's theorem, is called upon and the Lippmann-Schwinger equation requires no imposed boundary conditions on S since all boundary conditions are already incorporated in LS from linearity/superposition and causality (Equation (29)).

The appropriate Green function, for a closed surface integral in Green's theorem, with an arbitrary and known medium within the volume can be satisfied with any Green function satisfying the propagation properties within the volume and with Dirichlet, Neumann, or Robin boundary conditions on the closed surface. The issue and/or problem in exploration reflection seismology is the measurements are only on the upper surface.

Why Green's theorem for migration algorithms.

1. Allows a wave theoretical platform/framework for wavefield prediction from surface measurements that builds on quantitative and potential field theory history and evolution.

2. Allows $(\vec{x},\omega)$ processing without transform artifacts and yet is wave theoretic in a $(\vec{x},\omega)$ world where up-down is not so simple to define as in $(\vec{k},\omega)$. Deghosting (Zhang (2007)) and wavelet estimation (Weglein and Secrest (1990)) are other examples where Green's theorem provides $(\vec{x},\omega)$ advantage.

3. Allows avoidance of very common pitfalls and erroneous algorithm derivations based on qualitative (at best) methods launched from Huygens' principle or discrete matrix inverses and it allows the wave theoretic imaging conditions introduced by Clayton and Stolt (1981) and Stolt and Weglein (1985) to be used rather than the lesser cross-correlation of wavefield imaging concepts.

Backpropagation is quantitative from Green's theorem rather than these: G_0^{-1}, G_0^*, less wave theoretic more generalized inverse, discrete matrix thinking approaches for backpropagation.

For RTM and Green's theorem the data, D, at depth is definitely not

$$D \neq \int G_{0S}^{-1} \int G_{0R}^{-1} D \text{ (Huygens)}$$

where G_0^- indicates an anticausal Green function. This is OK with Huygens but violates Green's theorem and the equation is not dimensionally consistent with the right hand side not having the dimension of data, D. The data, D, at depth for one way waves is

$$D = \int_{S_s} \frac{\partial G_0^{-D}}{\partial z_s} \int_{S_g} \frac{\partial G_0^{-D}}{\partial z_g} D \, dS_g \, dS_s \text{ (Green)}$$

where D = Dirichlet boundary condition on top and G_0^- anticausal. This is OK with Green but not for two way RTM propagation. The data, D, at depth for two way waves is

$$D = \int_{S_s} \left[\frac{\partial G_0^{DN}}{\partial z_s} \int_{S_g} \left\{ \frac{\partial G_0^{DN}}{\partial z_g} D + \frac{\partial D}{\partial z_g} G_0^{DN} \right\} dS_g$$

$$+G_0^{DN}\frac{\partial}{\partial z_s}\int_{S_g}\left\{\frac{\partial G_0^{DN}}{\partial z_g}\,D+\frac{\partial D}{\partial z_g}G_0^{DN}\right\}\,dS_g\Bigg]\,dS_s \text{ (Green)}$$

where DN = Dirichlet and Neumann boundary conditions to be imposed on bottom and walls and G_0^{DN} is neither causal nor anticausal nor a combination.

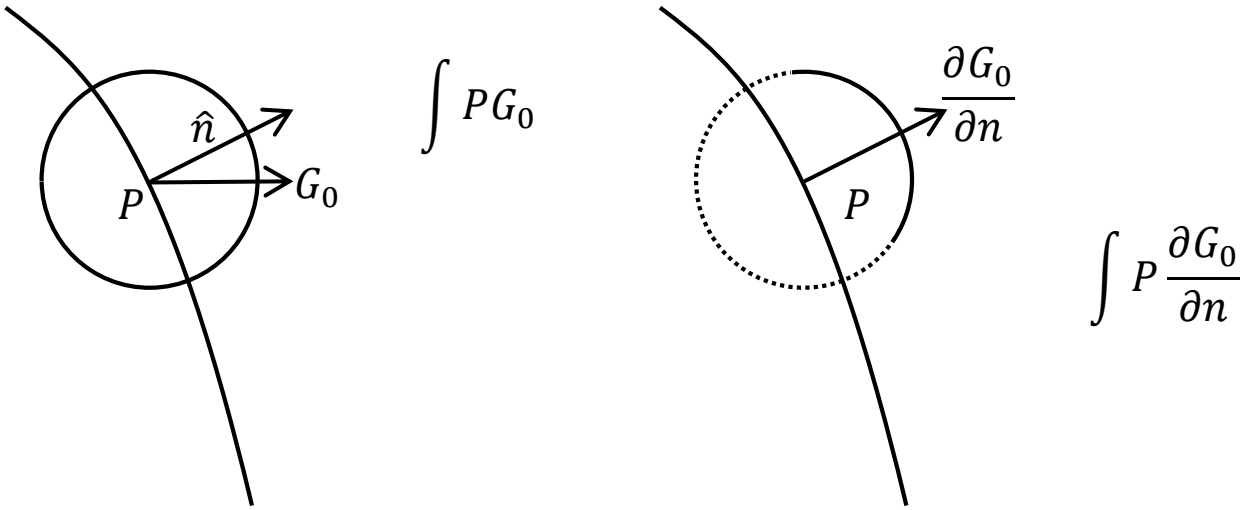

Figure 7: *Qualitative vs. quantitative wave propagation: (Left) Huygens, and e.g., Whitmore, McMechan, Fletcher et al. Berkhout, Claerbout, Schuster, Yi Luo; (Right) Green, and e.g., Morse and Feshbach, Born and Wolf, Stolt, Schneider, Esmersoy and Oristaglio (1988), Weglein and Secrest (1990), Weglein et al. (1997), Liu et al. (2006), Ramírez and Weglein (2009)*

14 Comments and future developments

In this manuscript, we provide a firm foundation for RTM based on Green's theorem. As in the case of interferometry (Ramírez and Weglein (2009)) misuse, abuse and/or misunderstanding of Green's theorem in RTM has also led to strange and curious interpretations, and to opinions being offered about the cause of artifacts and observed problems and communicating 'deep new insights' that are neither new nor accurate. We communicate here to simply understand and stick with Green's theorem as the guide and solution in both cases, interferometry and RTM. The original RTM methods of running the wave equation backwards with surface reflection data as a boundary condition is not a wave theory method for wavefield prediction, neither in depth nor in reversed time. In Huygens' principle the wavefield prediction doesn't have the dimension of a wavefield. In fact that idea corresponds to the Huygens' principle idea (Huygens (1690)) which was made into a wave theory predictor by George Green in 1826.

15 ACKNOWLEDGEMENTS

We thank the M-OSRP sponsors, NSF-CMG award DMS-0327778 and DOE Basic Sciences award DE-FG02-05ER15697 for supporting this research. We thank Adriana Ramírez and Einar Otnes of WesternGeco for useful discussions and suggestions regarding RTM. We thank Xu Li, Shih-Ying Hsu, Zhiqiang Wang and Paolo Terenghi of M-OSRP for useful comments and assistance in typing the manuscript.

16 Appendix A: Confirmation that the Green function Equation (49), when used in Green's theorem, will produce a two way wave for $a < z < b$ with only measurements on the upper surface.

$$
\begin{aligned}
& P(z,\omega) \\
= & \int_a^b dz' \left(\underbrace{\frac{-1}{2ik} e^{-ikz} e^{ikz'} + \frac{1}{2ik} e^{ik|z-z'|}}_{G_0(z,z',\omega)} \right) \underbrace{\rho(z',\omega)}_{0} \\
& + |_a^b \left((\underbrace{A e^{ikz'} + B e^{-ikz'}}_{P(z',\omega)}) \left(\underbrace{\frac{-1}{2ik} e^{-ikz} e^{ikz'} ik + \frac{1}{2ik} e^{ik|z-z'|} ik \ \operatorname{sgn}(z-z')(-1)}_{\frac{dG_0(z,z',\omega)}{dz'}} \right) \right. \\
& \left. - \left(\underbrace{\frac{-1}{2ik} e^{-ikz} e^{ikz'} + \frac{1}{2ik} e^{ik|z-z'|}}_{G_0(z,z',\omega)} \right) (\underbrace{A e^{ikz'} ik + B e^{-ikz'} (-ik)}_{\frac{dP(z',\omega)}{dz'}}) \right) \\
= & \frac{-1}{2} |_a^b (\cancel{A e^{ik(2z'-z)}} + A \ \operatorname{sgn}(z-z') e^{ikz'} e^{ik|z-z'|} \\
& + B e^{-ikz} + B \ \operatorname{sgn}(z-z') e^{-ikz'} e^{ik|z-z'|} \\
& - \cancel{A e^{ik(2z'-z)}} + A e^{ikz'} e^{ik|z-z'|} + B e^{-ikz} - B e^{-ikz'} e^{ik|z-z'|}) \\
= & \frac{-1}{2} (A \underbrace{\operatorname{sgn}(z-b)}_{-1} e^{ikb} e^{ik \underbrace{|z-b|}_{b-z}}
\end{aligned}
$$

$$
\begin{aligned}
&+\cancel{Be^{-ikz}} + B\underbrace{\operatorname{sgn}(z-b)}_{-1}e^{-ikb}e^{ik\underbrace{|z-b|}_{b-z}} \\
&+Ae^{ikb}e^{ik\underbrace{|z-b|}_{b-z}} + \cancel{Be^{-ikz}} - Be^{-ikb}e^{ik\underbrace{|z-b|}_{b-z}} \\
&-A\underbrace{\operatorname{sgn}(z-a)}_{1}e^{ika}e^{ik\underbrace{|z-a|}_{z-a}} \\
&-\cancel{Be^{-ikz}} - B\underbrace{\operatorname{sgn}(z-a)}_{1}e^{-ika}e^{ik\underbrace{|z-a|}_{z-a}} \\
&-Ae^{ika}e^{ik\underbrace{|z-a|}_{z-a}} - \cancel{Be^{-ikz}} + Be^{-ika}e^{ik\underbrace{|z-a|}_{z-a}}) \\
= \;& \frac{-1}{2}(-\cancel{Ae^{ik(2b-z)}} - Be^{-ikz} + \cancel{Ae^{ik(2b-z)}} - Be^{-ikz} \\
&-Ae^{ikz} - \cancel{Be^{-ik(2a-z)}} - Ae^{ikz} + \cancel{Be^{-ik(2a-z)}}) \\
= \;& \frac{-1}{2}(-2Ae^{ikz} - 2Be^{-ikz}) \\
= \;& Ae^{ikz} + Be^{-ikz}
\end{aligned}
$$

References

Berkhout, A. J. and C. P. A. Wapenaar. "Delft philosophy on inversion of elastic data." *58th Annual International Meeting, SEG, Expanded Abstracts* 7 (1988): 831–833.

Clayton, R. W. and R. H. Stolt. "A Born-WKBJ inversion method for acoustic reflection data." *Geophysics* 46 (1981): 1559–1567.

Bruin, C. G. M.de , C. P. A. Wapenaar, and A. J. Berkhout. "Angle-dependent reflectivity by means of prestack migration." *Geophysics* 55 (1990): 1223–1234.

Bruin, C. G. M.de , C. P. A. Wapenaar, and A. J. Berkhout. "Imaging for angle-dependent reflectivity in the presence of dip." *60th Annual International Meeting, SEG, Expanded Abstracts* 9 (1990): 1503–1506.

Dong, S., Y. Luo, X. Xiao, S. Chávez-Pérez, and G. T. Schuster. "Fast 3D target-oriented reverse-time datuming." *Geophysics* 74 (2009): WCA141–WCA151.

Esmersoy, Cengiz and Michael Oristaglio. "Reverse-time wave-field extrapolation, imaging, and inversion." *Geophysics* 53 (1988): 920–931.

Fletcher, R., P. Fowler, P. Kitchenside, and U. Albertin. "Suppressing unwanted internal reflections in prestack reverse-time migration." *Geophysics* 71 (2006): E79–E82.

Huygens, Christiaan. *Traité de la lumiere.* Leiden, Netherlands: Pieter van der Aa, 1690.

Liu, F., A.B. Weglein, K.A. Innanen, and B. G. Nita. "Multi-dimensional seismic imaging using the inverse scattering series." *76th Annual International Meeting, SEG, Expanded Abstracts* 25 (2006): 3026–3030.

Liu, F., G. Zhang, S. A. Morton, and J. P. Leveille. "An optimized wave equation for seismic modeling and reverse time migration." *Geophysics* 74 (2009): WCA153–WCA158.

Luo, Yi and Gerard T. Schuster. "Bottom-up target-oriented reverse-time datuming." *CPS/SEG Geophysics Conference and Exhibition* (2004): F55.

Ramírez, A. C. and A. B. Weglein. "Green's theorem as a comprehensive framework for data reconstruction, regularization, wavefield separation, seismic interferometry, and wavelet estimation: A tutorial." *Geophysics* 74 (2009): W35–W62.

Sava, P. and S. Fomel. "Time-shift imaging condition in seismic migration." *Geophysics* 71 (2006): S209–S217.

Sava, P. and I. Vasconcelos. "Efficient computation of extended images by wavefield-based migration." *79th Annual International Meeting, SEG, Expanded Abstracts* 28 (2009): 2824–2828.

Schneider, W. A. "Integral formulation for migration in two-dimensions and three-dimensions." *Geophysics* 43 (1978): 49–76.

Stolt, R. H. Migration by Fourier transform. Technical Report 23-48, Geophysics, 1978.

Stolt, R. H. and A. B. Weglein. "Migration and inversion of seismic data." *Geophysics* 50 (1985): 2458–2472.

Symes, W. W. "Reverse-time migration with optimal checkpinting." *Geophysics* 72 (2007): SM213–SM221.

Toselli, A. and O. Widlund. *Domain decomposition methods –Algorithms and theory*. springer, 2000.

Weglein, A. B., F. V. Araujo Gasparotto, P. M. Carvalho, and R. H. Stolt. "An inverse-scattering series method for attenuating multiples in seismic reflection data.." *Geophysics* 62 (1997): 1975–1989.

Weglein, A. B. and B. G. Secrest. "Wavelet estimation for a multidimensional acoustic or elastic Earth." *Geophysics* 55 (1990): 1975–1989.

Weglein, A. B. and R. H. Stolt. "Migration-inversion revisited (1999)." *The Leading Edge* 18 (1999): 950–952, 975.

Whitmore, D. N. "Iterative depth imaging by back time propagation." *53rd Annual International Meeting, SEG, Expanded Abstracts* (1983): 382–385.

Zhang, J. *Wave theory based data preparation for inverse scattering multiple removal, depth imaging and parameter estimation: analysis and numerical tests of Green's theorem deghosting theory*. PhD thesis, M-OSRP University of Houston, 2007.

Zhang, Y., J. Sun, and S. Gray. "Reverse-time migration: amplitude and implementation issues." *77th Annual International Meeting, SEG, Expanded Abstracts* 25 (2007): 2145–2149.